A Numerical Renormalization Group Approach to Dissipative Quantum Impurity Systems

Dissertation
zur Erlangung des Doktorgrades
der Naturwissenschaften

vorgelegt am Fachbereich Physik
der Johann Wolfgang Goethe-Universität in Frankfurt am Main

von David Roosen
aus Mönchengladbach

Frankfurt am Main
2011

vom Fachbereich Physik
der Johann Wolfgang Goethe-Universität als Dissertation angenommen.

Dekan	Prof. Dr. Michael Huth
Gutachter	Prof. Dr. Walter Hofstetter
	Prof. Dr. Peter Kopietz

Contents

Introduction

The miniaturization of electronics is reaching its limits. Structures necessary to build integrated circuits from semiconductors are shrinking and could reach the size of only a few atoms within the next few years. It will be at the latest at this point in time that the physics of nanostructures gains importance in our every day life.

This thesis deals with the physics of quantum impurity models. All models of this class exhibit an identical structure: the simple and small impurity only has few degrees of freedom. It can be built out of a small number of atoms or a single molecule, for example. In the simplest case it can be described by a single spin degree of freedom, in many quantum impurity models, it can be treated exactly. The complexity of the description arises from its coupling to a large number of fermionic or bosonic degrees of freedom (large meaning that we have to deal with particle numbers of the order of 10^{23}). An exact treatment thus remains impossible. At the same time, physical effects which arise in quantum impurity systems often cannot be described within a perturbative theory, since multiple energy scales may play an important role. One example for such an effect is the Kondo effect, where the free magnetic moment of the impurity is screened by a "cloud" of fermionic particles of the quantum bath.

The Kondo effect is only one example for the rich physics stemming from correlation effects in many body systems. Quantum impurity models, and the oftentimes related Kondo effect, have regained the attention of experimental and theoretical physicists since the advent of quantum dots, which are sometimes also referred to as as artificial atoms. Quantum dots offer a unprecedented control and tunability of many system parameters. Hence, they constitute a nice "playground" for fundamental research, while being promising candidates for building blocks of future technological devices as well.

Recently Loss' and DiVincenzo's proposal of a quantum computing scheme based on spins in quantum dots [1], increased the efforts of experimentalists to coherently manipulate and read out the spins of quantum dots one by one. In this context two topics are of paramount importance for future quantum information processing: since decoherence times have to be large enough to allow for good error correction schemes, understanding the loss of phase coherence in quantum impurity systems is a prerequisite for quantum computation in these systems. Nonequilibrium phenomena in quantum impurity systems also have to be understood, before one may gain control of manipulating quantum bits. As a first step towards more complicated nonequilibrium situations, the reaction of a system to a quantum quench, i.e. a sudden change of external fields or other parameters of the system can be investigated.

We give an introduction to a powerful numerical method used in this field of research, the numerical renormalization group method, and apply this method and its recent enhancements to various quantum impurity systems. A detailed structure of this thesis is given in the following section.

Structure of this thesis

The first part motivates the theoretical study presented in this thesis by explaining relevant effects and a few recent experiments on quantum impurity models. First, we give a brief historical review of the Kondo effect in real metals. We then explain how the Kondo effect manifests itself in quantum dots, which are sometimes also referred to as "artificial atoms" and are especially interesting because of their unique tunability of parameters, allowing for experimental verification of theoretical predictions. Afterwards, we discuss recent experimental efforts on coherently controlling single spins and give a short introduction to the new and exciting field of molecular electronics summarizing two recent experiments in this field.

The numerical renormalization group method is the subject of the second part of this thesis. This numerical method has been developed more than 30 years ago, but continues to be an important and state-of-the-art tool to study quantum impurity systems. The results presented in this work are to a large part obtained applying this method. Hence, we explain the different variants of this non-perturbative method, starting with its application to quantum impurity models dealing with a large number of fermionic or bosonic degrees of freedom. Recent enhancements of the method are illustrated as well: The density matrix numerical renormalization group method, the smart choice of a complete basis of the underlying Fock space, the time-dependent numerical renormalization group method, which allows to calculate the reaction of the system to a sudden change in parameters or "quantum quench", and the systematic way of dealing with the effects of finite temperatures plus a few "tricks" on how to improve the accuracy of numerical renormalization group calculations. We demonstrate the effects of the different variants using the single impurity Anderson model.

In the main part of this thesis, the third and last part, we describe the applications of the numerical renormalization group method to different quantum impurity models with fermionic and bosonic quantum "baths". First, we study the time-dependent magnetization of the ferromagnetic Kondo model asking how fast an initially polarized spin will reduce its magnetization due to spin flip scattering and investigate about the nature of the final state of the quantum system. Furthermore we investigate the anisotropic Kondo model and compare its static and time-dependent magnetization in the different spin-bath coupling regimes to the properties of the spin-boson model. The purpose of the comparison of the two models is to answer the question, whether the well-known bosonization mapping of the anisotropic Kondo model to the spin-boson model also holds for systems out of equilibrium. We apply the numerical renormalization group method to a system consisting of two spins, which are coupled via an Ising interaction to each other and at the same time are both coupled to a common quantum bath consisting of bosonic particles. We observe an interesting interplay between the direct and the bath-induced interaction between the two spins in both, the static as well as the "dynamic" (i.e. time-dependent) observables of the model. Our numerical results are compared to findings of other analytic methods in this chapter as well. Finally, we study a model describing an Aharanov-Bohm interferometer setup. Spinless electrons can tunnel from two lead electrodes to two parallel quantum dots, which are both coupled to a common Einstein phonon mode. We are particularly interested in the situation where the interferometer is tuned to complete destructive interference and the phonons couple differently to the quantum dots, such that only pure decoherent processes enable electronic transport through the interferometer. We ask ourselves how the conductance through the interferometer depends on the system parameters and investigate if there are incoherent transport processes at vanishing frequency, temperature and transport voltage, which are not captured in a perturbative

Part I

Experimental Motivation

Chapter 1

Kondo Effect

1.1 Kondo Effect in Metals

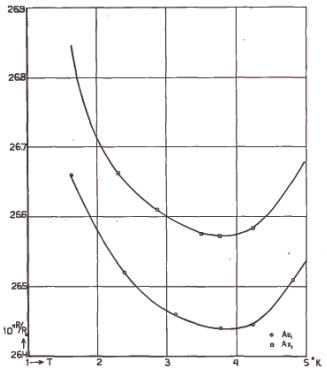

Figure 1.1: Resistance of 'not very pure' Au-wires between $T = 1\,\mathrm{K}$ and $T = 5\,\mathrm{K}$ (taken from Ref. [2])

Historically the first indications of the Kondo effect were found in a conductance measurement of gold at very low temperatures by de Haas and coworkers in 1934 [2]. As a function of temperature the resistivity increased when lowering the temperatures below 4K (see Fig. 1.1).

Although they already stated that their samples consisted of "not very pure gold wires", they could not explain the rising electrical resistivity ρ^{el} at this time. The standard way of calculating the resistivity of a metal was to add up partial resistivities according to Matthiesen's rule. The temperature dependence of the processes considered at that time were all such, that one would expect ρ^{el} to decrease upon lowering the temperature: the interaction between electrons and the vibrations of the crystal lattice, the phonons, increases rapidly with rising temperature, since more lattice vibrations are excited, and contributes $\rho^{el}_{ph} \propto T^5$. Fermi-liquid theory tells us that scattering between two electrons causes a resistivity $\rho^{el}_{e-e} \propto T^2$, and the scattering between electrons and static impurities only depends on the concentration of the impurities in the metal $\rho^{el} \propto c_{imp}$ and thereby is independent of temperature.

All mechanisms considered up to this point could not explain the observed minimum in resistivity as a function of temperature. This longstanding puzzle was only solved by Jun

Kondo in 1964 [3]. He showed how certain scattering processes from *magnetic* impurities (which have a local moment due to an unpaired electron in the atoms' $d-$ or $f-$ shell) could give rise to a partial resistivity scaling with temperature as $\log(T)$. These scattering processes were characterized by an exchange of the spin orientation of the unpaired electron on the impurity and the electrons in the conduction band and could explain the observed minimum in the resistivity of gold wires doped with iron impurities.

In his original work Kondo demonstrated the spin-flip mechanism using a simple *s-d* or Kondo-Hamiltonian (see Eq. (11.6)). Later Schrieffer and Wolff [4] gave a rigorous proof that this model is equivalent to the single impurity Anderson model in a certain parameter regime (for details of this transformation we refer the reader to Chap. 11).

In the following we want to illustrate the spin-flip mechanisms leading to the so called Kondo resonance using the more general single impurity Anderson model [5]. In second quantization the Hamilton operator for this model reads

$$\hat{\mathcal{H}}_A = \underbrace{\varepsilon_{d,\mu}\hat{d}^\dagger_\mu\hat{d}_\mu + U\left(\hat{d}^\dagger_\uparrow\hat{d}_\uparrow\right)\left(\hat{d}^\dagger_\downarrow\hat{d}_\downarrow\right)}_{\text{impurity}} + \underbrace{\sum_{\mathbf{k}}\varepsilon_{\mathbf{k}}\hat{c}^\dagger_{\mathbf{k}\mu}\hat{c}_{\mathbf{k}\mu}}_{\text{conduction band}} + \underbrace{\sum_{\mathbf{k}}V_{\mathbf{k}}\left(\hat{c}^\dagger_{\mathbf{k}\mu}\hat{d}_\mu + \hat{d}^\dagger_\mu\hat{c}_{\mathbf{k}\mu}\right)}_{\text{interaction}}, \tag{1.1}$$

where $\hat{d}^{(\dagger)}_\mu$ denotes the (creation) annihilation operator of an electron on the impurity (throughout the thesis we use the convention $\hbar = k_B = g = \mu_B = 1$ for the Planck constant, the Boltzmann constant, the gyromagnetic ratio and the Bohr magneton. We also sum over repeated spin indices μ using the Einstein notation). Within the single impurity Anderson model the impurity only has a single electronic level at energy $\varepsilon_{d,\mu}$, its spin's z-component either pointing up ($\mu =\uparrow$) or down ($\mu =\downarrow$). For a moment let us assume a situation, where all parameters of the model are independent of the electrons spin μ. If a second electron is located at the impurity site, an extra *on-site* energy of U has to be paid due to the Coulomb repulsion of the electrons. The electrons can tunnel from the impurity to the conduction band and occupy the non-interacting eigenstates created by the operators $\hat{c}^\dagger_{\mathbf{k}\mu}$. The structure of the Hamilton operator $\hat{\mathcal{H}}_A$ consisting of an impurity part, a part describing the non-interacting quantum bath and an interaction between the two is common to all quantum impurity models. The model is illustrated in the left panel of Fig. 1.2.

If the energy of the electronic level on the impurity lies below the Fermi level (defined by the occupation of eigenstates in the non-interacting conduction band), the impurity will be occupied by a single electron with a fixed spin orientation μ. The energy it takes for the electron to leave the impurity and occupy an eigenstate in the Fermi sea of non-interacting electrons in the conduction band can be of the order of a few electron-Volts, which following classical mechanics forbids such a process to take place (for the particle-hole symmetric case where $U = -2\varepsilon_d$ a doubly occupied impurity is classically forbidden as well). In quantum mechanics, however, the Heisenberg uncertainty principle allows such a *virtual* state, where the electron leaves the impurity, if after a very short time of the order of $h/|\varepsilon_d|$ (where h is the Planck constant) another electron from the conduction band tunnels to the impurity. Since the spin of the electron tunneling from the conduction band to the impurity must not point in the same direction as the electron occupying the impurity in the first place, this process can exchange (or flip) the spin of the electron on the impurity. If many of these spin-flip processes are taken together the energy spectrum (or density of states) of the system are changes qualitatively: a new eigenstate, the Kondo resonance, with an eigenenergy located exactly at the Fermi level is generated.

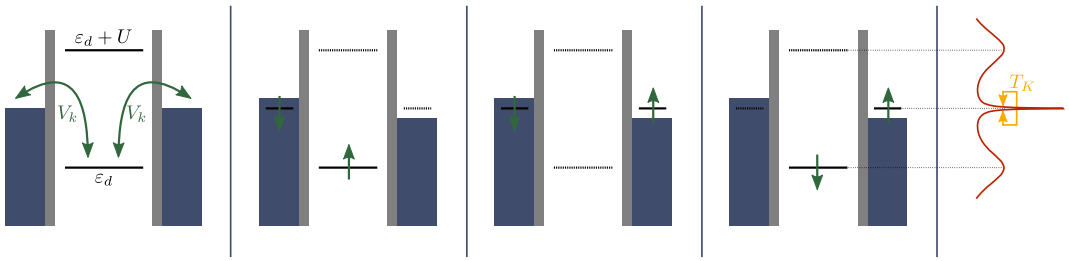

Figure 1.2: Illustrating the single impurity Anderson model and its relevant parameters (left panel). The next three panels to the right explain the spin-flip scattering mechanism. From left to right: initial situation, virtual intermediate state, final situation. To the very right, a sketch of the resulting density of states, including the many-body resonance at the Fermi level with a width determined by the Kondo temperature T_K is presented.

In his perturbative description of the resistivity Jun Kondo could show [3] that the second term in the perturbation series involving the spin-flip mechanisms contributes a terming scaling as $\log(T)$, which explains the minimal resistivity at a finite temperature. But even a more sophisticated perturbative treatment of the resistivity by Abrikosov [6] summing up the leading contributions of higher order scattering processes, led to a unphysical diverging resistivity in the limit $T \to 0$. The temperature scale at which the perturbative description becomes unreliable is nowadays known as the *Kondo temperature* T_K and the problem of the divergence of resistivity was referred to as *Kondo problem* (as shown in 1978 by Haldane [7] T_K is related to the parameters of the single impurity Anderson model by $T_K = \frac{\sqrt{\Gamma U}}{2} \exp(\frac{\pi \varepsilon_{d,\mu}(\varepsilon_{d,\mu}+U)}{\Gamma U})$, where $\Gamma = \pi \rho V_k^2$ and $\rho = \frac{1}{2W}$ the density of states for the free conduction band for a flat band).

Despite its simple mathematical description it took yet almost ten more years of concerted effort by the theoretical physics community to "solve" the Kondo problem. The physical picture emerging during that time was that the impurity spin is gradually screened by conduction electrons as the temperature is lowered [8].

In the late 1960's Anderson's poor man's scaling approach [9] set the theoretical framework for the understanding of the Kondo problem. In the scaling approach, the low-temperature properties of a system close to a critical point are assumed to be reproduced by a coarse grained model, where the high-energy degrees of freedom (i.e. the eigenstates close to the edge of the conduction band) are integrated out and the remaining degrees of freedom are described by a Hamilton operator of the same form as the original one. His work led to more sophisticated renormalization group methods, such as Wilson's numerical renormalization group method [10], which confirmed the physical picture emerged before and "solved" the Kondo problem. Since the non-perturbative numerical renormalization group method is the main method used to obtain results throughout this thesis, we refer to Chap. 4 for further details. The numerical renormalization group method allowed Nozières to develop an intuitive description of the low-temperature physics of Kondo systems [11, 12] in terms of quasiparticles within a Landau Fermi liquid theory. The density of states corresponding to these quasiparticles forms a narrow peak at the Fermi level with a width proportional to T_K, the Kondo resonance. Further confirmation of the quasiparticle interpretation of the Kondo effect came by the exact solution of the thermodynamics of the Kondo model by Bethe Ansatz calculations

(independently conducted by two different groups in the early 1980's, cf. Refs. [13, 14] and [15, 16]).

Besides the classical example of "not very pure" gold wires, *heavy fermion compounds* such as $La_{1-x}Ce_xCu_6$ or $Ce_{1-x}La_xPb_3$ ($0 < x \leq 1$), where a large number of magnetic impurities are present, but the Ruderman-Kittel-Kasuya-Yosida (RKKY) interaction between them is small, also exhibit a resistivity minimum as a function of temperature due to the Kondo effect. In this related and very active field of research, the magnetic impurities formed by the Cerium and Ytterbium ions can be treated as isolated scatterers and the scattering events of the conduction band electrons with the magnetic ions results in an enhancement of the effective mass of quasiparticles in a Fermi liquid description of the compounds. As in quantum impurity systems, the Kondo effect also plays an important role in the description of the heavy fermion compounds (see for example Ref. [17] and references therein).

1.2 Kondo Effect in Quantum Dots

The Kondo effect has regained interest among physicists during the last decade, caused by the advent of quantum dot fabrication (for a comprehensive reasoning on the "refreshed" interest in the Kondo effect see Ref. [18]). Quantum dots, which are sometimes also referred to as "artificial atoms" because their electronic properties resemble the ones of real atoms, are small confined regions in semiconductors. Exploiting the advances in semiconductor technology, the structures used to confine these regions have become as small as a few nanometers, which limits the number of electrons present in this region. Applying gate voltages the number of electrons in these quantum dots can be controlled one by one, allowing an unprecedented control of quantum impurity systems. The interaction between the different magnetic scatterers, which is always present in real metals with dilute magnetic impurities as well as heavy fermion compounds and is complicated to describe in a simple model, can either be eliminated completely isolating a single quantum dot or tuned in a controlled manner (for a short overview of recent process in the control over single spins in quantum dots, see Sec. 2.1).

The Kondo effect in quantum dots has been predicted independently by two different research teams in the late 1980's (see Refs. [19] and [20]). It was predicted for situations where the voltages on the gates are tuned such that an odd number of electrons is located on the dot exhibiting a finite magnetic moment acting as a magnetic impurity. Though the underlying mechanism is identical, there is a qualitative difference of the way the Kondo effect manifests itself in quantum dots and real metals, which is connected to their different geometries: the mixing of eigenstates with different momenta increases resistivity in real metals, where the electron states are described by plane waves. In quantum dots, in contrast, the mixing of eigenstates from different "leads" increases conductivity, since the electrons have to travel through the quantum dot (there is no way "around" it). The Kondo resonance at the Fermi edge thus facilitates the transport through the nanometer-sized structure. The spin-flip scattering consequently has the opposite effect on the resistivity of quantum dots and in real metals.

A first measurement of the current passing through a "single electron transistor" or quantum dot in the Coulomb blockade regime investigating the emerging Kondo resonance was performed by David Goldhaber-Gordon and coworkers in 1998 [21]. A scanning tunneling microscope image of the semiconductor structure defining the quantum dots and their tunneling to the "leads" is shown in Fig. 1.3.

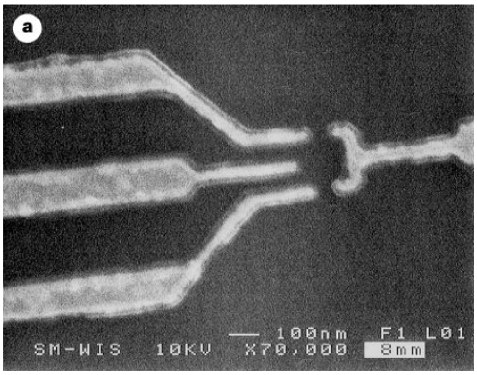

Figure 1.3: Image of the semiconductor structure used for the first measurement of the Kondo effect in quantum dots (taken from Ref. [21]). 'Three gate electrodes, the one on the right and the upper and lower ones on the left, control the tunnel barriers between reservoirs of the two-dimensional electron gas (the "leads" at top and bottom) and the droplet of electrons (the quantum dot itself). The middle electrode on the left is used as a gate to change the energy of the droplet relative to the two dimensional electron gas.' Source and drain electrodes are not shown.

In a subsequent experiment in the group of Leo Kouwenhoven in Delft [22], the control over the different parameters defining the quantum dot acting as an impurity was demonstrated. The conductance measured in this experiment reached values close to the so called "unitary limit" of $G = \frac{2e^2}{h}$ for temperatures well below the Kondo temperature and an odd number of electrons on the quantum dot (cf. Fig. 1.4).

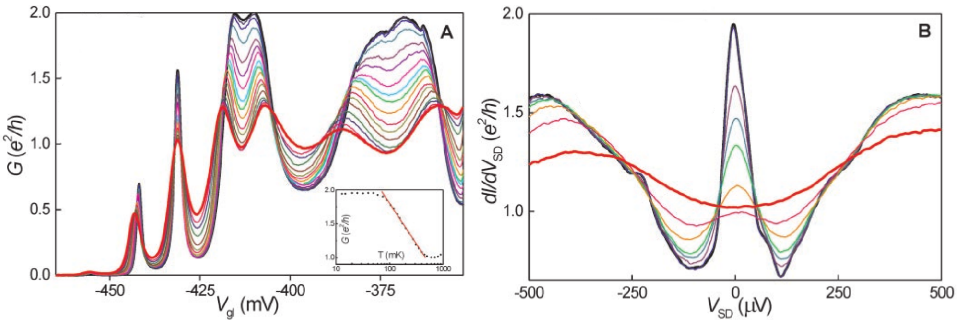

Figure 1.4: Lowering the temperature (going from the red to the dark blue curve) one observes a difference in the conductance through the quantum dot (left panel). If an even number of electrons is located on the dot, the conductance decreases, while for an odd number, the Kondo effect increases the conductance up to the unitary limit $G = \frac{2e^2}{h}$. In the right panel the differential conductance of a quantum dot with an odd number of electrons as a function of source-drain voltage is shown (both plots are taken from Ref. [22]).

Chapter 2

Coherent Control of Single Spins

In this chapter we want to outline some of the recent progress in coherently controlling the spins in solid state systems following the instructive review article by Hanson and coworkers, see Ref. [23]. We therefore focus on two different types of systems, single spins in quantum dots and N-V color centers in diamond structures.

2.1 Quantum Dots

One of the most important and widely used experimental setups to control single spins in solid state systems are quantum dots. In quantum dots the charge carriers are confined to small regions of the semiconductor using (electric and magnetic) fields and reducing the size of the semiconductor crystal in one or more dimensions. Because of this confinement, the eigenenergy spectra of quantum dots are gapped, resembling the spectra of real atoms. This is why they are commonly referred to as "artificial atoms" as well.

Fabricating Quantum Dots

There exist two different strategies building quantum dot structures: Starting from a two-dimensional electron gas (a layer of GaAs on a substrate, for example) electrical fields can be applied using surface gates or tailoring the band structure by edging material out of the semiconductor layer. This approach is very flexible allowing an almost unlimited variety of structures to be applied to the semiconductor. To reduce the decoherence induced by the fluctuation of the nuclear spins (Overhauser field), isotropically purified silicon or carbon layers can be used.

The second approach to build quantum dots is to grow nanocrystals of a certain material upon a substrate of a different material (for example InGaAs crystals on a GaAs layer). This approach has the advantage that a large number of quantum dots can be fabricated on a single substrate in a single process. Once the crystal is grown, the bandgap profile is fixed an cannot be changed anymore in contrast to the first approach, where one has more control adjusting voltages and thereby inducing electrical fields. On the other hand, these system offer a unique possibility to study self-organization of quantum dots on surfaces and allow to investigate interaction between a large number of quantum dots.

In the following we will highlight some of the advances in controlling single spins in quantum dots fabricated using the more flexible approach starting with a two-dimensional electron gas.

Exploiting Spin Selections Rules

First attempts to manipulate single spins in quantum dots using gate voltage pulses led to the observation that the decay times of single spins could be enlarged substantially (up to four orders of magnitude going from 10 ns to 200 μs), if the transition between the two eigenstates involved was forbidden by spin-selection rules [24]. The spin selection rules were also exploited to prolong the relaxation times of two-electron spin states up to a few milliseconds [25] and recently spin relaxation times on the order of a second have been observed in magnetic fields of a few Tesla in a recent experiment, see Ref. [26].

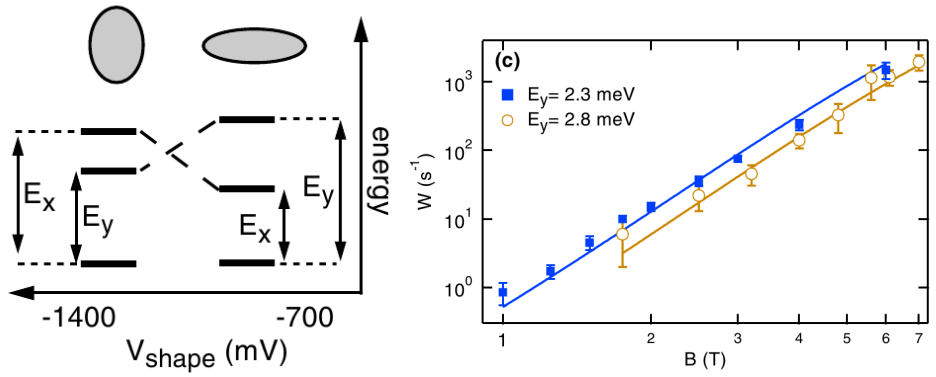

Figure 2.1: Left panel: Altering the gate voltage V_{shape} in the quantum dot setup chosen in Ref. [26], the shape of the dot and thus the eigenenergy spectrum is changed, enabling the exploitation of spin selection rules. Right panel: Spin relaxation rate for two different sets of gate voltages as a function of magnetic field $B(T)$. Note that the relaxation time $T_1 = W^{-1}$ exceeds $T_1 = 1s$ for $B = 1T$, where spin-orbit mediated coupling to phonons is the dominant relaxation mechanism. Taken from Ref. [26].

Quantum Dot SWAP-Gate

There are several proposals of building quantum computers using spins in semiconductors. In order to be able to do actual quantum computations using spins, it is necessary to perform certain operations on two-spin states additionally to single-spin operations. For several proposals of quantum computation using spins, this essential building block is an experimental realization of a SWAP gate in semiconductors (see for example Ref. [27]).

Controlling the strength of the interaction between two neighboring quantum dots is thus a necessary pre-condition for quantum computation. An essential step towards building a quantum SWAP gate was made by a group of experimentalists in Harvard [28]. They were able to observe coherent oscillations of two spins in a double quantum dot (Fig. 2.2 shows an image of their experimental setup). To be able to prepare, manipulate and measure the two-electron spin states they had to use fast electrical control of the exchange interaction between the two electrons. Reducing the dephasing due to the GaAs-host nuclei using spin-echo pulse sequences and other quantum control techniques, they observed Rabi oscillations of the two-electron spin states and demonstrated a 180-ps $\sqrt{\text{SWAP}}$ operation.

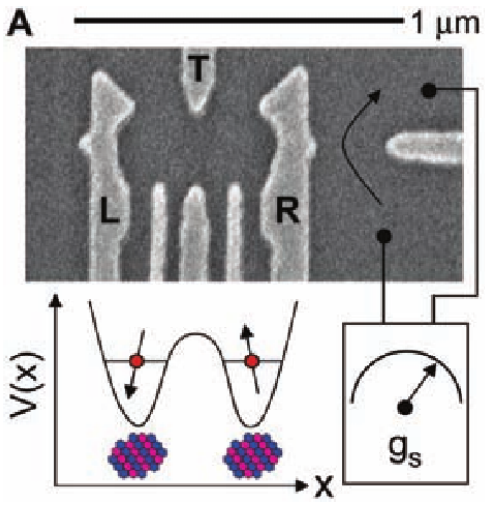

Figure 2.2: Scanning tunneling microscope image of the experimental setup demonstrating coherent control of a quantum two-level system. The gate T was used to tune the inter-dot tunneling couping, while the quantum point contact conductance g_s exhibits a strong dependence on the number of electrons on the right dot. Taken from Ref. [28].

Rotating Single Spins in Quantum Dots

Experiments demonstrating the coherent rotation of a single spins have been performed using magnetic resonance [29] as well as electric fields [30], where the spin transitions are mediated through the spin-orbit interaction. The rotations were performed on a time scale of about a 100 ns following the latter approach, which has the advantage that a fully electrical control is easier to implement on "a chip", since electrical fields can be confined more easily to small regions.

Explaining the complete experiment of Nowack and colleagues [30] in detail is beyond the scope of this thesis, since we only want point out some recent progress in experimental research in this chapter. Instead, let us only briefly explain the spin manipulation and detection scheme utilized to measure the spin rotation in Ref. [30], which is illustrated in Part C. of Fig. 2.3. There are four steps or stages within this scheme. First the two excess electrons in the double-dot structure are initialized in a triplet state with parallel spin. The triplet configuration , because of the small interdot coupling and the effects of nuclear fields. Using a gate voltage pulse, this configuration is "frozen", i.e. the two spins are isolated and tunneling to the reservoirs or between the dots is forbidden. The reason tunneling between the dots is forbidden, is because the eigenenergy of the triplet state on the right dot [not shown] is much larger than the energy of the singlet state [S(0,2)]. Since the electric field is stronger on the right quantum dot, the ac voltage burst applied in the third stage rotates the spin of the excess electron on the right dot by an angle depending on the length of the burst. In the read-out stage the excess electron on the left dot can tunnel to the right dot if the two electron spins are aligned antiparallel. Thereby the scheme allows a detection of the single spin rotation using electric fields.

According to the authors of Ref. [30], combining the $\sqrt{\text{SWAP}}$ gate mentioned in the preceding paragraph with the electrically driven single-spin resonance brings all-electrical

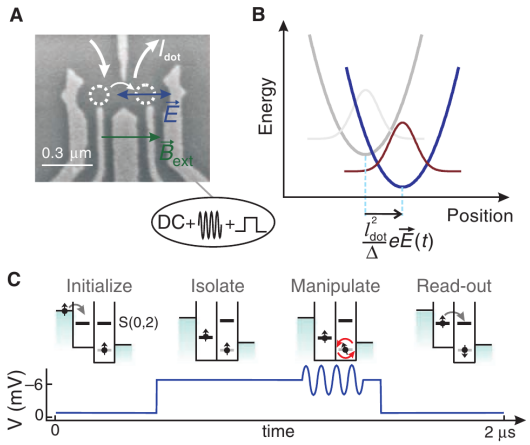

Figure 2.3: A. Scanning electron micrograph of device used in Ref. [30], where DC voltages, microwaves and fast pulses can be applied to the quantum dot. B. Illustration of the effect of the electric field on the potential: The center of the electron wave is displaced and the potential depth is changed. C. Schematic of the spin manipulation and detection scheme. Taken from Ref. [30].

universal control of electron spins within reach.

Optical Control of Quantum Dots

Using optical experimental techniques to control the spin of single electrons in quantum dots opens up new perspectives. If circular polarized light is shone onto the dot, a single electron hole pair with a well-defined spin state can be created. Detecting the polarization of light emitted upon recombination, the spin state can be read out as well using purely optical techniques. Recently the precession of a single spin in a magnetic field was measured time-resolved [31] using the rotation of a linearly polarized incident laser beam reflected from the quantum dot (which rotates due to the Kerr effect).

Shining circularly polarized light with a frequency slightly below the optical transition on the quantum dot, the spin state can be manipulated as well. Due to the ac-Stark effect [32] a short laser pulse shifts the eigenenergy for one spin species to lower values and acts as an effective magnetic field the electrons on the dot. Tuning the intensity and the detuning, single spin rotations on time scales as short as 30 ps have been achieved [33]. This speed-up of several orders of magnitude for the spin manipulation allows more manipulations within the spin's decoherence time and thus could prove to be an important step in the context of quantum error corrections.

2.2 Color Centers in Diamond

Single spins in solid state systems can be prepared in two different ways. Besides the previously described quantum dot approach, one way is to dope the semiconductor with another species of atoms (for example using phosphorus in silicon structures). If the concentration is low enough, individual impurities can be addressed.

An extremely successful approach of coherently controlling single spins emerging in the last few years has been to use the nitrogen-vacancy color center in diamond, which is made of a nitrogen atom substituting a single carbon atom next to a missing carbon atom (the vacancy) in the diamond structure (for an illustration, see Fig. 2.4).

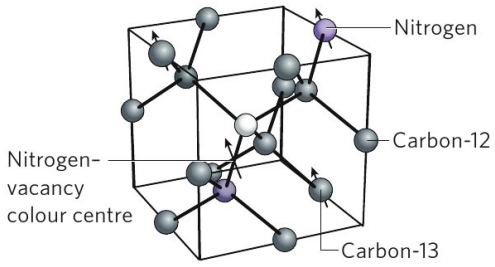

Figure 2.4: Diamond structure illustrating the N-V color center. Taken from Ref. [23]

The advantages of this new approach over the "classical" semiconductor systems consist in their long decoherence times even at room temperature and in the fully optical control for cooling, reading [34] and manipulating [35] the spins of the color centers using their strong optical transitions. The decoherence is dominated by the long-range dipole interaction between the nitrogen impurities acting as a spin bath to the color center. Applying strong magnetic fields and operating at low temperatures thermally polarizes the spins of the N atoms and the decoherence times increase up to few hundred microseconds for very small nitrogen concentrations. In these experiments the effect of carbon-13 isotopes with a natural abundance of 1.1% was observed. Due to the very fast rotation times of the order of 10 ns, more than 10000 error free operations can be performed during the coherence time of the spin.

Growing diamond structures by chemical vapor deposition techniques and ion-implanting the nitrogen defects in an isotopically purified diamond structure could open a route to "designing" spin environments for the color centers (for an article covering the potential of diamond structures for coherent manipulation of single spins see Ref. [36]).

Chapter 3

Molecular Electronics

In this last chapter of the first part we want to introduce two recent experiments as examples for systems of "molecular electronics". We focus on single (in general complex) molecules in the following, which are coupled to electronic leads, since they may be described by quantum impurity models. A sketch of a molecule in a three-terminal setup (source, drain and gate electrode) is given in the left panel of Fig. 3.1.

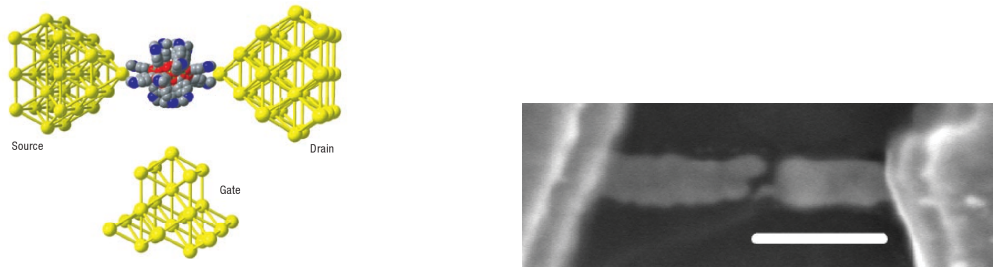

Figure 3.1: Left panel: Sketch of the single molecule magnet in a transistor geometry (taken from Ref. [37]) Right panel: STM image of the electrodes formed by electromigration. The size bar corresponds to 200nm (taken from Ref. [38]).

Despite the obvious advantages of scaling down the size of electronic components, the main goal of engineering electronic devices from single molecules is to use the molecule's structure and intrinsic properties (like its rotational symmetry, mechanical degrees of freedom imposed by its geometry or electronic structure) to tailor the electronic properties of nano-scale devices. Trapping single molecules and attaching them to electronic leads is experimentally feasible forming nanometer-sized gaps in gold wires on aluminum-oxide substrates by electromigration, for example (a scanning tunneling microscope image of such a junction is displayed in the right panel of Fig. 3.1).

The two experiments we introduce focus on conductance measurements through molecules trapped in these nanogaps. We introduce an experiment by the group from Delft in the Netherlands, where the conductance through a single molecule magnet [38] is measured and explain an experiment conducted in Grenoble, where a quantum phase transition in a C_{60}-molecule was observed [39].

3.1 C_{60}-Molecule Quantum Dots

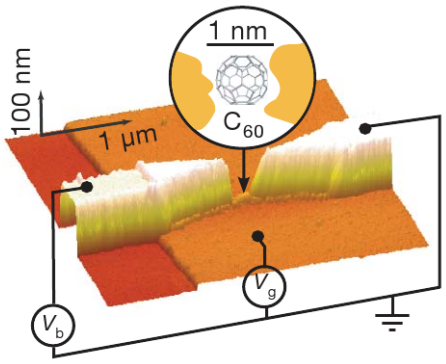

Figure 3.2: Atomic force microscope micrograph of the device used to measure the quantum phase transition in a C_{60}-molecule quantum dot (taken from Ref. [39]).

Many properties of strongly correlated electron systems such as high-temperature superconductors, are believed to be governed by quantum criticality, which forces a system to evolve between two distinct, competing ground states. We highlight an experiment on a molecular quantum dot made of a single C_{60} molecule trapped in a nanometer sized gap formed by electrodes using electromigration techniques [39] (see Fig. 3.2). The authors report an example of a quantum phase transition between two different Kondo phases observed at low temperature due to the strong coupling to the electronic leads. A gate voltage and not an additional magnetic field is used to drive a transition between two different types of electron spin states on the impurity (singlet and triplet). In both configurations the impurity molecule is occupied by an even number of electrons.

Measurements of differential conductance $\frac{\partial I}{\partial V}$ are conducted at temperatures $35mK < T < 20K$ and magnetic fields B up to $8T$ for different bias V_b and gate V_g voltages. The gate voltage fixes the occupancy of molecule (see right panel of Fig. 3.3): For an odd number of electrons, the "usual" Kondo effect leads to a single sharp resonance in the differential conductance at the Fermi level. The more interesting regime is obtained tuning the gate voltage such that an even number of electrons is located on the dot (the right panel of Fig. 3.3 shows a "zoom" into this region of the conductance map).

In this case, two distinct impurity configurations are observed. The electrons on the molecular quantum dot are either in a singlet or a triplet eigenstate. The energy splitting of the two configurations can be tuned by adjusting the gate voltage. The interpretation of the two eigenstates is confirmed by the observed shifting of the Kondo resonances altering the strength of the applied magnetic field. In both phases a finite bias anomaly at $V_b = \pm|E_s - E_t|$ is observed as well (here $E_{s/t}$ denotes the eigenenergy of the singlet/triplet eigenstate). Additionally on the triplet side, a zero-bias anomaly is related to a partially screened spin-1 Kondo effect.

Interestingly the zero-bias conductance at the singlet-triplet degeneracy point is not enhanced as one would expect for a Kondo resonance involving two screening channels (which was the case for vertical semiconductor quantum dots, see Ref. [40]). The absence of the singlet-triplet Kondo effect indicates that the quantum phase transition is of Kosterlitz-

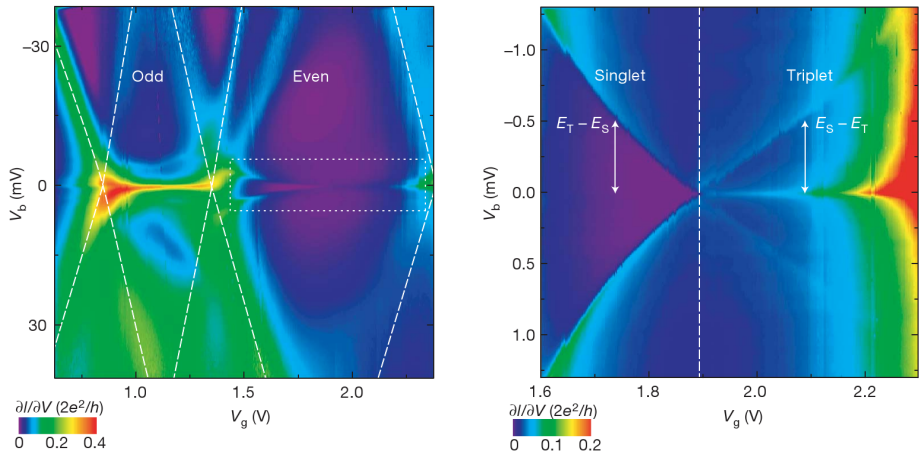

Figure 3.3: Differential conductance $\partial I/\partial V$ through the C_{60}-molecule quantum dot at $T = 35mK$ (taken from Ref. [39]). Left panel: For an odd number of electrons, the system displays a "usual" Kondo effect, characterized by the conductance peak at the Fermi level. Right panel: zoom into the conductance map for even electron number on the dot (white rectangle in the right panel) showing the singlet to triplet quantum phase transition.

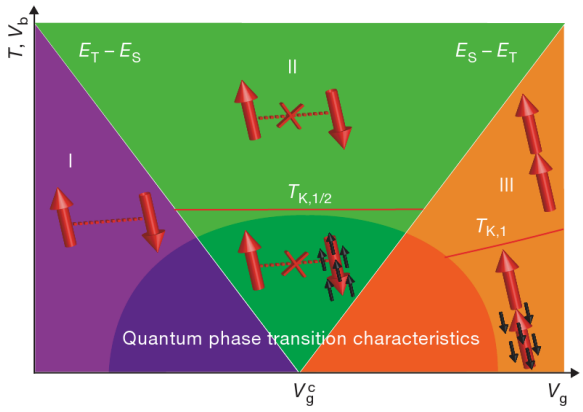

Figure 3.4: Sketch of the phase diagram as a function of V_g and V_b (or T). The molecule spin states are represented by large red arrows and screening electrons are represented by smaller, black arrows. In region I the spin state of the molecule is given by a strongly bound singlet. In region II the two spin states decouple from each other, and the spin, which is more strongly coupled to the leads, is fully screened by means of a spin-1/2 Kondo effect associated with the large Kondo temperature $T_{K,\frac{1}{2}}$. The ground state of the quantum dot in region III is a spin-1 triplet, which shows an becomes partially screened at the Kondo temperature $T_{K,1}$ (taken from Ref. [39]).

Thouless type, which has been predicted theoretically [41, 42] for multi-level quantum dots where a single screening channel couples to one of the two spin states of the single dot. Discussing the experimentally measured conductance in the vicinity of the quantum phase transition the authors observe the dissociation of the singlet and triplet states into two spin-1/2 impurities, each being screened independently as depicted in Fig. 3.4, which provides strong evidence for the Kosterlitz-Thouless character of the phase transition.

3.2 Single Molecule Magnets

An interesting new class of materials are single molecule magnets (SMMs), which contain a finite number of interacting spin centers (e.g. paramagnetic ions). Many single molecule magnets posses magnetic ground states and hysteresis effects of purely molecular origin can be observed. Two examples for molecular magnets are sketched in Fig. 3.5.

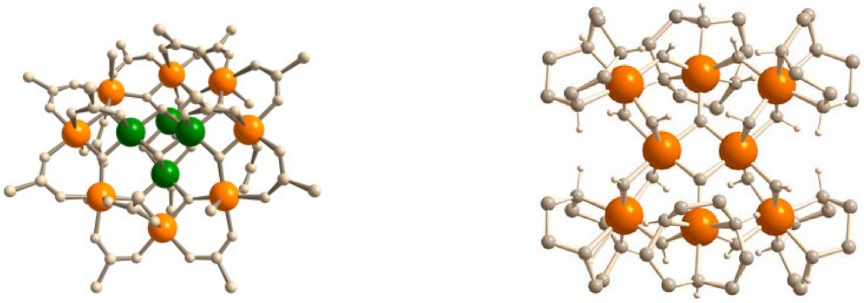

Figure 3.5: Illustrating the chemical structure of two single molecule magnets. Left panel: the Mn_{12}-acetate ($Mn_{12}O_{12}(CH_3COO)_{16}(H_2O)_4$). The Mn^{4+}-ions are depicted in green, the Mn^{3+}-ions in orange. Right panel: a Fe_8-compound ($(tacn)_6Fe_8(O)_2OH_{12}(H2O)$). The Fe^{3+}-ions are represented by orange spheres.

In case of the Mn_{12}-acetate, the molecule itself has a complicated structure where the Mn-ions are surrounded by ligands. Adding the spin moments of the magnetic ions, the molecule exhibits a total spin of $S = 10$. The ligands cause a crystal field, which has two effects: it favors the spin of the ions to point along a certain axis (i.e. generating an uniaxial anisotropy) and breaks the rotational invariance of the molecule, which causes an additional transverse anisotropy for the spin alignment. For a detailed description of the structure of the Mn_{12}-acetates, we refer the interested reader to Ref. [43].

The uniaxial anisotropy is of the order of a few meV, which is responsible for the very slow relaxation of the molecule's magnetic moment (reaching years at a temperature of $T = 2$ K [44]). The molecule's eigenergies taking into account the uniaxial (D) and transverse (B_2) anisotropies are sketched in Fig. 3.6. A large number of interesting quantum phenomena, like quantum tunneling of magnetization [45, 46], Berry phase interference [47] or quantum coherence [48] have all been observed in crystals of single molecule magnets.

More complex spintronics devices could be built in future include spin filters [49] made out of molecular magnets or arranging molecules to build multidot devices which could open up a way for solid-state quantum computation protocols [50] (for a recent review pointing out the potential of single molecule magnets in the field of spintronics, we refer to Ref. [37]).

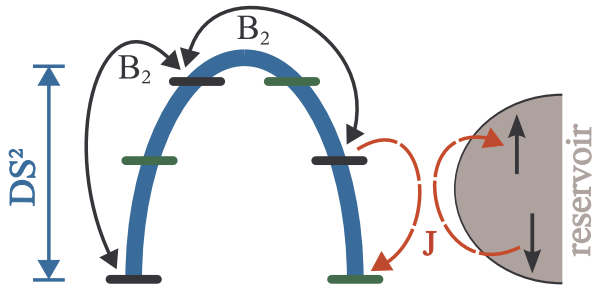

Figure 3.6: Energy diagram of the single molecule magnet. The levels indicate spin eigenstates $|S, M\rangle$ which are split in energy by the *uniaxial* (D) anisotropy. Two types of spin fluctuations occur: processes due to the intrinsic *transverse* anisotropy (B_2), resulting in quantum tunneling of magnetization, and, in case of SMMs coupled to metallic leads, exchange processes involving the conduction band electrons (J).

Experimentalists are trying to study these molecules depositing them on a surface and "accessing" them with the tip of a scanning tunneling microscope, but up to date the rather drastic experimental requirements to have not been reached yet.

In two recent publications, research teams [38, 51] managed to trap single molecule magnets in nanogaps between gold electrodes and measure electronic transport through them. If a single molecule is attached to metallic leads, the transport through the system measured in the Coulomb blockade regime is affected by the vibrational excitations of the molecule and in some cases also by its magnetic properties.

In the following we summarize the experiment of the Delft group [38]. They used acetyl-protected thiol end groups to synthesize Mn_{12}-molecules, which exhibit a strong affinity to the gold leads they used to "trap" the molecules. These ligands act as tunnel barriers as well, coupling the molecule only weakly to the gold surfaces. In their experiment [38] "Coloumb diamonds" were observed in the differential conductance as a function of bias and gate voltage (see Fig. 3.7). Lines running parallel to the Coulomb diamonds' edges indicate transport through excited states of the molecule, which might be due to phonon excitations of the molecule. This assumption is supported by Raman spectroscopy measurements and density function theory calculations [52].

The main observations of the experiment are the clear signatures of transport through a *single* molecule magnet. In Fig. 3.7 the current is fully suppressed at positive bias voltage above the left diamond edge (indicated by the dashed line). At the right degeneracy point, where the transport is observed all the way down to zero bias, two excitations are the most prominent observation: at 2 meV an excitation is visible as a bright white line (indicating positive differential conductance), while at 3 meV another excitation appears as a black line (indicating negative differential conductance). These excitations have not been measured in pure gold electrodes and can be explained by a spin-model of the SMM in a transistor geometry: a sequence of tunneling events can result in a nonequilibrium population of an excited level, which then only slowly depopulates violating the spin selection rules. This blocked transport leads to the negative differential conductance or complete suppression of the current observed in the experiment. The energy scale of the observed phenomena (current suppression and negative differential conductance) are of the order of the anisotropy barrier

of the molecule D, supporting the interpretation of the conductance map given in Ref. [38].

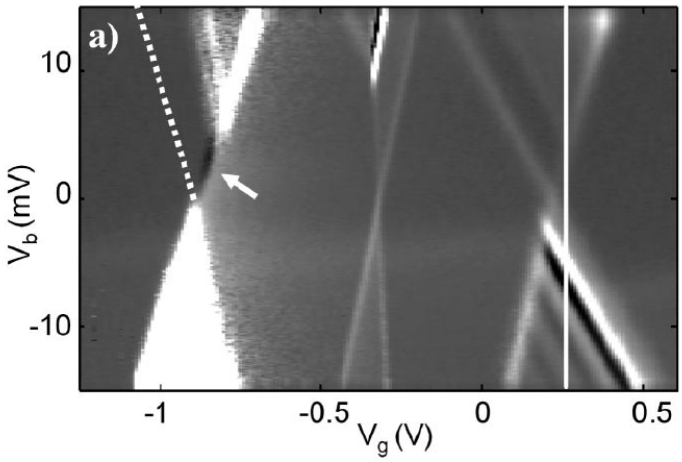

Figure 3.7: Differential conductance as function of gate V_g and bias voltage V_b of single molecule magnet in a transistor geometry. Regions of complete current suppression (arrow at left degeneracy point) and low-energy excitations with negative differential conductance (right degeneracy point) are observed (taken from Ref. [38]).

Part II

Numerical Renormalization Group

Chapter 4

Fermionic Baths

In the first part of the thesis we presented a selection of recent experiments involving different types of quantum dots and the interplay of Kondo physics and decoherence at very low temperatures. This part is dedicated to the methods used in our investigations and focuses on different extension to the *numerical renormalization group* (NRG) method first introduced by Wilson in the early 1970s [10].

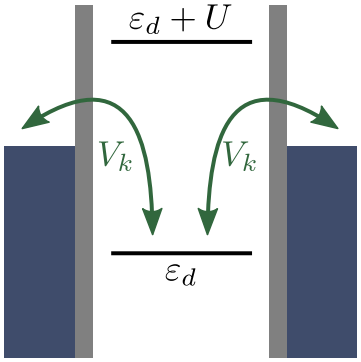

Figure 4.1: Illustration of the single impurity Anderson model (SIAM).

The numerical renormalization group method is, as its name already indicates, a numerical method, which was applied to a variety of quantum impurity problems throughout the last three decades and has led to numerous insights in the fields of Kondo physics and dissipative systems. It has become one of the standard tools to study correlation effects in quantum impurity models. One of its main advantages is that it is non-perturbative with respect to all system parameters (as opposed to many other renormalization group methods) and thus can treat interacting quantum many-body systems with a continuum of excitations spread over a broad interval of energies. For a recent review of the numerical renormalization group method and its applications, see Ref. [53].

For simplicity we explain the method itself and many of its extensions using the *single impurity Anderson model* (SIAM) [5] already mentioned in Chap. 1 of this thesis. The model describes a single localized energy level coupled to an electronic bath consisting of noninteracting spin-1/2 fermions and can be considered the paradigm of (fermionic) quantum impurity models. The Hamiltonian consists of three parts: A term describing the free

conduction band, a second one for the single localized impurity level and an interaction term coupling the impurity with the bath. It reads

$$\hat{\mathcal{H}}_A = \underbrace{\varepsilon_d \hat{d}^\dagger_\mu \hat{d}_\mu + U\left(\hat{d}^\dagger_\uparrow \hat{d}_\uparrow\right)\left(\hat{d}^\dagger_\downarrow \hat{d}_\downarrow\right)}_{\text{impurity}} + \underbrace{\sum_{\mathbf{k}} \varepsilon_{\mathbf{k}} \hat{c}^\dagger_{\mathbf{k}\mu} \hat{c}_{\mathbf{k}\mu}}_{\text{conduction band}} + \underbrace{\sum_{\mathbf{k}} V_{\mathbf{k}}\left(\hat{c}^\dagger_{\mathbf{k}\mu} \hat{d}_\mu + \hat{d}^\dagger_\mu \hat{c}_{\mathbf{k}\mu}\right)}_{\text{interaction}}. \tag{4.1}$$

The creation and annihilation operators for electrons of spin $\mu = \uparrow, \downarrow$ and momentum $\mathbf{k}$ are labeled $\hat{d}^{(\dagger)}_\mu$ for the impurity and $\hat{c}^{(\dagger)}_{\mathbf{k}\mu}$ for the conduction band. Throughout this thesis we use an Einstein sum convention, meaning that repeated indices are assumed to be summed over. ε_d ($\varepsilon_{\mathbf{k}}$) are the one-electron energies of the impurity (conduction band) states, U parameterizes the Coulomb repulsion between electrons on the impurity and $V_{\boldsymbol{k}}$ stands for the hybridization of the impurity and the conduction band electrons.

In the following we explain the steps performed in a NRG calculation. A very detailed description of how to apply the numerical renormalization group method to the single impurity Anderson model can be found in Ref. [54].

4.1 Reducing to One Dimension

To be able to deal with the single impurity Anderson model numerically, we have to apply some simplifications. First, we assume that the conduction band is fully isotropic (i.e. $\varepsilon_{\boldsymbol{k}} = \varepsilon_k$, where $k = |\boldsymbol{k}|$) ranging from $-W$ to W, where $\varepsilon_k = 0$ corresponds to the energy of the Fermi level. Furthermore, we also assume the exchange interaction between the impurity spin and the conduction band $V_{\boldsymbol{k}}$ to be independent of the momentum's orientation (i.e. $V_{\boldsymbol{k}} = V_k$). This corresponds to expressing the conduction band states in spherical harmonics around the impurity and only considering the s-wave states to be important in the scattering process of an electron from the impurity.

Now we rewrite the momentum dependence of variables using a dimensionless energy variable $l = \frac{\varepsilon}{W}$ and substitute the discrete sum by a continuous integral. Introducing a set new of creation and annihilation operators $\hat{a}^\dagger_{l\mu}, \hat{a}_{l'\nu}$, which fulfill the standard anti-commutation relations $\{\hat{a}^\dagger_{l\mu}, \hat{a}_{l'\nu}\} = \delta_{\mu,\nu}\delta(l - l')$, we obtain the following expression for the single impurity Anderson model:

$$\hat{\mathcal{H}}_A = W\left(\frac{\varepsilon_d}{W}\hat{d}^\dagger_\mu \hat{d}_\mu + \frac{U}{W}\hat{n}_\uparrow \hat{n}_\downarrow + \int_{-1}^{1} l\hat{a}^\dagger_{l\mu}\hat{a}_{l\mu}dl + \int_{-1}^{1} dl\sqrt{\frac{\Delta(l)}{\pi W}}(\hat{a}^\dagger_{l\mu}\hat{d}_{l\mu} + \hat{d}^\dagger_{l\mu}\hat{a}_{l\mu})\right). \tag{4.2}$$

Here we introduced the hybridization function $\Delta(l) = \pi \sum_k \delta(l - \frac{\varepsilon_k}{W})V_k^2$, which incorporates the density of states of the conduction band $\rho(\varepsilon) = \delta(\varepsilon - \varepsilon_k)$ as well as the exchange interaction between impurity electrons and electrons in the conduction band. In the following we assume the hybridization function to be energy-independent over the whole width of the conduction band $\Delta(l) = \Gamma$ if $-1 \leq l \leq 1$ (for a details on the more general case of a spin and energy dependent conduction band density of states, see for example Ref. [55]).

4.2 Logarithmic Discretization of Conduction Band

Dealing with an one-dimensional model like the one presented in Eq. (4.2), numerically still is a challenging task, since there is an infinite number of eigenstates of the system, which

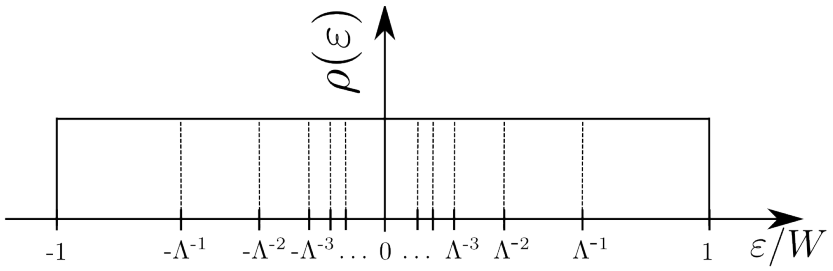

Figure 4.2: Logarithmic discretization of conduction band.

is due to the continuous bath of fermions in the conduction band. To proceed one has to determine the most important eigenstates of the conduction band, which in quantum impurity problems usually are the ones describing the low-energy physics adequately. For different numerical quantum many-body methods different strategies have been employed to single out the "most important" states. A well-defined and systematic way of doing so consists of determining the weight the eigenstates contribute to the density matrix of the full system and only keep the ones adding a relatively large percentage of the weight, as is done in the *density matrix renormalization group* method (DMRG) [56, 57]. For the numerical renormalization group method a different approach is chosen: one expects the low energy eigenstates of the conduction band to be more important describing the physics of the system, since a perturbative scaling analysis shows that the couplings diverge at low energy scales [9]. Thus, one starts introducing a discretization parameter $\Lambda > 1.0$ and discretizes the conduction band logarithmically, splitting it into intervals

$$\Lambda^{-(n+1)} < |l| < \Lambda^{-n} \qquad n = 1, 2, \ldots . \tag{4.3}$$

As depicted in Fig. 4.2 the intervals become smaller approaching the Fermi level $\varepsilon_F = 0$. In the following section we present how to choose a single state in each of these intervals, giving a better description of the system as close to the Fermi level, since more eigenstates with small eigenvalues are taken into account.

4.3 Mapping the Hamiltonian on a Semi-infinite Chain

In each of the intervals we defined in the previous section, we set up a Fourier series

$$\Psi^{\pm}_{np}(l) = \begin{cases} \frac{\Lambda^{n/2}}{(1-\Lambda^{-1})^{1/2}} e^{\pm i\omega_n p l} & \text{if } \Lambda^{-(n+1)} < \pm l < \Lambda^{-n} \\ 0 & \text{if } l \text{ outside the interval,} \end{cases} \tag{4.4}$$

where

$$\omega_n = \frac{2\pi}{\Lambda^{-n} - \Lambda^{-n-1}} \tag{4.5}$$

is the fundamental Fourier frequency, and p the integer Fourier index ranging from $-\infty$ to ∞. Expressing the creation and annihilation operators for the conduction band electrons in this basis

$$\hat{a}_{l\mu} = \sum_{np} \left(\hat{a}_{np\mu} \Psi^{+}_{np}(l) + \hat{b}_{np} \Psi^{-}_{np}(l) \right), \tag{4.6}$$

we have defined a new set of anti-commutating operators

$$\hat{a}_{np\mu} \equiv \int_{-1}^{1} dl [\Psi_{np}^{+}(l)]^{*} \hat{a}_{l\mu}, \qquad \hat{b}_{np\mu} \equiv \int_{-1}^{1} dl [\Psi_{np}^{-}(l)]^{*} \hat{a}_{l\mu}. \tag{4.7}$$

Rewriting the Anderson Hamiltonian of Eq. (4.2) using these newly defined operators $a_{np\mu}$ and $b_{np\mu}$, we obtain the following expression

$$\begin{aligned} \frac{\hat{\mathcal{H}}_A}{W} = \varepsilon_d \hat{d}_\mu^\dagger \hat{d}_\mu + U \hat{n}_\uparrow \hat{n}_\downarrow + \frac{1+\Lambda^{-1}}{2} \sum_{n,p} \Lambda^{-n} (\hat{a}_{np\mu}^\dagger \hat{a}_{np\mu} - \hat{b}_{np\mu}^\dagger \hat{b}_{np\mu}) \\ + \frac{1-\Lambda^{-1}}{2\pi i} \sum_{n,p' \neq p} \frac{\Lambda^{-n} e^{\frac{2\pi i (p-p')}{1-\Lambda^{-1}}}}{p-p'} (\hat{a}_{np\mu}^\dagger \hat{a}_{np'\mu} - \hat{b}_{np\mu}^\dagger \hat{b}_{np'\mu}) \\ + \sqrt{\frac{2\Gamma}{\pi W}} \left[\frac{1-\Lambda^{-1}}{2} \right]^{1/2} \sum_{n=0}^{\infty} \Lambda^{-n/2} \left((\hat{a}_{n0\mu}^\dagger + \hat{b}_{n0\mu}^\dagger) \hat{d}_\mu + \hat{d}_\mu^\dagger (\hat{a}_{n0\mu} + \hat{b}_{n0\mu}) \right). \end{aligned} \tag{4.8}$$

Notice that in the last term of Eq. (4.8) only the $p = 0$ terms couple to the impurity operators $\hat{d}_\mu^{(\dagger)}$ directly, which is a direct consequence of approximating the hybridization function by a constant $\Delta(l) = \Gamma$ and holds as well for the slightly more general case of a hybridization function, which is constant on each of the intervals $[\Lambda^{-(n+1)}, \Lambda^{-n}]$.

For $\Lambda \to 1$ it is easy to verify that the second line in Eq. (4.8) containing the $p \neq p'$ contribution for the conduction band vanishes and the states with different quantum number p thus decouple from each other. As first shown by Wilson [10], it is safe to neglect all terms with $p \neq 0$ even for discretization parameters as large as $\Lambda = 2.5$. Although this sounds like a crude approximation, it yields astonishingly good results and can be motivated physically looking at the extension of the states created by the operators $\hat{a}_{np}^\dagger, \hat{b}_{np}^\dagger$ in phase space. As sketched in Fig. 4.3, the states neglected by not taking into account the $p \neq 0$ terms in the Hamiltonian are eigenstates with large eigenenergies, which at the same time exhibit a spatial distribution peaked far away from the impurity site.

An analysis of the coupling term in the single impurity Anderson model given by the last line in Eq. (4.8), strongly suggests the definition of a new operator

$$\hat{f}_{0\mu} = \left[\frac{1-\Lambda^{-1}}{2} \right]^{1/2} \sum_{n=0}^{\infty} \Lambda^{-n/2} (\hat{a}_{n0\mu} + \hat{b}_{n0\mu}) = \frac{1}{\sqrt{2}} \int_{-1}^{1} dl \hat{a}_{l\mu},$$

which describes the eigenstate maximally localized around the impurity. Using this newly defined eigenstate the Hamiltonian reads:

$$\begin{aligned} \frac{\hat{\mathcal{H}}_A}{W} = \varepsilon_d \hat{d}_\mu^\dagger \hat{d}_\mu + U \hat{n}_\uparrow \hat{n}_\downarrow + \frac{1+\Lambda^{-1}}{2} \sum_{n=0}^{\infty} \Lambda^{-n} (\hat{a}_{n0\mu}^\dagger \hat{a}_{n0\mu} - \hat{b}_{n0\mu}^\dagger \hat{b}_{n0\mu}) \\ + \sqrt{\frac{2\Gamma}{\pi W}} \left(\hat{f}_{0\mu}^\dagger \hat{d}_\mu + \hat{d}_\mu^\dagger \hat{f}_{0\mu} \right). \end{aligned} \tag{4.9}$$

Observe that the eigenstates created by $\hat{f}_{0\mu}^\dagger$ are not orthonormal to the eigenstates defined by the conduction band operators $\hat{a}_{n0}^\dagger$ or $\hat{b}_{n0}^\dagger$. Setting up a new orthonormal basis, $\{\hat{f}_{n\mu}\}$, which contains $\hat{f}_{0\mu}$, we end up with a Hamiltonian with a term coupling the states $|f_{n\mu}\rangle$ and $|f_{m\mu}\rangle$

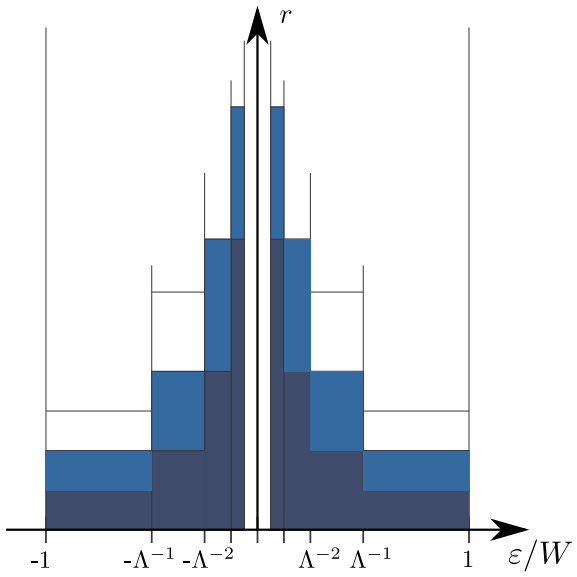

Figure 4.3: Schematic representation of phase space occupied by the states $|a_{np}\rangle$ and $|b_{np}\rangle$. The dark blue denote states with $p = 0$, the light blue ones are the first to be neglected, because of their larger distance to the impurity (in phase space).

where $m \neq n$. We exploit the freedom we have setting up this new eigenbasis, choosing the one set of orthonormal operators $\{\hat{f}_{n\mu}\}$, which yields the simplest Hamiltonian, where only a coupling between neighboring operators $\hat{f}^\dagger_{n,\mu}\hat{f}_{(n+1),\mu}$ remains. After this change of eigenbasis, the Hamiltonian is given by

$$\frac{\hat{\mathcal{H}}_A}{W} = \varepsilon_d \hat{d}^\dagger_\mu \hat{d}_\mu + U\hat{n}_\uparrow\hat{n}_\downarrow + \frac{1+\Lambda^{-1}}{2}\sum_{n=0}^{\infty}\Lambda^{-n/2}\xi_n[\hat{f}^\dagger_{n\mu}\hat{f}_{(n+1)\mu} + \hat{f}^\dagger_{(n+1)\mu}\hat{f}_{n\mu}] + \sqrt{\frac{2\Gamma}{\pi W}}\left(\hat{f}^\dagger_{0\mu}\hat{d}_\mu + \hat{d}^\dagger_\mu\hat{f}_{0\mu}\right), \quad (4.10)$$

where the hopping matrix elements for a constant hybridization function $\Delta(l) = \Gamma$ read

$$\xi_n = \frac{1-\Lambda^{-n-1}}{\sqrt{1-\Lambda^{-2n-1}}\sqrt{1-\Lambda^{-2n-3}}}. \quad (4.11)$$

For a more complicated form of the hybridization function (including the case of applying Oliveira's z-trick introduced in Sec. 10.2) the coefficients have to be calculated iteratively using a arbitrary precision routine (see Appendix A).

The operators chosen in such a way again obey the standard anti-commutation rules. The wave functions of the states created by $f^\dagger_{n\mu}$ are all peaked at at the impurity site and extend in position space as $\propto \Lambda^{n/2}$ (cf. Fig. 4.4)

The Hamiltonian in Eq. (4.10) now has the desired structure of a hopping Hamiltonian on a semi-infinite chain, which is often referred to as the *Wilson chain*. The hopping matrix elements ξ_n are essentially of order 1 for large n. The prefactor $\Lambda^{-n/2}$ in each of the summands of Eq. (4.10) ensures that the energies of the states in the conduction band decrease

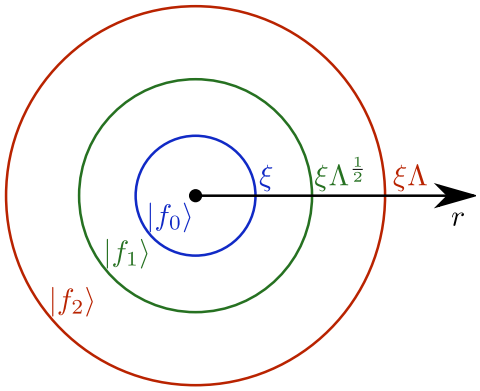

Figure 4.4: Sketch of the new orthonormal basis, where $|f_{0\mu}\rangle$ label the maximally localized state around the impurity and $|f_{n\neq 0\mu}\rangle$ depict the other states on the semi-infinite Wilson chain.

exponentially with n (see Fig. 4.5). This *separation of energy scales* allows us to calculate the terms in the sum appearing in the Hamiltonian of Eq. (4.10) one after the other, as we will describe in the following section. For models, which cannot be transformed to a semi-infite chain with exponentially decreasing coupling parameters the method does not give reasonable results. For example the one-dimensional Hubbard model can be transformed to a Hamiltonian of semi-infinite chain form, where the couplings ξ are constant, and thus should not be treated using the numerical renormalization group method, since the separation of energy scales is lacking.

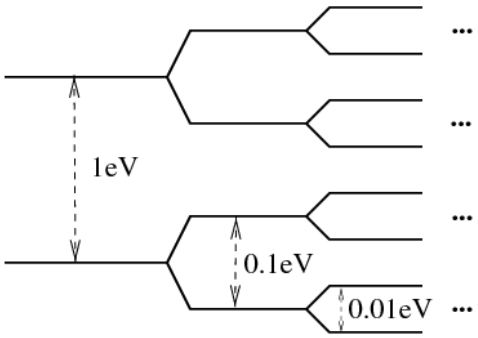

Figure 4.5: The eigenenergies of the transformed single impurity Anderson model are separated from each other: for iteration number n they are of the order of $\Lambda^{-n/2}$.

4.4 Iterative Diagonalization

Defining a series of Hamiltonians

$$\hat{H}_m = \Lambda^{(m-1)/2}\Bigg(\tilde{\varepsilon}_d \hat{d}^\dagger_\mu \hat{d}_\mu + \tilde{U}\hat{n}_\uparrow\hat{n}_\downarrow + \sum_{n=0}^{m-1}\Lambda^{-n/2}\xi_n[\hat{f}^\dagger_{n\mu}\hat{f}_{(n+1)\mu} + \hat{f}^\dagger_{(n+1)\mu}\hat{f}_{n\mu}] + \sqrt{\tilde{\Gamma}}\left(\hat{f}^\dagger_{0\mu}\hat{d}_\mu + \hat{d}^\dagger_\mu\hat{f}_{0\mu}\right)\Bigg), \quad (4.12)$$

where $\tilde{U} = \frac{2}{1+\Lambda^{-1}}\frac{U}{W}, \tilde{\varepsilon}_d = \frac{2}{1+\Lambda^{-1}}\frac{\varepsilon_d}{W}$, and $\tilde{\Gamma} = \left(\frac{2}{1+\Lambda^{-1}}\right)^2 \frac{2\Gamma}{\pi W}$, allows us to express our Hamiltonian of Eq. (4.10) as

$$\frac{\hat{\mathcal{H}}_A}{W} = \lim_{m\to\infty}\frac{1+\Lambda^{-1}}{2}\Lambda^{-\frac{m-1}{2}}\hat{H}_m. \quad (4.13)$$

Writing down the expression for $\hat{H}_m$ in Eq. (4.12) we have rescaled the eigenenergies such that the low-lying excitations are of order $\mathcal{O}(1)$ for all m. Two successive Hamiltonians in the series $\hat{H}_m$ and $\hat{H}_{m+1}$ are connected via the following recursion relation

$$\hat{H}_{m+1} = \Lambda^{1/2}\hat{H}_m + \xi_m[\hat{f}^\dagger_{m\mu}\hat{f}_{(m+1)\mu} + \hat{f}^\dagger_{(m+1)\mu}\hat{f}_{m\mu}], \quad (4.14)$$

and the initial Hamiltonian in the series is given by

$$\hat{H}_0 = \Lambda^{-1/2}\left(\tilde{\varepsilon}_d\hat{d}^\dagger_\mu\hat{d}_\mu + \tilde{U}\hat{n}_\uparrow\hat{n}_\downarrow + \sqrt{\tilde{\Gamma}}\left(\hat{f}^\dagger_{0\mu}\hat{d}_\mu + \hat{d}^\dagger_\mu\hat{f}_{0\mu}\right)\right). \quad (4.15)$$

Now let us comment on how to attack this problem numerically: we first set up a matrix describing the Hamiltonian H_0. This matrix can easily be diagonalized numerically. In the next step one starts the iterative procedure. Let us assume that we know all eigenstates of a Hamiltonian describing a Wilson chain of m sites $|r;m\rangle$. We construct a product basis of these states with the possible electronic configurations on site $m+1$ of the Wilson chain

$$|j;m+1\rangle = |r;m\rangle \otimes |\alpha_{m+1}\rangle, \quad (4.16)$$

where $|\alpha_{m+1}\rangle = \{|0\rangle, |\uparrow\rangle, |\downarrow\rangle, |\uparrow\downarrow\rangle\}$. The matrix elements of the Hamiltonian describing the enlarged Wilson chain with $m+1$ sites in this product basis are given by the following expression:

$$\langle j';m{+}1|\hat{H}_{m+1}|j;m{+}1\rangle = \Lambda^{1/2}\,E_{l,m}\,\delta_{\alpha\alpha'}\,\delta_{rr'} + \sum_\mu \Lambda^{m/2}\xi_m \times \times\left(\langle r';m|\hat{f}^\dagger_{m\mu}|r;m\rangle\,\langle\alpha'|\hat{f}_{(m+1)\mu}|\alpha\rangle + \langle\alpha'|\hat{f}^\dagger_{(m+1)\mu}|\alpha\rangle\,\langle r';m|\hat{f}_{m\mu}|r;m\rangle\right). \quad (4.17)$$

This expression includes the central idea of the numerical renormalization group method: due to the separation of energy scales for the different Hamiltonians $\hat{H}_m$ and $\hat{H}_{m+1}$, it is sufficient to know the eigenstates of $\hat{H}_m$ and the matrix elements of the operator $\hat{f}^\dagger_m$ in iteration m to solve the eigenvalue problem associated with $\hat{H}_{m+1}$.

Of course this is strictly speaking not an exact statement and can be reformulated as *"the" NRG approximation*, which states that the eigenergies of the full quantum impurity

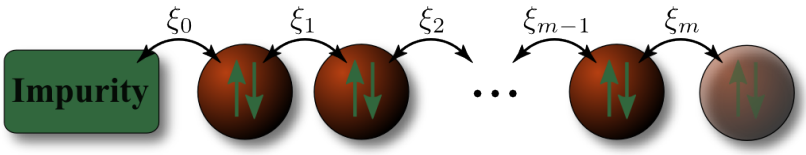

Figure 4.6: Sketch of a Wilson chain of length N.

Hamiltonian $\hat{\mathcal{H}}$ are to a very good approximation given by the eigenenergies of a Hamiltonian $\hat{H}_m$ describing a Wilson chain of m sites

$$\hat{\mathcal{H}}|r;m\rangle \approx \hat{H}_m|r;m\rangle = E_{r,m}|r;m\rangle. \tag{4.18}$$

We have mapped the complicated many-body problem to a series of Hamiltonians, which can be illustrated by a semi-infinite chain (see Fig. 4.6). We argued how this Wilson chain can be calculated numerically using iterative perturbation theory arguments presented above. Diagonalizing the Hamiltonian $\hat{H}_{m+1}$ set up in the product basis $|j;m{+}1\rangle$ defined in Eq. (4.16) and thereby changing the eigenbasis, can be described by a unitary transformation

$$|r';m+1\rangle = \sum_{\alpha_{m+1},r} U^{\alpha_{m+1}}_{r',r}|r;m\rangle \otimes |\alpha_{m+1}\rangle, \tag{4.19}$$

where $|r';m+1\rangle$ denotes the new diagonal eigenbasis for the Hamiltonian $\hat{H}_{m+1}$.

Since the size of the Hilbert space increases exponentially in the course of the iterative diagonalization procedure, we have to restrict the number of eigenstates of $\hat{H}_m$ taken into account to set up the new Hamiltonian $\hat{H}_{m+1}$. We thus only consider the N_{Lev} eigenstates with lowest eigenenergy in each iteration. This truncation of high-energy eigenstates is the second major approximation within the numerical renormalization group method and is well-justified by the separation of energy scales mentioned before. A sketch of the changes of the eigenspectrum in a single iteration step is shown in Fig. 4.7.

The recursion relation of Eq. (4.14) can be viewed as a renormalization group transformation $\hat{H}_{m+1} = \mathcal{R}[\hat{H}_m]$. To be more precise, the interesting renormalization group transformation is given by applying the recursion relation twice $\hat{H}_{m+2} = \mathcal{R}'[\hat{H}_m] = \mathcal{R}\left[\mathcal{R}[\hat{H}_m]\right]$, since for a given set of parameters in the initial SIAM Hamiltonian, applying $\mathcal{R}'$ does not change the eigenenergy spectrum of $\hat{H}_m$.

Here the renormalization group character of the method finally becomes evident: in a "standard" renormalization group treatment, like Anderson's *poor man's scaling analysis* of the Kondo problem[9], for example, one defines a transformation which maps a Hamiltonian $\hat{H}(\mathbf{K})$ specified by an initial set of parameters $\mathbf{K}$ to a Hamiltonian of the same form, but with a changed set of parameters $\hat{H}(\mathbf{K}')$. Within the *poor man's scaling* approach the mapping is performed by integrating out the high-energy degrees of freedom and changing the coupling between the impurity and the conduction band electrons to make up for it. The main goal is to find *fixed point Hamiltonians*, i.e. a set of parameters K^* for which the Hamiltonian does not change under the renormalization group transformation $\tilde{\mathcal{R}}[\hat{H}(\mathbf{K}^*)] = \hat{H}(\mathbf{K}^*)$. The system can then be described by this "effective" Hamiltonian $\hat{H}(\mathbf{K}^*)$.

For the single impurity Anderson model it is, in general, not possible to give a description by one effective Hamiltonian. Instead one can characterize the "flow" of parameters $\mathbf{K}$ by the

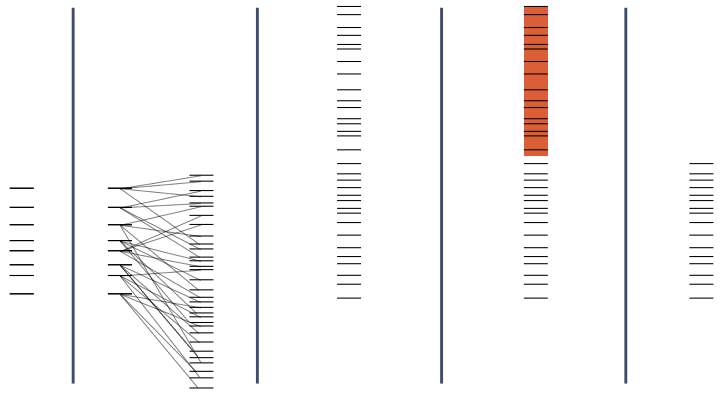

Figure 4.7: Sketch of a single iteration step: the very left columns shows the original eigenspectrum in iteration m. In the second column, the Hilbert space is enlarged by adding site $m+1$ to the Wilson chain. The eigenstates are rescaled with a factor $\Lambda^{1/2}$ and the ground state is normalized to zero. The remaining two columns show the truncation of the high energy eigenstates.

"flow" of eigenergies of $\hat{H}_m$ as one adds sites to the Wilson chain and identify several *fixed points* of the renormalization group transformation $\mathcal{R}'$. A detailed description of the different fixed points of the single impurity Anderson model is beyond the scope of this thesis. Instead we only briefly show the "flow" of the lowest lying eigenenergies of $\hat{H}_m$ for the single impurity Anderson model for a certain set of parameters in Fig. 4.8 and refer to Refs. [54, 58] for the physical interpretation of the different fixed points.

Once the energy scales corresponding to the temperature of interest or the regime of the fixed point under investigation is reached, the iterative diagonalization procedure is stopped at a certain iteration $m = N$. Static expectation values for impurity observables of interest can be calculated in a straightforward manner, setting up the desired observables in the initial steps of the iteration procedure and transforming them to the new basis using the unitary matrices $U^{\alpha_{m+1}}_{r',r}$ as one enlarges the Wilson chain. The temperature dependence of static observables, like for example the impurity magnetization, can be derived approximating the expectation value of the observable at a certain temperature T by its expectation value in iteration $m = N$, where $k_B T \approx \Lambda^{-N/2}$. This allows us to determine thermodynamic quantities like the specific heat $C_{\text{im}} = \frac{\partial U}{\partial T}$ or magnetic susceptibility $\chi_{\text{im}} = \frac{\partial M}{\partial h}$. More complicated dynamical quantities usually involve the calculation of correlation functions and are covered in later chapters of this thesis.

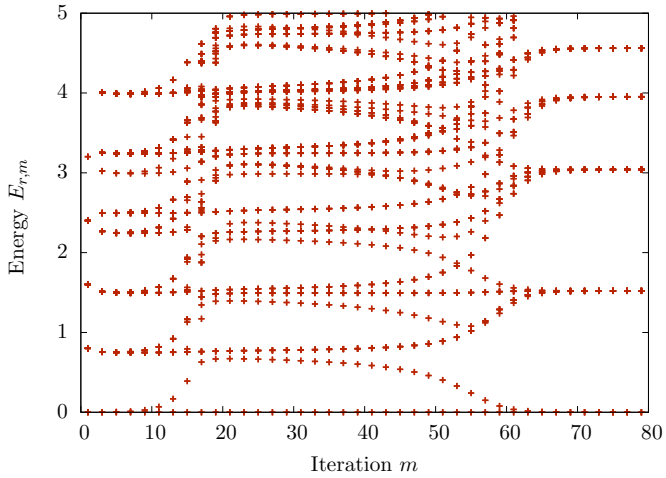

Figure 4.8: Flow of lowest-lying eigenergies of $\hat{H}_m$ plotted against (odd) iterations m in the iterative diagonalization of the single impurity Anderson model using the following parameters: $\varepsilon = -0.5 \cdot 10^{-3}W, U = 10^{-3}W, \Gamma = 2.5 \cdot 10^{-5}W$.

Chapter 5

Bosonic Baths

One distinguishes two different types of quantum impurity models containing bosonic degrees of freedom: on the one hand, there is a class of models, where bosonic baths with an infinite number of bosonic degrees of freedom are present. On the other hand, in contrast, models where the impurity couples only to a finite number of bosonic degrees of freedom (in the simplest case only a single phonon describing dissipation effects on the impurity is considered) and this "larger impurity" then interacts with a fermionic bath are frequently studied as well. The latter can be treated in the "usual" way described in detail in the preceding chapter, considering the system of impurity plus bosonic degree of freedom as a "larger" impurity. An example for this type of quantum impurity models is treated in Chap. 14 studying the dephasing in a destructive interferometer.

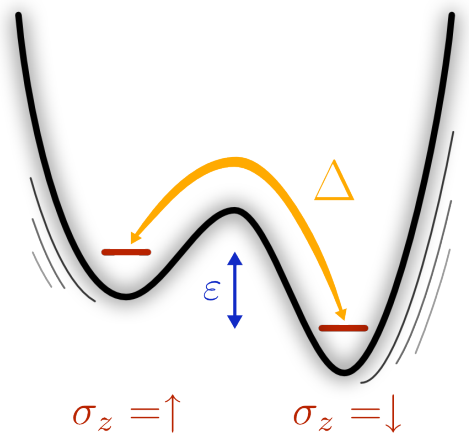

Figure 5.1: Sketch of the spin boson model with quantum tunneling term Δ and level asymmetry ε.

This chapter covers the application of the numerical renormalization group method to a model, where the impurity is coupled to an infinite number of bosonic quantum particles. Two different strategies can be pursued to solve this class of quantum impurity models using NRG: treating them indirectly by exploiting bosonization mappings to equivalent fermionic models (cf. Ref. [59]) and solving these fermionic models afterwards or a direct approach or applying the numerical renormalization group method carefully to the bosonic model itself

(cf. Refs. [60, 61]). In Chap. 12 we will compare the two strategies for real-time evolution of impurity observables after a quantum quench in two specific quantum impurity models and comment on the limitations of the indirect strategy. But let us first explain how the numerical renormalization group method can be applied to bosonic quantum impurity models directly.

One of the most prominent quantum impurity models with a bosonic bath is the spin-boson model, which describes dephasing and decoherence in a two state system coupled to a bosonic bath. The Hamiltonian for this model reads:

$$\hat{\mathcal{H}}_{SB} = \sum_i \omega_i \hat{a}_i^\dagger \hat{a}_i + \frac{\hat{\sigma_z}}{2} \sum_i \lambda_i \left(\hat{a}_i + \hat{a}_i^\dagger \right) + \Delta \frac{\hat{\sigma}_x}{2} + \varepsilon \frac{\hat{\sigma}_z}{2}, \tag{5.1}$$

where Δ denotes the spin tunneling term and ε the asymmetry of the two impurity eigenstates. The model is sketched in Fig. 5.1. The bosonic bath is fully characterized by its spectral function

$$J(\omega) \equiv \pi \sum_i \lambda_i^2 \delta(\omega_i - \omega) = 2\pi\alpha\omega_c^{1-s}\omega^s \Theta(\omega)\Theta(\omega_c - \omega), \tag{5.2}$$

which is the equivalent of the hybridazation function $\Delta(\varepsilon)$ found in quantum impurity models with fermionic baths, but highly asymmetric, since it is restricted to frequencies $0 < \omega < \omega_c$. The second part of Eq. (5.2) gives the common low-energy parametrization of the spectral function, where α measures the coupling of the two-level system to the bosonic bath and ω_c is the cutoff frequency. Throughout this thesis we assume a "hard" cutoff parametrized by the Heaviside functions in Eq. (5.2), in contrast to the also frequently used exponential cutoff, where the bosonic density of states falls off smoothly. One distinguishes three different regimes of dispersions of the free bosonic bath: the *subohmic* ($0 < s < 1$), *ohmic* ($s = 1$) and *superohmic* ($s > 1$) regime. These low energy properties of the bosonic bath determine the behavior of the system as a whole (see Fig. 5.2). A short overview of the rich physical systems modelled by the spin-boson model is given in Chap. 12. For the time being, we only want to mention that it arises naturally in the description of quantum dissipative systems [62].

Compared to the application to the single impurity Anderson model presented in the preceding chapter, two differences have to be taken into account:

- A single bosonic mode can be occupied by an infinite number of bosons. As a consequence, the Hilbert space describing the single bosonic mode would have to be infinite-dimensional. Thus a finite number of eigenstates for each bosonic mode N_b has to be selected (even for the "easy" case of just a single bosonic mode, a cutoff on the number of bosonic particles occupying each mode has to be introduced, as we will see in Chap. 14).

- The second main difference to the case introduced in the preceding chapter is the asymmetric non-constant spectral density for the bosonic particles, in contrast to the particle-hole symmetric hybridization function, which we even approximated by a constant $\Delta(\varepsilon) = \Gamma$ in case of a fermionic bath (cf. Figs. 5.2 and 4.2).

5.1 Star Hamiltonian

To see how these differences manifest themselves applying the numerical renormalization group method to the spin-boson model, we first continue as in the case of a fermionic bath and

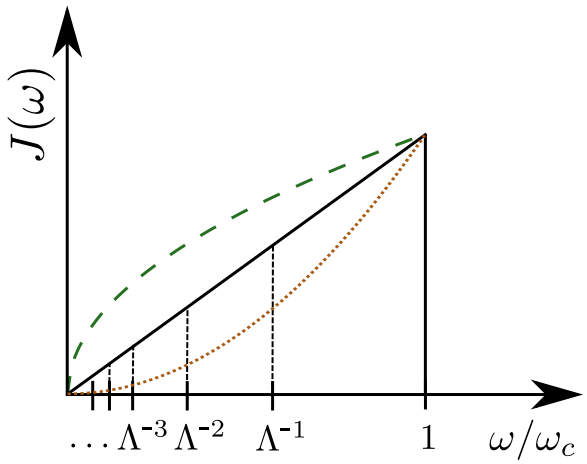

Figure 5.2: Spectral function $J(\omega)$ of the free bosonic bath in the spin-boson model for an ohmic ($s = 1$, black solid line), subohmic ($s = 0.5$, brown dotted line), and superohmic ($s = 2$, green dashed line) bath dispersion.

substitute the discrete sum over the bath modes by a continuous integral over a dimensionless energy variable $l = \frac{\omega}{\omega_c}$. We then obtain the following Hamiltonian

$$\frac{\hat{\mathcal{H}}_{SB}}{\omega_c} = \int_0^1 \mathrm{d}l g(l) \left(\hat{a}_l^\dagger \hat{a}_l\right) + \frac{\hat{\sigma}_z}{2} \int_0^1 \mathrm{d}l h(l) \left(\hat{a}_l + \hat{a}_l^\dagger\right) + \Delta \frac{\hat{\sigma}_x}{2} + \varepsilon \frac{\hat{\sigma}_z}{2}, \tag{5.3}$$

where

$$\frac{1}{\pi} J(x) = \frac{dg^{-1}(x)}{dx} h^2[g^{-1}(x)]. \tag{5.4}$$

Eq. (5.4) shows that there is some freedom in defining the functions $g(x)$ and $h(x)$, which we will use later on. But first, let us proceed as in the "usual" NRG case. Since the spectral function of the free bosonic bath $J(\omega)$ is restricted to *positive* frequencies $0 \leq \omega \leq \omega_c$, the integration in Eq. (5.3) is restricted to positive energies $l > 0$, in contrast to Eq. (4.2) where the free fermionic bath's hybridization function $\Delta(l)$ extents over the full conduction band covering eigenstates with positive as well as negative eigenenergies.

As we did before in the case of fermionic baths, we define intervals of logarithmically decreasing width $\Lambda^{-(n+1)} < l < \Lambda^{-n}$ using the discretization parameter $\Lambda > 1$ (cf. Fig. 5.2) and again set up a Fourier series on each of the intervals

$$\Psi_{np}(l) = \begin{cases} \frac{\Lambda^n}{1-\Lambda^{-1}} e^{i\omega_n p l} & \text{if } \Lambda^{-(n+1)} < l < \Lambda^{-n} \\ 0 & \text{outside interval,} \end{cases} \tag{5.5}$$

which allows us to reexpress our operators $\hat{a}_l^{(\dagger)}$ using a new set of operators $\hat{a}_{np}^{(\dagger)}$

$$\hat{a}_l^{(\dagger)} = \sum_{np} \hat{a}_{np}^{(\dagger)} \Psi_{np}^{(*)}(l). \tag{5.6}$$

Now we utilize the freedom we have choosing the two functions $g(l)$ and $h(l)$: since only the spectral function $J(\omega)$ is fixed in the original model, we can choose $h(l)$ to be constant in each of the intervals $\varepsilon \in [\Lambda^{-(n+1)} : \Lambda^{-n}]$.

$$h(l) = h_n = \left[\frac{1}{\Lambda^{-n} - \Lambda^{-(n+1)}} \int_{\Lambda^{-(n+1)}\omega_c}^{\Lambda^{-n}\omega_c} \frac{1}{\pi} J(\omega) \mathrm{d}\omega \right]^{1/2}. \tag{5.7}$$

Choosing constant values for h_n of course fixes the second function $g(l)$ via Eq. (5.4). It can be shown that with this choice for $h(l)$, the impurity now only couples to the $p = 0$-component directly and the $p \neq 0$ components only contribute via their coupling to the $p = 0$ term.

As in the case of a fermionic bath, we neglect all terms, where $p \neq 0$, which yields the so called *star*-Hamiltonian for the spin-boson model

$$\hat{\mathcal{H}}_{SB}^{star} = \sum_{n=0}^{\infty} \xi_n \left(\hat{a}_n^\dagger \hat{a}_n \right) + \frac{\hat{\sigma}_z}{2\sqrt{\pi}} \sum_{n=0}^{\infty} \gamma_n \left(\hat{a}_n + \hat{a}_n^\dagger \right) + \Delta \frac{\hat{\sigma}_x}{2} + \varepsilon \frac{\hat{\sigma}_z}{2}, \tag{5.8}$$

where

$$\xi_n = \gamma_n^{-2} \int_{\Lambda^{-(n+1)}\omega_c}^{\Lambda^{-n}\omega_c} J(x) x dx = \frac{s+1}{s+2} \frac{1 - \Lambda^{-(s+2)}}{1 - \Lambda^{-(s+1)}} \omega_c \Lambda^{-n} \tag{5.9}$$

$$\gamma_n^2 = \int_{\Lambda^{-(n+1)}\omega_c}^{\Lambda^{-n}\omega_c} J(x) dx = \frac{2\pi\alpha}{s+1} \omega_c^2 (1 - \Lambda^{-(s+1)}) \Lambda^{-n(s+1)}. \tag{5.10}$$

We have thereby approximated the spectral function $J(\omega)$ by a series of δ-peaks located at

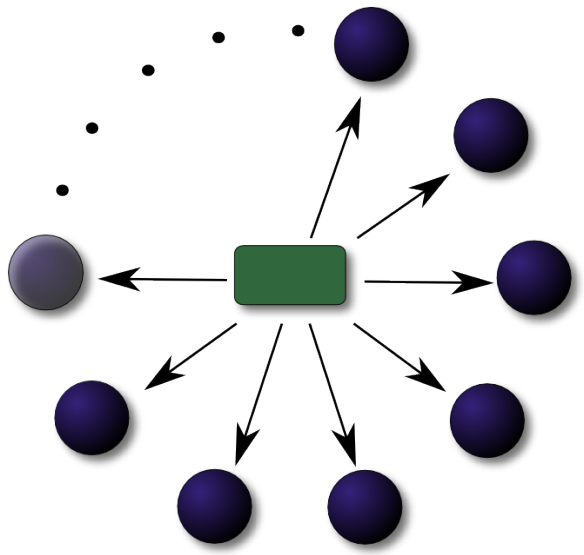

Figure 5.3: Illustration of the star Hamiltonian for the bosonic numerical renormalization group method.

energies ξ_n with weight $\propto \gamma_n^2$. The expressions given on the right hand side of Eq. (5.10) are obtained straightforwardly plugging in the parametrization of Eq. (5.2) for $J(\omega)$ in the integral expressions.

For an illustration of this Hamilton operator, see Fig. 5.3. According to Bulla and coworkers [61] it is possible to start an iterative diagonalization procedure directly on the *star*-Hamiltonian.

As opposed to the fermionic case, this turns out to be an advantage in some situations. Performing one "iteration step" $m \to m+1$, i.e. adding a bosonic degree of freedom, one has to choose a finite number of eigenstates giving the best possible description of the low-energy eigenstates of the enlarged Hamiltonian. Bulla and coworkers showed [60, 61] that for the subohmic spin-boson model deep inside the "localized" regime, the best description is not given by adding just the eigenstates with the lowest bosonic occupation for this degree of freedom, but instead by taking into account a finite number of (orthogonalized) displaced oscillator states (for details we refer to Ref. [61]). The displaced oscillator eigenstates can be constructed for the *star*-Hamiltonian, but have so far not been successfully implemented for the *chain*-Hamiltonian.

5.2 Chain Hamiltonian

In all other parameter regimes of the spin-boson model though, choosing the bosonic eigenstates with the lowest bosonic occupation to construct the "enlarged" Hamiltonian with one more bosonic degree of freedom is a successful strategy as well.

Hence let us follow the path we have outlined in Chap. 4 and apply a unitary transformation on the set of annihilation and creation operators $\hat{b}_n = \sum_{m=0}^{\infty} U_{nm}\hat{a}_m$ to map the *star*-Hamiltonian of Eq. (5.8) to a semi-infinite chain

$$\hat{\mathcal{H}}_{SB}^{chain} = \sqrt{\frac{\eta_0}{\pi}}\frac{\hat{\sigma}_z}{2}\left(\hat{b}_0 + \hat{b}_0^\dagger\right) + \sum_{n=0}^{\infty}\left[\epsilon_n \hat{b}_n^\dagger \hat{b}_n + t_n\left(\hat{b}_n^\dagger \hat{b}_{n+1} + \hat{b}_{n+1}^\dagger \hat{b}_n\right)\right] + \Delta\frac{\hat{\sigma}_x}{2} + \varepsilon\frac{\hat{\sigma}_z}{2}. \quad (5.11)$$

Consequently we will refer to this form of the Hamiltonian for the spin-boson model as the *chain*-Hamiltonian (you can find a sketch of its structure in Fig. 5.4).

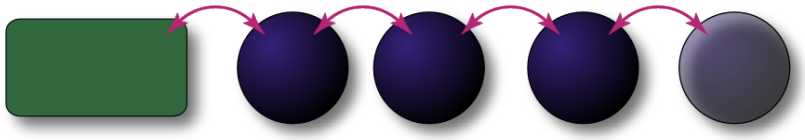

Figure 5.4: Illustration of chain Hamiltonian for the bosonic numerical renormalization group method.

We can define a series of Hamiltonians

$$\hat{\mathcal{H}}_{SB,m}^{chain} = \Lambda^m\left[\sqrt{\frac{\eta_0}{\pi}}\frac{\hat{\sigma}_z}{2}\left(\hat{b}_0 + \hat{b}_0^\dagger\right) + \sum_{n=0}^{m}\epsilon_n \hat{b}_n^\dagger \hat{b}_n + \sum_{n=0}^{m-1} t_n\left(\hat{b}_n^\dagger \hat{b}_{n+1} + \hat{b}_{n+1}^\dagger \hat{b}_n\right) + \Delta\frac{\hat{\sigma}_x}{2} + \varepsilon\frac{\hat{\sigma}_z}{2}\right], \quad (5.12)$$

for which it is trivial to show that the original bosonic *chain*-Hamiltonian of Eq. (5.11) is recovered in the limit

$$\hat{\mathcal{H}}_{SB}^{chain} = \lim_{m\to\infty}\Lambda^{-m}\hat{\mathcal{H}}_{SB,m}^{chain}. \quad (5.13)$$

The following steps of an iterative diagonalization and a truncation of the Hilbert space in each iteration are identical to the procedure for the fermionic bath numerical renormalization group method. The renormalization group transformation now reads

$$\hat{\mathcal{H}}^{chain}_{SB,m+1} = \Lambda \hat{\mathcal{H}}^{chain}_{SB,m} + \Lambda^{m+1} \left[\epsilon_{m+1} \hat{b}^\dagger_{m+1} \hat{b}_{m+1} + t_m \left(\hat{b}^\dagger_m \hat{b}_{m+1} + \hat{b}^\dagger_{m+1} \hat{b}_m \right) \right], \tag{5.14}$$

where the "hopping" parameter t_m and "on-site" energies ε_m can be determined self-consistently in advance (the details of this calculation (including the z-trick averaging explained in Sec. 10.2) can be found in Appendix A).

One additional difference to the case of a fermionic bath consists in the different scale, which separates the eigenenergies of states in different iterations from each other. As a direct consequence of the non-symmetric bath spectral function $J(\omega)$, the eigenenergies scale with iteration number m like Λ^{-m} (instead of $\Lambda^{-m/2}$ in the fermionic case). Thus, one usually chooses a smaller discretization parameter $\Lambda \approx 1.4$ to obtain the same energy resolution as for a fermionic quantum impurity model with a choice of $\Lambda = 2$.

As a last comment, we want to emphasize how the Hilbert space is restricted to a finite number of bosonic eigenmodes in case of a bosonic quantum impurity model. In the first step of the iterative diagonalization procedure of the chain Hamiltonian, the Hilbert space is still restricted to a small number of degrees of freedom, which allows us to take into account a relatively large number of bosonic modes $N_{b,0} \approx 600$. In the subsequent iteration steps, the number of bosonic modes has to be chosen smaller to keep the total number of eigenstates, and consequently the sizes of the matrices which are diagonalized, manageable. A common choice for the number of different bosonic modes added in later iterations is $N_{b,N} \approx 6$.

Chapter 6

Density Matrix Numerical Renormalization Group

6.1 Energy Scale Separation for Dynamical Quantities

The numerical renormalization group technique developed by Wilson in the 1970s [10] has been an extremely successful method, leading to a better understanding of the physics of metals at low temperatures. Nozières' interpretation of the strong coupling fixed point of the Kondo Hamiltonian using an intuitive Fermi-liquid picture [12] for example, would not have been possible without results of NRG-calculations. The NRG has become a standard tool for calculations on quantum impurity systems nowadays. Nevertheless it sometimes fails calculating dynamical properties such as Green's functions. As we will outline in this chapter, the reason for this failure often is connected to the appearance of a second energy scale, destroying the essential separation of energy scales (see Fig. 6.1).

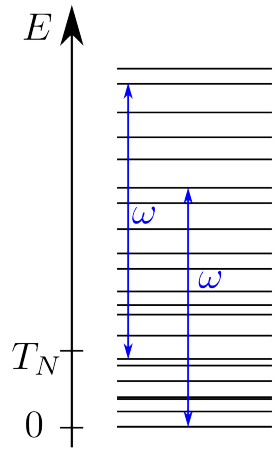

Figure 6.1: An additional energy scale set by the frequency of the excitation ω is introduced calculating dynamical quantities such as Green's functions using NRG.

We will demonstrate the difficulties one is facing calculating dynamical quantities using a

very general definition of a one-particle Green's function, which reads

$$G(\omega) = -i \int_0^\infty dt e^{i\omega t} \langle \left[\hat{A}(t), \hat{B}(0) \right]_\pm \rangle. \tag{6.1}$$

Here $\hat{A}$ and $\hat{B}$ are creation or annihilation operators for fermionic (or bosonic) particles, and $[\cdots, \cdots]_\pm$ denotes the anti-commutator (or commutator, if $\hat{A}$ and $\hat{B}$ denote bosonic operators). As an example we give an expression for the single particle spectral function of the single impurity Anderson model, which is directly proportional to the imaginary part of the model's Green's function

$$A_\mu(\omega) = -\frac{1}{\pi} \mathrm{Im}\{G_\mu(\omega)\} = -\frac{1}{\pi} \mathrm{Im}\{-i \int_0^\infty dt e^{i\omega t} \langle \left[\hat{d}_\mu(t), \hat{d}_\mu^\dagger(0) \right]_+ \rangle\} \tag{6.2}$$

$$= \sum_{ij} |\langle i|\hat{d}_\mu^\dagger|j\rangle|^2 \, \delta(\omega - E_i + E_j) \, \frac{e^{-\beta E_i} + e^{-\beta E_j}}{Z}, \tag{6.3}$$

where the second line gives the spectral function in its Lehmann representation and $Z = \sum_j e^{-E^j/T_N}$ denotes the partition function of the system.

The straightforward calculation of the spectral function using the numerical renormalization group would go as follows: if one is interested in $A_\mu(\omega)$ at temperatures T_N and wants to determine its contribution at energy scales ω, one chooses an appropriate iteration N', such that $\omega \approx \Lambda^{-\frac{N'}{2}}$. Choosing the iteration N', where the contribution is evaluated, we have to keep two things in mind. First, for excitations larger then the temperature $\omega = E_i - E_j \gg T_N$ the states $|i\rangle$ have to be available in the NRG iteration N', i. e. they should not have been discarded already because of their relatively large eigenenergy (compared to the temperature). On the other hand, the states $|j\rangle$ should be described "well enough" in this iteration.

Albeit many cases where the straightforward approach yields good physical results, this is not necessarily always the case. Take the single impurity Anderson model, for example, with an additional magnetic field applied to the impurity, such that the impurity part of the Hamiltonian given in Eq. (4.1) changes to

$$\hat{\mathcal{H}}_{A,\mathrm{imp}} \to \varepsilon_d \hat{d}_\mu^\dagger \hat{d}_\mu + U \hat{n}_\uparrow \hat{n}_\downarrow + h_z(\hat{n}_\uparrow - \hat{n}_\downarrow). \tag{6.4}$$

For spectral functions at very low temperatures $T \to 0$, the information about the correct ground state $|j\rangle = |0\rangle$ is not available in "early" iterations N', if we apply a very small magnetic field $h_z = \mathcal{O}(T_K)$, where $T_K \ll \Lambda^{-\frac{N'}{2}} = \omega$. The effects of the broken ground state symmetry would only be taken into account in "later" iterations $m > N'$. Thus the excitation energy introduces a second energy scale, which requires a better knowledge of the correct (symmetry broken) ground state in early stages of the iterative diagonalization procedure.

As a consequence of this, the impurity magnetization M of the SIAM calculated using the spectral function

$$\langle \hat{S}_z \rangle = \int_{-\infty}^0 d\omega \, (A_\uparrow(\omega) - A_\downarrow(\omega)) \tag{6.5}$$

shows a deviation from the result one obtains, if the magnetization is calculated directly by implementing the operator $\hat{S}_z = \hat{d}_\uparrow^\dagger \hat{d}_\uparrow - \hat{d}_\downarrow^\dagger \hat{d}_\downarrow$ as an observable in the NRG code and evaluating its thermodynamic expectation value directly (for an illustration of the deviation from the sum rule see Fig. 6.2).

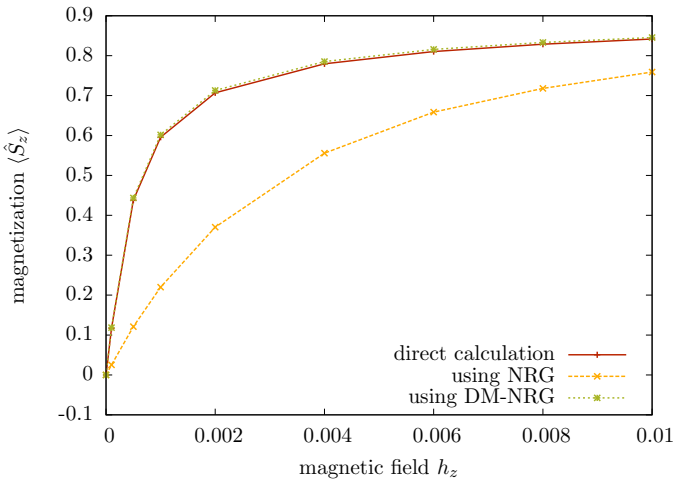

Figure 6.2: Magnetization of the SIAM applying a very small magnetic field $h_z = \mathcal{O}(T_K)$: Comparing the direct calculation and the result derived from the spectral functions calculated by the straightforward approach, one observes a deviation of the sum rule (compare red to yellow line). This deviation disappears, if one follows the DM-NRG approach using the reduced density matrix to account for the correct low-energy eigenstates of the system ($N_{\text{Lev}} = 1536$, $\Lambda = 2$, $-2\varepsilon_\mu = U = 0.1W$, $\Gamma_\mu = 0.01W$).

6.2 Reduced Density Matrix

One can circumvent this problem of the broken energy scale separation introducing the reduced density matrix of the full Fock space ρ_{eq} to account for the low-energy states in early steps of the iterative diagonalization procedure. As first realized by Hofstetter [63] the Green's function can be calculated within the NRG formalism using

$$G(\omega) = -i \int_0^\infty dt e^{i\omega t} \langle \left[\hat{A}(t), \hat{B}(0) \right]_\pm \rangle = -i \int_0^\infty dt e^{i\omega t} \text{Tr} \left\{ \hat{\rho}_{eq} \left[\hat{A}(t), \hat{B}(0) \right]_\pm \right\}, \tag{6.6}$$

where the correct ground state is determined *before* the contributions at different energy scales ω are evaluated.

As a first step, one performs the complete iterative diagonalization procedure not calculating the spectral function one is interested in. In the last iteration $m = N$ of this "NRG run", the equilibrium density matrix is set up

$$\hat{\rho}_{eq} = \sum_j |j, N\rangle \frac{\exp\left(-\beta E_{j,N}\right)}{Z_N} \langle j, N|, \tag{6.7}$$

where $Z_N = \sum_k e^{-\beta E_{k,N}}$ is the partition function, which takes into account all eigenstates available in the last iteration. Since the iteration N is chosen to fulfill $\Lambda^{-\frac{N}{2}} \approx T$ the low-energy eigenstates of the system at the temperature of interest are well described by the density matrix $\hat{\rho}_{eq}$. If we keep the unitary matrices transforming the eigenstates of iteration

m to the ones in iteration $m+1$

$$|r', m+1\rangle = \sum_{\alpha_{m+1}, r} U^{\alpha_{m+1}}_{r',r} |r, m\rangle \otimes |\alpha_{m+1}\rangle, \tag{6.8}$$

we can calculate the effect of the correct ground state on the transitions between eigenstates of all NRG iterations. This is done in the following way: we start by tracing out the last "site" N on the Wilson chain

$$\left[\rho^{red}(N-1)\right]_{r,r'} = \sum_{\alpha_N, jj'} U^{\alpha_N \dagger}_{j,r} \left[\rho^{red}(N)\right]_{j,j'} U^{\alpha_N}_{j',r'}. \tag{6.9}$$

This procedure can be iterated to determine the ground state density matrix of the full system reduced to the NRG eigenbasis of iteration m

$$\left[\rho^{red}(m)\right]_{t,t'} = \sum_{\{\alpha_i\}} U^{\alpha_{m+1}\dagger}_{s,t} \dots U^{\alpha_N \dagger}_{j,r} \left[\rho^{red}(N)\right]_{j,j'} U^{\alpha_N}_{j',r'} \dots U^{\alpha_{m+1}}_{s',t'}, \tag{6.10}$$

where we have abbreviated the summation using the Einstein convention. The transformation described in Eq. (6.10) can be interpreted as tracing out the environment $|k, N-m\rangle_{\text{env}}$, if we rewrite the density matrix separating the "system" and "environment" degrees of freedom (as depicted in Fig. 6.3)

$$\hat{\rho}_{eq} = \sum_j |j, N\rangle \frac{\exp\left(-\beta E_{j,N}\right)}{Z_N} \langle j, N| \tag{6.11}$$

$$= \sum_{ll',kk'} \rho_{lk,l'k'} |l,\ m\rangle_{\text{sys}} |k,\ N\text{-}m\rangle_{\text{env}\,\text{env}} \langle k',\ N\text{-}m|_{\text{sys}} \langle l',\ m|. \tag{6.12}$$

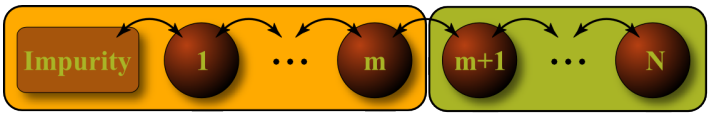

Figure 6.3: Wilson chain separated into system and environment degrees of freedom in iteration m.

Once we have completed these "backward iterations", we obtain a reduced density matrices for each iteration m $\hat{\rho}^{red}(m) = \sum_{ll'} \rho_{ll'} |l,\ m\rangle_{\text{sys}\ \text{sys}} \langle l',\ m|$, which encodes information about low-energy eigenstates of the *full* system in states of available on the m-site Wilson chain.

Using this additional information, we may now perform a second "NRG run" calculating the spectral function according to Eq. (6.6). For the Green's function of the single impurity Anderson model the density matrix numerical renormalization group (DM-NRG) method can be applied yielding

$$iG(\omega) = \int_0^\infty dt e^{i\omega t} \langle \left[\hat{A}(t), \hat{B}(0)\right]_\pm \rangle = \int_0^\infty dt e^{i\omega t} \text{Tr}\left\{\hat{\rho}_{eq} \left[\hat{A}(t), \hat{B}(0)\right]_\pm\right\} \tag{6.13}$$

$$= \sum_{l,l',l'',m} \int_0^\infty dt e^{i\omega t} \Big(e^{it(E_{l',m} - E_{l'',m})} \rho^{red}_{l,l'}(m) A_{l',l''}(m) B_{l'',l}(m)$$

$$\pm e^{it(E_{l'',m} - E_{l,m})} \rho^{red}_{l,l'}(m) B_{l',l''}(m) A_{l'',l}(m) \Big), \tag{6.14}$$

where we used an abbreviation for the matrix elements $A_{l'',l}(m) = \langle l''; m|\hat{A}|l; m\rangle$. In the Lehmann representation the expression for the final result reads

$$G(\omega) = \sum_{l,l',l'',m} \Big(\frac{1}{\omega + (E_{l',m} - E_{l'',m})} \rho^{red}_{l,l'}(m) A_{l',l''}(m) B_{l'',l}(m) \pm \frac{1}{\omega + (E_{l'',m} - E_{l,m})} \rho^{red}_{l,l'}(m) B_{l',l''}(m) A_{l'',l}(m) \Big). \quad (6.15)$$

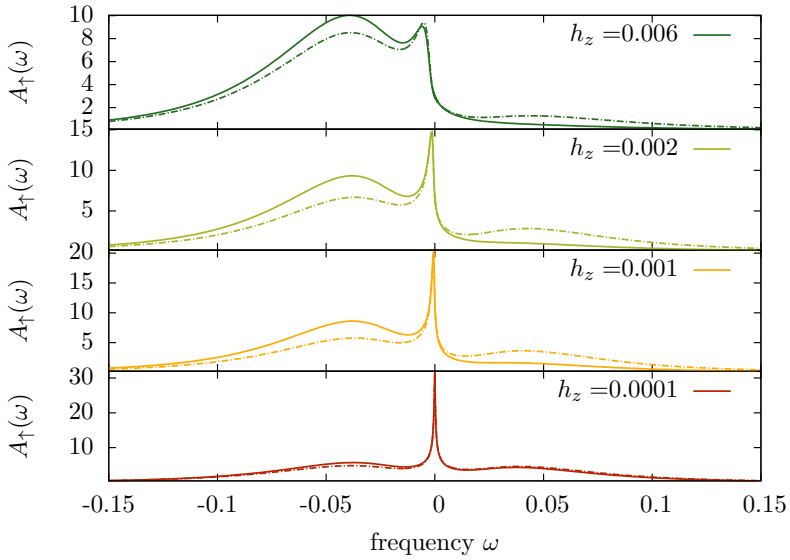

Figure 6.4: Spectral functions for the single impurity Anderson model applying a finite magnetic field $h_z(n_\uparrow - n_\downarrow)$. The dotted lines are calculated using the straightforward NRG approach, while the solid lines show the results of the NRG using the reduced density matrix to account for the correct ground state (DM-NRG). Parameters chosen as in Fig. 6.2.

Using the DM-NRG approach to calculate the spectral functions of the single impurity Anderson model with a ground state symmetry broken by a finite magnetic field, we observe a shift of weight for larger frequencies ω (cf. Fig. 6.4). Integrating the part of the spectral functions with negative eigenenergies, the magnetization calculated via Eq. (6.5) now coincides with the values obtained by directly calculation using a thermodynamic average in the last iteration (cf. green line in Fig. 6.2).

Chapter 7

Complete Basis

7.1 Over-counting

A general problem occurring in the calculation of dynamic quantities using the numerical renormalization group method, is the question how to combine the results from different NRG iterations. In general the separation of energy scales in different iterations ensures that a treatment of the problem using the iterative perturbation theory arguments is legitimate. Nevertheless, during the iterative diagonalization procedure, the eigenstates are refined and several eigenstates of subsequent iterations may be taken into account multiple times (if one interprets them as being eigenstates of the full Hamiltonian).

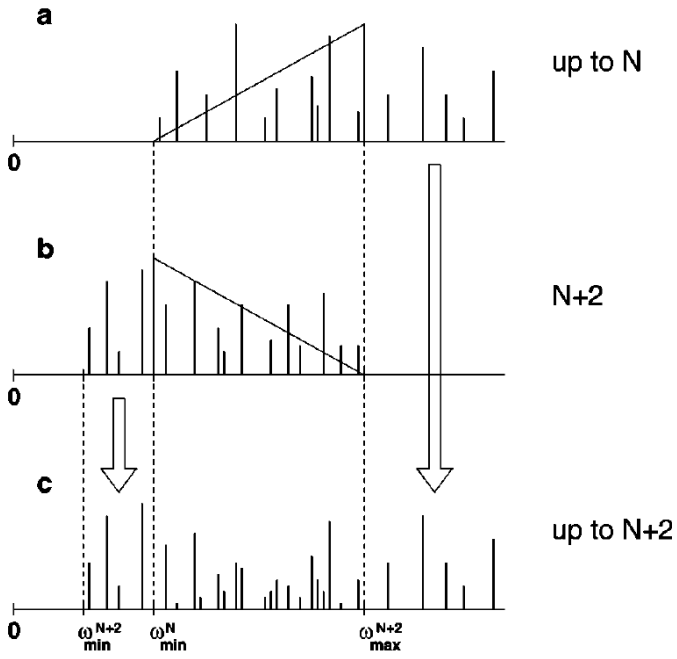

Figure 7.1: Illustration of the mixing procedure applied to avoid over-counting combining different NRG iterations (taken from Ref. [64]).

A common way to address this problem is to "mix" the matrix elements calculated in different iterations to obtain a good description of dynamic quantities such as the spectral function, for example. Different "mixing" procedures have been suggested and employed to yield the best results depending on the observables of interest. In Fig. 7.1 (taken from Ref. [64]), one of the mixing procedures is illustrated. Here, the contributions to the spectral function in every second NRG step are combined. Depending on the value of the frequency ω of the contribution in iteration $N+2$, they are either added as they are (if ω is smaller than the smallest frequency of all contributions added up in iterations $m < N$) or, in the frequency region where they overlap, the contributions of iterations smaller than N and the ones added in iteration $N+2$ are combined weighting them with a linear factor.

7.2 Complete Basis

The key point to setting up a more systematic way of avoiding the "over-counting" problem is to start from a different interpretation of each step in the iterative diagonalization procedure: instead of thinking of it as enlarging the Wilson chain by adding site $m+1$ it is useful to consider the Hamiltonians H_m for all $0 < m < N$ to act on the *full* Wilson chain of length N and interpret the m-th iteration step as assigning a finite value to the hopping parameter ξ_m, while ξ_i for $i = m+1, \cdots, N-1$ are zero (see Fig. 7.2).

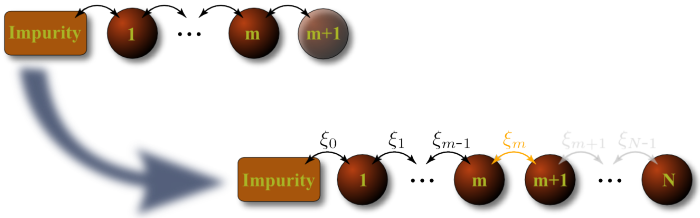

Figure 7.2: Sketch of the different interpretation of the step $m \to m+1$: All H_m act on the full chain, but in the "enlarging" step, ξ_m is assigned a finite value $\xi_m \neq 0$.

In the spirit of this new interpretation, we relabel the eigenstates in the different iterations in the following way: If all degrees of freedom on site i are labeled by $\{\alpha_i\}$, we may express the eigenstates of Hamiltonian $\hat{H}_m$ in iteration m, which now acts on the full chain, as

$$|\alpha_0, \alpha_1, \alpha_2, \cdots, \alpha_N\rangle = |\alpha_0, \alpha_1, \ldots, \alpha_m, \alpha_{m+1}, \ldots, \alpha_N\rangle = |r, e; m\rangle. \tag{7.1}$$

The new labeling also reflects the "splitting" of the full Wilson chain in iteration m into system and environment as already discussed in the previous chapter and sketched in Fig. 6.3. r now denotes all system degrees of freedom, while the configuration of the environment is labeled by e. Since changing the environment state does not alter the eigenenergy of the state $|r, e; m\rangle$ in iteration m, each eigenstate of the Hamiltonian H_m has a degeneracy of d^{N-m}, where d is the number of degrees of freedom on each site. Thus, the eigenstates in iteration N can formally be viewed as matrix product states [65], since they are generated applying the transformation matrices according to the relation

$$|r', e'; m+1\rangle = \sum_{\alpha_{m+1}, r} U^{\alpha_{m+1}}_{r',r} |r, e, \{\alpha_{m+1}\}; m\rangle. \tag{7.2}$$

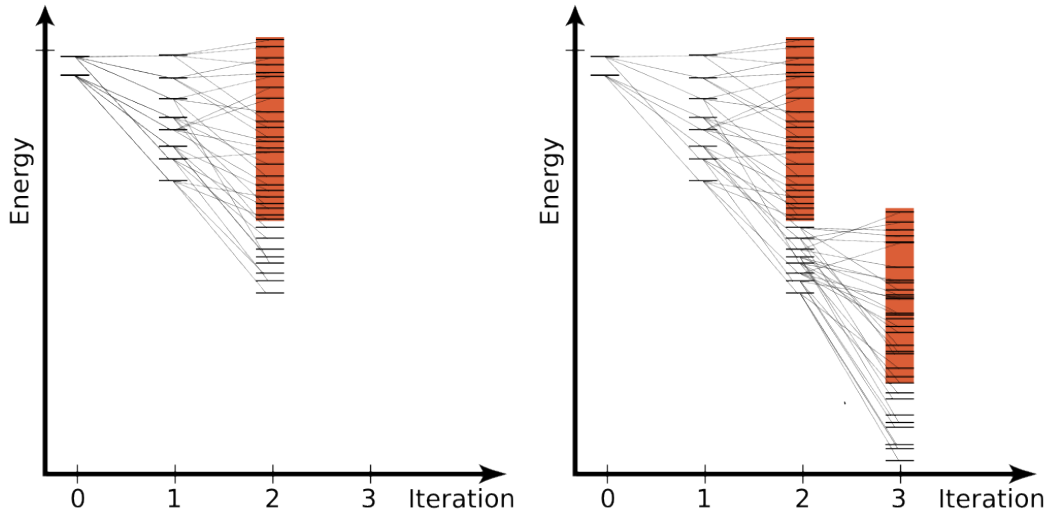

Figure 7.3: Sketching the eigenstates of Hamiltonians $\hat{H}_m$ in the first iterations. After a few iterations, the number of non-degenerate eigenstates becomes too large to consider all of them. Setting up and diagonalizing the Hamiltonian matrix one has to discard the states with the highest eigenenergies.

Although we interpreted the iterative diagonalization procedure in a different way, we still face the same problem already mentioned in Chap. 4: the number of non-degenerate eigenstates grows exponentially and after a few iterations, the matrices become too large to diagonalize them, if we would try to take into account all non-degenerate eigenstates of H_m. Thus, according to the iterative perturbation theory argument, we only keep the low-energy eigenstates to calculate the eigenstates of the Hamiltonian in the next iteration. The high energy states are discarded (cf. Fig. 7.3). The discarded eigenstates of each iteration are labeled with a special index $|r, e; m\rangle_{\text{dis}}$.

How does this help us to construct a complete basis of the Fock space of the full Hamiltonian $\hat{\mathcal{H}}$? As Anders and Schiller [66] first reasoned, collecting the discarded states of all iterations and considering all states available in the last iteration $m = N$ to be discarded, one constructs a complete basis of the Fock space in a smart way. The unity operator of the full Fock space can then be written as

$$\hat{\mathbb{1}} = \sum_{m=m_0}^{N} \sum_{r,e} |r, e; m\rangle_{\text{dis}}\ {}_{\text{dis}}\langle r, e; m|. \tag{7.3}$$

For a sketch of this idea, see Fig. 7.4. In their detailed review Ref. [67] Anders and Schiller nicely explained that this is an optimal choice of a complete basis of the Fock space treating any quantum impurity Hamiltonian $\hat{\mathcal{H}}$ using the numerical renormalization group method. Summing up their line of argumentation the reasons are the following:

1. Not a single state is eliminated without contributing to the full basis.

2. Every state is only considered once, because it is only discarded in one specific iteration.

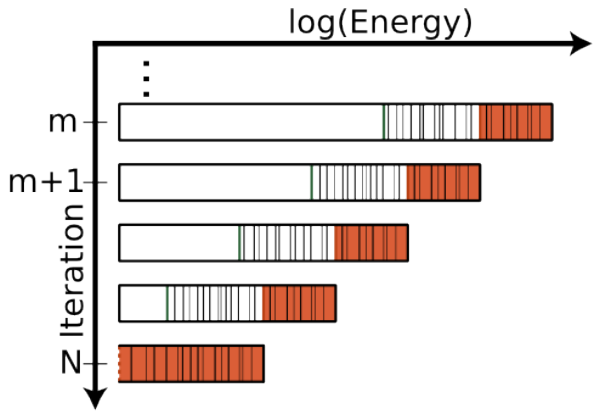

Figure 7.4: Illustration of the construction of a complete basis of the full Fock space of the original Hamiltonian $\hat{\mathcal{H}}$ collecting the discarded eigenstates of all iterations.

3. The empirical mixing procedures can be replaced by a systematic way of combining the eigenstates of different NRG iterations.

4. The energy resolution of the states discarded is the best possible for a given maximal number of eigenstates kept in each iteration N_{Lev}.

From the last point of this list, we can directly deduce a way of improving the accuracy of the calculation: Allowing larger sizes for the Hamiltonian matrices in all iterations, which is equivalent to keeping more eigenstates in each NRG iteration, the states will be discarded in later iterations, where their energy resolution is better. This, of course, increases the accuracy of the result at the cost of a longer and more demanding (considering memory requirements) calculations. Thus we typically restrict the number of kept eigenstates in each iteration to approximately $N_{\mathrm{Lev}} \approx 1000$, which is a good compromise between accuracy and computational cost.

7.3 Resummation

Additionally to this smart and systematic choice of a complete basis, Anders and Schiller also came up with a very useful resummation identity. Considering all of the states available in a specific iteration m we can distinguish the ones with large eigenenergies, which will be discarded in this same iteration from the low-energy ones which will be kept and "refined" in the next iteration. Projecting on the subspace of kept eigenstates in iteration m is equivalent to projecting on all eigenstates discarded in later iterations. In a more mathematical way one may formulate the following identity

$$\hat{\mathbb{1}}_m^+ = \sum_{k,e} |k,e;m\rangle_{\mathrm{kp\ kp}}\langle k,e;m| = \sum_{m'>m}\sum_{r',e'} |r',e';m'\rangle_{\mathrm{dis\ dis}}\langle r',e';m'|. \tag{7.4}$$

The resummation identity of Eq. 7.4 will turn out to be useful calculating various quantities using this complete basis. It is sketched in Fig. 7.5.

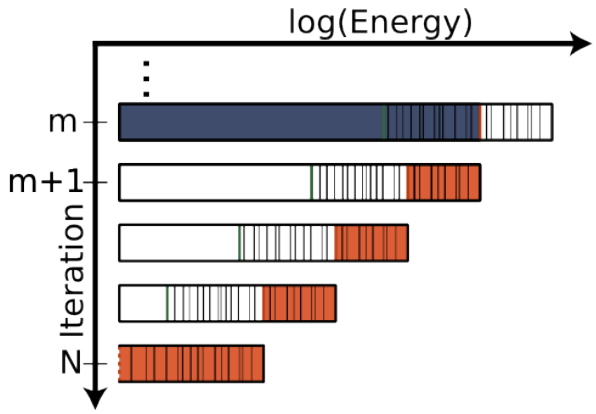

Figure 7.5: Projecting on the subspace of kept eigenstates in iteration m (including all of the degenerate eigenstates of the environment) is identical to projecting on all of the eigenstates discarded in later iterations $m' > m$. The resummation identity stated in Eq. (7.4) is illustrated here.

7.4 Application to Spectral Functions

Applying the idea of the complete basis, first introduced by Anders and Schiller, to the calculation of spectral functions for the single impurity Anderson model within NRG, Peters and coworkers [68], have demonstrated its advantages over the approaches described in the preceding chapters of this thesis. Though it is possible to improve the "straightforward" approach of calculating Green's functions within the NRG method using the complete basis of the Fock space, we will only comment on the improved version of the density matrix NRG approach described in Chap. 6.

We start by evaluating the expression for the spectral function of the single impurity Anderson model in the Lehmann representation using the complete basis

$$G(\omega) = -i \int_0^\infty dt\; e^{i\omega t} \langle \left[\hat{A}(t), \hat{B}(0) \right]_\pm \rangle = \mathrm{Tr} \left\{ \hat{\rho} \left(e^{it\hat{\mathcal{H}}} \hat{A} e^{-it\hat{\mathcal{H}}} \hat{B} \pm \dots \right) \right\}, \tag{7.5}$$

where

$$\mathrm{Tr} \left\{ \hat{\rho} e^{it\hat{\mathcal{H}}} \hat{A} e^{-it\hat{\mathcal{H}}} \hat{B} \right\} = \mathrm{Tr} \left\{ \hat{A} e^{-it\hat{\mathcal{H}}} \hat{B} \hat{\rho} e^{it\hat{\mathcal{H}}} \right\} = \mathrm{Tr} \left\{ \hat{A} e^{-it\hat{\mathcal{H}}} \cdot \hat{\mathbb{1}} \cdot \hat{B} \hat{\rho} e^{it\hat{\mathcal{H}}} \right\} \tag{7.6}$$

$$= \sum_{l,e;m} \sum_{l',e';m'} \langle l, e; m | \hat{A} e^{-it\hat{\mathcal{H}}} | l', e'; m' \rangle \langle l', e'; m' | \hat{B} \hat{\rho} e^{it\hat{\mathcal{H}}} | l, e; m \rangle. \tag{7.7}$$

After reordering of the double-summation and multiple applications of the resummation identity stated in Eq. (7.4) we end up with the general expression

$$G(\omega) = \frac{1}{Z_{N_T}} \sum_{l,l'} A_{l,l'}(N_T) B_{l',l}(N_T) \frac{e^{-\beta E_{l,N_T}} \pm e^{-\beta E_{l',N_T}}}{\omega + (E_{l,N_T} - E_{l',N_T})}$$
$$+ \sum_{l,k,k';m} B_{l,k'}(m) \rho^{red}_{k',k}(m) A_{k,l}(m) \frac{1}{\omega + (E_{k,m} - E_{l,m})}$$
$$\pm \sum_{l,k,k';m} A_{l,k}(m) \rho^{red}_{k,k'}(m) B_{k',l}(m) \frac{1}{\omega + (E_{l,m} - E_{k,m})}, \tag{7.8}$$

where compared to the "simple" DM-NRG expression, the summation is now not performed over all states in each iteration, but only a certain combination of states kept and discarded in iteration m is contributing to the spectral function. Serving a more compact notation, we have used a color coding for the states, labeling discarded states in red and their kept counterparts in blue instead of using a lengthy label. The details of the derivation of Eq. (7.8) are explained in Appendix B.

In the remainder of this chapter, we shortly want to comment on the merits of this approach: by construction the improved evaluation of the spectral function of the single impurity Anderson model does not involve any truncation error, which leads to an exact fulfillment of the sum rule independent of the number of eigenstates N_{Lev} kept in each iteration (for a prove of this statement we refer to Appendix A of Ref. [68]). Consequently calculations choosing a very small value for N_{Lev} yield astonishingly good results, allowing for an effective reduction of computational cost, while keeping the quality of spectral information. This is demonstrated in Fig. 7.7, where results for the spectral function of the SIAM for different values of N_{Lev} are presented.

Using the complete basis suggested by Anders and Schiller opens up a new route for using the numerical renormalization group method as an impurity solver for calculations using the dynamical mean-field theory [69, 70, 71], where a complex high-dimensional lattice model is mapped onto an effective quantum impurity model. A set of coupled Dyson equations then has to be solved self-consistently, which requires the calculation of a large number of spectral functions with varying input parameters. This of course requires "fast" impurity solvers. As the authors of Ref. [68] state, using the improved version of the numerical renormalization group method keeping only a small number of eigenstates in each iteration may proof to be especially useful in cases of symmetry phases, for example in the ferromagnetic Hubbard model, or the description of the Griffith's phase in disordered correlated systems [72].

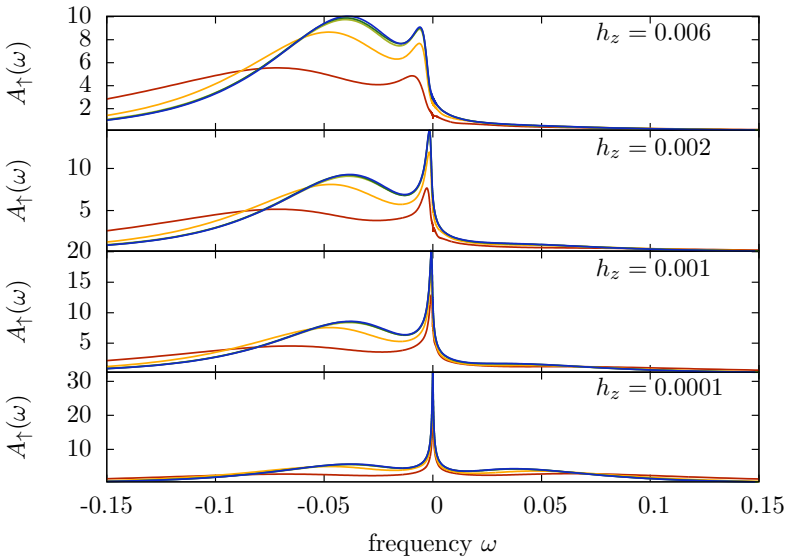

Figure 7.6: Spectral functions calculated using the complete basis set according to Eq. (7.8) for different number of kept levels in each iteration ($N_{\mathrm{Lev}} = 1024$ (blue), $N_{\mathrm{Lev}} = 512$ (green), $N_{\mathrm{Lev}} = 256$ (light green), $N_{\mathrm{Lev}} = 128$ (yellow), $N_{\mathrm{Lev}} = 64$ (red)). Parameters chosen as in Fig. 6.2.

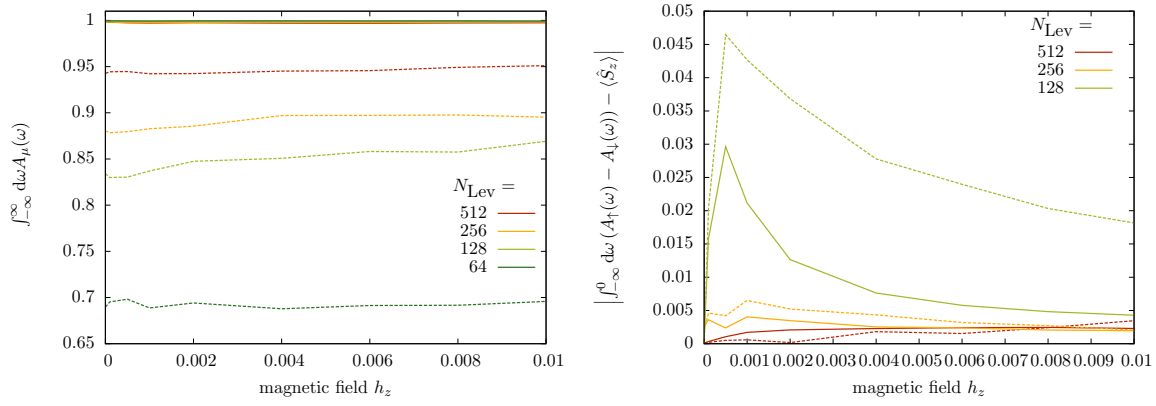

Figure 7.7: Comparing the Friedel sum rule (left plot) and the deviation of the magnetization derived from the spectral function from its exact value (right plot) for very small numbers of kept levels N_{Lev} in each iteration. Dashed lines are calculated using the DM-NRG approach, the solid lines represent improved versions result using the complete basis. Parameters chosen as in Fig. 6.2.

Chapter 8

Time-dependence

In this chapter we want to present an algorithm to calculate real-time nonequilibrium dynamics for quantum impurity systems as a reaction to a sudden change in parameters. This method is referred to as time-dependent numerical renormalization group (TD-NRG) and was first introduced by Anders and Schiller in 2005 [66].

8.1 Quantum Quenches

Quantum quenches can be modeled by sudden changes of parameters in the Hamiltonian. As illustrated in Fig. 8.1, we normalize the time-axis such that the quench takes place at $t = 0$. For times $t < 0$ the system is described by the initial Hamiltonian $\hat{\mathcal{H}}^i$, for later times $t > 0$ the time-evolution is governed by the final Hamiltonian $\hat{\mathcal{H}}^f$. It is assumed that the system is prepared in the equilibrium state of $\hat{\mathcal{H}}^i$ before the quantum quench is performed.

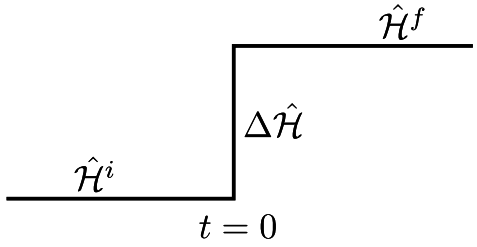

Figure 8.1: A quantum quench is a sudden change of parameters in the Hamiltonian

In practice the sudden change of parameters could, for example, be realized by switching a local magnetic field on or off or changing its orientation. Please notice that we have not restricted the state the system is prepared in initially (i.e. for times $t < 0$) other than it can be expressed as an equilibrium state of the initial Hamiltonian $\hat{\mathcal{H}}^i$: the system can, for example, be prepared in a complicated many-body ground state such as a Kondo screened impurity state, before we quench the system. To this extent the method is more general, than, for example, a real-time flow equation method, where the initial state always has to be a product state of impurity and a free quantum bath [73].

8.2 Time Evolution Formula

In this section we will explain how to derive a formula for the real-time evolution of a local operator of a quantum impurity model as a reaction to a quantum quench following Anders' and Schiller's concept presented in Ref. [67]. Let us point out important preceding works by Costi and coworkers, who were the first to try to describe the real-time evolution of quantum impurity systems using the numerical renormalization group method in Ref. [74]. Though their approach was limited to evaluate the time evolution on relatively short time scales, it cleared the way for the more systematic approach discussed here.

The goal of Anders' and Schiller's TD-NRG is to determine the real-time evolution of a local operator $\hat{O}$ (i. e. an operator only acting on the impurity and the first few sites on the Wilson chain) after a quantum quench. In all generality we can express the time-evolution as

$$\langle \hat{O} \rangle(t) = \mathrm{Tr}\left\{ \hat{O}\hat{\rho}(t) \right\}, \tag{8.1}$$

where the trace is performed over the product of the local operator and the time-dependent density matrix of the system. For a quantum quench at time $t = 0$ the latter is given by

$$\hat{\rho}(t) = \begin{cases} \hat{\rho}_{eq} & \forall t \leq 0 \\ e^{-i\hat{\mathcal{H}}^f t}\hat{\rho}_{eq}e^{i\hat{\mathcal{H}}^f t} & \forall t > 0. \end{cases} \tag{8.2}$$

Here $\hat{\rho}_{eq}$ denotes the equilibrium density matrix of the initial Hamiltonian $\hat{\mathcal{H}}^i$. As the second line of Eq. (8.2) states, the time-evolution of the density matrix for times $t > 0$ is governed by the final Hamiltonian $\hat{\mathcal{H}}^f$.

In the simplest case, the equilibrium density matrix $\hat{\rho}_{eq}$ is set up in the last NRG iteration

$$\hat{\rho}_{eq} = \sum_l |l; N\rangle^i \frac{\exp\left(-\beta E^i_{l,N}\right)}{Z^i_N} {}^i\langle l; N|, \tag{8.3}$$

where the partition sum is given by $Z^i_N = \sum_l e^{-\beta E^i_{l,N}}$. Before commenting on the details of the implementation, let us lay down the concepts of the derivation. To evaluate the trace in Eq. (8.1), we use the complete basis introduced in Chap. 7 (instead of using a lengthy index notation $|\rangle_{\mathrm{dis}}$ and $|\rangle_{\mathrm{k}}$ we use our color coding to distinguish the discarded from the kept states).

We start by evaluating the trace in Eq. (8.1) using the complete basis for the full Fock space of the final Hamiltonian we described in some detail in Sec. 7.2

$$\begin{aligned} \langle \hat{O} \rangle(t) &= \mathrm{Tr}\left\{ \hat{O}\hat{\rho}(t) \right\} \\ &= \sum_m \sum_{r,e} \langle r, e; m|\hat{O}\hat{\rho}(t)|r, e; m\rangle. \end{aligned} \tag{8.4}$$

Inserting an unity operator $\hat{\mathbb{1}}$ between the two factors

$$\langle \hat{O} \rangle(t) = \sum_m \sum_{r,e} \langle r, e; m|\hat{O}\left(\hat{\mathbb{1}}\right)\hat{\rho}(t)|r, e; m\rangle \tag{8.5}$$

$$= \sum_m \sum_{r,e} \langle r, e; m|\hat{O}\Big(\sum_{m'} \sum_{r',e'} |r', e'; m'\rangle\langle r', e'; m'|\Big)\hat{\rho}(t)|r, e; m\rangle, \tag{8.6}$$

we end up with a summation over matrix elements

$$\langle r', e'; m'|\hat{\rho}(t)|r, e; m\rangle \quad \text{and} \quad \langle r, e; m|\hat{O}|r', e'; m'\rangle,$$

where eigenstates are involved which, in general, are set up in different NRG iterations m and m'. Since there does not exist an easy and straightforward way to calculate these matrix elements within the numerical renormalization group method, we split up the double-sum into three different parts: $m' = m, m' > m,$ and $m' < m$ and try to simplify each of the three terms on its own.

$$\langle\hat{O}\rangle(t) = \sum_m \sum_{r,e} \langle r, e; m|\hat{O}\Big(\sum_{m'=m}\sum_{r',e'} |r', e'; m'\rangle\langle r', e'; m'|\Big)\hat{\rho}(t)|r, e; m\rangle \qquad (m' = m) \quad (8.7)$$

$$+ \sum_m \sum_{r,e} \langle r, e; m|\hat{O}\Big(\sum_{m'>m}\sum_{r',e'} |r', e'; m'\rangle\langle r', e'; m'|\Big)\hat{\rho}(t)|r, e; m\rangle \qquad (m' = m) \quad (8.8)$$

$$+ \sum_m \sum_{r,e} \langle r, e; m|\hat{O}\Big(\sum_{m'<m}\sum_{r',e'} |r', e'; m'\rangle\langle r', e'; m'|\Big)\hat{\rho}(t)|r, e; m\rangle \qquad (m' = m). \quad (8.9)$$

The first case in Eq. (8.7) by definition only contains eigenstates discarded in iteration $\mathbf{m' = m}$ and can be evaluated easily.

For the second part of the double-summation, where $\mathbf{m' > m}$, we apply the resummation identity of Eq. (7.4)

$$\sum_{k,e} |k, e; m\rangle\langle k, e; m| = \sum_{m'>m}\sum_{r',e'} |r', e'; m'\rangle\langle r', e'; m'|$$

to simplify the expression as follows

$$\begin{aligned}(8.8) &= \sum_m \sum_{r,e} \langle r, e; m|\hat{O}\Big(\sum_{m'>m}\sum_{r',e'} |r', e'; m'\rangle\langle r', e'; m'|\Big)\hat{\rho}(t)|r, e; m\rangle \\ &= \sum_m \sum_{r,e} \langle r, e; m|\hat{O}\Big(\sum_{k,e'} |k, e'; m\rangle\langle k, e'; m|\Big)\hat{\rho}(t)|r, e; m\rangle \\ &= \sum_m \sum_{r,e} \sum_{k,e'} \langle r, e; m|\hat{O}|k, e'; m\rangle\langle k, e'; m|\hat{\rho}(t)|r, e; m\rangle. \qquad (8.10)\end{aligned}$$

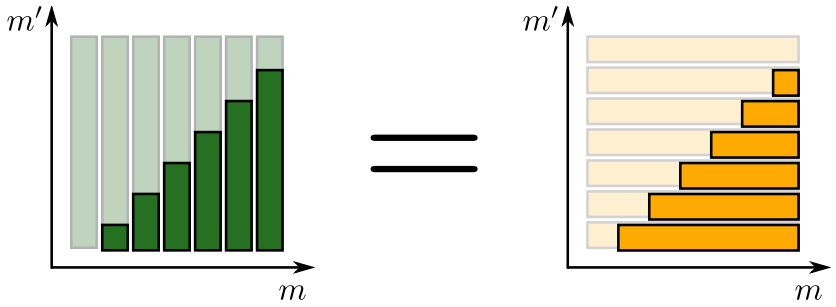

Figure 8.2: The double sum $\sum_m \sum_{m'<m}$ can be rewritten as $\sum_{m'} \sum_{m>m'}$ interchanging the roles of m and m'.

The third and last part, where $\mathbf{m}' < \mathbf{m}$, is more complicated to simplify: before we can apply the resummation identity, we have to change the order of the summations as indicated in Fig. 8.2

$$(8.9) = \sum_{m} \sum_{m'<m} \sum_{r,e} \sum_{r',e'} \langle r', e'; m'|\hat{\rho}(t)|r, e; m\rangle \langle r, e; m|\hat{O}|r', e'; m'\rangle \tag{8.11}$$

$$= \sum_{m'} \sum_{m>m'} \sum_{r,e} \sum_{r',e'} \langle r', e'; m'|\hat{\rho}(t)|r, e; m\rangle \langle r, e; m|\hat{O}|r', e'; m'\rangle \tag{8.12}$$

$$= \sum_{m'} \sum_{r',e'} \langle r', e'; m'|\hat{\rho}(t)\Big(\sum_{k,e} |k, e; m'\rangle \langle k, e; m'|\Big)\hat{O}|r', e'; m'\rangle \tag{8.13}$$

$$= \sum_{m} \sum_{k,e'} \sum_{r,e} \langle k, e'; m|\hat{O}|r, e; m\rangle\langle r, e; m|\hat{\rho}(t)|k, e'; m\rangle \tag{8.14}$$

Combining the three parts, we obtain the following expression for the time-dependency of the operator $\hat{O}$:

$$\begin{aligned}\langle\hat{O}\rangle(t) = \mathrm{Tr}\left\{\hat{O}\hat{\rho}(t)\right\} &= \sum_{m} \sum_{r,e} \langle r, e; m|\hat{O}\Big(\sum_{m'} \sum_{r',e'} |r', e'; m'\rangle \langle r', e'; m'|\Big)\hat{\rho}(t)|r, e; m\rangle \\ &= \sum_{m} \sum_{r,e} \sum_{r',e'} \langle r, e; m|\hat{O}|r', e'; m\rangle \langle r', e'; m|\hat{\rho}(t)|r, e; m\rangle \\ &\quad + \sum_{m} \sum_{r,e} \sum_{k,e'} \langle r, e; m|\hat{O}|k, e'; m\rangle \langle k, e'; m|\hat{\rho}(t)|r, e; m\rangle \\ &\quad + \sum_{m} \sum_{k,e'} \sum_{r,e} \langle k, e'; m|\hat{O}|r, e; m\rangle\langle r, e; m|\hat{\rho}(t)|k, e'; m\rangle. \end{aligned} \tag{8.15}$$

Abbreviating this result we write

$$\langle\hat{O}\rangle(t) = \sum_{m=m_0}^{N} \sum_{r,s}^{\mathrm{dis}} \sum_{e,e'} \langle r, e; m|\hat{O}|s, e'; m\rangle\langle s, e'; m|\hat{\rho}(t)|r, e; m\rangle, \tag{8.16}$$

where the sum $\sum_{r,s}^{\mathrm{dis}}$ indicates that *at least one* of the states r, s is discarded in iteration m. We want to emphasize that after these exact simplifications, we are only dealing with matrix elements between eigenstates of one single NRG iteration m.

Carefully inspecting Eq. (8.16), we notice that the two states of the matrix elements $|r, e; m\rangle$ and $|s, e'; m\rangle$ still have different environment labels e and e'. This simplifies, if one takes into account, that the operator $\hat{O}$ is local. Assuming that it only acts on the sites on the Wilson chain, where still all of the eigenstates are kept, we may conclude that it is diagonal in the environment

$$\langle r, e; m|\hat{O}|s, e'; m\rangle = \delta_{e,e'}\langle r, e; m|\hat{O}|s, e; m\rangle = O_{r,s}(m) \tag{8.17}$$

Inserting the expression for the time-dependent density matrix $\hat{\rho}(t) = e^{-it\hat{\mathcal{H}}^f}\,\hat{\rho}_{eq}\,e^{it\hat{\mathcal{H}}^f}$ given in Eq. (8.2) yields

$$\langle\hat{O}\rangle(t) = \sum_{m=m_0}^{N} \sum_{r,s}^{\mathrm{dis}} \sum_{e} O_{r,s}(m)\langle s, e; m|e^{-it\hat{\mathcal{H}}^f}\,\hat{\rho}_{eq}e^{it\hat{\mathcal{H}}^f}|r, e; m\rangle. \tag{8.18}$$

Now we employ "the" NRG approximation already discussed in Eq. (4.18) in Chap. 4 assuming that the eigenenergy of a state in iteration m $|r,e;m\rangle$ is given by the eigenvalue of the matching summand of the series of Hamiltonians

$$\hat{\mathcal{H}}|r,e;m\rangle \approx \hat{H}_m|r,e;m\rangle = E_{r,m}|r,e;m\rangle. \tag{8.19}$$

The expression for the time-dependency of the operator after a quantum quench can now be written in the simple form

$$\langle\hat{O}\rangle(t) = \sum_{m=m_0}^{N}\sum_{r,s}^{\text{dis}} O_{r,s}(m)e^{it(E^f_{r,m}-E^f_{s,m})}\sum_e \langle s,e;m|\hat{\rho}_{eq}|r,e;m\rangle \tag{8.20}$$

$$= \sum_{m=m_0}^{N}\sum_{r,s}^{\text{dis}} O_{r,s}(m)e^{it(E^f_{r,m}-E^f_{s,m})}\rho^{red}_{s,r}(m). \tag{8.21}$$

We still have not commented on the part concerning the density matrix

$$\rho^{red}_{s,r}(m) = \sum_e \langle s,e;m|\hat{\rho}_{eq}|r,e;m\rangle = \sum_e {}^f\langle s,e;m|\hat{\rho}^i_{eq}|r,e;m\rangle^f. \tag{8.22}$$

As the abbreviation already indicates, summing over the environment degrees of freedom and thereby tracing out the environment in each iteration m, we "reduce" the density matrix to the "systems" degrees of freedom (i.e. to the degrees of freedom on a Wilson chain of length m). In the following section we will comment on the additional complications caused by the fact that the eigenstates we use to express the trace are eigenstates of the final Hamiltonian $\hat{\mathcal{H}}^f$, while the density matrix $\hat{\rho}^i_{eq}$ is set up using the eigenstates of the initial Hamilton operator $\hat{\mathcal{H}}^i$. Deriving the formula for the time-dependency in Eq. (8.18), the concept of a reduced density matrix first introduced by Hofstetter for spectral functions [63] and discussed in some detail in Chap. 6, arises "naturally".

8.3 Transforming $\hat{\rho}_{eq}$

In Eq. (8.22) we give an explicit expression for the reduced density matrix $\rho^{red}_{s,r}(m)$. It involves expressing the equilibrium density matrix of the initial Hamiltonian $\hat{\rho}^i_{eq}$ using the eigenstates of the final Hamiltonian $|r,e;m\rangle^f$ and $|s,e;m\rangle^f$. How can this be done in detail?

To answer this question, we will first describe how to set up the initial density matrix: a general expression for the equilibrium density matrix in the complete NRG basis reads

$$\hat{\rho}^i_{eq} = \sum_{l,e;m} |l,e;m\rangle \frac{\exp\big(-\beta E_{l,m}\big)}{Z}\langle l,e;m|, \tag{8.23}$$

where Z denotes the partition sum of the full Wilson chain. Since in this chapter we restrict ourselves to study the time-evolution at low temperatures $T \to 0$ (and consequently $\beta \to \infty$), where the low energy eigenstates contribute dominantly to the equilibrium density matrix, we may approximate the equilibrium density matrix using only the eigenstates of the last NRG iteration $m = N$:

$$\hat{\rho}^i_{eq} \approx \sum_j |j,N\rangle^i \frac{e^{-\beta E^i_{j,N}}}{Z^i_N}\,{}^i\langle j,N|, \tag{8.24}$$

where the partition sum now reads $Z_N^i = \sum_k e^{-\beta E_{k,N}^i}$. Following the path that led to Eq. (6.12) in Sec. 6.2, we separate the system from the environment degrees of freedom in each NRG iteration and rewrite

$$\hat{\rho}_{eq}^i = \sum_{l'l''} \sum_{k'k''} \rho^i_{l'k',l''k''} |l',\ m\rangle^i_{\text{sys}} |k',\ N\text{-}m\rangle^i_{\text{env}}\ {}^i_{\text{env}}\langle k'',\ N\text{-}m|\ {}^i_{\text{sys}}\langle l'',\ m| \tag{8.25}$$

$$= \sum_{l'l''} \sum_{e'e''} \rho^i_{l'e',l''e''} |l', e'; m\rangle^{i\ i}\langle l'', e''; m|. \tag{8.26}$$

This allows us to derive an expression for the reduced density matrix in the basis of the final Hamiltonian given in Eq. (8.22)

$$\rho^{red}_{s,r}(m) = \sum_e {}^f\langle s, e; m|\hat{\rho}^i_{eq}|r, e; m\rangle^f$$

$$= \sum_{l'l''} \sum_{e,e',e''} \rho^i_{l'e',l''e''}\ {}^f\langle s, e; m|l', e'; m\rangle^{i\ i}\langle l'', e''; m|r, e; m\rangle^f \tag{8.27}$$

$$= \sum_{l'l''e} \rho^i_{l'e,l''e}\ {}^f\langle s, e; m|l', e; m\rangle^{i\ i}\langle l'', e; m|r, e; m\rangle^f, \tag{8.28}$$

where the last step can be performed, because the environments for the two Hamiltonian $\hat{\mathcal{H}}^i$ and $\hat{\mathcal{H}}^f$ are identical in the same iteration m. We trace out the environment in the basis of the initial Hamiltonian and obtain the following expression

$$\rho^{red}_{s,r}(m) = \sum_{l'l''e} \rho^i_{l'e,l''e}\ {}^f\langle s, e; m|l', e; m\rangle^{i\ i}\langle l'', e; m|r, e; m\rangle^f$$

$$= \sum_{l'l''} {}^f\langle s, m|l', m\rangle^i \rho^{red,i}_{l',l''}(m)\ {}^i\langle l'', m|r, m\rangle^f. \tag{8.29}$$

Now we only have to find a smart way of calculating the overlap matrix elements between the eigenstates of the initial and final Hamiltonian in each NRG iteration ${}^i\langle l'', e; m|r, e; m\rangle^f$. Since both Hamilton operators describe the same quantum impurity model, the overlap between their eigenstates in the first step of the iterative diagonalization procedure is trivial: the eigenstates for the impurity and the first site on the Wilson chain have to be set up for both, the initial and the final Hamiltonian, in an adequate basis (e. g. the $\hat{S}_z$-eigenbasis for the single impurity Anderson model). In this initial basis, in which the Hamiltonians are in general non-diagonal, the eigenstates are identical leading to ${}^i\langle k, \tilde{e}; 0|r', \tilde{e}; 0\rangle^f = \delta_{kr'}$. Starting from their initial values, we use the unitary matrices transforming the eigenstates in iteration m to the ones in iteration $m+1$ ($U^{\alpha_m i}_{k',k}$ and $U^{\alpha_m f}_{r'',r'}$ respectively) to iteratively determine the overlap matrices in later iterations ${}^i\langle l'', e; m|r, e; m\rangle^f$.

8.4 Implementing the Algorithm

A few words on the actual implementation of the TD-NRG algorithm: in total we have to perform two independent NRG "runs", meaning that we first solve the iterative diagonalization for the initial Hamiltonian $\hat{\mathcal{H}}^i$ and afterwards perform another NRG calculation changing the parameters in the Hamiltonian to the ones given by $\hat{\mathcal{H}}^f$ (of course $\hat{\mathcal{H}}^i$ and $\hat{\mathcal{H}}^f$ describe the same model, where only the values of the parameters entering the model are different, otherwise the calculation does not describe a quantum quench in a physical situation).

In the first "run" we perform an usual NRG calculation using the initial Hamiltonian $\hat{\mathcal{H}}^i$ and store all transformation matrices

$$|l,e;m\rangle^i = \sum_{k,\alpha_m} U^{\alpha_m i}_{l,k} |k,\alpha_m,e;m-1\rangle^i. \tag{8.30}$$

In the last iteration of the first "run", we set up the equilibrium density matrix

$$\hat{\rho}^i_{eq} = \sum_j |j,N\rangle \frac{e^{-\beta E^i_{j,N}}}{Z^i_N} \langle j,N|, \tag{8.31}$$

which we directly transform to the eigenstates of $\hat{\mathcal{H}}^i$ in previous iterations using the stored transformation matrices $U^{\alpha_m i}_{l,k}$ of Eq. (8.30)

$$\left[\rho^{red}(m)\right]_{l',l''} = \sum_{\{\alpha_i\}} U^{\alpha_{m+1} i\dagger}_{s,l'} \ldots U^{\alpha_N i\dagger}_{j,r} \left[\rho^{red}(N)\right]_{j,j'} U^{\alpha_N i}_{j',r'} \ldots U^{\alpha_{m+1} i}_{s',l''}. \tag{8.32}$$

This is equivalent to "reducing" the density matrix, tracing out the environment of the environment of the Wilson chain of length m.

We start a second NRG calculation now using the final Hamiltonian $\hat{\mathcal{H}}^f$. In the first iteration $m = 0$, we initialize the overlap matrices between the eigenstates of the two different NRG "runs" ${}^i\langle k,\tilde{e};0|r',\tilde{e};0\rangle^f$. Using the transformation matrices of the initial $U^{\alpha_m i}_{l,k}$ and the final Hamiltonian $U^{\alpha_m f}_{r',r''}$, we determine the overlap matrices in the subsequent iterations ${}^i\langle l'',e;m|r,e;m\rangle^f$, which we use to rotate the initial equilibrium reduced density matrix ${}^i\langle l',e;m|\hat{\rho}_{eq}|l'',e;m\rangle^i$ to the basis of the final Hamiltonian and thus obtain $\rho^{red}_{s,r}(m)$. Now we only have to combine the matrix elements for $\rho^{red}_{s,r}(m)$, the ones for the local operator $O_{r,s}(m)$ (which we set up in the first iteration of the second NRG "run" and transform to later iterations as in every standard NRG calculation), and the eigenenergies of the final Hamiltonian $E^f_{r,m}$ to evaluate the formula for the real-time dependence of a local operator after a quantum quench

$$\langle \hat{O}\rangle(t) = \sum_{m=m_0}^{N} \sum_{r,s}^{\text{dis}} e^{it(E^f_{r,m}-E^f_{s,m})} O_{r,s}(m)\rho^{red}_{s,r}(m). \tag{8.33}$$

For applications of the time-dependent numerical renormalization group method to different quantum impurity models, we refer to Chaps. 11, 12 and 13. As a "teaser" we present the time-evolution of the impurity magnetization for the single impurity Anderson model switching off a strong magnetic field applied to the impurity $h^i_z \gg W$ at time $t = 0$ in Fig. 8.3.

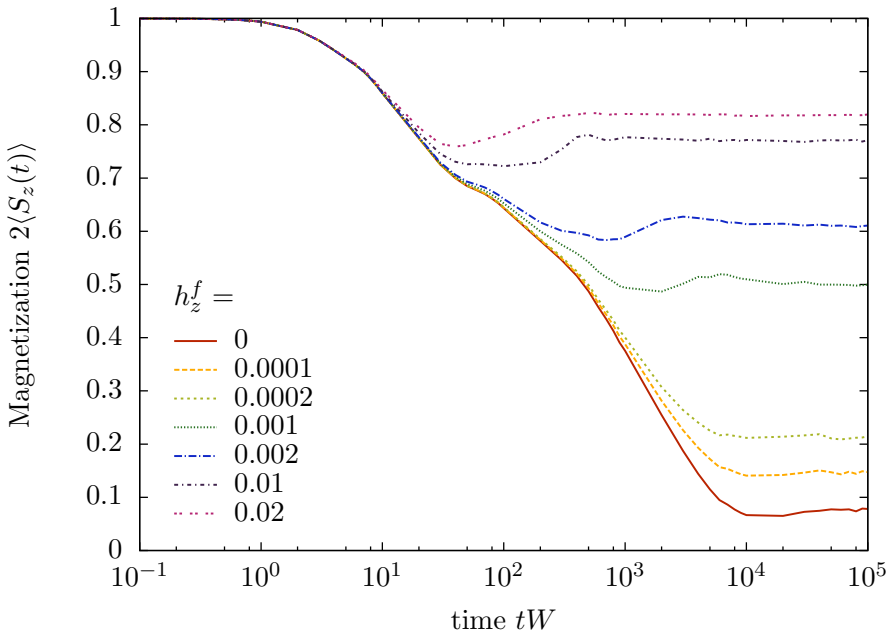

Figure 8.3: Time evolution of the magnetization in the single impurity Anderson model. For times $t < 0$ the impurity is fully polarized by applying a strong magnetic field $h_z^i = 10W$, which is abruptly switched to a smaller value h_z^f at time $t = 0$. Remaining parameters chosen as in Fig. 6.2.

Chapter 9

Finite Temperatures

9.1 Single Shell Approximation

The standard way of calculating static expectation values, as well as Green's functions, at finite temperatures within the numerical renormalization group method involves using a *single shell approximation* to the finite temperature density matrix. Let us briefly comment on this, before explaining an improved approach.

As already mentioned in the previous chapters, the energy scales for the eigenenergies decrease exponentially performing the steps of the iterative diagonalization procedure. This separation of energy scales ensures that the perturbation theory arguments hold. It can be exploited to approximate the density matrix at finite temperature T by evaluating the expression

$$\hat{\rho}_{N_T} = \sum_l |l; N_T\rangle \frac{\exp\left(-\beta E_l\right)}{Z_{N_T}} \langle l; N_T| \tag{9.1}$$

at an iteration N_T chosen such that

$$k_B T \approx \Lambda^{-(N_T-1)/2} \tag{9.2}$$

and terminating the iterative diagonalization afterwards. Here the *single shell* partition sum is given by $Z_{N_T} = \sum_l e^{-\beta E_{l,N_T}}$ and $\beta = (k_B T)^{-1}$ denotes the inverse temperature.

Even if the discretization parameter Λ and the length of the Wilson chain N_T are chosen wisely, such that Eq. (9.2) is fulfilled to good accuracy, still a little bit of arbitrariness remains, since eigenstates of iterations $N_T \pm 1$ would surely contribute to the "real" finite temperature density matrix as well and are not taken into account. Especially many eigenstate $|i\rangle$ with lower eigenenergy $E_i < T$ are not taken into account [63].

9.2 Full Density Matrix

Following the line of argumentation first given by Weichselbaum and von Delft [75], one can improve the calculation of finite temperature properties of quantum impurity systems within the NRG method by constructing a *full* density matrix

$$\hat{\rho}_T = \sum_{l,e;m} |l, e; m\rangle_{\text{dis}} \frac{\exp\left(-\beta E_{l,m}\right)}{Z} {}_{\text{dis}}\langle l, e; m|. \tag{9.3}$$

Here the label dis again indicates that we only consider the states which are discarded in each NRG iteration, thus exploiting the complete basis for the Fock space introduced before. As done throughout this thesis we adopt a color coding labeling discarded states in each NRG iteration in red and kept states in blue henceforth, omitting the indices for improved readability. The *full* partition sum Z is split up into its contribution of the different iterations

$$Z = \sum_m d^{N-m} Z_m = \sum_{l;m}^{\text{dis}} d^{N-m} e^{-\beta E_{l,m}}, \tag{9.4}$$

where we again only consider the eigenstates discarded in each iteration. The degeneracy of the eigenstates of a Wilson chain of length m has been taken into account in the expression for the partition sum by adding the factor d^{N-m}, where d is the number of degrees of freedom added in each NRG iteration. Along these lines, we may split up the contributions of each NRG iteration m to the final full density matrix

$$\hat{\rho}_T = \sum_{l,e;m} |l,e;m\rangle \frac{\exp\big(-\beta E_{l,m}\big)}{Z} \langle l,e;m| \tag{9.5}$$

$$= \sum_{l,e;m} \frac{Z_m}{Z} d^{N-m} |l,e;m\rangle \frac{\exp\big(-\beta E_{l,m}\big)}{d^{N-m} Z_m} \langle l,e;m| \tag{9.6}$$

$$= \sum_{l,e;m} \frac{Z_m}{Z} d^{N-m} \hat{\rho}_{m,T} = \sum_m \mathcal{W}_m \hat{\rho}_{m,T}. \tag{9.7}$$

A sketch of the distribution of $\mathcal{W}_m$ for different temperatures and fixed discretization pa-

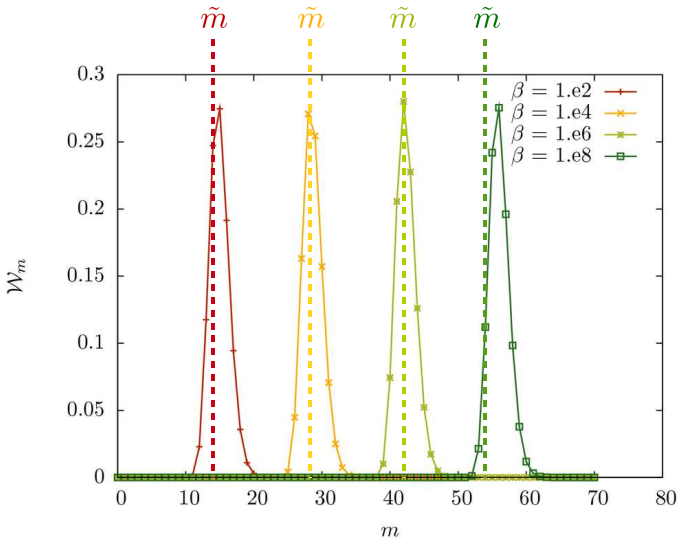

Figure 9.1: Distribution of weights $\mathcal{W}_m$ added to the full density matrix $\hat{\rho}_T$ at each NRG iteration m for different values of the inverse temperature $\beta = (k_B T)^{-1}$. The vertical lines labeled by $\tilde{m}$ show the iteration chosen for the single shell approximation, such that $k_B T = \Lambda^{-(N_T-1)/2}$.

rameter Λ is plotted in Fig. 9.1. The distributions of weight added to the finite temperature

density matrix depends on the discretization parameter Λ as well as the number of eigenstates kept in each NRG iteration N_{Lev}. Increasing Λ the relevant energy scale, where the main contributions to the finite temperature spectral function are added, shifts to smaller iterations, while the opposite is true for the number of kept eigenstates per NRG iteration: increasing N_{Lev} eigenstates with a given eigenenergy E_r are discarded, and thus contribute to the full density matrix, in later iterations. Depending on the choice for the two parameters the peak width of the weight distribution $\mathcal{W}_m$ ranges from ≈ 5 to ≈ 10 iterations.

9.3 Spectral Functions

A detailed derivation showing how to combine the "full" finite temperature density matrix and the complete basis for the Fock space to calculate finite temperature Green's functions (following Ref. [75]) can be found in Appendix B.

The result of the derivation in the Appendix reads

$$\begin{aligned} G(\omega) = & \frac{1}{Z}\sum_{m}\sum_{l,l'.e} A_{l,l'}(m)B_{l',l}(m)\frac{e^{-\beta E_{l,m}} \pm e^{-\beta E_{l',m}}}{\omega + (E_{l,m} - E_{l',m})} \\ & + \frac{1}{Z}\sum_{m}\sum_{l,k,e} A_{l,k}(m)B_{k,l}(m)\frac{e^{-\beta E_{l,m}}}{\omega + (E_{l,m} - E_{k,m})} \\ & + \sum_{\substack{l,j,k \\ m}} B_{l,j}(m)[\tilde{\rho}_T^{red}(m)]_{j,k}A_{k,l}(m)\frac{1}{\omega + (E_{k,m} - E_{l,m})} \\ & \pm \frac{1}{Z}\sum_{m}\sum_{l,k,e} A_{k,l}(m)B_{l,k}(m)\frac{e^{-\beta E_{l,m}}}{\omega + (E_{k,m} - E_{l,m})} \\ & \pm \sum_{\substack{l,j,k \\ m}} A_{l,j}(m)[\tilde{\rho}_T^{red}(m)]_{j,k}B_{k,l}(m)\frac{1}{\omega + (E_{l,m} - E_{j,m})}. \end{aligned} \tag{9.8}$$

As an example we show the results of the improved version of the finite temperature spectral for the single impurity Anderson model in Fig. 9.2.

A comparison of the two approaches using the *single shell* and the "full" density matrix to calculate the spectral function for the single impurity Anderson model for different values of the inverse temperature β is shown in Fig. 9.3. The results show that information for frequencies down to $\omega \lesssim T/5$ can be obtained using the improved algorithm to calculate the spectral function, while in the *single shell* approach unphysical oscillations begin to set in at frequencies $\omega \approx T$.

The improved approach of calculating spectral functions of quantum impurity systems at finite temperatures presented here adds another powerful method toolbox of the condensed matter physicist, complementing methods like the t-DMRG approach to finite temperature spectral functions in one dimension [76].

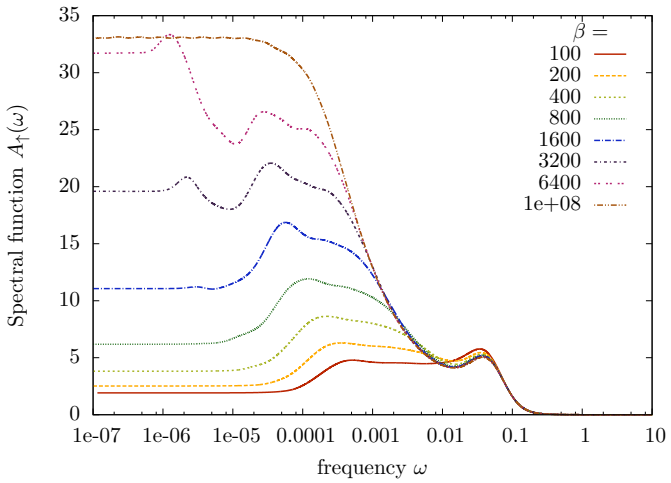

Figure 9.2: Finite temperature spectral functions for the single impurity Anderson model using the improved "full" density matrix approach. Parameters chosen as in Fig. 6.2.

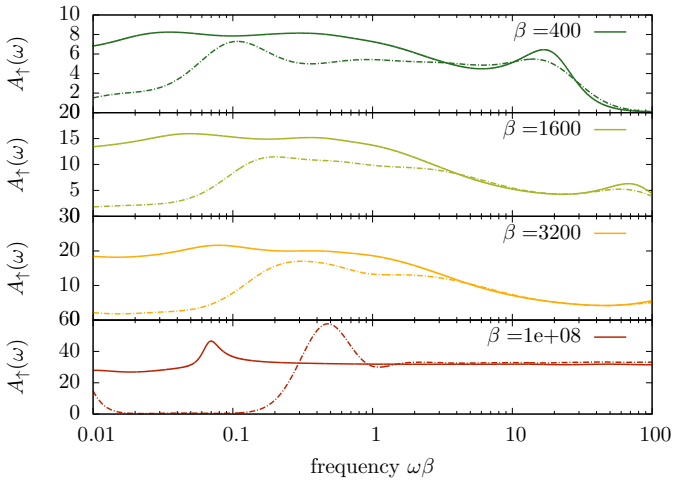

Figure 9.3: Comparison of *single shell* (dashed lines) and "full" (solid lines) density matrix approach to finite temperature spectral functions for the SIAM. Notice that the unphysical oscillatory behavior sets in at higher frequencies for the *single shell* approach (can be seen best in the lowest panel). Parameters chosen as in Fig. 6.2.

Chapter 10

Improving Accuracy

In this chapter we will explain some of the most important strategies to improve the accuracy of NRG calculations.

10.1 Using Symmetries

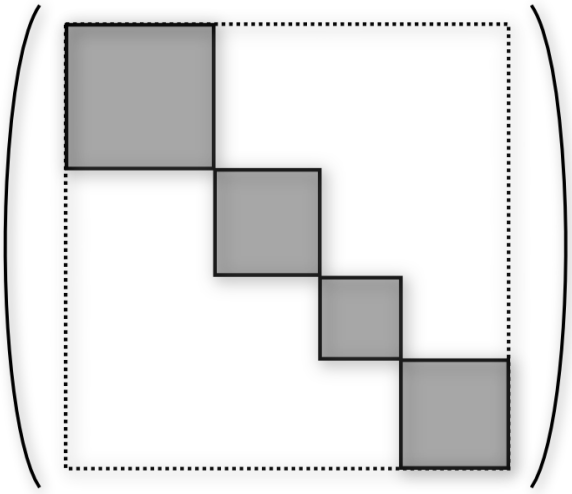

Figure 10.1: Using the symmetries of the quantum impurity models, we can convert the Hamiltonian matrices to a block-diagonal structure.

The first and most important strategy consist of using the model's symmetries. Since a differentiable symmetry of the action of a physical system has a corresponding conservation law according to Noether's theorem [77], we may as well talk about exploiting conservation laws. In case of fermionic quantum impurity models, the most commonly conserved quantities are the total charge of the system Q, and/or one of it's spin components S_z . The conservation of the total spin $\mathbf{S^2}$ is also often found in fermionic quantum impurity problems without an additional magnetic field. It is harder to implement, because one has to worry about reduced matrix elements and the corresponding Clebsch-Gordon coefficients (for details on the correct implementation of the total spin quantum number, see Appendix B of Ref. [54], for example).

Exploiting the symmetries the Hamilton operator can be written in block-diagonal matrices defined by fixed values for the conserved quantities and each of the blocks can be diagonalized separately. This effectively reduces the size of the matrices one has to diagonalize within the NRG method and allows to keep a larger number of eigenstates N_{Lev} in each iteration step, which, as discussed before, increases the accuracy of the calculation.

10.2 Oliveira's z-Trick

Calculating different dynamic quantities like the time-evolution of local operators or the different Green's functions within the numerical renormalization group method a common problem encountered relates to the finite number of eigenstates used to describe the system. Since we discretize the quantum bath and single out a finite number of eigenstates, the result

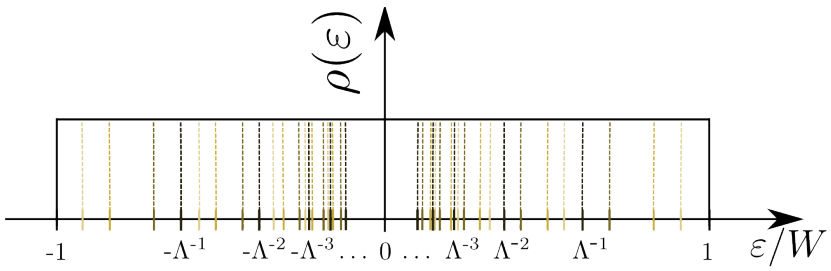

Figure 10.2: Different discretization scheme for the constant density of states of a free fermionic bath applying the z-trick (different colors stand for different choices of z).

will always consist of the quantity being studied at a finite number of frequencies. For the real-time evolution this may lead to unphysical oscillations, and for Green's functions the discretization effects are evident, since all result only consist of a finite number of δ-peaks instead of continuous smooth functions.

One attempt to restore a continuous quantum bath was first introduced by Oliveira and coworkers [78] and is commonly referred to as the z-trick . Employing the z-trick one introduces a number of slightly altered discretizations of the quantum bath and averages over the results obtained in these independent NRG calculations afterwards.

For a constant density of states in case of a fermionic quantum bath the trick is illustrated in Fig. 10.2: The discretization points on the conduction band are shifted according to $\pm\Lambda^{-n} \to \pm\Lambda^{-n+z}$ for $n \geq 1$. This leads to slightly different intervals (changing Eq. (4.3)) and to a shift of the eigenfrequencies. Choosing N_z different values for $z = \frac{1}{N_z}, \frac{2}{N_z}..\frac{N_z}{N_z}$ (where N_z should be a multiple of four to obtain the best cancellation of unphysical oscillations for time-dependent observables calculated within the TD-NRG method [67]), it is an embarrassingly easy task to parallelize the calculations and average over the results afterwards. An example of the improved resolution at finite frequencies applying the z-trick is shown in Fig. 10.3.

Applying the z-trick to the calculation of spectral functions, the energy resolution at finite frequencies can be improved drastically. Recently this approach has been developed further by Zitko and Pruschke [79] to scale down the discretization effects even more. They observed that calculating the spectral function on the first site of the Wilson chain $A_{f_0}(\omega)$ in absence of the impurity, the result does not reproduce the original density of states of the conduction band $\rho(\omega)$ for the discretization scheme suggested in the original version of the z-trick.

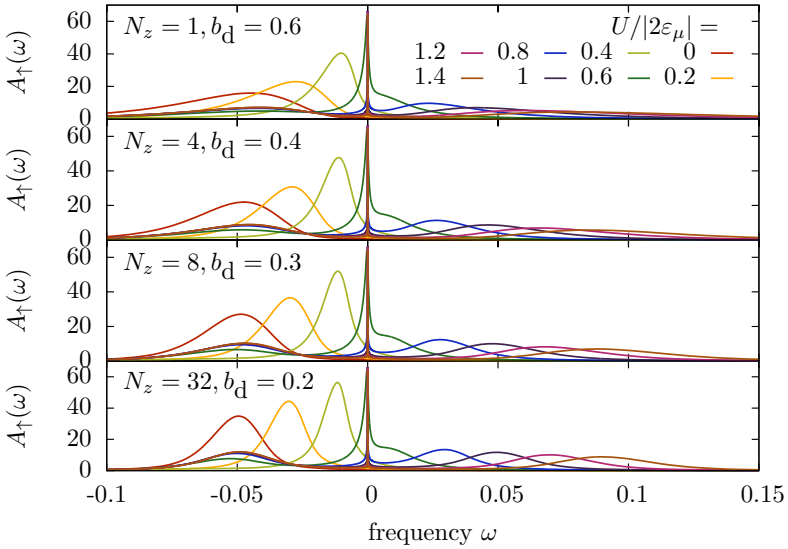

Figure 10.3: The energy resolution at large frequencies can be improved applying the z-trick averaging. The plots show spectral functions for the single impurity Anderson model for different values of N_z. The damping parameter b_d is tuned accordingly, such that unphysical oscillations vanish and no discretization effects are visible ($\Gamma_\mu = 0.005W, \varepsilon_\mu = -0.05W, B = 0W, N_\mathrm{Lev} = 1536, \Lambda = 2.0$).

They were able to drastically decrease the unphysical structures observed especially at the edges of the conduction band, by solving a differential equation for the positions of the discretization points, such that the expected result $A_{f_0}(\omega) = \rho(\omega)$ was reproduced. As they claim, this leads to a sizable improvement in the calculation of high-resolution spectral functions, which are important for the reliability of the NRG method as an impurity solver for the dynamic mean-field theory, where the self-consistency loop couples low- and high-energy scales with each other [79].

10.3 Damping and Broadening

In many cases, applying the z-trick with sufficiently large values for N_z and exploiting the symmetries of the quantum impurity model, leads to good results for the real-time evolution of local observables after a quantum quench calculated by TD-NRG. In some cases though, we still see unphysical oscillations in the time evolution of the observables of interest, which are a direct consequence of the discretization of the quantum bath and the resulting finite set of frequencies determining the oscillations. To suppress these artifacts we introduce a *scale dependent damping factor* α_d substituting

$$e^{it(E^f_{r,m}-E^f_{s,m})} \to e^{it(E^f_{r,m}-E^f_{s,m})} \cdot e^{-\alpha_\mathrm{d} t|E^f_{r,m}-E^f_{s,m}|} \tag{10.1}$$

in Eq. (8.33), where α_d is of the order of $\mathcal{O}(10^{-2})$. Converted to frequency space, this corresponds to broadening each δ-peak in the finite set of contributions with a Lorentzian kernel. Note that this choice of damping does not lower the long-time limit of the time

evolution $\langle \hat{O}(t \to \infty) \rangle$, since the important contributions from degenerate eigenstates $E^f_{r,m} = E^f_{s,m}$ are not affected by our choice of damping.

The situation differs calculating spectral functions. Eq. (9.8), for example, only yields a finite set of delta peaks for the finite temperature spectral function, instead of a smooth and continuous curve. Different choices for damping kernels have been suggested throughout the literature. Folding the δ-peaks with a Gaussian [79], a logarithmic Gaussian [68] or a combination of the two [53] are among the commonly found choices. For the calculations in this thesis, we have adopted the third option: The δ-peaks stored in the "raw" data $G^{\mathrm{raw}}_\mu(\omega')$ are broadened with a kernel $K(\omega, \omega')$ according to

$$G_\mu(\omega) \equiv \int d\omega' K(\omega, \omega') G^{\mathrm{raw}}_\mu(\omega').$$

For the broadening kernel we choose

$$K(\omega, \omega') = L(\omega, \omega') h(\omega') + G(\omega, \omega')[1 - h(\omega)], \tag{10.2}$$

where

$$L(\omega, \omega') = \frac{\theta(\omega\omega')}{\sqrt{\pi} b_{\mathrm{d}} |\omega'|} e^{-\left(\frac{\log|\omega'/\omega|}{b_{\mathrm{d}}} + \gamma - \frac{b_{\mathrm{d}}}{2}\right)^2},$$

$$G(\omega, \omega') = \frac{1}{\sqrt{\pi}\omega_0} e^{-\left(\frac{\omega - \omega'}{\omega_0}\right)^2} \text{ and}$$

$$h(\omega) = \begin{cases} 1 & \text{if } |\omega| \geq \omega_0 \\ e^{-\left(\frac{\log|\omega/\omega_0|}{b_{\mathrm{d}}}\right)^2} & \text{if } |\omega| < \omega_0 \,. \end{cases}$$

The logarithmic Gaussian part of the kernel for all frequencies $\omega > \omega_0$ is optimal for the NRG, since its width depends on the frequencies ω' and it has a longer "tail" at larger absolute values of ω', accounting for the increasingly dense raw data going to smaller values of ω'. Only for very small frequencies $\omega \leq \omega_0 \ll T$ the logarithmic Gaussian is replaced by a normal Gaussian on a linear grid, which interpolates between the regions $\omega \geq \omega_0$ and $\omega \leq -\omega_0$. Connecting these two regions turns out to be crucial for the calculation of spectral functions at finite temperatures, where we usually choose ω_0 to be smaller than the smallest energy scale of the problem $\omega_0 \approx T/3$ and b_{d} in the range of $b_{\mathrm{d}} = 0.7$ (without z-trick averaging) and $b_{\mathrm{d}} = 0.2$ (including z-trick averaging with sufficiently large N_z).

10.4 Self-Energy Trick

The spectral functions of the single impurity Anderson model at temperatures $T \to 0$ should fulfill the *density of states rule* for the height of the resonance at $\omega = 0$

$$A_\mu(\omega \to 0) = \frac{1}{\pi\Gamma}. \tag{10.3}$$

This exact statement, which sometimes is referred to as Friedel sum rule as well, is not accurately fulfilled in our NRG calculations, instead the height of the resonance deviates approximately 5% from the one predicted by Eq. (10.3).

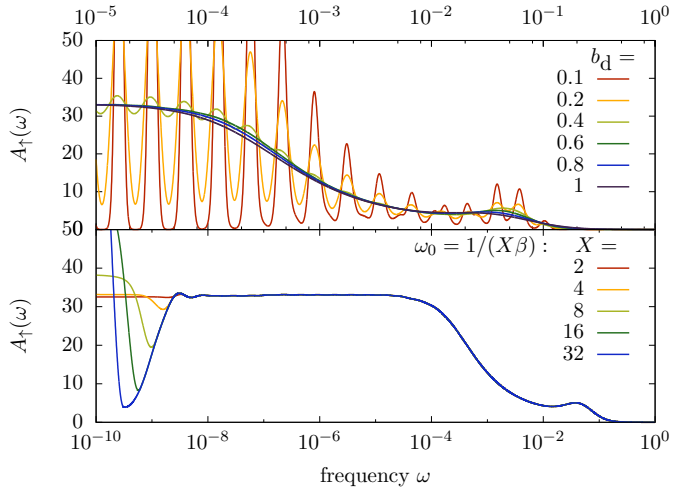

Figure 10.4: Effect of the broadening kernel of Eq. (10.2) chosen for spectral functions throughout this dissertation: The upper panel shows the effect of tuning the width b_d of the logarithmic Gaussian applied for frequencies $\omega > \omega_0$. Notice the reduction of the Hubbard peak choosing the width too large $b_\mathrm{d} \geq 0.8$. The lower panel shows the effect of the (normal) Gaussian broadening for frequencies $\omega < \omega_0$, allowing for a "smooth" transition going from negative to positive frequencies.

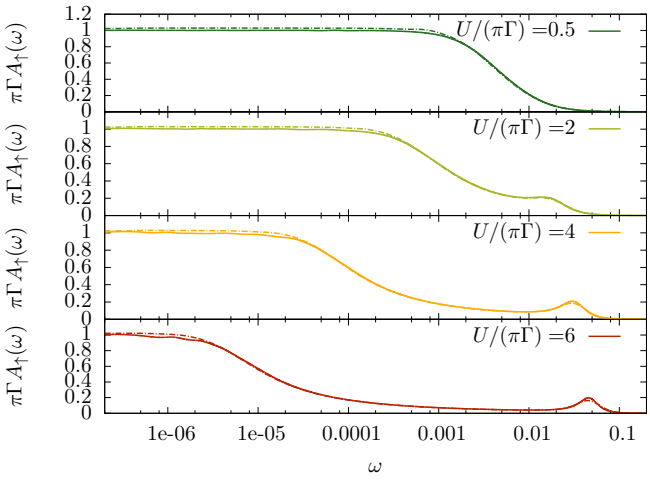

Figure 10.5: The results for the spectral function for the single impurity Anderson model obtained using the self-energy trick (solid lines) deviate less from the exact relation $A_\mu(\omega \to 0) = \frac{1}{\pi\Gamma}$ then the direct calculation (dashed lines). Notice that the height of the Hubbard peaks (at $\omega = 0.04W$ for $U/(\pi\Gamma = 6)$) changes as well ($N_z = 32$, $\varepsilon_\mu = -U/2$, $\Gamma_\mu = 0.005W$).

Expressing the Green's function (from which the spectral function $A_\mu(\omega) = \frac{1}{\pi}\mathrm{Im}\{G_\mu(\omega)\}$ is derived) as a ratio of two correlation functions one can improve the height of the resonance at $\omega = 0$ as first shown by Bulla and coworkers [80]. Let us briefly comment on how this improved Green's function is calculated. We formally define the Green's function introducing the self-energy $\Sigma_\mu(\omega)$

$$G_\mu^{\mathrm{imp}}(\omega) = \frac{1}{\omega - \varepsilon_{d,\mu} - \Sigma_\mu(\omega)}. \tag{10.4}$$

The self-energy can be decomposed in two parts $\Sigma_\mu(\omega) = \Delta_\mu(\omega) + \Sigma_\mu^U(\omega)$. While the part independent of the on-site interaction U can be calculated straightforwardly

$$\Delta_\mu(\omega) = \sum_k V_k^2 \frac{1}{\omega - \varepsilon_k},$$

the interaction contribution to the self energy $\Sigma_\mu^U(\omega)$ is highly non-trivial. Using an equation of motion technique to express the self-energy in terms of standard impurity correlation functions [80], it can be verified that $\Sigma_\mu^U(\omega)$ is given by the following ratio

$$\Sigma_\mu^U(\omega) = U \frac{F_\mu(\omega)}{G_\mu(\omega)}. \tag{10.5}$$

Here $G_\mu(\omega)$ is the "normal" Green's function

$$G_\mu(\omega) = -i \int_0^\infty dt e^{i\omega t} \langle \left[\hat{d}_\mu(t), \hat{d}_\mu^\dagger(0) \right]_+ \rangle$$

and $F_\mu(\omega)$ is the correlation function given by the expression

$$F_\mu(\omega) = -i \int_0^\infty dt e^{i\omega t} \langle \left[[\hat{d}_\mu \hat{d}_{-\mu}^\dagger \hat{d}_{-\mu}](t), \hat{d}_\mu^\dagger(0) \right]_+ \rangle. \tag{10.6}$$

Both correlation functions $G_\mu(\omega)$ and $F_\mu(\omega)$ can be calculated in the "standard" way described in the proceeding chapters. As a result, the improved Green's function contains less unphysical small wavy features caused by the logarithmic discretization of the conduction band, since they cancel out taking the ratio $\frac{F_\mu(\omega)}{G_\mu(\omega)}$. Since $\Sigma_\mu^U(\omega \to 0) \to 0$ for $T = 0$, the spectral sum rule is fulfilled with better accuracy as well (cf. Fig. 10.5, where the height of the resonance peak for the spectral functions calculated with the self-energy approach now only deviate $\approx 0.5\%$ from the expected value).

10.5 High-Accuracy NRG Spectral Functions as Benchmark

We exploit all "tricks" improving the calculation of finite temperature spectral functions for the single impurity Anderson model described above. These high-accuracy results obtained by the numerical renormalization group method serve as a benchmark [81] for a new approach to calculate spectral functions within the functional renormalization group in one of our collaborations. A selection of the results obtained in this comparison is shown in Fig. 10.6. For a recent review on the function renormalization group, see Ref. [82].

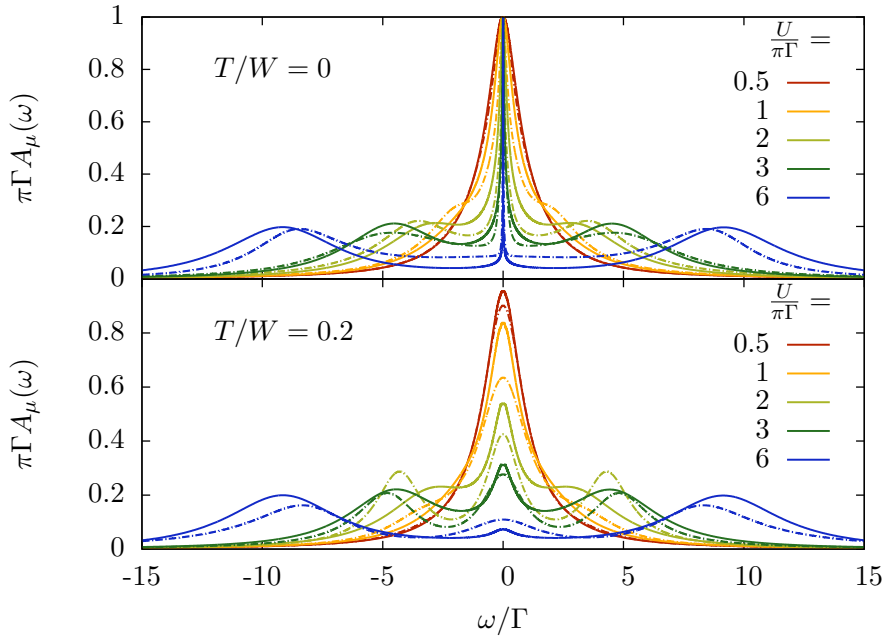

Figure 10.6: High quality NRG data for the spectral function of the single impurity Anderson model including all improvements discussed so far (solid lines) are compared against results from functional renormalization group method. For details see Ref. [81]. Parameters for NRG: $N_{\mathrm{Lev}} = 1536$, $\Lambda = 2$, $N_z = 32$, $b_{\mathrm{d}} = 0.3$, $\omega_0 = -T/2$, $\varepsilon_\mu = -U/2$, $\Gamma_\mu = 0.005W$.

Part III

Applications

Chapter 11

Ferromagnetic Kondo Model

Although the Kondo Hamiltonian describing a single impurity spin coupled to the spins of electrons of a fermionic quantum bath via a Heisenberg interaction has been studied in great detail, its ferromagnetic regime has often been neglected. An exception is the investigation of the spatial equal-time spin-correlations of an underscreened spin-1 impurity [83]. In this chapter, we present our study of the time-evolution of a ferromagnetically coupled spin in a collaboration combining the results of two different methods, the time-dependent numerical renormalization group method [66, 67] and a recent extension to the flow-equation method [84, 73].

In the first section, we explain the origins of ferromagnetic interaction between spins on impurity and conduction band mentioning two different experimental realizations of the ferromagnetic Kondo model with isotropic and anisotropic exchange interaction. A short section on the equilibrium properties of the ferromagnetic Kondo model follows, before we have a detailed look at the time-evolution of the impurity spin magnetization abruptly switching off a magnetic field polarizing the impurity spin. We highlight the differences found for isotropic and anisotropic exchange interation. Two important questions are asked in this chapter: How fast does an initially polarized impurity spin reduce its magnetization due to spin flip scattering and what is the nature of the final state of the quantum system for ferromagnetic exchange interaction?

11.1 Experimental Realizations

We want to explain two different realizations of the Kondo Hamiltonian with ferromagnetic exchange interaction between the impurity spin and the spins of the conduction band electrons: In case of a molecule with large spin, which is partially screened due to the underscreened Kondo effect, the remaining exchange interaction is ferromagnetic. For single molecule magnets with an additional charge degree of freedom, a careful derivation of the Kondo Hamiltonian can yield a ferromagnetic exchange interaction as well.

11.1.1 Schrieffer-Wolff Transformation

Let us start by quickly deriving the transformation of the single impurity Anderson model given by the Hamilton operator

$$\hat{\mathcal{H}}_A = \varepsilon_d \hat{d}^\dagger_\mu \hat{d}_\mu + U \hat{n}_\uparrow \hat{n}_\downarrow + \sum_k \varepsilon_k \hat{c}^\dagger_{k\mu} \hat{c}_{k\mu} + \sum_k V_k \left(\hat{c}^\dagger_{k\mu} \hat{d}_\mu + \hat{d}^\dagger_\mu \hat{c}_{k\mu} \right), \tag{11.1}$$

already introduced in Eq. (4.1) of the method section, to a Kondo Hamiltonian only accounting for the spin interaction between impurity and conduction band electrons and eliminating the charge degree of freedom. As first demonstrated by Schrieffer-Wolff in the 1960's [4] a canonical transformation of the Anderson Hamiltonian

$$\hat{\mathcal{H}}_K = e^{\hat{S}} \hat{\mathcal{H}}_A e^{-\hat{S}} \tag{11.2}$$

eliminates the coupling term including V_k to first order. To reach this goal we choose the anti-hermitian operator $\hat{S}$, such that the commutator with the non-interacting part of the Hamiltonian $\hat{\mathcal{H}}_0$ (first three terms in Eq. (11.1)) yields the interacting part $\hat{\mathcal{H}}_{\text{int}}$ (last terms in Eq. (11.1))

$$\left[\hat{\mathcal{H}}_0, \hat{S} \right] = \hat{\mathcal{H}}_{\text{int}}. \tag{11.3}$$

As a consequence the generator of this canonical transformation reads

$$\hat{S} = \sum_{k\mu} \left(\frac{V_k}{\varepsilon_k - (\varepsilon_d + U)} \hat{n}_{-\mu} \hat{c}^\dagger_{k\mu} \hat{d}_\mu + \frac{V_k}{\varepsilon_k - \varepsilon_d} (1 - \hat{n}_{-\mu}) \hat{c}^\dagger_{k\mu} \hat{d}_\mu \right) - h.c. \tag{11.4}$$

and the transformed Hamiltonian reduces to

$$\hat{\mathcal{H}}_K = \hat{\mathcal{H}}_0 + \frac{1}{2} \left[S, \hat{\mathcal{H}}_{\text{int}} \right] + \frac{1}{3} \left[S, \left[S, \hat{\mathcal{H}}_{\text{int}} \right] \right] + \frac{1}{8} \left[S, \left[S, \left[S, \hat{\mathcal{H}}_{\text{int}} \right] \right] \right] + \dots \, . \tag{11.5}$$

In the limit of small coupling to the conduction band and large on-site energies $V_k \ll \{-\varepsilon_d, U\}$ the transformed Anderson Hamiltonian reduces to the Kondo or *s-d* Hamiltonian

$$\hat{\mathcal{H}}_K = \sum_k \varepsilon_k \hat{c}^\dagger_{k\mu} \hat{c}_{k\mu} + \sum_{k,k'} J_{k,k'} (\hat{c}^\dagger_{k\mu} \frac{\hat{\boldsymbol{\sigma}}_{\mu\nu}}{2} \hat{c}_{k'\nu}) (\frac{\hat{\boldsymbol{\tau}}}{2}), \tag{11.6}$$

where $\hat{\boldsymbol{\sigma}}_{\mu\nu}$ denotes the Pauli matrix for the spin of the conduction band electrons and $\hat{\boldsymbol{\tau}}$ the spin matrix on the impurity. Performing this Schrieffer-Wolff transformation on the single impurity Anderson model always leads to an antiferromagnetic Kondo interaction for lateral quantum dots. For momentum-independent exchange interaction $V_k = V_{k_F}$ the spin-spin interaction reads

$$J = 2|V_{k_F}|^2 \frac{U}{\varepsilon_d(\varepsilon_d + U)} < 0. \tag{11.7}$$

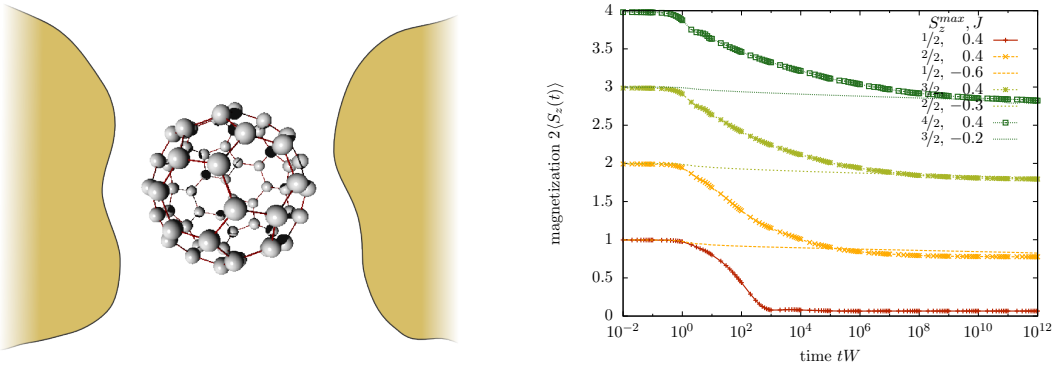

Figure 11.1: Left panel: Sketch of C_{60}-molecule attached to metallic leads. Right panel: The logarithmic decay of $\langle S_z(t)\rangle$ due to underscreening of the local moment for different spin sizes $S_z^{\max}$ ($J = 0.4$) is compared to the relaxation of a spin $S' = S - 1/2$, whose effective ferromagnetic coupling $J' < 0$ is chosen according to [85]. (NRG parameters: $\Lambda = 2.5$, $N = 60$, $N_{\mathrm{Lev}} = 2000$).

11.1.2 Underscreened Kondo Effect

An isotropic ferromagnetic exchange interaction between the spin of the conduction band electrons and the spin on the impurity occurs in systems with a partially screened large impurity spin. The experiment of Wernsdorfer and coworkers [39] highlighted in Sec. 3.1 of this thesis is a prime example for this type of interaction. There the phase transition of a single C_{60} molecule attached to metallic leads is studied (a sketch of the experimental setup is given in the left panel of Fig. 11.1). In a certain gate voltage regime, the impurity spin state is given by a spin-1 triplet, which lowering the temperature is partially screened by conduction band electrons, since a single channel coupling only to one of the two spin states of the molecule dominates the screening (see region III of Fig. 3.4 for a sketch of the triplet phase).

The underscreened Kondo physics observed studying the phase transition of the single molecule transistor in Ref. [39] can be related to an earlier observation of ours [86], where we calculated the real-time evolution of the magnetization in a Kondo model with a large spin $S > 1/2$ abruptly switching off a magnetic field initially polarizing the impurity spin. We observed that, in contrast to the $S = 1/2$ case, the interaction between the impurity and the conduction electrons does not quench the magnetic moment on the impurity completely. In a naïve picture the equilibrium underscreened Kondo effect [12, 87, 16, 14, 88, 85] can be described as a two-stage process: first, the magnetization is reduced to $S - 1/2$ by screening due to the spin-1/2 electrons in the conduction band. This effective spin $S' = S - 1/2$ then couples ferromagnetically ($J' < 0$) to the conduction band and becomes asymptotically free at low energies [87]. Our results in Fig. 11.1 show how this energy dependence of the effective couplings translates into the real-time dynamics of the impurity spin. For different values of S and $J = 0.4$ we observe an initial drop of the magnetization by approximately $1/2$, followed by a logarithmically slow further relaxation.

Comparing the low energy excitations for a spin S and antiferromagnetic coupling to those of a spin $S' = S - 1/2$ impurity coupled ferromagnetically, Koller and coworkers [85] have

determined the value of the renormalized ferromagnetic interaction J' for the underscreened Kondo effect. In Fig. 11.1 we show that this correspondence can also be observed in the real-time dynamics, by comparing the underscreened relaxation dynamics for $J = 0.4$ with a $S' = S - 1/2$ Kondo impurity and an effective ferromagnetic $J' < 0$ as calculated in Ref. [85]. Good asymptotic agreement for the two cases was found in the real-time evolution, which confirms our identification of time-resolved underscreening.

11.1.3 Single Molecule Magnets

For more complicated impurities describing single molecule magnets, which we already introduced in Sec. 3.2, the anisotropy for the spin requires a more careful microscopic derivation of the corresponding Kondo Hamiltonian. We outline how the Schrieffer-Wolff transformation is applied on the Hamilton operator describing single molecule magnets following Ref. [89].

The microscopic Hamiltonian describing a single molecule magnet attached to metallic leads with an additional gate voltage can be divided into three parts

$$\hat{\mathcal{H}}_{\mathrm{SMM,A}} = \hat{\mathcal{H}}_{\mathrm{imp}} + \hat{\mathcal{H}}_{\mathrm{bath}} + \hat{\mathcal{H}}_{\mathrm{int}}, \tag{11.8}$$

where the bath and interaction term are very similar to the original Anderson Hamiltonian

$$\hat{\mathcal{H}}_{\mathrm{bath}} = \sum_{k} \varepsilon_k \hat{c}^\dagger_{k\mu} \hat{c}_{k\mu} \tag{11.9}$$

$$\hat{\mathcal{H}}_{\mathrm{int}} = \sum_{n,k} V_{n,k} \left(\hat{c}^\dagger_{k\mu} \hat{d}_{n\mu} + \hat{d}^\dagger_{n\mu} \hat{c}_{k\mu} \right). \tag{11.10}$$

In contrast to the simple single impurity Anderson model, we now account for the different charge states of the impurity introducing the operators $d^{(\dagger)}_{n\mu}$, where n labels the charge state of the impurity and μ the spin state.

The impurity part describing the molecule itself on the other hand is more complicated than its simple counterpart in Eq. (11.1):

$$\hat{\mathcal{H}}_{\mathrm{imp}} = \hat{\mathcal{H}}_{\mathrm{spin}} + \hat{\mathcal{H}}_{\mathrm{orb}} + \frac{q^2 U}{2} - qeV_g. \tag{11.11}$$

Here V_g is the additional potential caused by the gate voltage, which can be tuned to compensate for the charging energy $\frac{q^2U}{2}$ (q labels the excess charge). The orbital part of the impurity Hamiltonian is generalized to

$$\hat{\mathcal{H}}_{\mathrm{orb}} = \sum_{n\mu} \varepsilon_{n\mu} \hat{d}^\dagger_{n\mu} \hat{d}_{n\mu}, \tag{11.12}$$

while the spin part

$$\hat{\mathcal{H}}_{\mathrm{spin}} = -D_q \hat{S}^2_{q,z} + \frac{B_{2,q}}{2} \left(\hat{S}^2_{q,+} + \hat{S}^2_{q,-} \right) + \frac{B_{4,q}}{3} \left(\hat{S}^4_{q,+} + \hat{S}^4_{q,-} \right) - \mathbf{h}\hat{\mathbf{S}}_q \tag{11.13}$$

accounts for the longitudinal (D_q) and transversal ($B_{2,q}, B_{4,q}$) anisotropy for the spin alignment, which as the spin operators themselves depend on the charge state of the molecule q. The low-energy eigenstates of the Hamiltonian are given by symmetric or antisymmetric

combinations of the eigenstates of the $\hat{S}_{q,z}$ operator with maximal spin-component pointing along the molecule's easy axis $|\pm S^{\max}_{q,z}\rangle$:

$$|+,q\rangle = \frac{|+S^{\max}_{q,z}\rangle + |-S^{\max}_{q,z}\rangle}{\sqrt{2}}, \qquad |-,q\rangle = \frac{|+S^{\max}_{q,z}\rangle - |-S^{\max}_{q,z}\rangle}{\sqrt{2}}. \tag{11.14}$$

For each charge state of the impurity q, we can write down an expression for the impurity Hamiltonian $\hat{\mathcal{H}}_q$. Since the charge state of the Hamiltonian only changes by single electrons "hopping" on or off the impurity, which is described by the interaction part of the Hamilton operator $\hat{\mathcal{H}}_{\text{int}}$, only neighboring charge sectors are coupled in the full description of the model.

Focusing on the three charge sectors $q = 0, \pm 1$ and assuming that the interaction strength between impurity and conduction band $V_{n,k}$ is small compared to the charging and on-site energies $\varepsilon_{n\mu}, U$, the authors of Ref. [89] showed that the coupling of the Hamilton operator $\hat{\mathcal{H}}_0$ to the other charge sectors $q = \pm 1$, can be eliminated to first order in $V_{n,k}/U$ performing a Schrieffer-Wolff transformation. The Hamilton operator then reduces to the form of the anisotropic Kondo Hamiltonian

$$\hat{\mathcal{H}}_K = \sum_{k\mu} \varepsilon_k \hat{c}^\dagger_{k\sigma}\hat{c}_{k\sigma} + \frac{J_\perp}{2}\sum_{kk'}(\hat{c}^\dagger_{k\uparrow}\hat{c}_{k'\downarrow}\hat{S}^- + \hat{c}^\dagger_{k\downarrow}\hat{c}_{k'\uparrow}\hat{S}^+) \quad + \frac{J_\parallel}{2}\sum_{kk'}(\hat{c}^\dagger_{k\uparrow}\hat{c}_{k'\uparrow} - \hat{c}^\dagger_{k\downarrow}\hat{c}_{k'\downarrow})\hat{S}_z, \tag{11.15}$$

where $\hat{\mathbf{S}}$ now denotes a pseudo-spin-1/2 operator of the single molecule magnet whose eigenstates are the two maximally polarized $\hat{S}_{q,z}$-eigenstates $|\pm S^{\max}_{q,z}\rangle$.

The exchange couplings between the spin of the conduction band electrons and the new pseudo-spin $\hat{\mathbf{S}}$ are given by

$$\begin{aligned} J_\perp &= 4V^2\left[\frac{\Delta_1}{(U+\Delta_0)^2-\Delta_1^2} + \frac{\Delta_1}{(U-\Delta_0)^2-\Delta_1^2}\right] \text{ and} \\ J_\parallel &= \pm 2V^2\left[\frac{U+\Delta_0}{(U+\Delta_0)^2-\Delta_1^2} + \frac{U-\Delta_0}{(U-\Delta_0)^2-\Delta_1^2}\right] \end{aligned} \tag{11.16}$$

up to leading order in $\frac{\Delta_q}{U}$, where Δ_q denotes the energy difference between the eigenstates $|+,q\rangle$ and $|-,q\rangle$ (for brevity the tunnel splitting for the "charge excited" states are assumed to be identical $\Delta_1 = \Delta_{-1}$ and the charge and momentum dependence of the exchange interaction $V = V_{n,k}$ is neglected. For details of the calculation, see Appendix A of Ref. [89]).

While a simple algebra on Eq. (11.16) demonstrates that the spin-exchange is always anisotropic $|J_\perp| < |J_\parallel|$, the sign of $J_\parallel$ stems from the different effect a change in the charge state of the impurity ($q = 0 \to \pm 1$) has on its maximal spin $S^{\max}_{q,z}$. One can summarize the results of the detailed derivation given in Appendix A of Ref. [89] as follows:

- If adding or subtracting an electron to the impurity *decreases* the spin of the impurity ($S^{\max}_{q=\pm1,z} = S^{\max}_{q=0,z} - \frac{1}{2}$), the longitudinal spin exchange interaction is always *antiferromagnetic* ($J_\parallel > 0$).
- If adding or subtracting an electron to the impurity *increases* the spin of the impurity ($S^{\max}_{q=\pm1,z} = S^{\max}_{q=0,z} + \frac{1}{2}$), the longitudinal spin exchange interaction is always *ferromagnetic* ($J_\parallel < 0$).

In the latter case, single molecule magnets attached to metallic leads thus give an experimental realization of the anisotropic ferromagnetic Kondo model.

11.2 Equilibrium Properties

Before focusing on the time-dependent magnetization of the ferromagnetic Kondo model, let us first summarize its equilibrium properties.

Anderson's poor man's scaling analysis of the Kondo model [9] already mentioned in Secs. 1.1 and 4.4 divides conduction band eigenstates into ones with eigenenergies $0 < |\varepsilon| < D - \delta D$ which are retained, and the ones with eigenenergies close to the band edge $D - \delta D < |\varepsilon| < D$, which are integrated out. The eliminated states are "integrated" in the new description of the model renormalizing the interactions. Within the perturbative poor man's scaling approach the scaling equations for the renormalized couplings read:

$$\frac{dJ_\parallel}{d\ln(\Lambda)} = -\rho_F J_\perp^2 \quad \text{and} \tag{11.17}$$

$$\frac{dJ_\perp}{d\ln(\Lambda)} = -\rho_F J_\perp J_\parallel, \tag{11.18}$$

where Λ parameterizes the flowing cutoff energy and ρ_F denotes the density of states of the free conduction band at the Fermi level. We assume a flat density of states $\rho = \rho_F = \frac{1}{2W}$ for the free conduction band electrons with eigenenergies $-W < \varepsilon < W$. The "flow" of the renormalized couplings following Eqs. (11.17) and (11.18) is sketched in Fig. 11.2. In the strong coupling regime (where the flow of the coupling is depicted by blue lines in Fig. 11.2) the couplings diverge $J_\perp \to \infty$ and $J_\parallel \to \infty$, which leads to a failure of the perturbative description of the associated Kondo effect.

In the ferromagnetic regime in contrast, where the couplings obey $|J_\perp| \leq -J_\parallel$ (depicted by green lines in Fig. 11.2), the perturbative renormalization is controlled. In the isotropic case $|J_\perp| = -J_\parallel$ both couplings renormalize to zero and the impurity becomes asymptotically free, since both couplings obey the scaling relation

$$J(\Lambda) = \frac{J}{1 + \rho_F J \ln(\frac{\Lambda}{W})}. \tag{11.19}$$

For anisotropic couplings in the ferromagnetic regime $|J_\perp| < -J_\parallel$, the longitudinal coupling $J_\parallel$ remains finite, while the transverse coupling renormalizes to zero following the power-law

$$J_\perp(\Lambda) \propto \Lambda^{\rho_F \sqrt{J_\parallel^2 - J_\perp^2}} \tag{11.20}$$

and the conserved quantity $J_\parallel^2 - J_\perp^2$ defines the scaling trajectory.

Applying a magnetic field h_z to the impurity the Hamilton operator of Eq. (11.15) acquires an additional Zeeman-term $\hat{H}_Z = h_z \hat{S}_z$, which polarizes the asymptotically free impurity spin. The static impurity magnetization in equilibrium $\langle S_z \rangle$ applying a small symmetry breaking magnetic field can be obtained from a perturbative calculation summing over parquet diagrams in the ferromagnetic regime [6]. The result reads

$$\langle S_z \rangle = S \left(1 - \frac{x(\rho_F J)^2}{1 + (\rho_F J)x} \right), \tag{11.21}$$

where $x = \ln(\varepsilon_F / h_z)$ leading to a small reduction of the impurity magnetization scaling as $(\rho_F J)/2$ for small magnetic fields $h_z \ll W$.

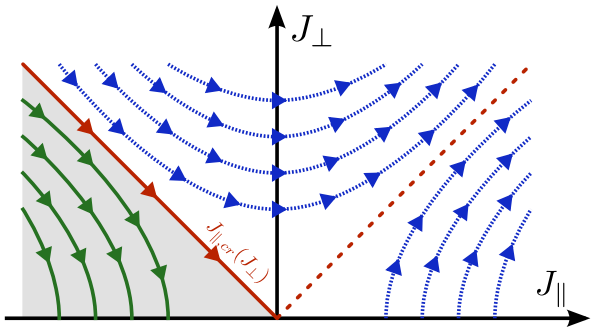

Figure 11.2: Sketch of the poor man's scaling phase diagram of the anisotropic Kondo model. The flow of the renormalized interactions is visualized for the different regimes of antiferromagnetic (dashed blue lines) and ferromagnetic (solid green lines) exchange couplings.

11.3 Nonequilibrium Magnetization

We investigate the real-time dynamics of the impurity magnetization in the ferromagnetic Kondo model after a sudden change of parameters in the Hamiltonian. Preparing the system in a well-defined spin state and measuring the real-time spin dynamics experimentally can be achieved using electrical [30] or optical [90, 91] field pulses. Although experimental challenges in applying these techniques to molecular quantum dots still remain, there has been an active development of theoretical methods to calculate the real-time evolution of quantum impurity models after a quantum quench.

Besides the extension to the numerical renormalization group method (TD-NRG) [66] already introduced in the method part in Sec. 8.1 a number of different theoretical methods have been developed to calculated the time-dependence in systems of correlated electrons in the past decade: An extension to the density matrix renormalization group method [56, 57] able to calculate time-dependent observables [92, 93, 94], real-time renormalization group methods [95], real-time path integral Monte Carlo approaches [96], and iterative summation of real-time path integrals [97] to name only a few.

We present a short introduction to a recent extension of the flow equation method in the following, since we compare our TD-NRG results to results obtained by this method. The flow equation method was originally invented independently by Wegner [98] and Głazek and Wilson [99, 100]. It is a perturbative renormalization group method, which uses a sequence of infinitesimal unitary transformations to diagonalize the Hamilton operator $\hat{\mathcal{H}}$. Splitting the Hamilton operator into a diagonal part $\hat{\mathcal{H}}_0(B)$ and an interaction part $\hat{\mathcal{H}}_{\rm int}(B)$, one defines an anti-hermitian generator $\hat{\eta}(B) = \left[\hat{\mathcal{H}}_0(B), \hat{\mathcal{H}}_{\rm int}(B)\right]$ and solves the differential equations also referred to as the "flow equations"

$$\frac{d\hat{\mathcal{H}}(B)}{dB} = [\eta(B), \hat{\mathcal{H}}(B)] \tag{11.22}$$

to obtain a family of unitarily equivalent Hamiltonians $\hat{\mathcal{H}}(B)$, where $\hat{\mathcal{H}}(B=0)$ is the initial Hamiltonian and the maximal energy separation between two eigenstates in the Hamiltonian $\hat{\mathcal{H}}(B)$ decays as $B^{-\frac{1}{2}}$. The high energy contributions are treated expanding the high order interaction terms using a suitable expansion parameter (for the ferromagnetic Kondo model

the expansion parameter is given by the interaction strength J). The flow equation method obeys the principle of energy scale separation and leads to a diagonal Hamiltonian in the limit $B \to \infty$ (for a recent review, see Ref. [84]). It is closely connected to the Schrieffer-Wolff transformation, where only a *single* unitary transformation on the single impurity Anderson Hamiltonian is performed to obtain the Kondo Hamiltonian describing the low-energy properties of the original Hamiltonian in a certain parameter regime.

In a recent work the underlying renormalization group scheme was extended [73] to calculate real-time evolution of observables in quantum impurity systems [101, 102, 103, 104]. A schematic explanation of the extended flow equation approach to calculate time-dependency is sketched in Fig. 11.3, a detailed derivation of the flow equations for the ferromagnetic Kondo model can be found in Ref. [102].

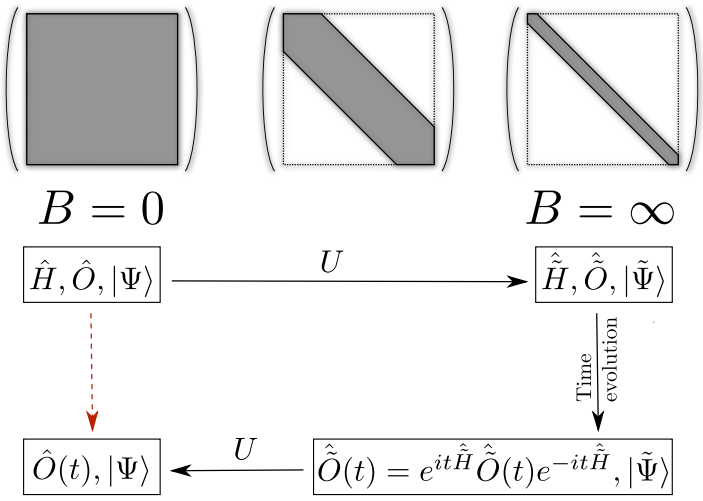

Figure 11.3: Sketch of the extended renormalization group scheme of the flow equation following Ref. [73]. The initial Hamiltonian $\hat{H}(B = 0)$ is diagonalized using a sequence of unitary transformations abbreviated by U. The time-evolution of local impurity observables in this new eigenbasis is trivial to evaluate $\hat{\tilde{O}}(t)$. To obtain the non-perturbative solution for the Heisenberg equations for $\hat{O}(t)$, a backwards transformation has to be applied.

The main advantage of the extended flow equation method — which can be seen as a quantum mechanical analog to canonical perturbation theory — is its analytic nature allowing a derivation of "exact" analytical results for the long time behavior of a certain class of quantum impurity problems. Since secular terms are avoided, this perturbative approach remains controlled even at very long times and allows an extraction of the nature of the final quantum state.

Before having a detailed look at the spin relaxation in the ferromagnetic Kondo model for the different coupling regimes, let us present some general results of the flow equation method for the ferromagnetic Kondo model. The flowing spin operator obeys

$$S_z(B) = h(B)S_z + \sum_{kk'} \gamma_{k'k}(B) : (S^+ s^-_{k'k} + S^- s^+_{k'k}) :, \tag{11.23}$$

where the initial form of the operator is obtained for $B = 0$. The coupling constants $h(B)$

and $\gamma_{k'k}(B)$ are described by the flow equations

$$\frac{dh}{dB} = \sum_{kk'} (\varepsilon_{k'} - \varepsilon_k) J^{\perp}_{k'k}(B) \gamma_{kk'}(B) n(k')(1 - n(k))$$
$$\frac{d\gamma_{k'k}}{dB} = h(B)(\varepsilon_{k'} - \varepsilon_k) J^{\perp}_{k'k}(B) + O(J^2), \tag{11.24}$$

where $n(k)$ denotes the Fermi distribution function. In addition, the flowing couplings $J^{\perp}_{k'k}(B)$ and $J^{\parallel}_{k'k}(B)$ of the Hamiltonian enter, which have to be calculated separately [84]. After solving the Heisenberg equation of motion for the operator S_z, the formal result for the magnetization reads

$$\langle S_z(t) \rangle = \frac{\tilde{h}}{2} + \sum_{kk'} \frac{\tilde{\gamma}^2_{kk'}}{2} \big(e^{it(\varepsilon_k - \varepsilon_{k'})} - \frac{1}{2} \big) n(k')(1 - n(k)). \tag{11.25}$$

11.3.1 Isotropic Kondo Exchange

In the case of isotropic ferromagnetic exchange interaction, we prepare the system in a product state of a polarized impurity spin and a free sea of fermions,

$$|\psi\rangle = |\uparrow\rangle \otimes |FS\rangle, \tag{11.26}$$

before suddenly switching on the interaction $J_{\parallel} = J_{\perp} = J < 0$ at time $t = 0$.

Applying the extended flow equation approach to this case, we find that the initial short-time decay is independent of $J_{\parallel}$ and given by

$$\langle S_z(t) \rangle = \frac{1}{2} \left[1 - (2 J_{\perp} t)^2 \right]. \tag{11.27}$$

The asymptotic behavior of the time-dependent magnetization on the other hand is obtained as

$$\langle S_z(t) \rangle = \frac{1}{2} \left(\frac{1}{\ln(tW) - \frac{1}{\rho_F J}} + 1 + \rho_F J + O(J^2) \right). \tag{11.28}$$

Note that these results can also be derived in an alternative way, which can be directly related to the poor man's scaling equations of the Kondo model [105]. The steady state magnetization

$$\langle S_z(t \to \infty) \rangle = \frac{1}{2} (1 + \rho_F J + O(J^2)) \tag{11.29}$$

thus differs from the equilibrium value as given by Eq. (11.21). The reduction from full polarization is $\rho_F J/2$, which is twice the equilibrium value. This can be attributed to the fact that the nonequilibrium dynamics starts with an impurity spin that is not dressed with a conduction band electron cloud: it therefore relaxes to a smaller value of the magnetization as compared to the dressed impurity spin in equilibrium. The implication that the ferromagnetic Kondo model retains a memory of its initial state at all times is to a certain extent surprising.

For an exactly solvable toy model describing two fermionic particles connected via an SU(2)-symmetric coupling to a spin-1/2 impurity, twice the reduction of the magnetization in the long time limit compared to the equilibrium expectation value can be observed as well

[102], which is not surprising for a system being described within a finite Hilbert space. For a certain class of discrete quantum systems a theorem guaranteeing the universality of the factor 2 between the time-averaged expectation value of the time-evolved initial state and the equilibrium ground state has even been proven [103, 106].

A direct numerical solution of the flow equations allows to accurately determine the relaxation process also at intermediate and short time scales. Together with the analytical result from Eq. (11.28), this calculation can be compared to TD-NRG calculations. Calculating the time-evolution of the impurity spin for the ferromagnetic Kondo model within the numerical renormalization group method, we face different challenges: For a direct comparison to the flow-equation method we are restricted to the regime of small coupling strengths $J < 0$. Even for the largest coupling strength taken into account in our comparison, the effect of the ferromagnetic interaction is quite small: Compared to the initial value of the spin, the magnetization only relaxes by approx. 4,5% at times $t = 10^4/W$. We thus have to choose NRG parameters leading to very accurate data, which in case of the isotropic Kondo model means keeping $N_{\mathrm{Lev}} = 2048$ level in each step of the iterative diagonalization procedure and choosing a relatively large value for the discretization parameter $\Lambda = 2.5$ to allow for a good fitting of the relaxation at large times $t > 10^7/W$.

Both methods, the TD-NRG as well as the numerical evaluation of the flow-equation method, yield very good agreement up to time scales of order $t \approx 10^4/W$ where the asymptotic logarithmic relaxation is clearly visible, see Fig. 11.4. Increasing deviation of the curves for larger coupling strength J can be explained by the $O(J^2)$ corrections to the flow equation result, which were neglected in the flow-equation calculation. We checked that the relative deviation of the two methods in terms of the quantity $\langle S_z(t)\rangle - 1/2$ at some large but fixed time indeed grows approximately linearly in J. A fit of the TD-NRG curves and the numerical implementation of the flow equation approach are in good agreement with the analytical result of Eq. (11.28).

Allowing a larger value for the impurity spin moment $S_z^{max} > 1/2$ for the anisotropic Kondo model, the analytic results for the time-dependent spin magnetization can be "scaled" according to

$$\langle \tilde{S}_z(t)\rangle = S_z^{max} \langle S_z(t)\rangle, \tag{11.30}$$

where $\langle \tilde{S}_z(t)\rangle$ denotes the time-evolution for large spins and $\langle S_z(t)\rangle$ the result for the spin-1/2 impurity. This result is exact up to $O(J^2S^2)$ from higher order flow equations [102]. We have verified the flow-equation prediction calculating the time-evolution of large impurity spin Kondo models within the TD-NRG. The results including their deviation from each other, which scales as $O(J^2S^2)$, is displayed in Fig. 11.5.

11.3.2 Anisotropic Kondo Exchange

Studying the anisotropic Kondo model we restrict ourselves to the experimentally relevant case $|J_\perp| < |J_\parallel|$ in the following. In this parameter regime of the ferromagnetic Kondo model a stable fixed point of the flow equations of Eqs. (11.17) and (11.18) is reached for

$$\tilde{g}_\parallel = -\sqrt{J_\parallel^2 - J_\perp^2} \quad \text{and} \tag{11.31}$$

$$\tilde{g}_\perp = 0. \tag{11.32}$$

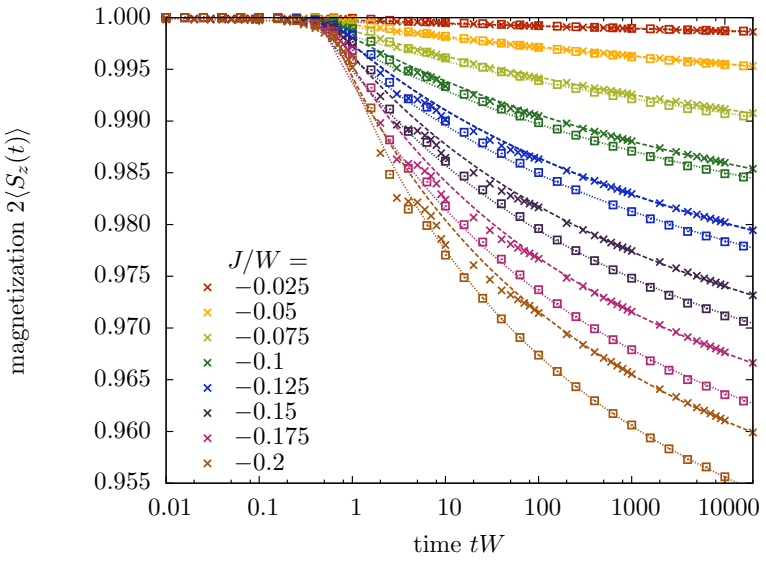

Figure 11.4: Results for the *isotropic* ferromagnetic Kondo model (×: TD-NRG data, □: flow equation data). Using our analytical result we fitted our data against $\langle S_z(t)\rangle = (1 + aJ + (\ln(tW) - 1/(cJ))^{-1})/2$ using a, c as fit parameters (lines).

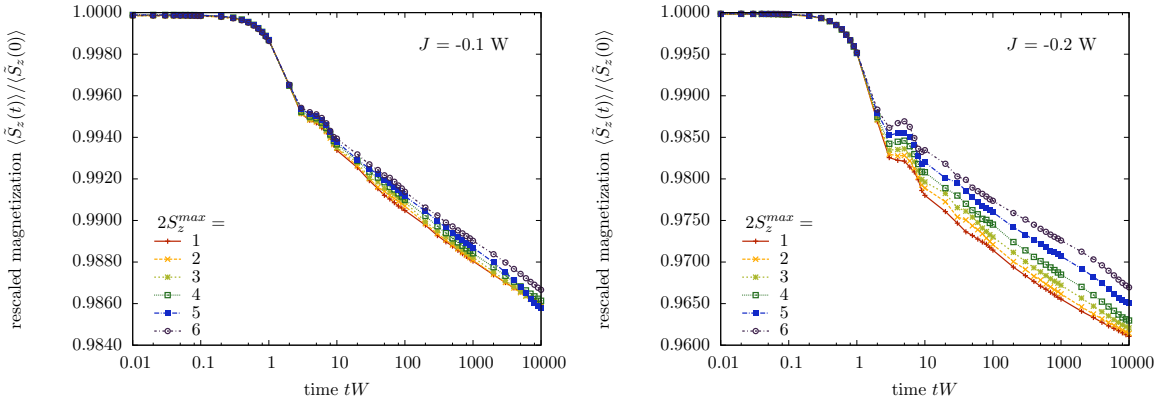

Figure 11.5: For larger spin $S_z^{max} > \frac{1}{2}$, the time-dependent magnetization differs only by terms of the order $O(J^2S^2)$ from the predicted "scaled" result given in Eq. (11.30).

As we already mentioned in Sec. 11.2 at the beginning of this chapter, the transverse coupling $J_\perp$ renormalizes to according to

$$J_\perp(\Lambda) \propto \Lambda^{\rho_F \sqrt{J_\parallel^2 - J_\perp^2}} = \Lambda^{-\rho_F \tilde{g}_\parallel} \tag{11.33}$$

(cf. Eq. (11.20)). This renormalization determines the asymptotic long-time relaxation of the spin. The flow equations of Eq. (11.24) thus yield

$$\langle S_z(t)\rangle = 0.5\left(1 - \frac{\alpha^2}{2\tilde{g}_\parallel}(tW)^{2\tilde{g}_\parallel} + \frac{\alpha^2}{2\tilde{g}_\parallel} + O(J^2)\right). \tag{11.34}$$

Here the constant α derives from the scaling equations for $J_\perp$ and $J_\parallel$. Numerical checks show that it can be replaced by $\alpha \approx J_\perp$ as long as $J_\parallel \lesssim 2J_\perp$. In comparison to the isotropic case, the power law decay of spin flip scattering at low energies leads to much faster relaxation of the magnetization, whereas the steady state magnetization is enhanced. This behavior is reproduced by our numerical calculations shown in Fig. 11.6.

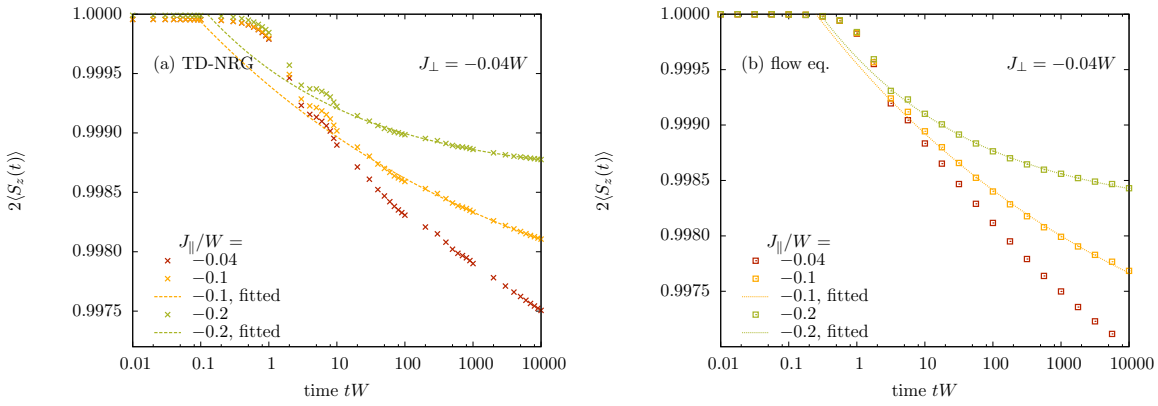

Figure 11.6: For the *anisotropic* ferromagnetic Kondo model our numerical findings coincide with our analytical results. Fitting our data against $\langle S_z(t)\rangle = a \cdot (tW)^{-\sqrt{J_\parallel^2 - J_\perp^2}} + c$ we found good agreement for the fit parameters a, c using the different methods (see Tab. 11.1).

	$J_\parallel = -0.01W$		$J_\parallel = -0.02W$	
	a	c	a	c
TD-NRG	$1.13 \cdot 10^{-3}$	0.4985	$4.6 \cdot 10^{-4}$	0.4993
flow-eq.	$1.16 \cdot 10^{-3}$	0.4981	$7.1 \cdot 10^{-4}$	0.4991

Table 11.1: Results for the parameters a, c fitting the data for the anisotropic ferromagnetic Kondo model for $J_\perp = -0.04W$ against $\langle S_z(t)\rangle = a \cdot (tW)^{-\sqrt{J_\parallel^2 - J_\perp^2}} + c$.

Let us point out that for the anisotropic Kondo model, our methods are starting from slightly different initial states. Using the flow equation approach one is restricted to a situation where the spin is initially completely decoupled from the fermionic bath. On the other hand, stability of the TD-NRG algorithm in the anisotropic model requires preparing the polarized

spin at time $t < 0$ by applying a large magnetic field, while still allowing for a small exchange coupling to the metallic leads. The same long-time power-law relaxation was obtained with both methods, cf. Tab. 11.1. However, the slightly different initial states used in both methods become significant on short and intermediate time scales.

11.4 Summary

We analyzed the real-time evolution of a ferromagnetically coupled Kondo spin, which is initially prepared in a polarized state. We managed to tune the parameters for the time-dependent numerical renormalization group method calculations such that the accuracy of the numerical data was sufficiently high to allow a good quantitative comparison of the subtle changes in the impurity spin magnetization with the "exact" analytical results obtained by the extended flow-equation method.

For the isotropic ferromagnetic Kondo model the long-time relaxation is logarithmic in time, whereas anisotropic couplings lead to a power-law decay at large times. Furthermore, we showed that the asymptotic nonequilibrium magnetization differs from the equilibrium magnetizations. Using both, the flow-equation as well as the time-dependent NRG method, we confirmed that the local quantum impurity retains a memory of the initial preparation for asymptotically large times. This is due to the combined effect of nonequilibrium preparation and ergodicity breaking already in the equilibrium system.

Chapter 12

Fermionic vs. Bosonic Bath

The anisotropic Kondo model [3] studied in some detail in the preceding chapter, Chap. 11, can be related to the spin-boson model, which describes a single spin coupled to a bath of bosonic particles, and has been introduced in Chap. 5. The main physical concept behind the bosonization technique connecting the two quantum impurity models is illustrated in Fig. 12.1: Particle-hole excitations in the fermionic model are rewritten in terms of bosonic operators acting on the fermionic quantum bath, which can be expressed in terms of bosonic eigenstates as well.

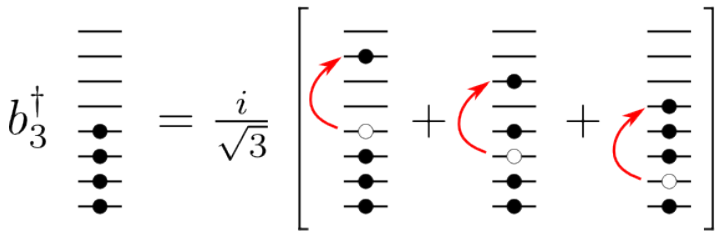

Figure 12.1: Particle-hole excitations in the fermionic model can be expressed as bosonic quasiparticles. As an example we illustrate the action of the bosonic operator $b_3^\dagger$ defined in Eq. (12.4) on the ground state of the free fermionic bath.

Using the bosonization technique the equivalence of these two models, in the sense of a unitary transformation, has been shown [107]. In particular, this implies that the two models have the same ground state energies, which, according to the Hellmann-Feynman theorem, leads to coinciding static longitudinal spin magnetizations ($2\langle S_z\rangle$ for the Kondo and $\langle\sigma_z\rangle$ for the spin-boson model). The observable corresponding to $\hat{S}_x$ is not simply $\hat{\sigma}_x$ in the spin-boson model, but more complicated and involves bath degrees of freedom as well.

In this chapter we want to investigate whether the bosonization mapping of the anisotropic Kondo model to the spin-boson model also holds for dynamical quantities. Specifically, we focus on the real-time evolution of impurity observables in the two systems after a sudden parameter quench, e. g. an external magnetic field applied to the impurity spin. Experimentally a quench in quantum impurity systems can be realized applying electrical [30] or optical [91, 90] field pulses, as mentioned before. A detailed understanding of the nonequilibrium dynamics of impurity spins interacting with different quantum baths is, in addition to its fundamental theoretical interest, important for the development of spintronic devices [37]. The

main quantitative study of the real-time evolution of spin observables in response to an abrupt change of parameters is performed using the time-dependent numerical renormalization group method (TD-NRG) [66, 67] introduced in Chap. 8.

The outline of this chapter is as follows: First, we specify experimental realizations of the spin-boson model and explain the different physical regimes of both models. We then briefly sketch the bosonization mapping connecting the two models. In Sec. 12.3 we discuss the static spin magnetization in the two different models, focusing on its characteristics close to the quantum phase transition between the localized and delocalized phase (in case of the spin-boson model) or the asymptotically free or screened impurity (in case of the Kondo model). The subsequent Section 12.4 covers the real-time dynamics of the impurity spin observables after a quantum quench. We perform a detailed quantitative study of the different physical regimes. In terms of the spin-boson model these are: Weak coupling $\alpha < 0.5$, Toulouse point $\alpha = 0.5$, intermediate coupling $0.5 < \alpha < 1.0$, and strong coupling $\alpha \geq 1$, as well as an additional subsection comparing the entanglement of the single spin with the respective bath. Our conclusion in Sec. 12.5 summarizes the main results of our study on the equivalence of the two models for nonequilibrium situations.

12.1 Spin-Boson Model

12.1.1 Model Hamiltonian

The simplest model describing decoherence and dephasing of a single spin in a bosonic bath is the well-known spin-boson model [62, 108, 109]. Within this model the impurity consists of a two-state system, which can be described by a spin-$\frac{1}{2}$ particle, and which interacts with a bath of free bosons $\mathcal{H}_{SB,b} = \sum_n \omega_n \left(\hat{a}_n^\dagger \hat{a}_n + \frac{1}{2}\right)$. To distinguish the impurity spin operators from the ones in the anisotropic Kondo model, we use the standard Pauli matrices $\hat{\sigma}_x$ and $\hat{\sigma}_z$ to describe the impurity degrees of freedom in the spin-boson model. The motion in the two-dimensional Hilbert space of the isolated impurity is completely described introducing a bias for the longitudinal spin orientations $\varepsilon\frac{\hat{\sigma}_z}{2}$ and a tunneling between the two $\hat{\sigma}_z$-eigenstates $\Delta\frac{\hat{\sigma}_x}{2}$. The full Hamilton operator of the spin-boson model reads

$$\mathcal{H}_{SB} = \sum_n \omega_n \left(\hat{a}_n^\dagger \hat{a}_n + \frac{1}{2}\right) + \frac{\hat{\sigma}_z}{2} \sum_n \lambda_n \left(\hat{a}_n + \hat{a}_n^\dagger\right) - \Delta\frac{\hat{\sigma}_x}{2} - \varepsilon\frac{\hat{\sigma}_z}{2}. \tag{12.1}$$

The spectral function

$$J(\omega) \equiv \pi \sum_i \lambda_i^2 \delta(\omega_i - \omega) = 2\pi\alpha\omega_c^{1-s}\omega^s\theta(\omega)\theta(\omega_c - \omega) \tag{12.2}$$

fully describes the bosonic quantum bath. As already mentioned in Chap. 5, the second part of Eq. (12.2) gives the common low-energy parametrization of the spectral function, where α measures the coupling of the two-level system to the bosonic bath and ω_c is the cutoff frequency. In this chapter we focus on bosonic baths, where the low-energy dispersion is linear, i.e. $J(\omega) \propto \omega^s$ with $s = 1$, which in literature is referred to as the ohmic case and investigate the spin-boson model for a "hard" cutoff at $\omega = \omega_c$.

12.1.2 Experimental Realizations

Implementations of the spin-boson model are numerous. Examples include electron transfer in chemical reactions [110, 111], and qubit designs based on the Josephson effect [112, 113, 114]. As an example for the experimental realization of the spin-boson model, Fig. 12.2 illustrates the device used in Ref. [114].

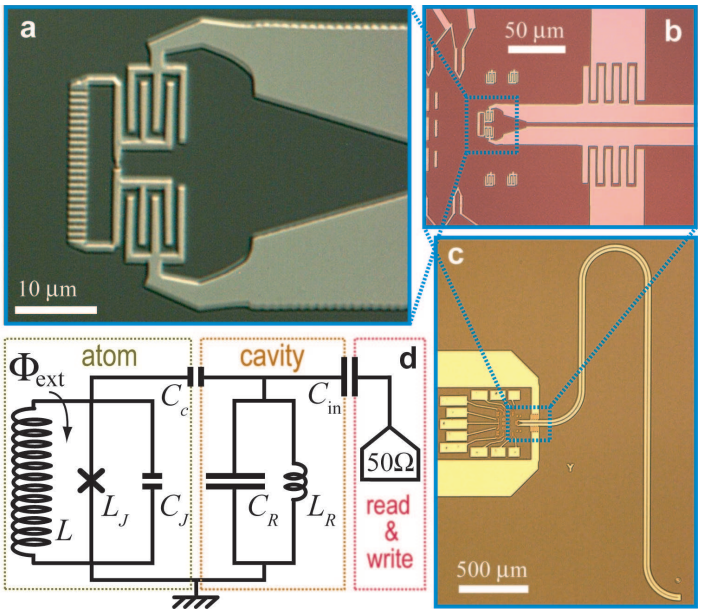

Figure 12.2: Experimental setup used in Ref. [114] to observe coherent oscillations between two states differing by the presence or absence of a single fluxon trapped in the superconducting loop interrupted by a Josephson tunnel junction. Panel a-c show optical photographs of the quantum bit design at different scales, while panel d shows the minimal circuit model emulating the atom plus cavity system.

Other systems that are described by the spin-boson Hamiltonian are trapped ions [115], quantum emitters coupled to surface plasmons [116], and the cold-atom quantum dot setup [117, 118, 119, 120]. Further variants of spin-boson models involve two-level atoms interacting with a single quantized mode of an electromagnetic cavity [121, 122, 123, 124].

The environmental influence on the phase coherence between the two spin states is of crucial importance in the field of quantum computing, as it sets a limit to the timescale where coherent quantum logical operations can be performed. A good starting point for investigations of the spin-boson model is the book of Weiss (see Ref. [108]) and the review article by Legget and coworkers (see Ref. [62]).

12.1.3 Physical Regimes

Let us comment on the physical regimes of the two quantum impurity models we study throughout this chapter. As a reminder we give the Hamilton operator for the anisotropic

Kondo model (akm)

$$\hat{\mathcal{H}}_K = \sum_{k\sigma} \varepsilon_k \hat{c}^\dagger_{k\sigma} \hat{c}_{k\sigma} + \frac{J_\perp}{2} \sum_{kk'} \left(\hat{c}^\dagger_{k\uparrow} \hat{c}_{k'\downarrow} \hat{S}^- + \hat{c}^\dagger_{k\downarrow} \hat{c}_{k'\uparrow} \hat{S}^+ \right) + \frac{J_\parallel}{2} \sum_{kk'} \left(\hat{c}^\dagger_{k\uparrow} \hat{c}_{k'\uparrow} - \hat{c}^\dagger_{k\downarrow} \hat{c}_{k'\downarrow} \right) \hat{S}_z - h_z \hat{S}_z. \tag{12.3}$$

Both models exhibit a quantum phase transition. In case of the ohmic spin-boson model the transition located at $\alpha_c = 1 + O(\frac{\Delta}{\omega_c})$ separates a phase where the impurity spin is localized due to the dissipative bath (for $\alpha > \alpha_c$) from a phase where the impurity spin is delocalized (for $\alpha < \alpha_c$). In the delocalized phase the impurity spin's expectation value vanishes due to the fact that the dissipation induced by the bosonic bath is not strong enough to prohibit spin-flips and thus freeze the impurity spin [62]. For the anisotropic Kondo model, the two phases can be characterized by either an asymptotically free impurity (in the case of ferromagnetic coupling $J_\parallel < 0$ and $J_\perp < J_\parallel$) or a strongly coupled phase where the impurity spin is screened by a cloud of fermionic particles. In the latter case both couplings diverge $J_\parallel, J_\perp \to \infty$ within a poor man's scaling approach [9], leading to the Kondo effect.

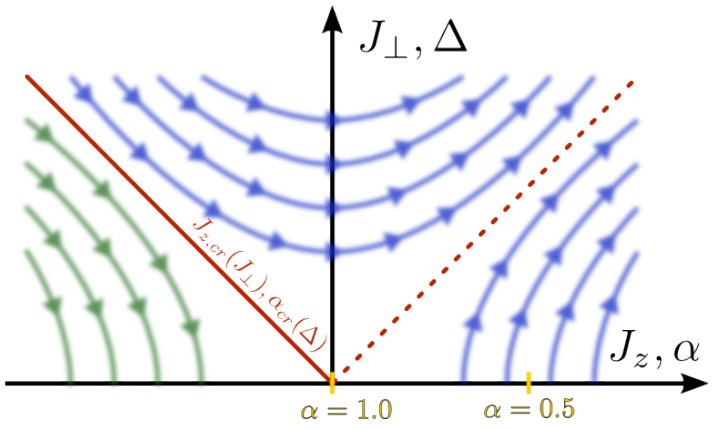

Figure 12.3: Illustration of the different physical regimes of both models studied in this chapter.

For the spin-boson model the other "special" value of the spin-bath coupling is given by $\alpha = 0.5$. In the so called Toulouse limit, the model can then be mapped onto the non-interacting resonant level model, for which an exact analytic solution exists. The Toulouse limit at $\alpha = 0.5$ also separates two regimes of the spin-boson model, for which the relaxation of a spin prepared in a polarized state differs qualitatively: As we will show in some detail in Sec. 12.4 the impurity spin performs damped oscillations for $0 < \alpha < 0.5$, while for $0.5 < \alpha < 1.0$ the oscillations disappear and the spin decays purely incoherently.

12.2 Bosonization Mapping

As first realized by Chakravarty [125] and independently by Bray and Moore [126], the anisotropic Kondo model can be mapped on the spin-boson model with an ohmic spectral function ($s = 1$) using bosonization.

The conceptual basis of the bosonization method is sketched in Fig. 12.1: each state of the fermionic system can be expressed as a linear combination of particle-hole excitations of the fermionic ground state. These excitations have bosonic character and consequently are described by a set of operators

$$b_{q\eta}^{\dagger} \equiv \frac{i}{\sqrt{n_q}} \sum_{k=-\infty}^{+\infty} c_{k+q\eta}^{\dagger} c_{k\eta}, \qquad b_{q\eta} \equiv \frac{-i}{\sqrt{n_q}} \sum_{k=-\infty}^{+\infty} c_{k-q\eta}^{\dagger} c_{k\eta} \tag{12.4}$$

obeying bosonic commutation relations.

Thus, introducing the so called Klein-factors $F_{\eta}^{\dagger}, F_{\eta}$, which connect the various $\vec{N}$-particle Hilbert spaces with one another, the fermionic fields ψ_{η} for the different species η can be rewritten in terms of bosonic fields ϕ_{η}

$$\psi_{\eta}(x) = F_{\eta}\, a^{-1/2}\, e^{-i\Phi_{\eta}(x)} \qquad \text{with} \qquad \Phi_{\eta}(x) \equiv \phi_{\eta}(x) + \frac{2\pi}{L}(\widehat{N}_{\eta} - \frac{1}{2}\delta_b)x\ . \tag{12.5}$$

Details of the "constructive" derivation [127] of the bosonization formula given in Eq. (12.5) following the work of von Delft and Schoeller [59] can be found in Appendix C of this thesis.

The free fermionic bath with a linear dispersion relation can easily be transformed to a bosonic one using the bosonization formula given in Eq. (12.5) (see e.g. Refs. [59, 62, 107]). Strictly speaking the two free baths are only equivalent for unbounded fermionic fields. Introducing a cut-off in the interaction term of the fermionic model, it is supposed that the limit $a \to 0$ or equivalently $L \to \infty$ is always taken, which means that the models are strictly speaking only equivalent in the so called long-time limit $t \gg a$ [107].

Mapping the anisotropic Kondo model to the spin-boson model turns out to be more complex. To make any progress, one first expresses the anisotropic Kondo model in terms of bosonic fields Φ_{η}. We label this bosonized form of the Kondo model by $\tilde{\hat{\mathcal{H}}}_K$ in the following. Transforming to bosonic charge- ($\Phi_c = \frac{1}{\sqrt{2}}[\Phi_{\uparrow} + \Phi_{\downarrow}]$) and spin-fields ($\Phi_s = \frac{1}{\sqrt{2}}[\Phi_{\uparrow} - \Phi_{\downarrow}]$), one notices that Φ_c completely decouples from the remaining Hamilton operator (see Ref. [128] for an instructive explanation of the bosonization method for a more general two-spin model). Afterwards a general Emery-Kivelson transformation

$$U_{\gamma} = \exp\left[i\gamma S_z \Phi_s(0)\right], \tag{12.6}$$

parametrized by γ, is applied to the bosonized form of the anisotropic Kondo model $\hat{\mathcal{H}}_{\gamma} = U_{\gamma}\tilde{\hat{\mathcal{H}}}_K U_{\gamma}^{\dagger}$ (see Ref. [128]). For a special value of $\gamma = \sqrt{2}$ the resulting Hamilton operator is identical to the spin-boson Hamiltonian $\hat{\mathcal{H}}_{\gamma=\sqrt{2}} = \hat{\mathcal{H}}_{SB}$.

Performing this bosonization mapping, one obtains the relations [107]

$$(\rho J_{\perp}) \to \frac{\Delta}{\omega_c} \ \text{ and } \ \left(1 + \frac{2\delta_e}{\pi}\right)^2 \to \alpha, \tag{12.7}$$

where δ_e denotes the phase shift of scattering of electrons from a potential $\frac{J_{\parallel}}{4}$ [74].

There is no unique way rewriting the phase shift δ_e as a function of the anisotropic Kondo Hamiltonian's parameters, in contrast different expressions for δ_e stem from different regularization procedures of a delta potential occurring in an intermediate step of the bosonization

akm	sbm	relation
$J_\parallel$	α	$\alpha = \left(1 + \frac{2\delta_e}{\pi}\right)^2$
$J_\perp$	Δ	$\frac{\Delta}{\omega_c} = \rho J_\perp$
h_z	ε	$\frac{\varepsilon}{\omega_c} = \frac{h_z}{W}$

Table 12.1: Equivalence of parameters for the anisotropic Kondo and the spin-boson model. The exact value of the phase shift δ_e acquired by scattering on the impurity depends on the details of the bosonization technique. For a common choice of regularization of the singular δ-potential one obtains $\delta_e = \arctan\left(-\frac{\pi\rho J_\parallel}{4}\right)$ (see Ref. [107] for details).

mapping (for details we refer to Sec. IV of Ref. [107]). For our comparison of static expectation values as well as the nonequilibrium dynamics of the two quantum impurity models we employ the regularization procedure leading to

$$\delta_e = \arctan\left(-\frac{\pi\rho J_\parallel}{4}\right), \tag{12.8}$$

where ρ denotes the density of states of the free fermionic bath, which we assume to be flat for all of our calculations (i.e. $\rho(\varepsilon) = \frac{1}{2W}\Theta(W - |\varepsilon|)$ where $2W$ is the conduction electron bandwidth). A summary of the parameter equivalences for the two models is listed in Tab. 12.1.

Finally, in the *Toulouse limit* (which corresponds to $\alpha = 0.5$ or $J_z \approx 1.26W$) both, the spin-boson model and the anisotropic Kondo model, can be mapped onto an analytically solvable *resonant level* model, using another "special value" of the parameter in the Emery-Kivelson transformation $\gamma = \sqrt{2} - 1$. We will introduce the corresponding resonant level model in Sec. 12.4.2 discussing its analytic solution as well.

12.3 Static Magnetization

For finite level asymmetry $\varepsilon \neq 0$ a Bethe-Ansatz calculation [129, 130] yields the following results for the longitudinal static magnetization of the spin-boson model in the delocalized phase (for $\alpha < \alpha_c$):

$$\lim_{\varepsilon \ll T_K} \langle \sigma_z \rangle = -\frac{2e^{\frac{b}{2(1-\alpha)}}}{\sqrt{\pi}} \frac{\Gamma[1 + 1/(2-2\alpha)]}{\Gamma[1 + \alpha/(2-2\alpha)]} \left(\frac{\varepsilon}{T_K}\right), \tag{12.9}$$

$$\lim_{\varepsilon \gg T_K} \langle \sigma_z \rangle = -1 + \left(\frac{1-2\alpha}{2}\right) C_2(\alpha) \left(\frac{T_K}{\varepsilon}\right)^{2-2\alpha}, \tag{12.10}$$

where

$$b = \alpha \ln \alpha + (1-\alpha)\ln(1-\alpha) \quad \text{and} \tag{12.11}$$

$$C_2(\alpha) = \frac{2e^{-b}}{\sqrt{\pi}(1-2\alpha)} \frac{\Gamma(\frac{3}{2} - \alpha)}{\Gamma(1-\alpha)}. \tag{12.12}$$

The static transverse spin magnetization $\langle\sigma_x\rangle$ can also be calculated using the Bethe-Ansatz (see Ref. [130] for details). The resulting expression reads

$$\lim_{\varepsilon\ll T_K}\langle\sigma_x\rangle = \frac{1}{2\alpha-1}\frac{\Delta}{\omega_c} + C_1(\alpha)\frac{T_K}{\Delta}, \tag{12.13}$$

$$\lim_{\varepsilon\gg T_K}\langle\sigma_x\rangle = \frac{1}{2\alpha-1}\frac{\Delta}{\omega_c} + C_2(\alpha)\frac{T_K}{\Delta}\left(\frac{T_K}{\varepsilon}\right)^{1-2\alpha}, \tag{12.14}$$

where

$$C_1(\alpha) = \frac{e^{-\frac{n}{2(1-\alpha)}}}{\sqrt{\pi}(1-\alpha)}\frac{\Gamma[1-1/(2-2\alpha)]}{\Gamma[1-\alpha/(2-2\alpha)]}$$

and $C_2(\alpha)$ as given in Eq. (12.12). In the localized phase on the other hand, the longitudinal magnetization reads $\langle\sigma_z\rangle \approx -1 + \mathcal{O}((\frac{\Delta}{\omega_c})^2)$ and the transverse magnetization $\langle\sigma_x\rangle$ vanishes [131].

Following Ref. [130], we verify these analytical results for the spin-boson model using numerical renormalization group calculations in Figs. 12.4 and 12.5, where a direct comparison of the static magnetizations of the spin-boson model and the anisotropic Kondo model for the corresponding parameters according to Tab. 12.1 against the analytic Bethe-Ansatz results is shown.

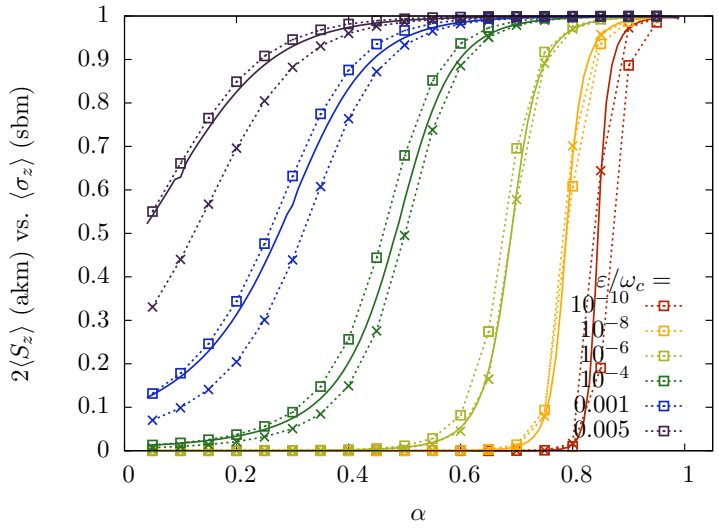

Figure 12.4: Comparison of NRG results for the longitudinal static magnetization of the spin-boson model $\langle\sigma_z\rangle$ (rectangles) against the longitudinal static magnetization of the anisotropic Kondo model $2\langle S_z\rangle$ (crosses) and the prediction of the Bethe-Ansatz (full lines) for different impurity bath couplings (α and the corresponding values of $J_\parallel$) and various ε and h_z respectively.

In contrast to the spin-boson model, the transverse spin magnetization $\langle S_x\rangle$ of the anisotropic Kondo model always vanishes in the absence of a magnetic field in x-direction (cf. Fig. 12.5). This has direct consequences for the entanglement of the spin with the respective bath in the

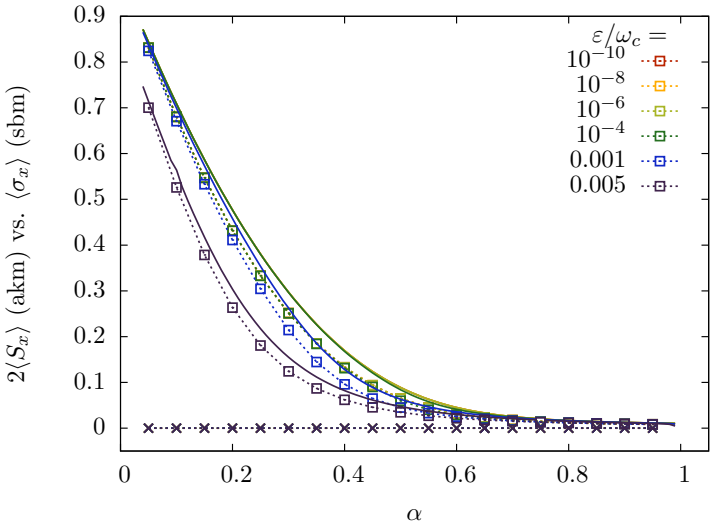

Figure 12.5: Comparing the transverse static magnetization for the spin-boson model $\langle\sigma_x\rangle$ (rectangles) against the transverse magnetization for the anisotropic Kondo model $2\langle S_x\rangle$ (crosses) and the prediction of the Bethe-Ansatz (lines) for different impurity bath couplings (α and the corresponding values of $J_\parallel$) and various ε and h_z respectively.

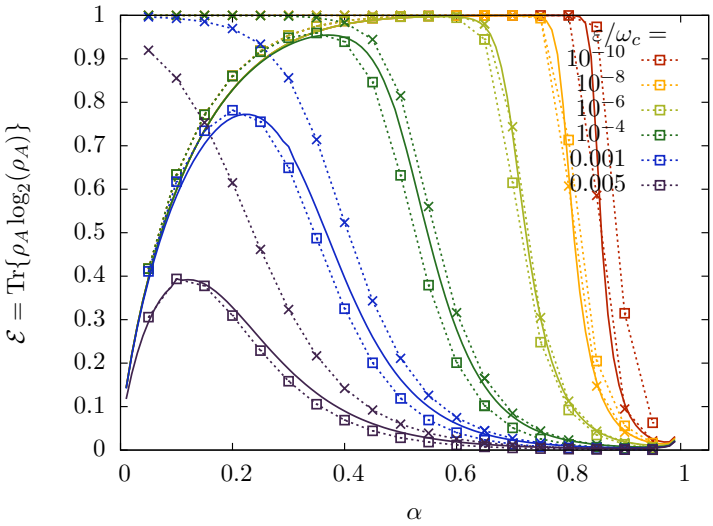

Figure 12.6: Comparing the static entanglement entropy for the spin-boson model (rectangles) against the entanglement entropy in the anisotropic Kondo model (crosses) for different impurity-bath couplings (α and the corresponding values of $J_\parallel$) and various ε and h_z respectively.

two models. To quantify the amount of entanglement between the impurity and the respective bath we employ the von Neumann entropy [132, 133, 134]

$$\mathcal{E} = -\mathrm{Tr}\left\{\rho_A \log_2(\rho_A)\right\}, \tag{12.15}$$

where ρ_A denotes the reduced density matrix of the impurity spin. For systems with relatively strong coupling $\alpha \geq 0.5$ the entanglement entropy $\mathcal{E}$ is dominated by the longitudinal magnetizations $\langle\sigma_z\rangle$ (and $\langle S_z\rangle$ respectively) and thus almost identical for the anisotropic Kondo model and the spin-boson model (cf. Fig. 12.6). An increase of $\mathcal{E}$ is observed lowering α, its exact position depending on the value of the level asymmetry (ε, h_z).

For smaller spin-bath coupling $\alpha \leq 0.4$ on the other hand the entanglement of a single spin with a bosonic bath shows a different behavior than the entanglement entropy between the impurity spin and the fermionic bath in the anisotropic Kondo model. In the spin-boson model the entanglement entropy $\mathcal{E}$ is dominated by the finite expectation value of the transverse magnetization $\langle\sigma_x\rangle$ leading to a vanishing entanglement for very small spin-bath coupling. As depicted in Fig. 12.6 the entanglement in the corresponding parameter regime of the anisotropic Kondo does not show this behavior. Due to the vanishing transverse magnetization $\langle S_x\rangle$, the entanglement entropy saturates at its maximal value $\mathcal{E} = 1$.

12.4 Comparing Spin Dynamics

In the current section we focus on the real-time evolution of the impurity spin after an abrupt change of parameters of the Hamiltonian. We divide this section into five subsections, where in each of the first four subsections we compare the longitudinal magnetization in a different parameter regime of the two models. We classify the regimes according to the increasing coupling strength to the bosonic bath, starting with Sec. 12.4.1, where the impurity spin is coupled weakly to the bosonic bath in the spin boson model ($0 < \alpha < 0.5$). For the equivalent parameters in the anisotropic Kondo model the impurity is strongly coupled to the fermionic bath antiferromagnetically. We investigate if the damped harmonic oscillations of the longitudinal spin magnetization, which are well-known from previous studies of the spin-boson model [62], carry over to the nonequilibrium spin dynamics of the anisotropic Kondo model. In Sec. 12.4.2, we focus on the Toulouse point at $\alpha = 0.5$. Exploiting a mapping of both the anisotropic Kondo- as well as the spin-boson model to an exactly solvable resonant level model [135], we compare and benchmark our TD-NRG calculations for the different models. In subsection Sec. 12.4.3, we analyze the spin dynamics for intermediate spin-bath coupling in the spin-boson model ($0.5 < \alpha < 1.0$). Since we observe very slow relaxation in both models, we propose a new analytic form for the spin dynamics (cf. Eq. (12.42)). In subsection Sec. 12.4.4, we compare the spin dynamics for strong spin-bath coupling in the localized phase of the spin-boson model ($\alpha > 1$) to the dynamics of the equivalent ferromagnetically coupled spin in the anisotropic Kondo model, which we studied in detail in Chap. 11 of this thesis.

The last subsection, Sec. 12.4.5, focuses on the entanglement of the spin with the respective bath. We investigate the dynamics in the spin-boson model for weak coupling and the anisotropic Kondo model in the corresponding parameter regime. Let us emphasize that we restrict ourselves to the investigation of the spin dynamics in the zero temperature limit $T \to 0$, where the bath exhibits very long memory times, leading to strong quantum effects in the relaxation dynamics.

12.4.1 Weak Coupling $0 < \alpha < 0.5$

The dynamics of the spin-boson model in this parameter regime has been previously investigated using various methods. Apart from master equation calculations (see Refs. [136, 137] and references therein), which are limited to very small coupling strengths, mixed quantum classical and semiclassical methods (cf. Ref. [138] and references therein), and path integral calculations (cf. Ref. [139] and references therein), one of the most prominent methods employed is the Non-Interacting Blip Approximation (NIBA) [62, 140, 141, 108]. For the case of small tunneling Δ the NIBA method predicts the following dynamics for an initially polarized impurity spin in the spin-boson model [108]

$$\langle \sigma_z(t) \rangle = \sum_{m=0}^{\infty} \frac{(-1)^m}{\Gamma\left[1 + (2-2\alpha)m\right]} (\Delta_{\text{eff}} t)^{(2-2\alpha)m}. \tag{12.16}$$

Following the NIBA calculations the effective tunneling rate Δ_{eff} is given by

$$\Delta_{\text{eff}} = \left[\Gamma(1-2\alpha)\cos(\pi\alpha)\right]^{1/(1-\alpha)} \Delta \left(\frac{\Delta}{\omega_c}\right)^{\alpha/(1-\alpha)} \tag{12.17}$$

$$\approx \Delta \left(\frac{\Delta}{\omega_c}\right)^{\alpha/(1-\alpha)}, \tag{12.18}$$

where the second approximation is valid as long as $\alpha < 1$.

For short times $\Delta_{\text{eff}} t \ll 1$ the leading term for the time-dependent spin magnetization is given by

$$\langle \sigma_z(t) \rangle = 1 - \frac{(\Delta_{\text{eff}} t)^{2-2\alpha}}{\Gamma(3-2\alpha)} + \mathcal{O}\left[(\Delta_{\text{eff}} t)^{4-4\alpha}\right]. \tag{12.19}$$

Investigating the Laplace transform of Eq. (12.16), one finds two different contributions determining the spin magnetization dynamics for longer times $\Delta_{\text{eff}} t \gg 1$ and very strong bias $\varepsilon \gg 1$ for the initial Hamiltonian (i.e. at times $t < 0$):

$$\langle \sigma_z(t) \rangle = \langle \sigma_z(t) \rangle_{\text{coh}} + \langle \sigma_z(t) \rangle_{\text{inc}}, \tag{12.20}$$

$$\langle \sigma_z(t) \rangle_{\text{coh}} = \frac{1}{1-\alpha} \cos(\Omega t) \exp^{-\gamma t}, \tag{12.21}$$

$$\langle \sigma_z(t) \rangle_{\text{inc}} = \sum_{n=1}^{\infty} \frac{(-1)^{n-1}}{\Gamma(1-(2-2\alpha)n)} \frac{1}{(\Delta_{\text{eff}} t)^{(2-2\alpha)n}}. \tag{12.22}$$

The NIBA results for the frequency Ω and the decay rate γ in the coherent part of the relaxation $\langle \sigma_z(t) \rangle_{\text{coh}}(t)$ of Eq. (12.21) read

$$\Omega = \Delta_{\text{eff}} \cos\left(\frac{\pi\alpha}{2(1-\alpha)}\right), \tag{12.23}$$

$$\gamma = \Delta_{\text{eff}} \sin\left(\frac{\pi\alpha}{2(1-\alpha)}\right). \tag{12.24}$$

The coherent part of the relaxation was also found in a conformal field theory study by Lesage and Saleur [142], except for a tunneling rate Δ_{LS}, which deviates slightly ($< 3,8\%$)

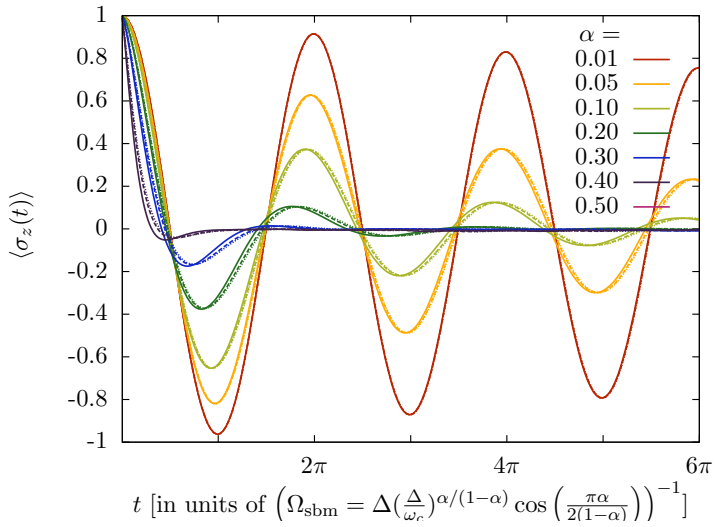

Figure 12.7: Time-dependent magnetization for an initially fully polarized spin in the spin-boson model coupled weakly to the bath $\alpha < 0.5$ for various spin-flip couplings Δ. The solid lines correspond to $\Delta = 0.0005\omega_c$, the dashed to $\Delta = 0.02\omega_c$ and the dotted to $\Delta = 0.1\omega_c$.

from $\Delta_{\rm eff}$. For the incoherent part of the relaxation $\langle\sigma_z(t)\rangle_{\rm inc}$ the situation is different: While the NIBA predicts an algebraic series written down in Eq. (12.22), where the leading contribution decays as $1/(\Delta_{\rm eff}t)^{2-2\alpha}$ (please note that for $\alpha = \{0, 0.5\}$ $\langle\sigma_z(t)\rangle_{\rm inc}$ vanishes), Lesage and Saleur do not find the incoherent algebraic long-time tail for $\langle\sigma_z(t)\rangle_{\rm inc}(t)$ at all [142].

Using the TD-NRG approach we verify the damped oscillations in the longitudinal magnetization for the spin-boson model. The results are displayed in Fig. 12.7. A fit of our results against $\langle\sigma_z(t)\rangle = \cos(\Omega_i^{\rm sbm}t)e^{-\gamma_i^{\rm sbm}t}$ using the oscillation frequency $\Omega_i^{\rm sbm}$ and decay rate $\gamma_i^{\rm sbm}$ as fit parameters yields quality factors for the coherent part of the oscillation, which are in good agreement to the ones predicted by NIBA calculations (see Fig. 12.8). Surprisingly we find a better agreement for the oscillation frequencies and the decay rates using

$$\Delta_{\rm eff}^{\rm sbm} = \Delta\left(\frac{\Delta}{\omega_c}\right)^{\alpha/(1-\alpha)} \tag{12.25}$$

thus approximating the first factor in Eq. (12.17) by unity (cf. Fig. 12.7).

We could not observe an incoherent part in the oscillations, which suggests that the claim in Ref. [142] is true: there is no relevant incoherent part in the longitudinal magnetization oscillations for weak damping.

The equivalence of parameters obtained from the mapping of the spin-boson model to the anisotropic Kondo model [107] (see Tab. 12.1) strictly speaking only holds for small Δ [108]. Exploiting this equivalence of parameters, an impurity spin weakly coupled to the bosonic bath in the spin-boson model corresponds to strong antiferromagnetic coupling of the impurity spin to the fermionic bath in the anisotropic Kondo model $J_\parallel > W$, where W is the half-bandwidth of the fermionic bath.

We investigate the dynamics of the impurity spin in this regime of the anisotropic Kondo model by initially preparing the system in a fully polarized state. As in the case of a spin

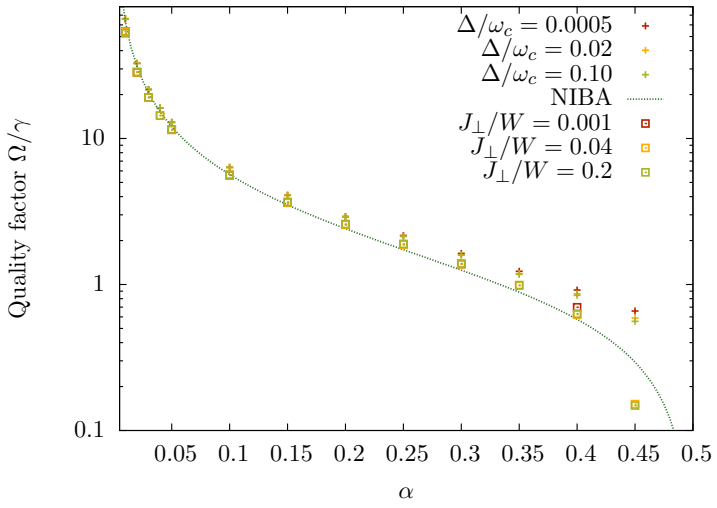

Figure 12.8: Quality factor $Q = \Omega/\gamma$, for the spin-boson model (crosses) and the anisotropic Kondo model (squares) extracted from the NRG calculations, one verifies the relation: $\Omega/\gamma = \cot\left(\frac{\pi\alpha}{2(1-\alpha)}\right)$ predicted by NIBA [108] (cf. Eqs. (12.21), (12.23), and (12.24)).

weakly coupled to a bosonic bath, we observe damped oscillations for a spin with strong antiferromagnetic coupling to a fermionic bath (cf. Fig. 12.9). From the fit results for the exponential decay rate γ_i^{akm} and oscillation frequency Ω_i^{akm} a quality factor can be extracted, which shows the same α-dependence as in the spin-boson model, see Fig. 12.8. The resulting values for Ω^{akm} and γ^{akm} on the other hand are not given by a direct "translation" of Eqs. (12.23, 12.24) using Eq. (12.25) and the relation between the different cut-offs Eq. (12.29), which yields

$$\Delta_{\text{eff}}^{\text{akm}} \approx \frac{J_\perp}{2}\left(\frac{J_\perp}{2W}\right)^{\alpha/(1-\alpha)}\frac{\omega_c}{W}. \tag{12.26}$$

Instead, we find the best empirical description of the α-dependence of Ω^{akm} and γ^{akm} by replacing the expression for the renormalized coupling given in Eq. (12.25) by

$$\Delta_{\text{eff}}^{\text{akm}} \approx J_\perp\left(\frac{J_\perp}{2W}\right)^{\alpha/(1-\alpha)}. \tag{12.27}$$

12.4.2 Toulouse Limit $\alpha = 0.5$

At the Toulouse limit $\alpha = 0.5$ the system can be mapped exactly onto a non-interacting resonant level model [129]

$$\hat{\mathcal{H}}_{RLM} = \sum_k \varepsilon_k \hat{c}_k^\dagger \hat{c}_k + E_d(t) d^\dagger d + V(t)\sum_k \left(\hat{c}_k^\dagger \hat{d} + \hat{d}^\dagger \hat{c}_k\right), \tag{12.28}$$

where a single fermionic level $d^\dagger$ with energy $E_d(t)$ is coupled by hybridization $V(t)$ to a bath of spinless fermions $c_k^\dagger$. Preparing the Kondo model in a highly polarized state ($h_z \gg W$ for

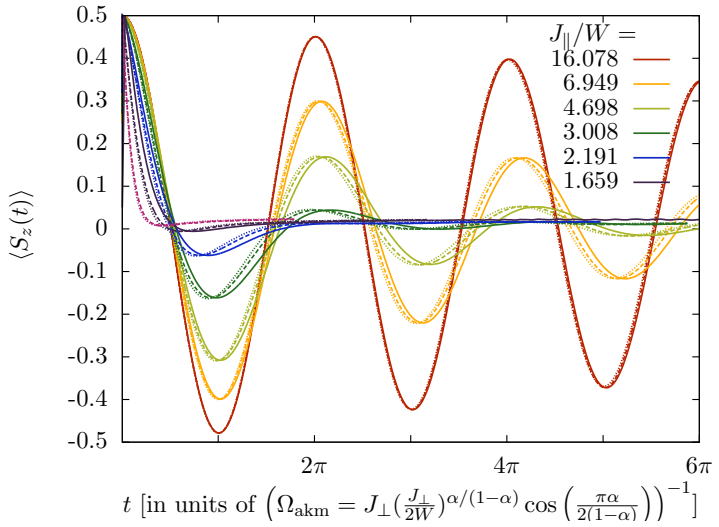

Figure 12.9: Time-dependent longitudinal spin magnetization for the anisotropic Kondo model. The parameters are chosen to be equivalent to the ones in Fig. 12.7 (solid lines: $J_\perp = 0.001W$, dashed lines: $J_\perp = 0.04W$, and dotted lines: $J_\perp = 0.2W$).

times $t < 0$) or starting from a strongly biased configuration in the bosonic system ($\varepsilon \gg \omega_c$ for times $t < 0$) is equivalent to a non-interacting resonant level model, where the eigenenergy of the single fermionic level is given by $E_d \ll 0$ for times $t < 0$.

The spin dynamics of the resonant level model can be solved exactly using the Keldysh formalism [135, 67]. The Kondo energy scale takes the form $T_K \sim J_\perp^2/W$, where the conduction electron bandwidth $2W$ in the Kondo model is related to the bosonic high-frequency cutoff ω_c through the formula

$$\left(\frac{W}{\omega_c}\right)^{2\alpha} = -\frac{2\Gamma(\frac{3}{2}-\alpha)\alpha^{-\alpha}(1-\alpha)^{\alpha-1}}{\sqrt{\pi}(2\alpha-1)\Gamma(1-\alpha)\Gamma(1-2\alpha)}. \tag{12.29}$$

For a derivation of the relation between the two cutoffs using Bethe-Ansatz techniques we refer to Appendix C of Ref. [129].

Using the Keldysh formalism [135], we obtain:

$$\langle S_z(t) \rangle + \frac{1}{2} = T_K \int_{-W}^{W} \frac{d\omega}{2\pi} |A(\omega, t)|^2, \tag{12.30}$$

where

$$A(\omega, t) = \int dt_1 G^r(t, t_1) \exp i\omega(t - t_1). \tag{12.31}$$

At the Toulouse limit $\alpha = 0.5$, assuming $t \geq 0$, we get the exact retarded Green's function:

$$G^r(t, t_1) = -i\theta(t - t_1) \exp -T_K(t - t_1) \exp(-iht_1 + i\delta ht), \tag{12.32}$$

if $t_1 < 0$, and

$$G^r(t, t_1) = -i\theta(t - t_1) \exp -T_K(t - t_1) \exp(-i\delta ht_1 + i\delta ht), \tag{12.33}$$

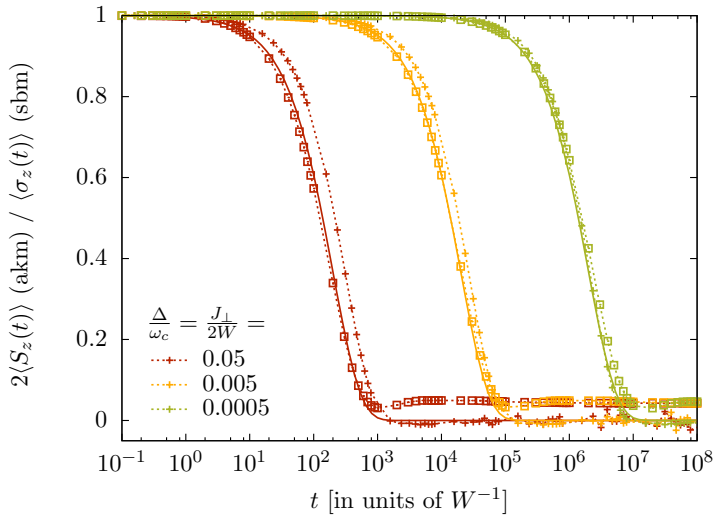

Figure 12.10: At the Toulouse point ($\alpha = 0.5, J_\parallel \approx 1.26W$) the deviation in the time-evolution of the magnetization in the spin-boson model (crosses) and the corresponding anisotropic Kondo model (squares) increases with increasing tunneling $\frac{\Delta}{\omega_c} = \frac{J_\perp}{2W}$. The solid lines represent the analytic result given by Eq. (12.37) using $T_K = \frac{\Delta^2}{W}$.

if $t_1 > 0$. Then, this results in:

$$\begin{aligned} A(\omega,t) &= \frac{-ie^{-T_K t}e^{i\omega t + i\delta h t}}{T_K - i(h+\omega)} \\ &+ \frac{-i}{T_K - i(\delta h+\omega)}\left(1 - e^{-T_K t}\exp(i(\delta h+\omega)t)\right). \end{aligned} \tag{12.34}$$

Assuming $h \to -\infty$, we get:

$$A(\omega,t) \approx \frac{-i}{T_K - i(\delta h+\omega)}\left(1 - e^{-T_K t}\exp(i(\delta h+\omega)t)\right). \tag{12.35}$$

In the limit of very large bandwidth $W \to +\infty$ for $\delta h = 0$ this results in:

$$\begin{aligned} \langle S_z(t)\rangle + \frac{1}{2} &= e^{-2tT_K}\int_{-\infty}^{0}\frac{d\omega}{\pi}\frac{T_K}{\omega^2+T_K^2} \\ &\quad + \int_{-\infty}^{0}\frac{d\omega}{\pi}\frac{T_K}{\omega^2+T_K^2} \\ &= 1/2(1+e^{-2tT_K}). \end{aligned} \tag{12.36}$$

Assuming $\delta h = 0$ for positive times, we get:

$$\langle\sigma_z(t)\rangle = 2\langle S_z(t)\rangle = e^{-2tT_K}. \tag{12.37}$$

We confirmed this exact analytic result using TD-NRG calculations. In the limit $J_\perp = 2\Delta \to 0$ the agreement is almost perfect as shown in Fig. 12.10, while for larger values of $J_\perp = 2\Delta$ the time-dependent longitudinal magnetization of the anisotropic Kondo model

shows a slower decay than the spin-boson model and the analytic Keldysh result for equivalent parameters. For large times the small remnant magnetization observed for the anisotropic Kondo model is due to incomplete thermalization unavoidable in a finite size system as studied by NRG with discretization parameter $\Lambda > 1$; see also Refs. [66, 67].

12.4.3 Intermediate Coupling $0.5 < \alpha < 1.0$

For even stronger coupling of the impurity spin to the bosonic bath in the spin-boson model $\alpha > 0.5$ the NIBA results given in Eqs. (12.21) and (12.22) are known to be wrong [108]. There is no coherent contribution in the spin-relaxation anymore and the power-law behavior for the incoherent part $\langle\sigma_z(t)\rangle_{\rm inc}$ predicted by NIBA does not describe the relaxation correctly either.

Although it is known that the non-interacting blip approximation fails, there is no agreement on the "correct" real-time dynamics of the spin-boson model in this parameter regime: Beyond NIBA a systematic expansion around the Toulouse limit $\alpha = 0.5$ gives the same results for the coherent part (up to order $O(\kappa)$, where $\alpha = 0.5 - \kappa$). For the incoherent part the following results can be found [108]:

$$\langle\sigma_z(t)\rangle_{\rm inc} = -2\kappa \frac{\exp(-\Delta_{\rm eff}t/2)}{(\Delta_{\rm eff}t)^{1+2\kappa}} \qquad \text{if } \kappa > 0 \tag{12.38}$$

$$\langle\sigma_z(t)\rangle_{\rm inc} = 8|\kappa| \frac{\exp(-\Delta_{\rm eff}t/2)}{(\Delta_{\rm eff}t)^{1+2|\kappa|}} \qquad \text{if } \kappa < 0 \tag{12.39}$$

Other functional forms suggested for the relaxation of an initially polarized spin in this parameter regime are a combination of an exponential and an algebraic decay [143]

$$\langle\sigma_z(t)\rangle = 8|\alpha - 0.5| \frac{\exp(\Delta_e t/2)}{(\Delta_e t)^{1+2|\alpha-0.5|}} \tag{12.40}$$

or a multi-exponential form [142, 144]

$$\langle\sigma_z(t)\rangle = \sum_n a_n e^{-b_n t}. \tag{12.41}$$

In this regime of intermediate coupling to the bosonic bath $0.5 < \alpha < 1$, we compared the results of our TD-NRG calculations against the various analytic forms of the relaxation suggested. Interestingly we could not confirm any of these predictions. Instead our numerical data suggest yet a different form: An exponential function with a power-law exponent

$$\langle\sigma_z(t)\rangle = \exp\left(-\left(tT^*\right)^{a_i}\right). \tag{12.42}$$

Our results for the spin-boson model are plotted in Fig. 12.11. The exponents a_i show a linear dependence on the deviation from the Toulouse point.

The same expression can be used to describe the relaxation for the anisotropic Kondo model. Our numerical data again show a very good fit with Eq. (12.42), see Fig. 12.12. In both cases we extracted the low-energy scale determining the characteristic relaxation time scale by measuring the level width of the spin autocorrelation function $C(\omega)$ (for a bosonic bath) or the Kondo temperature T_K (in case of a fermionic bath). The power-law exponent in the exponential function (12.42) extracted by fitting the time-evolution decreases linearly with the distance from the Toulouse point $a_i \propto 1-(1.26-J_\parallel/W)$ or equivalently $a_i = 1-(\alpha-0.5)$ (cf. Fig. 12.13). A direct comparison of the relaxation dynamics in the two quantum impurity models is shown in Fig. 12.14.

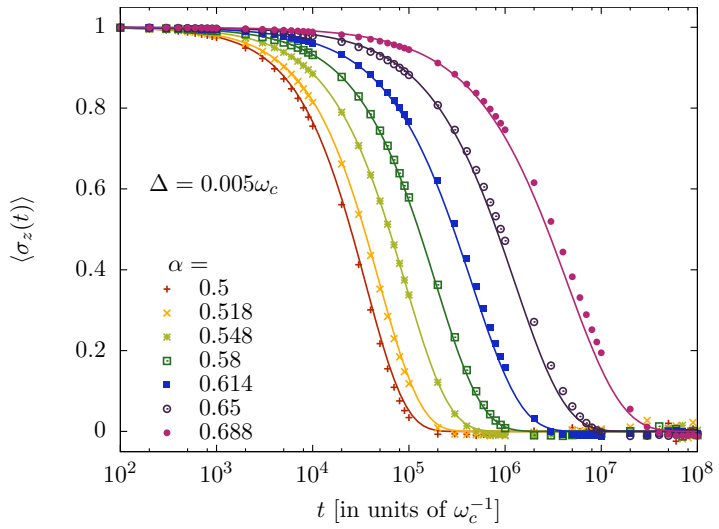

Figure 12.11: In the regime $0.5 < \alpha < 1$, we again find an exponential decay, where the exponent depends like a power law on time $\langle\sigma_z(t)\rangle = \exp\left(-\left(tT^*\right)^{a_i}\right)$.

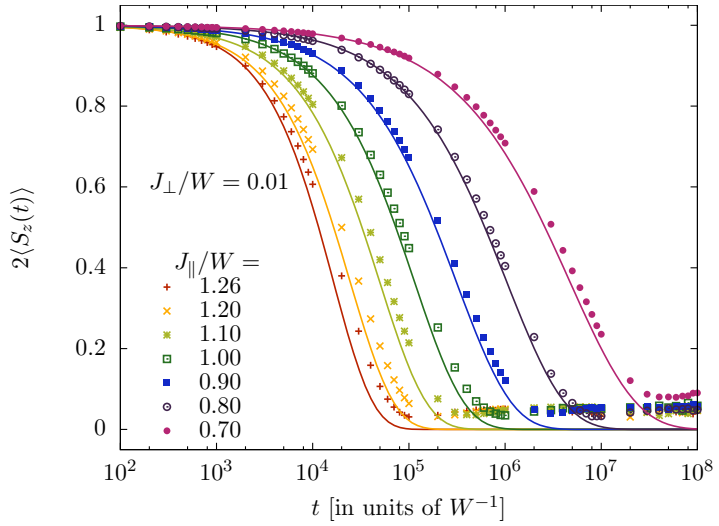

Figure 12.12: Time-dependent magnetization of the anisotropic Kondo model in the vicinity of the Toulouse limit. In the fit function analogous to Eq. (12.42) we used the "real" Kondo temperature $T^* = T_K$ derived from the width of the central peak in the spectral function.

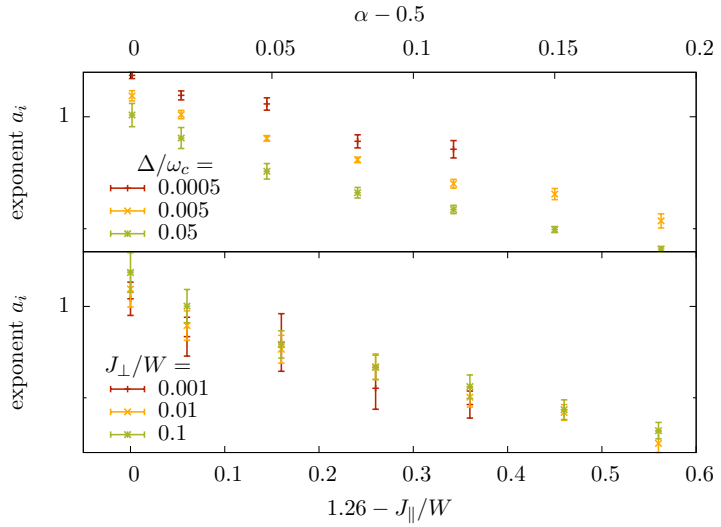

Figure 12.13: Fitted exponents of the spin-dynamics (12.42) for the spin-boson model Fig. 12.11 (upper panel) and anisotropic Kondo model Fig. 12.12 (lower panel).

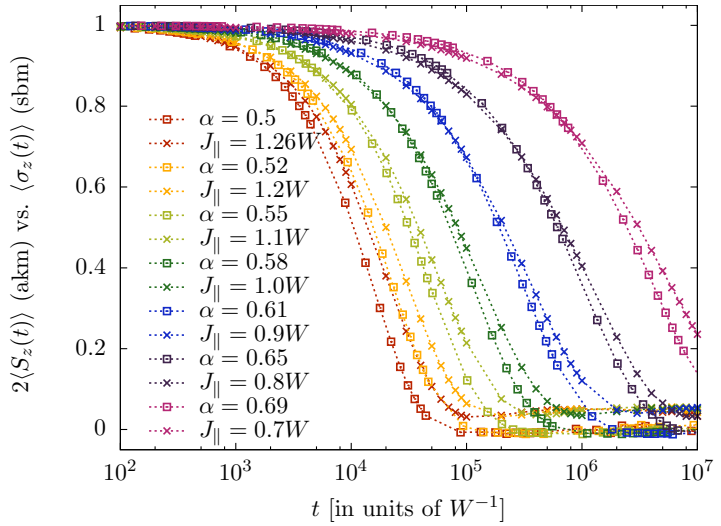

Figure 12.14: Comparison of the relaxation dynamics of the spin-boson and the anisotropic Kondo model in the parameter regime of intermediate coupling $0.5 < \alpha < 1$ for $\Delta = 0.005\omega_c$ (or equivalently $1.26W > J_\parallel > 0$ and $J_\perp = 0.01W$).

12.4.4 Strong Coupling $\alpha > 1.0$

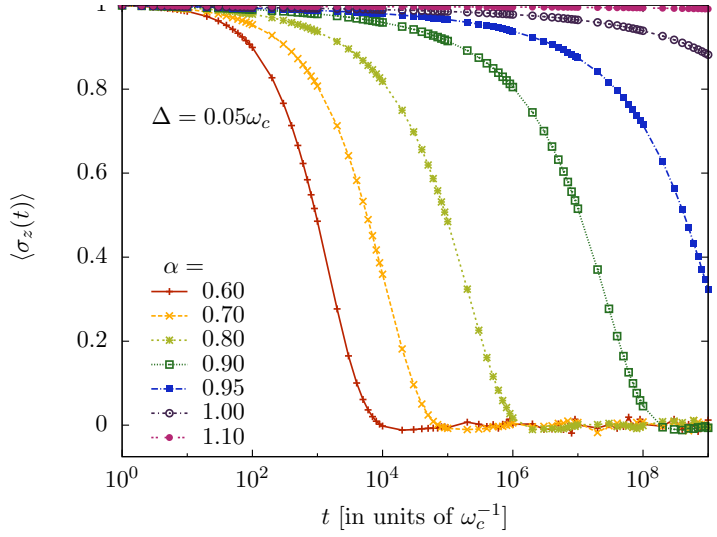

Figure 12.15: "Localization" observed for very strong coupling $\alpha > 1.0$ in the spin-boson model.

For even stronger coupling to the bosonic bath, a quantum phase transition to a localized phase can be observed in the spin-boson model. For $\alpha \approx 1 + O(\frac{\Delta}{\omega_c})$, a spin initially polarized in one direction will keep its magnetic moment and not relax to its equilibrium ground state, once the initial bias $\varepsilon > 0$ is switched off. This "localized" phase can be observed in the real-time evolution of the spin-boson model using the TD-NRG method. We show the transition to the localized phase in Fig. 12.15.

For the anisotropic Kondo model this parameter regime corresponds to ferromagnetic exchange interaction $J_\parallel < 0$, which we have studied in the preceding chapter Chap. 11. Let us briefly sum up the main results found in this investigation, combining TD-NRG results with an extended flow-equation approach: For isotropic coupling the time-dependent magnetization of an initially fully polarized spin reads

$$2\langle S_z(t)\rangle = \frac{1}{\ln(t) - \frac{1}{\rho J}} + 1 + \rho J + O(J^2), \tag{12.43}$$

while if $J_\perp > J_\parallel$ one finds

$$2\langle S_z(t)\rangle = 1 - \frac{\alpha^2}{2\tilde{g}} t^{2\tilde{g}} + \frac{\alpha^2}{2\tilde{g}} + O(J^2), \tag{12.44}$$

where $\tilde{g} = -\rho\sqrt{J_\parallel^2 - J_\perp^2}$ (details are published in Ref. [101] and can be found in Chap. 11).

A comparison of the impurity spin dynamics of the Kondo- and the spin-boson model in this regime is shown in Fig. 12.16 for isotropic ferromagnetic coupling between the impurity spin and the fermionic bath in the Kondo model and the corresponding parameters of the spin-boson model. Fig. 12.17 displays a similar comparison for the anisotropic ferromagnetic Kondo model ($J_\perp > J_\parallel$). We fit our numerical results against the analytic functions given

by Eq. (12.43) (for the isotropic case in Fig. 12.16) and Eq. (12.44) (for the anisotropic case in Fig. 12.17). The magnetization dynamics of the spin-boson model in the localized phase ($\alpha > 1$) is described by the same analytic function, although quantitative differences between the dynamics in the two models are observed.

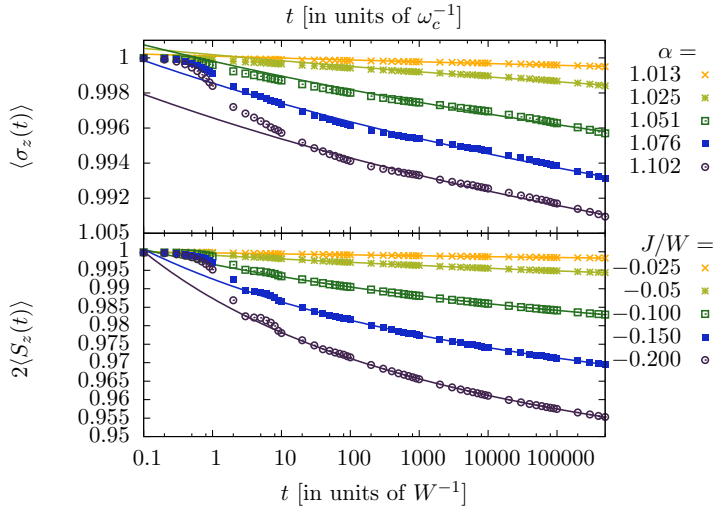

Figure 12.16: Time evolution of the impurity spin of the ferromagnetic *isotropic* Kondo model (lower panel) and of the spin-boson model for equivalent parameters in the localized regime (upper panel, $\Delta = \frac{J}{2}$ for matching color codes). Points represent TD-NRG results, lines represent fits according to Eq. (12.43).

12.4.5 Entanglement Entropy

Up to now we have focused on the time-dependent longitudinal spin magnetization $\langle\sigma_z(t)\rangle$, and $\langle S_z(t)\rangle$ respectively. Now we consider the real-time evolution of entanglement between the impurity spin and the respective bath in the two models. In order to quantify the amount of entanglement we use the von Neumann entropy already introduced in Eq. (12.15) for the time-dependent impurity density matrix $\rho_A(t) = \mathrm{Tr}_{\mathrm{bath}}\rho(t)$:

$$\mathcal{E}(t) = -\mathrm{Tr}\left\{\rho_A(t)\log_2(\rho_A(t))\right\}. \tag{12.45}$$

$\rho_A(t)$ can be expressed in terms of the different components of the impurity spin $\langle\sigma_i(t)\rangle$ or $\langle S_i(t)\rangle$.

In the case of the anisotropic Kondo model, one expects $\langle S_{x,y}\rangle(t) \to 0$ both at short times (choosing large initial polarizing field h_z for times $t < 0$), and at long times because of the Kondo effect.

The anisotropic Kondo model (given in Eq. (12.3)) has two conserved quantities S_x, S_y due to $[\hat{\mathcal{H}}_K, \hat{S}_x] = [\hat{\mathcal{H}}_K, \hat{S}_y] = 0$, which allows us to rewrite the time-dependent entanglement entropy in terms of the longitudinal magnetization as

$$\mathcal{E}(t) = -p_+(t)\log_2 p_+(t) - p_-(t)\log_2 p_-(t), \tag{12.46}$$

where $p_\pm(t) = \frac{1}{2} \pm \langle S_z(t)\rangle$. This relation can also be verified by comparing two different calculations, one where we directly evaluated the time-dependent entanglement entropy $\mathcal{E}(t)$

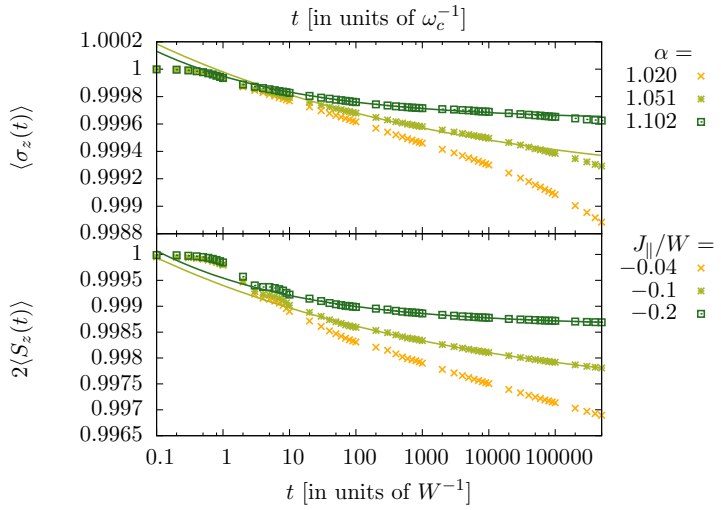

Figure 12.17: Time evolution of the impurity spin of the ferromagnetic *anisotropic* Kondo model (lower panel, $J_\perp = -0.04$) and of the spin-boson model for equivalent parameters in the localized regime (upper panel, $\Delta = -0.02$). Points represent TD-NRG results, lines represent fits according to Eq. (12.44).

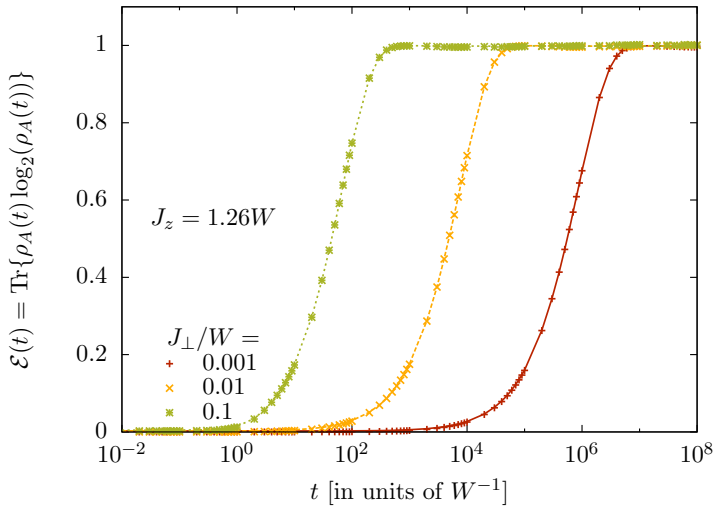

Figure 12.18: Comparison of the directly calculated entanglement entropy (lines) and the results obtained from $\langle S_z(t)\rangle$ via Eq. (12.46) (crosses).

by keeping track of the time-dependence of the full reduced density matrix $\rho_A(t)$ and a second one, where we calculated $\mathcal{E}(t)$ according to Eq. (12.46) using our numerical results for $\langle S_z(t)\rangle$. Fig. 12.18 shows the results of both TD-NRG calculations in the Toulouse limit (i. e. for $J_\parallel \approx 1.26W$) after abruptly switching off a strong initial magnetic field h_z at time $t = 0$.

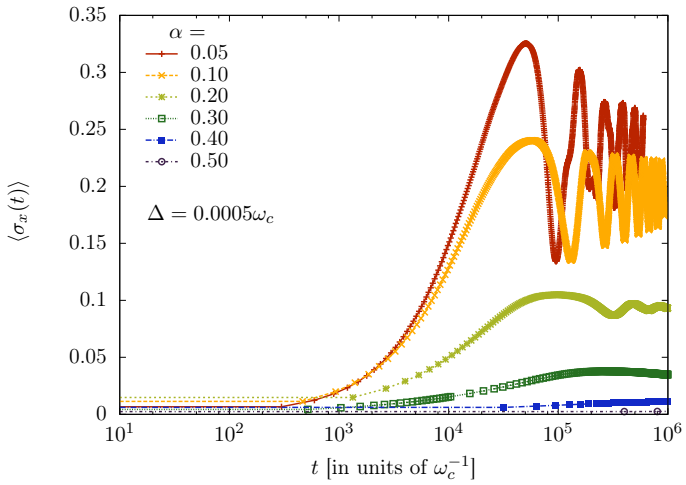

Figure 12.19: Time evolution of the transverse spin magnetization $\langle\sigma_x(t)\rangle$ in the spin-boson model after switching off a strong field $\varepsilon \gg \omega_c$ initially polarizing the spin in z-direction for times $t < 0$.

The situation is different for the spin-boson model. Because of the finite tunneling amplitude in the Hamiltonian $\Delta \neq 0$, we rather expect a contribution of $\langle\sigma_x(t)\rangle$ to the entanglement entropy. Investigating $\langle\sigma_x(t)\rangle$ for small spin-bath coupling $\alpha < 0.3$ (cf. Fig. 12.19), one observes damped oscillations around a finite value $\langle\sigma_x(t \to \infty)\rangle$. This finite value for $\langle\sigma_x(t)\rangle$ dominates the entanglement entropy $\mathcal{E}(t)$ for large times in the spin boson model (see Fig. 12.20).

To better characterize the time-dependent transverse magnetization $\langle\sigma_x(t)\rangle$ in the spin-boson model, we perform a quench of the tunneling $\Delta^{\text{ini}} \gg \omega_c \to \Delta^{\text{fin}}$. For small α and $\Delta^{\text{fin}} = 0$ the model is solvable analytically applying the so called polaron transformation to the Hamiltonian $U^\dagger \mathcal{H} U$, where $U = e^{-\frac{1}{2}\sigma_z \Omega}$ and $\Omega = -i\sum_n \frac{\lambda_n}{\omega_n}(a_n^\dagger - a_n)$ (cf. Ref. [62]). A small calculation yields

$$\langle\sigma_x(t)\rangle = \mathrm{Tr}\left\{\rho\sigma_x(t)\right\} \tag{12.47}$$

$$= \cos(\varepsilon t)\cos\left(\frac{Q_1(t)}{\pi}\right) e^{-\frac{1}{\pi}Q_2(t)}, \tag{12.48}$$

where $Q_1(t) = \int_0^\infty \frac{d\omega}{\omega^2} J(\omega)\sin(\omega t) = 2\pi\alpha\tan^{-1}(\omega_c t)$ and $Q_2(t) = \int_0^\infty \frac{d\omega}{\omega^2} J(\omega)\left(1 - \cos(\omega t)\right) = \pi\alpha\ln(1 + \omega_c^2 t^2) + f(t,\beta)$. For vanishing bias $\varepsilon = 0$, small α and large β Eq. (12.48) can be simplified to

$$\langle\sigma_x(t)\rangle \approx \langle\sigma_x(0)\rangle(\omega_c t)^{-2\alpha}. \tag{12.49}$$

The corresponding results of our TD-NRG calculation are shown in Fig. 12.21. The power-law decay is clearly visible (compare to the red dashed line). The decay is cut off at a time scale $\tau \propto (\Delta^{\text{fin}})^{-1}$ upon increasing Δ^{fin}.

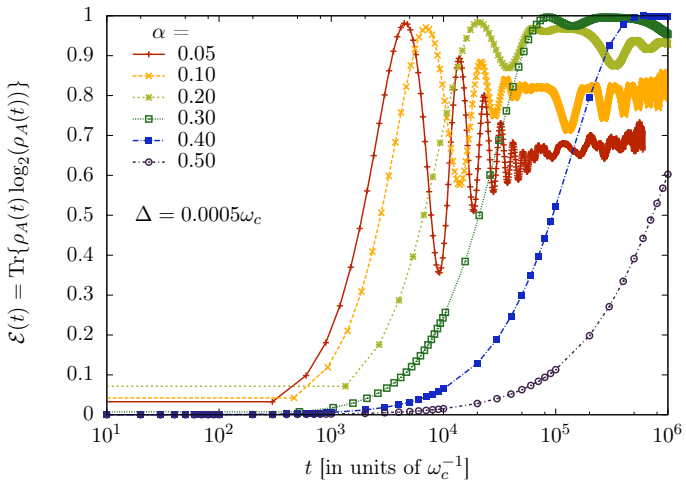

Figure 12.20: Time evolution of the entanglement entropy $\mathcal{E}(t)$ in the spin-boson model for the same parameters as in Fig. 12.19.

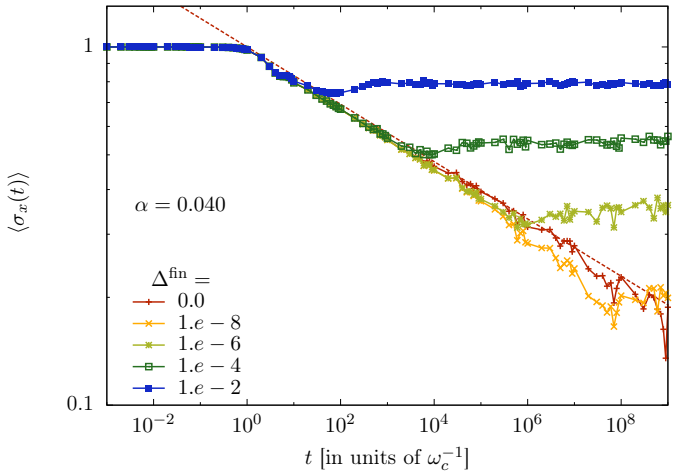

Figure 12.21: Transverse magnetization $\langle\sigma_x(t)\rangle$ for small spin-bath coupling $\alpha = 0.04$ and quench of an initial bias $\Delta^{\mathrm{ini}} \gg 0 \to \Delta^{\mathrm{fin}}$. The red dashed line indicates the power-law decay $f(t) = (\omega_c t)^{-2\alpha}$.

12.5 Summary

We have compared the static and time-dependent impurity magnetization for two different quantum impurity systems: The anisotropic Kondo model and the spin-boson model. We quantitatively verified that the equivalence of the anisotropic Kondo model and the ohmic spin-boson model holds for the longitudinal nonequilibrium magnetization of the impurity spin by studying the time evolution for different coupling strengths of the impurity spin to the respective bath.

We found identical functional descriptions to fit the time evolutions of the longitudinal spin dynamics, while different quantitative values were found for the frequency and relaxation time scales in all regimes except the Toulouse limit. Our results justify a careful application of the low-energy mapping between the two models to the longitudinal spin dynamics far from equilibrium.

Moreover we have demonstrated that the spin-bath entanglement differs in the two models. In the case of the anisotropic Kondo model, the entanglement is completely determined by the longitudinal magnetization $\langle S_z(t)\rangle$. For the spin-boson model, on the other hand, the entanglement entropy is a function of the full impurity density matrix $\rho_A(t)$. We showed that for small spin-bath coupling α the contribution of the transverse spin magnetization $\langle \sigma_x(t \to \infty)\rangle$ even dominates the time-dependent entanglement entropy at large times.

Chapter 13

Two Spins in a Bosonic Bath

We investigate two Ising coupled spins under the influence of a common bosonic bath, i. e. a generalization of the spin-boson model treated in the preceding chapter, Chap. 12. As in the simple single spin-boson model, a phase transition between a phase of "free" spins and a phase where the spins are "localized" due to the interaction with the bosonic bath is observed. We compare the phase diagrams for different dispersion of eigenmodes of the free bosonic bath (ohmic and subohmic) against each other and study the scaling of the spin magnetization with the system's parameters (tunneling $\Delta_{1,2}$, bias $\varepsilon_{1,2}$ and Ising interaction K) at the phase boundary for a subohmic dispersion. Furthermore, we focus on the spin dynamics after a quantum quench modeled by a sudden change of parameters in the Hamiltonian. We investigate the system's rich dynamical behavior arising from the complex interplay between spin-spin and spin-bath interactions. Interestingly, spin oscillations can synchronize due to the proximity of the common non-Markovian bath and the system displays highly entangled steady states for certain nonequilibrium initial preparations.

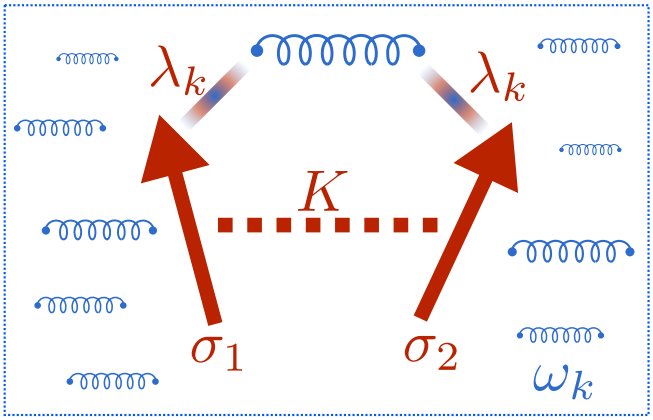

Figure 13.1: Two quantum spins-$\frac{1}{2}$, $\boldsymbol{\sigma}_1$ and $\boldsymbol{\sigma}_2$, coupled through an Ising interaction K. The spins are also entangled, via their $\hat{\sigma}^z$-components, to a common reservoir of bosonic oscillator modes with frequencies ω_k. The bath is characterized by the spectral density $J(\omega) = 2\pi\omega^s\omega_c^{1-s}\theta(\omega)\theta(\omega_c - \omega)$, where $s = 1$ ($s < 1$) refers to an ohmic (subohmic) bosonic environment.

13.1 Generalized Two-Spin Boson Model

In the preceding chapter, Chap. 12, we have introduced some aspects of the spin-boson model, which has been widely studied as a paradigm of quantum dissipation and quantum-to-classical transitions [53]. The environmental influence on the phase coherence between the two spin states in the "usual" spin-boson model is of crucial importance in the context of quantum computing (for example for quantum bits designs based on the Josephson effect [112, 113, 114]), as it sets a limit to the timescale where coherent quantum logical operations can be performed. In this context, it is essential to extend the system to multiple two-level systems (or qubits), as operations involving two qubits, e. g. , the CNOT gate, are required to obtain a complete set of quantum-logical operations. In addition, the presence of a second spin allows to address the competition between spin-spin and spin-bath interactions and the resulting interplay between quantum control and dissipation.

In this chapter, we investigate such a generalization of the single spin-boson model and consider two quantum spins (labeled by $\boldsymbol{\sigma}_1$ and $\boldsymbol{\sigma}_2$), which are coupled to each other via an Ising-type coupling and interact with a common bath of harmonic oscillator modes, as described by the Hamiltonian (see also Fig. 13.1)

$$\mathcal{H}_{2SB} = \sum_n \omega_n \left(\hat{a}_n^\dagger \hat{a}_n + \frac{1}{2} \right) + + \sum_{\alpha=1}^{2} \left\{ \frac{\hat{\sigma}_\alpha^z}{2} \sum_n \lambda_{\alpha,n} \left(\hat{a}_n + \hat{a}_n^\dagger \right) + \Delta_\alpha \frac{\hat{\sigma}_\alpha^x}{2} + \varepsilon_\alpha \frac{\hat{\sigma}_\alpha^z}{2} \right\} + \frac{K}{4} \hat{\sigma}_1^z \hat{\sigma}_2^z. \tag{13.1}$$

Here, $\hat{\sigma}_{1,2}^{x,y,z}$ are the usual Pauli matrices describing the two spins and a_n is the bosonic annihilation operator of the bath mode with frequency ω_n. The free (spin) part of the Hamiltonian contains the tunneling amplitudes $\Delta_{1,2}$, bias fields $\varepsilon_{1,2}$ and the bare Ising interaction constant K. For the spin-bath interaction, for simplicity, we use identical coupling constants λ_n for both spins. The effects of the bosonic environment on the spins are fully captured by the bath spectral density [62, 108, 109]

$$J(\omega) \equiv \pi \sum_i \lambda_i^2 \delta(\omega_i - \omega) = 2\pi\alpha\omega_c^{1-s}\omega^s \theta(\omega)\theta(\omega_c - \omega), \tag{13.2}$$

which, as in case of the single spin-boson model (cf. Eq. (12.2)), we assume to behave as a power law ω^s ($s > 0$) up to the cutoff frequency ω_c. Hereafter, we will be studying exponents in the range $\frac{1}{2} \leq s \leq 1$, where the case $s = 1$ ($s < 1$) refers to an ohmic (subohmic) bosonic environment. The strength of the coupling to the bath is characterized by the dimensionless dissipation constant $\alpha \geq 0$.

Using identical coupling constants for both spins λ_i corresponds to the case where the spins are spatially close to each other. Specifically, we assume their separation d_{12} to be smaller than the shortest wavelength of the bath excitations: $d_{12} \lesssim \lambda_c = v_s/\omega_c$, where v_s is the sound velocity in the bath [118, 145].

There are several reasons for considering an Ising-like coupling $\frac{K}{4}\hat{\sigma}_1^z\hat{\sigma}_2^z$ between the two spins. First, there are experimental situations where such an SU(2)-broken coupling is realized, for instance in capacitively coupled quantum dots where the operators $\hat{\sigma}_j^z$ describe charge states on the dot [146, 147, 148]. Other examples are the cold-atom quantum dot setting, trapped ions and superconducting qubits. Second, since the bath couples to the $\hat{\sigma}^z$ component of the spins, it automatically induces an indirect (ferromagnetic) Ising interaction between the spins, which is mediated by a coherent exchange of phonons. This results in

a renormalization of K to $K_r = K - 4\alpha\omega_c/s$. Therefore, even for zero K, the spins are Ising-coupled. We note that, in general, the bath induced interaction decays with the spatial distance between the spins d_{12} on a lengthscale given by $\lambda_c \sim \omega_c^{-1}$ [118, 145].

The two-spin boson model allows to address the competition between spin-spin entanglement, characterized for instance by the concurrence, and spin-bath entanglement, characterized for instance by the entanglement entropy [149, 150, 151, 152, 145, 153].

We will show below that for a particular initial preparation, the system exhibits a nontrivial steady-state that is different from the ground state, where the spins are strongly entangled with the bath while maintaining coherence between different spin configurations.

Whereas for some experimental realizations the description of independent bosonic reservoirs is appropriate, e. g. , in the case of quantum dots coupled to independent leads [146], there are others, where the spins couple to a common bath, e. g. , the cold-atom [117, 118, 119, 120] and trapped ion setup [115]. Here, we assume a common bath because we are mostly interested in studying the competition between the coherent and dissipative parts of the interaction induced by the bath leading to dynamical spin synchronization and highly entangled steady states. The other situation has been addressed for instance in Refs. [128, 154, 155].

In the following, we aim to investigate not only the static properties of the ground state but also the nonequilibrium dynamics of the system, both for an ohmic and a subohmic boson bath. In the subohmic case, we mainly consider the experimentally relevant situation of $s = 1/2$ [156, 157].

This chapter is outlined as follows: In Sec. 13.2, we calculate the zero temperature phase diagram as a function of dissipation strength α and Ising coupling K, both for $s = 1/2$ and $s = 1$. As a reminiscence of the single spin-boson model, it contains a delocalized phase ($\langle\sigma^z_{1,2}\rangle = 0$) for small dissipation and a localized phase ($\langle\sigma^z_{1,2}\rangle \neq 0$ for $\varepsilon_{1,2} = 0^+$) for large dissipation. We give a physically intuitive explanation for the asymmetry between the ferromagnetic ($K < 0$) and antiferromagnetic ($K > 0$) regions of the phase diagram.

In Sec. 13.3, we investigate the critical properties at the phase transitions such as the behavior of the entanglement entropy across the transition, or the scaling of spin expectation values that occurs for a subohmic bath.

In Sec. 13.4, we explore the nonequilibrium dynamics of the two spins after a quantum quench. We typically polarize the spins initially by applying large bias fields along the z or x-direction that we switch off at time $t = 0$. We begin our analysis in Sec. 13.4.1 with the exactly solvable case of zero transverse fields $\Delta_{1,2} = 0$, where we show that our TD-NRG results perfectly agree with the exact analytical solution. In Sec. 13.4.2, we investigate the regime of weak spin-bath coupling, and compare TD-NRG to the commonly employed perturbative Bloch-Redfield approach. We give quantitative limits on the applicability of the Redfield method. In Sec. 13.4.3, we find that, interestingly, the bath is able to synchronize spin oscillations via a coherent exchange of phonons, even at weak spin-bath coupling. This phenomenon is not captured in the Bloch-Redfield master equation approach, where the backaction of the bath on the spins is neglected. This method thus fails to correctly describe the spin dynamics even in the perturbative regime. In Sec. 13.4.4, we investigate the spin dynamics for vanishing (renormalized) Ising interaction $K_r = 0$ and highlight similarities and differences to the single spin-boson model. We first elaborate on the case of weak-dissipation in Sec. 13.4.4, where we compute the quality factor of the damped oscillations. Afterwards, we discuss the dynamics at the generalized Toulouse point $\alpha = 1/2$ in Sec. 13.4.4. In Sec. 13.4.5, we examine the crossover to the regime of strong spin-bath coupling for general Ising coupling, and point out differences between the case of an ohmic and a subohmic bath. In Sec. 13.4.6,

we describe that a highly entangled steady state can emerge from the dynamics if the system is prepared far from equilibrium. The main results of this chapter are summarized in Sec. 13.5.

13.2 Ground State Phases

In this Section, we employ the numerical renormalization group method for bosonic baths [61], already introduced in Chap. 5, to calculate the ground state phase diagram corresponding to the Hamiltonian of Eq.(13.1) as a function of dissipation strength α and Ising coupling K. We present the results for the ohmic, $s = 1$, as well as the subohmic case of $s = 1/2$. We point out similarities and differences to the situation of the single spin-boson model discussed in Chap. 12 and with that of a two-spin model with two separate baths.

Throughout this chapter we employ the following parameters for our NRG calculations (we use the common notation): A discretization parameter of $\Lambda = 1.4$, a total of $N_{b,0} = 599$ bosonic modes in the first iteration and $N_{b,N} = 6$ in the following ones, while keeping $N_{\mathrm{Lev}} = 200$ low-energy levels in each NRG iteration. Compared to the single spin case, this signifies a reduction of the levels kept and bosonic modes "added" in each iteration. This is unavoidable due to the enlarged Hilbert space describing the impurity degrees of freedom (and to keep the computational cost manageable).

We obtain a qualitative understanding of the phase diagram by using the fact that the fast bath modes follow the spin dynamics adiabatically in the sense known from the famous Born-Oppenheimer approximation [62, 108]. The spins are dressed by the bath phonons, and as a result the energy separation of the two lowest-energy spin states becomes renormalized. This situation is reminiscent of the single spin-boson model. There, the tunneling splitting Δ also becomes renormalized by the bath, and in the ohmic case, one finds a renormalized value of $\Delta_{\mathrm{eff}} = \Delta(\frac{\Delta}{\omega_c})^{\alpha/(1-\alpha)}$ for $\alpha < 1$ (cf. Eq. (12.16)) and a complete quench of the tunneling for $\alpha > 1$, where the system is thus localized [62, 108].

13.2.1 Phase Diagrams

Using the numerical renormalization group method for static quantities, we have determined the phase diagram of the two-spin boson model in Eq. (13.1). We present results for an ohmic bath [158, 159], in the left panel of Fig. 13.2 and for a subohmic bath with $s = 1/2$ in the right panel of Fig. 13.2. Different curves correspond to different values of Δ/ω_c. Here, we assume equal tunneling amplitudes of the two spins $\Delta_1 = \Delta_2 \equiv \Delta$. Introducing slightly asymmetric tunneling elements $\Delta_1 \neq \Delta_2$, however, does not affect the location of the phase boundary much. Hereafter, we use units of the bath cutoff frequency, i. e. , we set $\omega_c = 1$, and we shall be mainly interested in the case where both $\Delta_{1,2} \ll \omega_c$ and $\varepsilon_{1,2} \ll \omega_c$.

As shown in Fig. 13.2, the two-spin boson model exhibits two ground state phases: A *delocalized phase*, where the spin expectation values $\langle\sigma^z_{1,2}\rangle$ vanish in the ground state (for $\varepsilon_{1,2} \to 0$), and a *localized phase*, where the spins develop a finite magnetization $\langle\sigma^z_1\rangle = \langle\sigma^z_2\rangle = \pm m$ ($m > 0$) for infinitesimal bias fields $\varepsilon_{1,2} = 0^{\mp}$. Like in the single spin-boson model, the system is delocalized for weak dissipation and enters a localized phase upon increasing α. The phase boundary, however, now explicitly depends on the Ising interaction constant K.

Let us first focus on the ohmic model displayed in the left panel of Fig. 13.2. For ferromagnetic Ising interaction $K < 0$, the phase boundary only weakly depends on K and is located at $\alpha_c \approx 0.15 + \mathcal{O}(\frac{\Delta}{\omega_c})$, which is a much smaller value than in the single spin case,

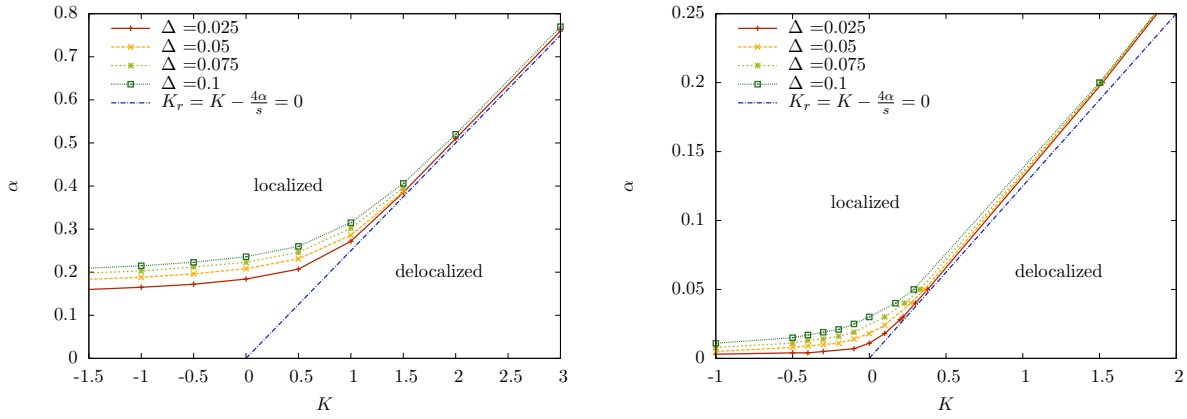

Figure 13.2: Phase diagram of the ohmic two-spin boson model ($s = 1$, left panel) and the subohmic spin-boson model ($s = 1/2$, right panel) as a function of the dissipation strength α and Ising coupling K. Different curves correspond to different values of tunneling amplitudes $\Delta_1 = \Delta_2 \equiv \Delta$. For infinitesimal bias fields $\varepsilon_{1,2} = -10^{-8}\omega_c$ the ground state of the system in the localized region is given by $|\uparrow\uparrow\rangle \otimes |\Omega\rangle$, where $|\Omega\rangle$ is a shifted bath vacuum [see Eq. (13.5)]. The dashed line indicates where the renormalized Ising interaction vanishes: $K_r = 0$.

where the transition occurs at $\alpha_c^{\text{single}} = 1 + \mathcal{O}(\frac{\Delta}{\omega_c})$ [109]. For antiferromagnetic $K > 0$, we find that the delocalized region extends up to larger values of α and we observe that the phase boundary occurs at the line $K = 4\alpha\omega_c/s$ for larger values of K. At this value of K the renormalized Ising interaction K_r, which takes into account the bath induced ferromagnetic spin-spin interaction ($-4\alpha\omega_c/s$), vanishes. We will give a short derivation of this formula in Sec. 13.2.2.

Let us now turn to the subohmic case displayed in the right panel of Fig. 13.2. It shows the same qualitative features as the ohmic one, however, the system enters the localized phase for even smaller values of α. On the ferromagnetic side $K < 0$, our results suggest that $\alpha_c \approx 0 + \mathcal{O}(\frac{\Delta}{\omega_c})$, in agreement with the single spin case [160]. For antiferromagnetic $K > 0$, the system again remains delocalized up to larger values of α and the phase transition occurs close to the line $K_r = 0$. Note that K_r depends on the bath exponent s.

We distinguish the two phases by applying small bias fields $\varepsilon_{1,2} = 10^{-8}\omega_c$ and measure $\langle\sigma_{1,2}^z\rangle$. The latter vanishes in the delocalized region, but remains nonzero $\langle\sigma_1^z\rangle = \langle\sigma_2^z\rangle = -m$ ($m > 0$) in the localized part of the phase diagram.

We have also applied an antiferromagnetic bias field configuration: $\varepsilon_1 = -\varepsilon_2 = 10^{-8}\omega_c$ and find that, for a fixed value of K, the system remains delocalized up to larger values of α, but eventually localizes in one of the *ferromagnetic* spin states $|\uparrow\uparrow\rangle, |\downarrow\downarrow\rangle$. This shows that the system does not localize in any of the antiferromagnetic spin configurations. We provide a physical explanation for this phenomenon in Sec. 13.2.2. Results for $\langle\sigma_{1,2}^z\rangle$ as a function of α for both bias field configurations and different values of K are shown in Fig. 13.3.

13.2.2 Qualitative Understanding of the Phase Diagram

From the previous considerations, immediately the questions arise why the phase diagram is not symmetric under the combined transformation of $\{K \to -K, \boldsymbol{\sigma}_2 \to -\boldsymbol{\sigma}_2\}$, and why the

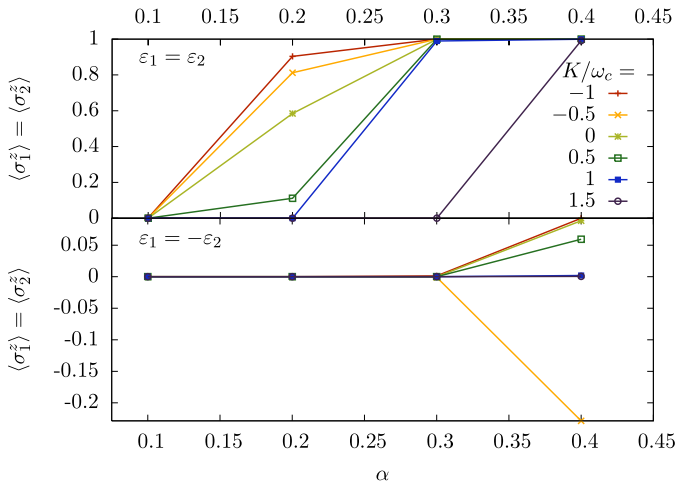

Figure 13.3: $\langle\sigma_{1,2}^z\rangle$ as a function of α for various values of K and $\Delta = 0.025\omega_c$. Different bias field configurations are shown in the upper part (ferromagnetic, $\varepsilon_1 = \varepsilon_2 = 10^{-8}\omega_c$) and lower part (antiferromagnetic, $\varepsilon_1 = -\varepsilon_2 = 10^{-8}\omega_c$) of the figure. This plot shows that spins are always aligned in the localized phase. The phase transition is shifted to larger values of α applying an infinitesimal antiferromagnetic bias field.

system cannot localize in one of the antiferromagnetic spin states $\{|\uparrow\downarrow\rangle, |\downarrow\uparrow\rangle\}$.

In order to answer these questions, we perform a strong-coupling analysis which relies on the fact that the fast modes of the bath ($\omega_n \gg \Delta$) adiabatically renormalize the energy separation of different spin states [62]. In physical terms, assuming that the bath oscillators follow the spin transitions immediately (Born-Oppenheimer approximation), the spins are dressed by phonons with frequencies larger than Δ. Thus, transitions between different spin states are suppressed, if they involve a readjustment of the excitations in the bath. We will consider the ferromagnetic and antiferromagnetic cases separately.

We first consider that the bath induces a ferromagnetic interaction between the spins, which renormalizes the value of the Ising constant K to

$$K_r = K - \frac{4\alpha\omega_c}{s}\,. \tag{13.3}$$

This is most easily derived by applying the polaron unitary transformation $U = \exp[-\frac{1}{2}(\hat{\sigma}_1^z + \hat{\sigma}_2^z)\sum_n \frac{\lambda_n}{\omega_n}(\hat{a}_n^\dagger - \hat{a}_n)]$ to the Hamiltonian in Eq. (13.1), which yields for $\tilde{\mathcal{H}} = U^{-1}\hat{\mathcal{H}}U$:

$$\tilde{\mathcal{H}} = \sum_n \omega_n \left(\hat{a}_n^\dagger \hat{a}_n + \frac{1}{2}\right) + \sum_{j=1}^{2}\left[\frac{\Delta_j}{2}(\hat{\sigma}_j^+ e^{i\hat{\Omega}} + \text{h.c.}) + \frac{\varepsilon_j}{2}\hat{\sigma}_j^z\right] + \frac{K_r}{4}\hat{\sigma}_1^z\sigma_2^z, \tag{13.4}$$

where $|\Omega\rangle = e^{i\hat{\Omega}}|0\rangle$ is the so-called displaced oscillator bath state, which occurs if all oscillators equilibrate in contact with spins that are held fixed in position $|\uparrow\uparrow\rangle$. The bath displacement operator reads $\hat{\Omega} = -i\sum_n \frac{\lambda_n}{\omega_n}(\hat{a}_n^\dagger - \hat{a}_n)$ and $|0\rangle$ is the ground state of the free bath part of the Hamiltonian $\hat{\mathcal{H}}_B = \sum_n \omega_n \hat{a}_n^\dagger \hat{a}_n$. This form of the Hamiltonian makes explicit the bath induced ferromagnetic Ising interaction. In particular, if the bare Ising coupling is antiferromagnetic

$K > 0$, the effective interaction changes sign at a dissipation strength of $\alpha = \frac{sK}{4\omega_c}$. For larger values of $K \geq \omega_c$, the phase transition occurs close to this critical value of α, as shown in Fig. 13.2. From $\tilde{H}$, we can also learn immediately that a spin flip is associated with a complex excitation of the bosonic bath into a coherent state $|\Omega\rangle = e^{i\hat{\Omega}}|0\rangle$, where $|0\rangle$ is the ground state of the free bath part of the Hamiltonian $H_B = \sum_n \omega_n \left(\hat{a}_n^\dagger \hat{a}_n + \frac{1}{2}\right)$.

Let us begin with the *ferromagnetic situation* $K < 0$, and assume that $|K| \gg \Delta_{1,2}$ and zero bias $\varepsilon_{1,2} = 0$. For $\Delta_{1,2} = 0$, the two lowest energy spin states are given by the two ferromagnetic states $\{|\uparrow\uparrow\rangle, |\downarrow\downarrow\rangle\}$. If we now turn on the tunneling $\Delta_1 = \Delta_2 = \Delta$, we find that the energy splitting between the two lowest states is of the order

$$\delta E \sim \frac{2\Delta^2}{|K|}\langle\Omega| - \Omega\rangle. \tag{13.5}$$

where $|\Omega\rangle = e^{i\hat{\Omega}}|0\rangle$ again is the displaced oscillator bath state, which occurs when all oscillators equilibrate in contact with spins that are held fixed in position $|\downarrow\downarrow\rangle$. In terms of the spectral density, the bath renormalized energy splitting becomes

$$\delta E \sim \frac{2\Delta^2}{|K|} \exp\Big[-\frac{1}{\pi}\int_{p\delta E}^{\infty} d\omega \frac{J(\omega)}{\omega^2}\Big], \tag{13.6}$$

where $p \gg 1$. To be consistent with the adiabatic renormalization scheme, the energy splitting δE shows up as an infrared cutoff for the oscillator frequencies that are summed over. Since the bath renormalizes the energy splitting to smaller values $\delta E < \frac{2\Delta^2}{|K|}$, one can solve Eq. (13.6) iteratively [62, 108]. In the case that δE is renormalized to zero, the ground state is doubly degenerate and the system localizes. This situation, where the displaced bath states $|\Omega\rangle$ and $|-\Omega\rangle$ are orthogonal to each other, is known as orthogonality catastrophe [108]. If δE is renormalized to a nonzero value, the ground state is unique and the system delocalized.

For a subohmic spectral density, the iteration process yields $\delta E = 0$ for any positive value of α, and the system is localized as soon as $\alpha > 0$. In the ohmic case, on the other hand, we find that as long as $\alpha < 1/2$, the energy splitting renormalizes to the finite value $\delta E = \delta E_0 \big(\frac{\delta E_0}{\omega_c}\big)^{2\alpha/(1-2\alpha)}$ where $\delta E_0 = 2\Delta^2/|K|$. For $\alpha > 1/2$, however, one finds $\delta E = 0$ and the system is localized. The phase transition occurs at the critical value $\alpha_c = 1/2$. The same value was recently found using a variational treatment [159].

Let us remark that in the case of the single spin-boson model, one has to calculate the overlap integral $\langle\frac{\Omega}{2}|-\frac{\Omega}{2}\rangle = \exp[-\frac{1}{2\pi}\int_0^\infty d\omega \frac{J(\omega)}{\omega^2}]$, which leads to $\alpha_c^{\rm single} = 1$ [62, 108]. This also implies that the delocalized phase in the two-spin case is characterized by a distinct Kondo scale compared to the single spin-boson model [62].

Our numerical renormalization group method calculation, which goes beyond this simple approximation and the variational approach of Ref. [159], indeed shows that the critical value of α in the ferromagnetic regime only weakly depends on K. In the ohmic case we observe, however, that α_c rather converges to $\alpha_c(s = 1) \approx 0.15$ for large $|K|$ and $\frac{\Delta}{\omega_c} \to 0$ instead of the approximated value $\alpha_c = 1/2$. In the subohmic case, on the other hand, our NRG calculations agree with the predicted value of $\alpha_c = 0$ as we find $\alpha_c(s = 1/2) \approx 0$ for $\frac{\Delta}{\omega_c} \to 0$.

We now turn to the *antiferromagnetic situation* $K > 0$. In this case the effective interaction K_r changes sign at a dissipation strength of $\alpha = \frac{sK}{4\omega_c}$. For larger values of $K \geq \omega_c$, the phase transition occurs close to this critical value of α, as shown in Fig. 13.2.

Since we want to investigate the antiferromagnetic regime, we assume that $K_r > 0$ (or $K \to \infty$ for any value of α) in the following. Then, the two lowest energy states for zero

tunneling ($\Delta = 0$) are degenerate in energy and given by $\{|\uparrow\downarrow\rangle, |\downarrow\uparrow\rangle\}$. If we turn on tunneling, the two states hybridize and the energy difference between the two lowest energy states reads

$$\Delta E \sim \frac{2\Delta^2}{K}\langle 0|0\rangle = \frac{\Delta^2}{K}\,, \tag{13.7}$$

where $|0\rangle$ is the unshifted bath vacuum. Hence, any nonzero value of Δ leads to a unique ground state, because the quenching of the tunneling amplitude due to the bath does not occur for a total spin zero state [compare with Eq. (13.5)]. (This can also be interpreted as the disappearance of Kondo-type entanglement for a spin zero state [109].) As a result, the system is always delocalized for an antiferromagnetic Ising coupling $K_r > 0$, and the phase transition to the localized state is shifted to much larger values of α necessary to compensate the antiferromagnetic spin-spin coupling constant K.

13.2.3 Recovering the Single Spin-Boson Model

Before going into further detail and investigating the entanglement entropy of the spin system with the bath and the nature of the phase transition for a subohmic bath in Sec. 13.3, let us comment on another issue: Our idea is to recover the "simple" single spin-boson model phase diagram by slowly decreasing the coupling of one spin to the bath. We choose $\alpha_2 \to \varepsilon = 0^+$. For both dispersion relations, ohmic and subohmic bath spectral functions, we test the phase boundaries and find the single spin-boson behavior only to be recovered for the case where $K = 0$ (see Fig. 13.4). As a side remark: As $\alpha \to 0$ the shifting of the phase boundary to the

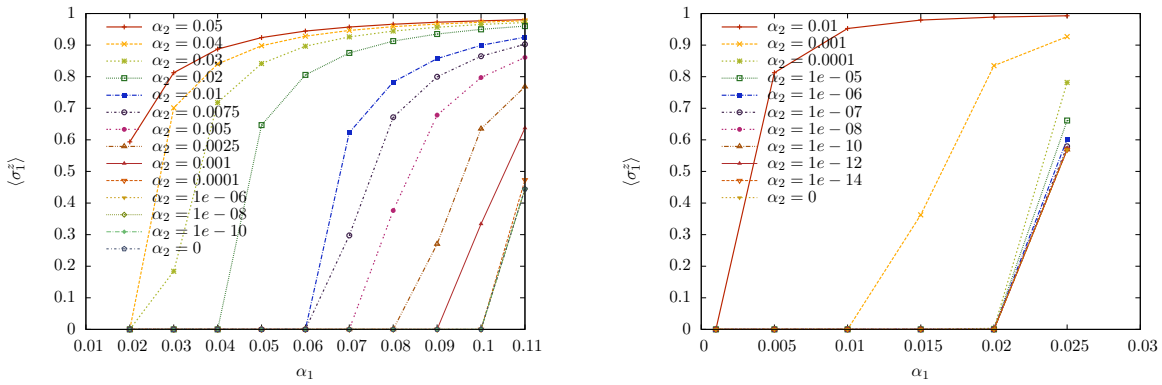

Figure 13.4: The "simple" single spin–boson model phase boundary ($\alpha_c^{1spin} = 0.1$) is recovered for the two-spin subohmic spin–boson model only if we switch off the couplings between one of the spins and the bath as well as the coupling between the two spins (left panel). If we still allow for a finite Ising coupling between the two spins, the phase boundary is shifted even if one of the spins is decoupled from the bath (see right panel, where $K = -4$).

value of the single spin-boson model is accompanied by a vanishing entanglement of the two spins, which can as well be seen in the concurrence of the two spins.

13.3 Phase Transitions and Scaling

In this Section, we investigate the behavior of the system close to the localization phase transition in more detail. It is known, that the transition is in the Kosterlitz-Thouless univer-

sality class for the ohmic system [109, 128], but it is of continuous type in the subohmic case [161, 129]. Since recent studies show that the numerical renormalization group method is not well-suited to describe the system correctly close to the transition for $s < 1/2$ [162, 163], we restrict ourselves to $s \geq 1/2$.

In Sec. 13.3.1, we first study the behavior of the entanglement entropy in the ohmic system. It indicates that the phase coherence of oscillations in the delocalized phase is lost prior to localization, a phenomenon known from the single spin-boson case [130, 164, 129]. We then turn to the subohmic system and examine in Sec. 13.3.2 the scaling of the spin expectation values $\langle \sigma^z_{1,2} \rangle$ close to the phase transition. We compare the scaling exponents we extract from NRG calculations to the critical exponents that can be found from mean-field scaling relations using an effective spin action functional as shown in Appendix D.

13.3.1 Static Entanglement Entropy

To quantify the entanglement between the two-spin and the bosonic bath, we again employ the von Neumann entropy [132, 133, 134] (cf. Eq. (12.15))

$$\mathcal{E} = -\mathrm{Tr}\{\rho_A \log_2(\rho_A)\}\,, \tag{13.8}$$

where $\rho_A = \mathrm{Tr}_B \rho$ now denotes the reduced density matrix of the two spins. One finds that $0 \leq \mathcal{E} \leq \log_2 4 = 2$, where $\mathcal{E} = 0$ in the absence of entanglement between spin and bath. In the left panel of Fig. 13.5 we show results for the entanglement entropy in the ohmic system as a function of dissipation α for different values of Ising coupling K. Like in the case of the single spin-boson model, the entanglement entropy is nonzero only in the delocalized phase and rapidly falls to zero at the phase transition. It reaches a plateau for $\alpha \approx \alpha_c/2$, indicating that coherence is lost already before the system becomes localized. The plateau characterizes a region of maximal decoherence, where the spin dynamics is incoherent. This coherent-to-incoherent crossover is known from the single spin system [130, 164, 129], where it occurs exactly at the Toulouse point $\alpha^{\mathrm{single}} = 1/2$. In Sec. 13.4.4, we discuss the equivalent of the Toulouse point in the two spin model to occur at $\alpha = 1/2$ and $K = 2\omega_c$.

Surprisingly, as we show in the inset of the left panel of Fig. 13.5, the plateau shrinks considerably if we go to larger positive values of $K \gtrsim \omega_c$. The plateau more and more resembles a peak-like structure. Coherence is lost only right at the transition (similar to the subohmic case discussed below). This is different from the single spin case, where the incoherent regime extends between $1/2 \leq \alpha \leq 1$ and is thus much larger.

Note that in the case of a subohmic bath the entanglement entropy rather reaches a maximum (peak) right at the localization quantum phase transition, both for the single [129] and the two-spin boson system (see right panel of Fig. 13.5). The coherence of the spin oscillations (continuously) decreases towards the phase transition, but there is no region where the spin transitions are completely incoherent. In fact, coherent spin oscillations of $\langle \sigma^z(t) \rangle$ even persist into the localized phase, where they occur around a nonzero expectation value $\langle \sigma^z \rangle \neq 0$ [160].

13.3.2 Subohmic System: Scaling of Magnetization

In this Section, we investigate the scaling of the spin expectation values $\langle \sigma^z_{1,2} \rangle$ (magnetization) at the phase transition in the subohmic system. For the single spin-boson system, it is known that the phase transition is continuous for $s < 1$, and scaling exponents have been extracted

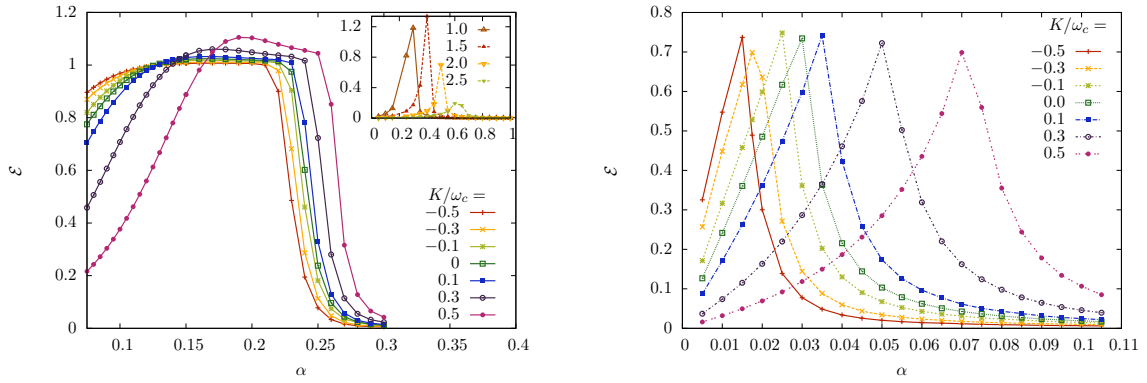

Figure 13.5: Entanglement entropy $\mathcal{E}$ as a function of dissipation α in the two-spin boson model, shown for different values of the Ising coupling K/ω_c and $\Delta_{1,2} = 0.1\omega_c$. Left panel: For an ohmic bath ($s = 1$) the rapid drop to zero around $\alpha_c \approx 0.25$ signifies the transition to the localized phase. The plateau for smaller dissipation indicates the loss of phase coherence at $\alpha \approx \alpha_c/2$ similar to the single spin-boson case. The inset shows larger values of K/ω_c where the (incoherent) plateau shrinks to a peak-like structure, indicating that coherence is lost only right at the phase transition. Right panel: For an subohmic bath ($s = 0.5$) the entanglement entropy $\mathcal{E}$ reaches a maximum at the phase transition (see also right panel of Fig. 13.2), and falls off continuously to both sides of the transition.

using NRG [165, 166, 129] and Quantum Monte-Carlo calculations [162]. Recently, it was realized that NRG is not well-suited to describe scaling correctly for $s < 1/2$ in the single spin-boson model [165]. Therefore, we only consider exponents in the range $1/2 \leq s < 1$.

We define the critical exponents describing the scaling of the magnetization as

$$\langle \sigma^z_{1,2} \rangle \sim |\Delta - \Delta_c|^\beta \tag{13.9}$$

$$\langle \sigma^z_{1,2} \rangle \sim |\varepsilon_{1,2}|^{1/\delta} \tag{13.10}$$

$$\langle \sigma^z_{1,2} \rangle \sim |K - K_c|^\zeta \,. \tag{13.11}$$

Mean-field values for the critical exponents are derived in Appendix D. There, we set up an effective spin action functional and employ a mean-field-like decoupling of the Ising interaction term: $\frac{K_r}{4}\hat{\sigma}^z_1\hat{\sigma}^z_2 \approx \frac{K_r}{4}[\hat{\sigma}^z_1\langle\sigma^z_2\rangle + \langle\sigma^z_1\rangle\hat{\sigma}^z_2]$. The main results of the derivation in Appendix D, namely the scaling exponents are displayed in Table 13.1.

Numerically, we investigate the cases $s = \{\frac{1}{2}, \frac{3}{4}, \frac{9}{10}\}$. After carefully determining the position of the phase transition, we keep all but one parameter fixed at their critical values, and study the scaling of the magnetization as a function of this remaining parameter. Typically, we find power law scaling over more than two orders of magnitude, and we find the exponents from simply fitting the slope in a log-log plot. We have checked that the extracted value of the exponent is independent on the position in the phase diagram where we cross the phase boundary. As an example, in Fig. 13.6, we show the scaling of $\langle\sigma^z_1\rangle$ as a function of $|K - K_c|$ (left panel) and as a function of ε (right panel). Different curves are for different values of the transverse field Δ, and we extract the value of $\zeta(s = \frac{1}{2}) = 0.5$, which is is perfect agreement with the mean-field prediction of $\zeta_{MF}(s = \frac{1}{2}) = 1/2$. In Table 13.1 we show a full comparison of the critical exponents derived in the mean-field approximation and

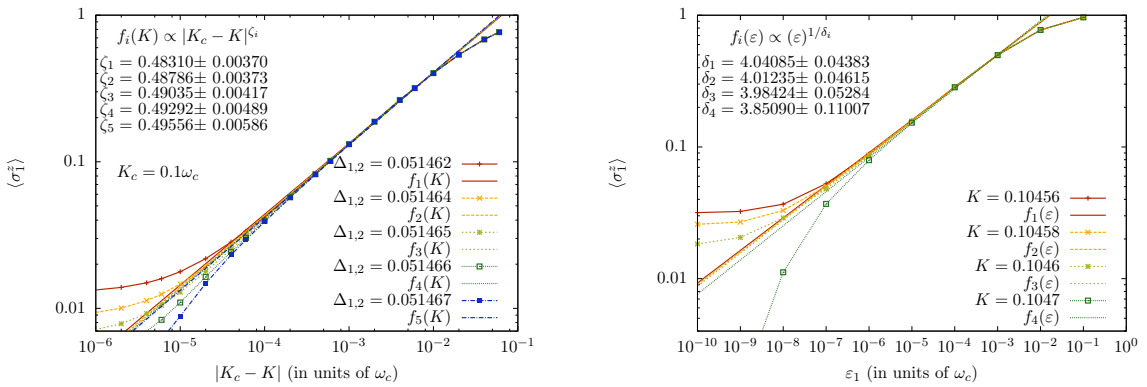

Figure 13.6: Scaling of magnetization at the phase transition in the subohmic system with $s = \frac{1}{2}$. Left panel: We fit $\langle \sigma_1^z \rangle$ as a function of the Ising interaction against a power-law $\langle \sigma_1^z \rangle \sim |K - K_c|^{\zeta}$, and find $\zeta = 0.5$. Right panel: We fit $\langle \sigma_1^z \rangle$ as a function of the bias $\varepsilon_{1,2}$ against a power-law $\langle \sigma_1^z \rangle \sim \varepsilon^{\frac{1}{\delta_i}}$, and find $\delta = 4$. Different lines represent fits using $f_i \propto |K - K_c|^{\zeta_i}$. Results of the fit and error bars for ζ_i (or δ_i), as well as the different values of $\Delta_{1,2}$ (or K) used, are shown in the plot.

Exponent	$s = \frac{1}{2}$	$s = \frac{3}{4}$	$s = \frac{9}{10}$
δ	4	10	40
δ_{MF}	3	7	19
ζ	0.5	0.2	0.1
ζ_{MF}	1/2	$1/6 \simeq 0.17$	$1/18 \simeq 0.06$
β	0.5	0.2	0.09
$\beta_{\mathrm{MF}}(\nu = 1/s)$	1/2	1/6	1/18
$\beta_{\mathrm{MF}}(\nu = 1/\sqrt{2(1-s)})$	1/4	$1/4\sqrt{2} \simeq 0.18$	$1/4\sqrt{5} \simeq 0.11$

Table 13.1: Comparison of critical exponents as predicted by the mean-field analysis in App. D $\{\delta_{\mathrm{MF}}, \zeta_{\mathrm{MF}}, \beta_{\mathrm{MF}}\}$ and as extracted from NRG $\{\delta, \zeta, \beta\}$.

extracted from our numerical renormalization group calculations. The agreement is good for the exponents ζ and β for all values of s (using the different expansions of ν as a function of s). For the exponent δ, however, the agreement is not so good in the cases $s = \{\frac{3}{4}, \frac{9}{10}\}$. Note that the trend is captured correctly and that δ diverges as $s \to 1$ which makes it increasingly hard to extract its value numerically.

13.4 Nonequilibrium Spin Dynamics

Let us now turn to the dissipative nonequilibrium dynamics of the two-spin boson model of Eq. (13.1). We will concentrate on the ohmic ($s = 1$) as well as the subohmic case of $s = \frac{1}{2}$. To access the system's rich dynamical behavior arising from the interplay of spin-spin and spin-bath interactions, we employ the time-dependent numerical renormalization group technique (TD-NRG) [66, 67] already introduced in Chap. 8. Using this extension of the standard bosonic numerical renormalization group [61, 53, 167] (see also Chap. 5), we are able to calculate the real-time evolution of an impurity observable as a reaction to a single sudden change of parameters. We note that a first dynamical study of the ohmic system in a very limited region of parameter space was given in Ref. [168].

As common to all applications of the numerical renormalization group method to bosonic quantum impurity models, we have to restrict the maximal number of bosonic degrees of freedom that are added in each step of the iterative diagonalization procedure performed within the NRG method. We have checked that this cutoff does not alter our results. We use the same NRG parameters as for the equilibrium calculations: A discretization parameter of $\Lambda = 1.4$, a total of $N_{b,0} = 599$ bosonic modes in the first iteration and $N_{b,N} = 6$ in the following ones, while keeping $N_{\mathrm{Lev}} = 200$ low-energy levels in each NRG iteration. For the TD-NRG calculations we have additionally averaged the real-time data using $N_z = 8$ independent NRG runs (for details on the z-trick averaging, see Sec. 10.2). In the following, we discuss a number of different nonequilibrium situations.

In Sec. 13.4.1, we show that TD-NRG results perfectly agree with the exact solution that is available for zero transverse field $\Delta_{1,2} = 0$, where the Hamiltonian only contains the z-component of the spin operators.

We elaborate in Sec. 13.4.2 on the breakdown of the Bloch-Redfield description, and provide more quantitative limits at which dissipation strength this method begins to fail.

In Sec. 13.4.3, we discuss the fascinating phenomenon of dynamical synchronization of the spin oscillations induced by the bath. Most importantly, this feature occurs even at weak spin-bath coupling and synchronization can thus be observed over many oscillation periods. It relies on the coherent exchange of bath excitations between the two spins, which gives rise to the bath induced part of the Ising interaction. The phenomenon cannot be observed in the commonly employed perturbative Bloch-Redfield master equation approach, where the backaction of the bath on the spins is neglected.

In Sec. 13.4.4, we investigate the spin dynamics for vanishing (renormalized) Ising coupling $K_r = 0$. Qualitatively, the system behaves like a single spin-boson model for $0 < \alpha < 1/2$, where it exhibits damped coherent oscillations. The quality factor of the oscillations, however, is smaller in the two-spin case as the damping is stronger. Yet most importantly, for larger values of α we find that the two spins remain delocalized for $K_r = 0$ up to a dissipation strength as large as $\alpha = 1.5$ in the ohmic case. The single spin-boson model, in contrast, becomes localized at $\alpha = 1$, where the spin remains frozen in its initial state.

In the first part of Sec. 13.4.4, we elaborate on the region $0 < \alpha < 1/2$, and use an approximation that is known to be equivalent to the Non-Interacting Blip Approximation (NIBA) [62, 141] in the single spin case. It allows us to understand the dynamics qualitatively. Then, in the remainder of Sec. 13.4.4, we focus on the generalized Toulouse point $\alpha = 1/2$ and $K_r = 0$, where $\langle\sigma^z_{1,2}(t)\rangle$ decays purely exponentially. We show that one obtains slightly different decay rates for the single and two-spin boson model. We qualitatively explain this difference by employing a bosonization mapping to a fermionic resonant level model. In the single spin case, the fermionic model can be solved exactly. For two spins, however, the fermionic model contains an additional interaction term that stems from the Jordan-Wigner transformation of the spins and impedes an exact solution.

We discuss the spin dynamics at large spin bath coupling in Sec. 13.4.5. Comparing the ohmic and subohmic cases, we find that while coherence is lost prior to localization in the ohmic system, the spins exhibit oscillations even inside the localized regime for a subohmic bath, a feature only recently discovered [160] in the single spin-boson system.

Finally, as presented in Sec. 13.4.6, an interesting situation arises if we prepare the spins in an antiferromagnetic initial state at a location in the phase diagram which corresponds to a localized (ferromagnetic) ground state. Following the spin's dynamics over time, we observe a non-trivial steady-state, where the spins are highly entangled with the bath while developing and maintaining coherence between the two antiferromagnetic spin states. We give a simple physical explanation for this behavior.

13.4.1 Decoherence Without Transverse Field

In this section, we discuss a specific case where one can exactly solve for the (non-trivial) dissipative spin dynamics of the two-spin boson model. We compare the exact solution to the TD-NRG results and find perfect agreement, which provides another validation of this powerful method in the strong coupling regime.

For vanishing transverse fields, $\Delta_{1,2} = 0$, the Hamiltonian of Eq. (13.1) takes the form

$$\hat{\mathcal{H}}[\Delta_{1,2}=0] = \sum_{j=1}^{2}\Big\{\frac{\hat{\sigma}^z_j}{2}\big[\varepsilon_j + \sum_{n>0}\lambda_n(\hat{a}^\dagger_n + \hat{a}_n)\big]\Big\} + \frac{K}{4}\hat{\sigma}^z_1\hat{\sigma}^z_2 + \sum_{n>0}\omega_n\left(\hat{a}^\dagger_n\hat{a}_n + \frac{1}{2}\right), \quad (13.12)$$

which only contains the z-component of the spin operators. Thus, the spin dynamics is non-trivial only if the initial state of the spins contains a transverse component (in the x or y-direction). For instance, spins that are initially polarized along the x-direction ($\langle\sigma^x_{1,2}(t=0)\rangle = -1$) will undergo damped oscillations in $\langle\sigma^x_{1,2}\rangle$ as exactly described by [169]

$$\langle\sigma^x_{1,2}(t)\rangle = -\cos\Big[\big(\varepsilon_{1,2} + \frac{K_r}{2}\big)t\Big]\cos\Big[\frac{Q_1(t)}{\pi}\Big]\exp\Big[\frac{-Q_2(t)}{\pi}\Big], \quad (13.13)$$

with functions $Q_1(t) = \int_0^\infty d\omega J(\omega)\sin\omega t$ and $Q_2(t) = \int_0^\infty d\omega J(\omega)[1-\cos\omega t]$. For an ohmic spectral density with exponential cutoff, they read [62]

$$Q_1(t) = 2\pi\alpha\tan^{-1}\omega_c t \quad (13.14)$$

$$Q_2(t) = \pi\alpha\ln[1+\omega_c^2 t^2]\,. \quad (13.15)$$

Note that Eq. (13.13) can also be derived using the polaron transformation of Sec. 13.2.2. In Fig. 13.7, we compare our TD-NRG results with this exact analytical prediction for bath exponents $s = \frac{1}{2}$ and $s = 1$, and we find perfect agreement between them.

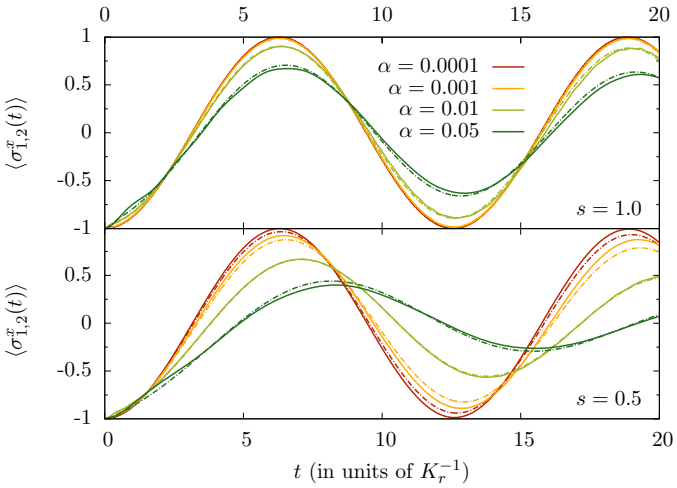

Figure 13.7: Comparison of $\langle \sigma^x_{1,2}(t) \rangle$ between exact solution of Eq. (13.13) (dashed) and TD-NRG result (solid) for different values of α and bath exponents $s = 1$ (upper) and $s = \frac{1}{2}$ (lower panel). Parameters used are $\varepsilon_{1,2} = \Delta_{1,2} = 0$, $K = 0$, $\omega_c = 1$, and α as specified in the inset.

13.4.2 Beating and Decoherence: Breakdown of Master Equation Description

In this Section, we compare the results from TD-NRG with those from the commonly employed Bloch-Redfield [108, 170] formalism at weak spin-bath coupling. We give quantitative limits on the applicability of this perturbative Markovian technique.

Let us briefly outline the Bloch-Redfield approach to dissipative spin dynamics. The time-evolution of the spin reduced density matrix $\rho_S = \mathrm{Tr}_B(\rho)$, where Tr_B denotes tracing out the bath degrees of freedom and ρ is the full density matrix of the spin-boson system, is given by the Bloch-Redfield equations

$$\dot{\rho}_{S,ab}(t) = -i\omega_{ab}\rho_{S,ab}(t) - \sum_{k,l} R_{abkl}\rho_{S,kl}(t)\,, \tag{13.16}$$

where $a, b, k, l = 1, \ldots, 4$ label the eigenstates (with eigenenergy E_a) of the free spin part of the Hamiltonian $\hat{\mathcal{H}}_S = \sum_{j=1}^{2}\left[\frac{\Delta_j}{2}\hat{\sigma}^x_j + \frac{\varepsilon_j}{2}\hat{\sigma}^z_j\right] + \frac{K}{4}\hat{\sigma}^z_1\hat{\sigma}^z_2$, and $\omega_{ab} = E_a - E_b$ are eigenenergy differences. For zero bias $\varepsilon_{1,2} = 0$, the eigenenergies are given by $E_{1,2} = \mp\Omega_-/2$ and $E_{3,4} = \mp\Omega_+/2$ with $\Omega_\pm = \sqrt{(\Delta_1 \pm \Delta_2)^2 + K^2/4}$. The relevant transition frequencies for which $\langle a|\hat{\sigma}^z_{1,2}|b\rangle \neq 0$, read $\omega_{41} = \omega_{23} = \Omega$ and $\omega_{42} = \omega_{13} = \delta$ with $\Omega = \frac{1}{2}(\Omega_+ + \Omega_-)$ and $\delta = \frac{1}{2}(\Omega_+ - \Omega_-)$. For nonzero bias $\varepsilon_{1,2} \neq 0$, one can easily diagonalize $\hat{\mathcal{H}}_S$ numerically for a specific choice of parameters.

The Redfield tensor R_{abkl} describes the effect of the bath onto the spin dynamics in the Born-Markov approximation [171]. The real part of R_{abkl} describes the damping induced by the bath, and the imaginary part the renormalization of the transition frequencies, wchi we expand up to second order in the spin-bath coupling.

The Redfield tensor is given by golden rule transition rates and reads

$$R_{abkl} = \delta_{bl} \sum_r \Gamma^{(+)}_{arrk} + \delta_{ak} \sum_r \Gamma^{(-)}_{lrrb} - \Gamma^{(+)}_{lbak} - \Gamma^{(-)}_{lbak} \,. \tag{13.17}$$

The golden rule rates at temperature $T = 1/\beta$ are calculated to

$$\Gamma^{(\pm)}_{lbak} = \frac{\Lambda_{lbak} \tilde{J}(\omega_{ij})}{4} [\coth(\beta\hbar\omega_{ij}/2) \mp 1] \tag{13.18}$$

$$+ \frac{i\Lambda_{lbak}}{2\pi} \mathcal{P} \int_0^\infty d\omega \frac{\tilde{J}(\omega)}{\omega^2 - \omega_{ij}^2} [\coth(\beta\hbar\omega/2)\omega_{ij} \mp \omega] \,, \tag{13.19}$$

where $ij = lb$ for the plus rate and $ij = ak$ for the minus rate. Here, we have defined the matrix element

$$\Lambda_{lbak} = \sigma^z_{1,lb}\sigma^z_{1,ak} + \sigma^z_{1,lb}\sigma^z_{2,ak} + \sigma^z_{2,lb}\sigma^z_{1,ak} + \sigma^z_{2,lb}\sigma^z_{2,ak} \tag{13.20}$$

and a spectral density that is antisymmetrically continued to negative frequencies $\tilde{J}(\omega) = \mathrm{sign}(\omega)\pi\alpha|\omega|^s\theta(\omega_c - |\omega|)$. For a Drude bath cutoff $J(\omega) = 2\pi\alpha\omega^s/(1 + \frac{\omega^2}{\omega_c^2})$ the principal part integral can be performed analytically [170, 172] and at zero temperature the rates become

$$\mathrm{Re}\Gamma^{(\pm)}_{lbak} = \frac{\Lambda_{lbak}}{4} J(\omega_{ij}) \tag{13.21}$$

$$\mathrm{Im}\Gamma^{(\pm)}_{lbak} = \frac{\Lambda_{lbak}}{4\pi} \frac{\pi\alpha\omega_{ij}\omega_c^2}{\omega_{ij}^2 + \omega_c^2} \Big[2\ln\frac{\omega_c}{\omega_{ij}} \mp \frac{\pi\omega_c}{\omega_{ij}} \Big] \,, \tag{13.22}$$

where again $\omega_{ij} = \omega_{ak}$ for the plus rate and $\omega_{ij} = \omega_{lb}$ for the minus rate. Note that the real part in Eq. (13.21) vanishes unless $\omega_{ij} > 0$.

In the Redfield approach, the total density matrix is assumed to always factorize into a spin and a bath part. Further, by taking the long time limit in Eq. (13.17), any reversible energy exchange between spins and bath, and thus any backaction of the bath on the spins is neglected. Therefore, the Redfield approach does not capture the bath induced non-dissipative spin-spin interaction $K_r = -4\alpha\omega_c/s$ correctly. As we will discuss in Sec. 13.4.3, this has the important consequence that the phenomenon of a bath induced dynamical synchronization of the spin oscillations could not be observed within the Redfield approach.

In the following, we want to focus on a symmetric setup of the two spin system ($\Delta_1 = \Delta_2 \equiv \Delta$) and zero bias $\varepsilon_{1,2} = 0$. In Fig. 13.8 we compare TD-NRG results for $\langle\sigma^z_{1,2}(t)\rangle$ with Bloch-Redfield solutions given in Eq. (13.16) for an ohmic and a subohmic bath. Both results agree for very weak spin-bath coupling $\alpha \ln \frac{\omega_c}{\Delta} < 0.01$. However, already at $\alpha \ln \frac{\omega_c}{\Delta} = 0.01$ we find significant differences, which are more pronounced in the subohmic case, and grow with the coupling strength. Even in the absence of direct Ising coupling term $K = 0$, we observe beatings in the oscillations due to the bath induced Ising interactions. In Fig. 13.9 we show results for a system with a direct Ising coupling, where the beatings are stronger. Here, we find significant differences between the TD-NRG and Bloch-Redfield results to occur already for $\alpha = 0.005$ or $\alpha \ln \frac{\omega_c}{\Delta_{1,2}} \approx 0.01$.

In summary, since the Redfield approach does not correctly account for the bath induced Ising interaction, its breakdown occurs not just when $\alpha \ln \frac{\omega_c}{\omega_{ij}} \sim 1$, but already for $\alpha\omega_c \sim \omega_{ij}$. Here, ω_{ij} is a (nonzero) transition frequency of the system which is of the order $\{\Omega, \delta\}$. Since $\omega_c \gg \omega_{ij}$ the breakdown of the master equation description occurs for much smaller values of α compared to the single spin case, where it takes place when $\alpha \ln \frac{\omega_c}{\omega_{ij}} \approx 1$.

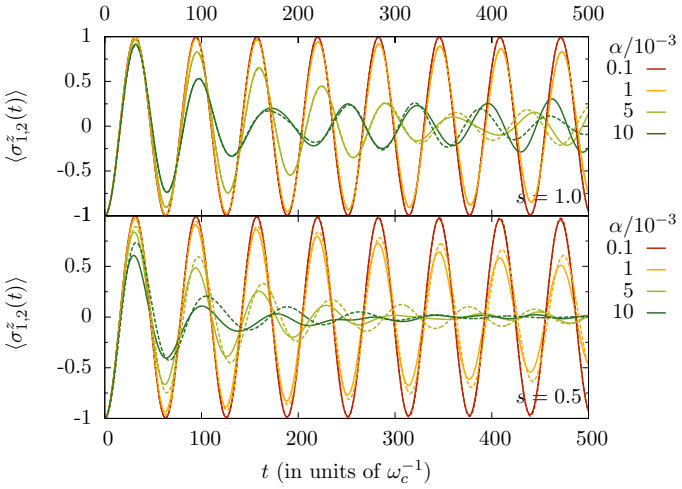

Figure 13.8: Comparison of the results for $\langle\sigma^z_{1,2}(t)\rangle$ from TD-NRG (solid) and Bloch-Redfield approach (dashed) for $K = \varepsilon_{1,2} = 0$, $\Delta_{1,2} = 0.1\omega_c$ in the perturbative regime $\alpha \ln \frac{\omega_c}{\Delta} \ll 1$. Upper (lower) part shows the case $s = 1$ ($s = \frac{1}{2}$). Deviations are visible already for $\alpha \ln \frac{\omega_c}{\Delta} = 0.01$. Note the beatings in oscillations due to the bath induced Ising coupling.

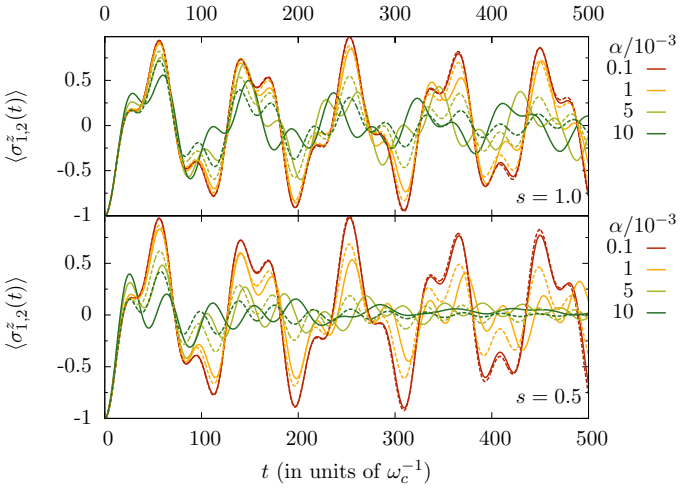

Figure 13.9: Comparison of results for $\langle\sigma^z_{1,2}(t)\rangle$ obtained with TD-NRG (solid) and Bloch-Redfield approach (dashed) for $K = 0.2\,\omega_c$, $\varepsilon_{1,2} = 0$. Other parameters as in Fig. 13.8.

13.4.3 Synchronization of Spin Dynamics

In this Section, we address how the coupling of spins to a common bath can be employed to obtain a *dynamical synchronization* of spin oscillations. Notably, this feature occurs already at weak spin-bath coupling, where the bath induced decoherence is small. It provides an alternative technique to synchronize the dynamics of a two-spin system, when a strong direct coupling of the spins is unavailable.

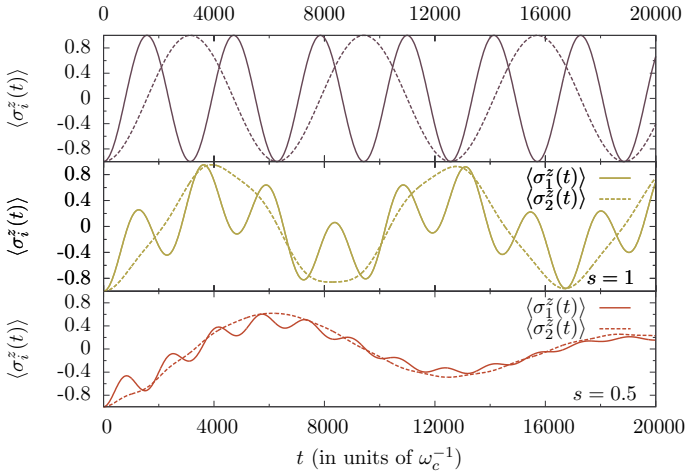

Figure 13.10: Synchronization of two spins with different spin-flip terms $\Delta_2 = \frac{1}{2}\Delta_1 = 10^{-3}\omega_c$ by weak coupling to a common bath. There is no direct coupling between the spins $K = 0$. The upper part of the figure shows the uncoupled case $\alpha = 0$. The middle part shows the ohmic case and the lower part the subohmic one with $s = \frac{1}{2}$. We use the same strength $\alpha = 8 \cdot 10^{-4}$ for the different bath dispersions, which lies in the perturbative regime: $\alpha \ln \frac{\omega_c}{\Delta_2} = 6{\cdot}10^{-3} \ll 1$.

Let us start with two free and uncoupled spins ($K = \alpha = 0$) that are driven by different tunneling amplitudes, say $\Delta_1 = 2\Delta_2$. As shown in the upper part of Fig. 13.10, the spins will then undergo undamped Rabi oscillations with frequencies Δ_1 and Δ_2, respectively. We now consider a weak coupling to the bath in the perturbative regime where $\alpha \ln \frac{\omega_c}{\Delta_{1,2}} \ll 1$. The frequency corrections in $\Delta_{1,2}$ are small in this case. However, the bath induced Ising interaction $K_r = -4\alpha\omega_c/s$ can still be comparable to $\Delta_{1,2}$, because it scales with the (large) bath cutoff frequency ω_c. In this case, where K_r and $\Delta_{1,2}$ are of the same order of magnitude, the bath is capable of synchronizing the spin oscillations as depicted in the two lower parts of Fig. 13.10 for an ohmic (middle) and a subohmic bath with $s = 1/2$ (bottom). The synchronization is more complete for the subohmic system, since there is an increased number of slow oscillator modes present and the induced Ising interaction, which scales as s^{-1}, is twice as large for the same value of α.

The two oscillation frequencies $\{\Omega, \delta\}$ that occur in Fig. 13.10 can be calculated from the free spin dynamics of Eq. (13.1) if we set the Ising interaction K equal to its renormalized value $K = K_r = -4\alpha\omega_c/s$.

For zero bias $\varepsilon_{1,2} = 0$, the free spin part of Eq. (13.1) reads $\hat{\mathcal{H}}_S = \sum_{j=1}^{2} \frac{\Delta_j}{2}\hat{\sigma}_j^x + \frac{K}{4}\hat{\sigma}_1^z\hat{\sigma}_2^z$ with eigenvalues $E_{1,2} = \mp\Omega_-/2$ and $E_{3,4} = \mp\Omega_+/2$, where $\Omega_\pm = \sqrt{(\Delta_1 \pm \Delta_2)^2 + K^2/4}$. We can find the spin dynamics from $\langle\sigma_{1,2}^z(t)\rangle = \mathrm{Tr}[\rho_S(t)\sigma_{1,2}^z]$ where the spin density matrix $\rho_S(t)$

evolves in time according to the von-Neumann equation of motion $\dot{\rho}_S = -i[H_S, \rho_S]$. With initial condition $\rho_S(0) = |\downarrow\downarrow\rangle\langle\downarrow\downarrow|$, we find

$$\begin{aligned}\langle\sigma^z_{1,2}\rangle &= \sum_{a,b} \rho_{S,ab}(0) e^{-i\omega_{ab}t} \langle b|\hat{\sigma}^z_{1,2}|a\rangle \\ &= 2A^{(1,2)}_\Omega \cos\Omega t + 2A^{(1,2)}_\delta \cos\delta t\,, \end{aligned} \tag{13.23}$$

where a, b label the eigenstates of $\hat{\mathcal{H}}_S$ and $\omega_{ab} = E_a - E_b$ are the transition frequencies. They obey $\omega_{41} = \omega_{23} = \Omega$ and $\omega_{42} = \omega_{13} = \delta$. The two oscillation frequencies that appear in Fig. 13.10 are thus given by $\Omega = \frac{1}{2}(\Omega_+ + \Omega_-)$ and $\delta = \frac{1}{2}(\Omega_+ - \Omega_-)$. For the other transitions, we find that the matrix element $\langle b|\sigma^z_{1,2}|a\rangle$ is equal to zero. The two oscillation amplitudes are given by

$$A^{(1,2)}_\Omega = \rho_{S,41}(0)\langle 1|\hat{\sigma}^z_{1,2}|4\rangle + \rho_{S,23}(0)\langle 3|\hat{sigma}^z_{1,2}|2\rangle \tag{13.24}$$

$$A^{(1,2)}_\delta = \rho_{S,42}(0)\langle 2|\hat{\sigma}^z_{1,2}|4\rangle + \rho_{S,13}(0)\langle 3|\hat{sigma}^z_{1,2}|1\rangle\,. \tag{13.25}$$

They are shown in Fig. 13.11 as a function of Ising coupling K, and are responsible for the synchronization phenomenon. At $K = 0$, the first spin oscillates with frequency $\Omega(K = 0) = \Delta_1$ and $A^{(1)}_\Omega = 1$. The second spin oscillates with frequency $\delta(K = 0) = \Delta_2$ and $A^{(2)}_\delta = 1$. As we increase K, the amplitude $A^{(1)}_\delta$ increases, while $A^{(1)}_\Omega$ decreases, and $A^{(2)}_{\Omega,\delta}$ remains almost the same. For large $K \gg \Delta_{1,2}$ both spins oscillate with frequency $\delta \simeq 2\Delta_1\Delta_2/K$.

In fact, we can derive analytical expressions for $A^{(1,2)}_{\Omega,\delta}$ if we solve the Heisenberg equation of motion for $\sigma^z_{1,2}(t) = i[\hat{\mathcal{H}}_S, \sigma^z_{1,2}(t)]$ in Laplace space [155]. One finds that

$$\langle\sigma^z_1(\lambda)\rangle = \frac{\lambda(\frac{K^2}{4} + \Delta_2^2 + \lambda^2)}{(\lambda^2 + \Omega^2)(\lambda^2 + \delta^2)} \tag{13.26}$$

$$\langle\sigma^z_2(\lambda)\rangle = \frac{\lambda(\frac{K^2}{4} + \Delta_1^2 + \lambda^2)}{(\lambda^2 + \Omega^2)(\lambda^2 + \delta^2)}\,, \tag{13.27}$$

which yields Eq. (13.23) in real space. We identify the amplitudes $A^{(1,2)}_{\Omega,\delta}$ as the respective residues of Eqs. (13.26) and (13.27) at Ω and δ. Explicitly, they read

$$A^{(1)}_{\Omega,\delta} = \frac{\pm[-K^2 + 4(\Delta_1^2 - \Delta_2^2)] + w}{4w} \tag{13.28}$$

$$A^{(2)}_{\Omega,\delta} = \frac{\pm[-K^2 + 4(\Delta_2^2 - \Delta_1)^2] + w}{w}\,, \tag{13.29}$$

where $w = \sqrt{[K^2 + 4(\Delta_1^2 + \Delta_2^2)]^2 - 64\Delta_1\Delta_2}$ and the upper sign relates to $A^{(1,2)}_\Omega$. Synchronization sets in when $A^{(1)}_\Omega \simeq A^{(1)}_\delta$, which occurs for an Ising interaction strength of

$$K = 2\sqrt{|\Delta_1^2 - \Delta_2^2|}\,. \tag{13.30}$$

The damping rates of the oscillation amplitudes are proportional to $J(\Omega)$ and $J(\delta)$, respectively. Since $J(\omega) \sim \alpha\omega^s$ they are small for the parameters chosen in Fig. 13.10, and the synchronized oscillations can be observed over many periods.

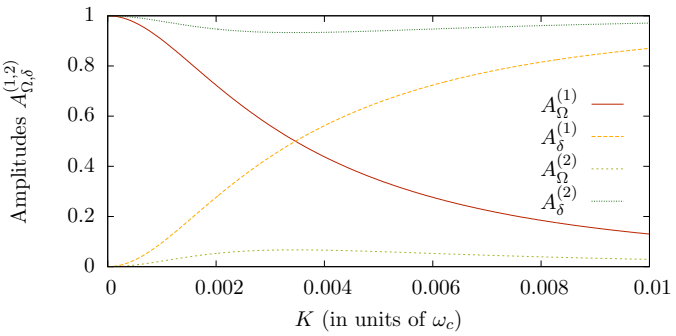

Figure 13.11: Oscillation amplitudes $A^{(1,2)}_{\Omega,\delta}$ as a function of Ising coupling K. The two spin expectation values $\langle\sigma^z_{1,2}(t)\rangle$ evolve according to Eq. (13.23).

We like to emphasize that the synchronization effect cannot be seen in the Bloch-Redfield master equation treatment, which does not correctly account for the bath induced Ising interaction K_r. The damping rates in Fig. 13.10, however, agree with the ones calculated with the perturbative Redfield approach. In the next Section 13.4.2, we analyze the breakdown of the master equation in more detail.

In summary, the bath induced Ising interaction scales with the bath cutoff frequency like $K_r \sim \alpha\omega_c$ whereas the bath induced damping is proportional to $\alpha\Omega^s$ and $\alpha\delta^s$, where $\{\Omega, \delta\}$ are spin transition frequencies. A common bath can thus synchronize spin oscillations at weak coupling if the bath cutoff frequency is large $\omega_c \gg \Omega, \delta$.

13.4.4 Vanishing Ising Interaction $K_r = 0$: Similarities and Differences with the Single Spin-Boson Model

In this Section, we investigate the spin dynamics along the line $K_r = 0$ in the phase diagram, i.e. for a vanishing renormalized Ising interaction (see Fig. 13.2). At first sight, one might expect that the dynamics would be identical to that of two uncoupled spin-boson systems. However, as can be seen from the perturbative treatment in Sec. 13.4.2 already, the two spins do not decouple from each other even to linear order in α, and the golden rule rates in Eq. (13.19) contain the terms $\sigma^z_{1,lb}\sigma^z_{2,ak}$ and $\sigma^z_{2,lb}\sigma^z_{1,ak}$. Qualitatively though, as displayed in Fig 13.12, the spin dynamics of the single and two-spin boson models agree for $K_r = 0$ and small α.

In the ohmic case (see left panel of Fig. 13.12), we observe a crossover from damped coherent oscillations at $0 \leq \alpha < 1/2$ to incoherent behavior at $\alpha \geq 1/2$ in both models. In the two-spin case, however, we find stronger damping due to the terms proportional to $\sigma^z_1\sigma^z_2$ mentioned above. This results in a smaller quality factor of the oscillations. We compare the quality factor of oscillations for the single and two-spin boson system computed with TD-NRG and Bloch-Redfield in Fig. 13.13. A detailed discussion of the dynamics at the special Toulouse point $\alpha = 1/2$ is given separately in Sec. 13.4.4.

If we further increase α, we surprisingly observe that the two-spin boson model does not enter the localized phase (for $K_r = 0$). Unlike the single spin case, the two spins remain delocalized up to values of $\alpha > 1$. Our time-dependent numerical results in Fig. 13.12 show that $\langle\sigma^z_{1,2}\rangle$ relax to zero even for values as large as $\alpha = 1.5$. We note that this is in agreement

with the NRG phase diagram in the right panel of Fig. 13.2, which shows that the position of the localization phase transition converges towards the line $K_r = 0$ from the side where $K_r < 0$.

We show the same comparison between single and two-spin boson model for a subohmic bath with $s = 1/2$ in the right panel of Fig. 13.12. As before, for increasing dissipation the coherence of the spin oscillations is lost more rapidly, but the system does not localize along $K_r = 0$. Again, this is in agreement with the NRG phase diagram of Fig. 13.2.

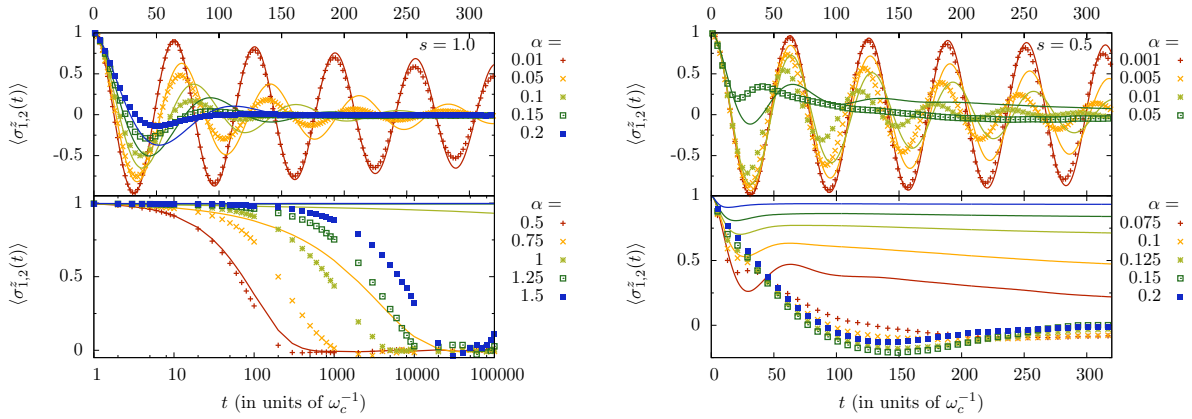

Figure 13.12: Comparison of spin dynamics between the single spin-boson (lines) and two-spin boson model with $K_r = 0$ (dots) for ohmic ($s = 1$, left panel) and subohmic ($s = 0.5$, right panel) spin baths. Different curves correspond to different values of dissipation strength α. Ising interaction is chosen accordingly to be $K = 4\alpha\omega_c/s$. Other parameters are $\Delta_{1,2} = \Delta = 0.1\,\omega_c$, $\varepsilon_{1,2} = \varepsilon = 0$. The upper panels show that the spin dynamics coincide for weak dissipation (up to $\alpha \lesssim 0.01$ for the ohmic and $\alpha \lesssim 0.001$ for the subohmic bath). For larger α ($\alpha \gtrsim 0.01$ for $s = 1$ and $\alpha \gtrsim 0.001$ for $s = 0.5$) the two-spin oscillations have slightly larger frequencies and are much stronger damped. The lower panel show the case of strong dissipation $\alpha \geq 1/2$ for $s = 1$ (and $\alpha \geq 0.1$ for $s = 0.5$ equivalently). Both systems display incoherent decay. For even larger values of α, we observe that, in contrast to the single spin-boson model which localizes at $\alpha_c = 1$ in the ohmic case and $\alpha_c = 0.107$ in the subohmic case $s = 1/2$, the two-spin dynamics remain delocalized along $K_r = 0$, in agreement with the phase diagram of Fig. 13.2.

In the following, we first derive in Sec. 13.4.4 a decoupling approximation that is equivalent to the well-known Non-Interacting Blip Approximation (NIBA) for the single spin-boson dynamics. In this approximation the spins decouple completely for $K_r = 0$. It allows us to understand the spin dynamics along the line $K_r = 0$ qualitatively. In contrast to the case of the single spin-boson model, however, the approximation does not give quantitatively correct results for two spins, not even to linear order in α. The reason is that dissipative second-order processes that involve both spins [see Eqs. (13.20) and (13.21)] are neglected.

Then, in Sec. 13.4.4 we focus on the so-called Toulouse point $\alpha = 1/2$ of the ohmic model. For a single spin, one can solve for the dynamics exactly and $\langle\sigma^z(t)\rangle$ exhibits pure exponential decay. The exact solution can most easily be derived by employing a bosonization mapping to a non-interacting fermionic resonant level model. In the two-spin case, we explicitly show that this mapping does not lead to a non-interacting fermionic model, which hence cannot be

solved exactly. Further, our numerical results prove that the two-spin dynamics at $\alpha = 1/2$ differs slightly from the single spin case. We associate this with the influence of the retarded part of the bath induced Ising interaction which is still present even at $K_r = 0$ [see also Eq. (D.4)].

Weak Dissipation: The Non-Interacting Blip Approximation (NIBA)

In this Section, we derive a decoupling approximation that allows us to qualitatively understand the spin dynamics for $K_r = 0$, but not necessarily small α. In this approximation, the two spins decouple completely for $K_r = 0$, and their Heisenberg equations of motion are identical to the ones of the single spin-boson model in the well-known Non-Interacting Blip Approximation (NIBA) [141].

Our starting point is to investigate the dynamics is the polaron transformed Hamiltonian in Eq. (13.4). For zero detuning and at $K_r = 0$ it reduces to

$$\tilde{\mathcal{H}} = \sum_n \omega_n \left(\hat{a}_n^\dagger \hat{a}_n + \frac{1}{2} \right) + \sum_{j=1}^{2} \frac{\Delta_j}{2} (\hat{\sigma}_j^+ e^{i\hat{\Omega}} + \text{h.c.}) \tag{13.31}$$

where $\hat{\Omega} = -i \sum_n \frac{\lambda_n}{\omega_n} (\hat{a}_n^\dagger - \hat{a}_n)$. The Heisenberg equation of motion for $\hat{\sigma}_j^z(t)$ with $j = 1, 2$ reads

$$\dot{\hat{\sigma}}_j^z(t) = -i\Delta_j \hat{\sigma}_j^+(t) e^{i\hat{\Omega}(t)} + \text{h.c.}\,. \tag{13.32}$$

It contains the elements $\hat{\sigma}_j^\pm(t)$ which are given by

$$\hat{\sigma}_j^+(t) = -\frac{i\Delta_j}{2} \int_{-\infty}^{t} ds \hat{\sigma}_j^z(s) e^{-i\hat{\Omega}(s)}\,, \tag{13.33}$$

and $\hat{\sigma}_j^- = (\hat{\sigma}_j^+)^*$. Inserting Eq. (13.33) in Eq. (13.32) yields

$$\dot{\hat{\sigma}}_j^z(t) = -\frac{\Delta_j^2}{2} \int_{\infty}^{t} ds [\hat{\sigma}_j^z(s) e^{i\hat{\Omega}(t)} e^{-i\hat{\Omega}(s)} + \text{h.c.}] \tag{13.34}$$

Note that the two spins are still coupled via the (time-dependent) bath operator $\hat{\Omega}(t)$. This coupling is the retarded part of the bath induced Ising interaction that we have seen already in the spin effective action of Eq. (D.4). If we neglect this interaction, the two spins decouple from each other.

More formally, we employ two approximations which are known to be equivalent to the famous Non-Interacting Blip Approximation (NIBA) in the single spin case [141]. First, we assume that the bath evolves freely $\hat{a}_n(t) = \hat{a}_n(0) e^{-i\omega_n t}$, neglecting any backaction of the bath on the spins. The reduced density matrix of the bath remains unaffected by the spins. Second, we trace out the bath degrees of freedom in a weak-coupling sense

$$\text{Tr}_B[e^{i\hat{\Omega}(t)} e^{-i\hat{\Omega}(s)}] = \exp\Big\{ \frac{1}{\pi} \big[iQ_1(t-s) - Q_2(t-s) \big] \Big\}\,, \tag{13.35}$$

which contains the bath correlation functions $Q_1(t) = \int_0^\infty d\omega J(\omega) \sin \omega t$ and $Q_2(t) = \int_0^\infty d\omega J(\omega)[1 - \cos \omega t]$. As a result, the two spins are now completely decoupled from each other and their dynamics is described by

$$\dot{\hat{\sigma}}_j^z(t) = -\Delta_j^2 \int_{\infty}^{t} ds \Big\{ \hat{\sigma}_j^z(s) \cos\left[\frac{Q_1(t-s)}{\pi} \right] e^{-Q_2(t-s)/\pi} \Big\}\,. \tag{13.36}$$

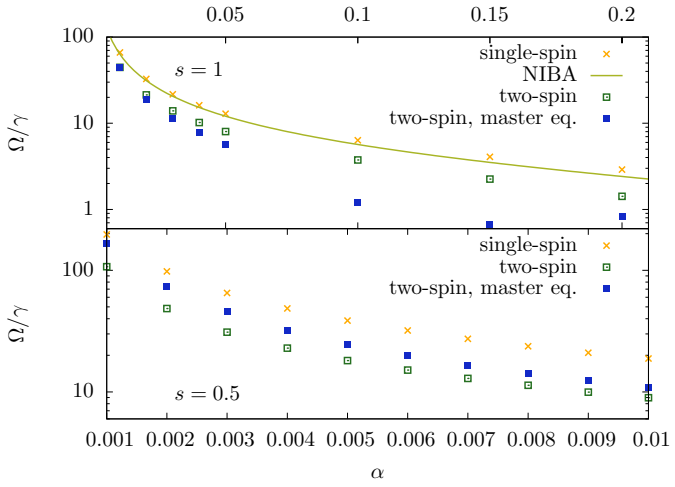

Figure 13.13: Quality factor of oscillations in the ohmic ($s = 1$, upper panel) and subohmic ($s = 0.5$, lower panel) single and two-spin boson models. TD-NRG results for the single (two-spin) boson model are shown as crosses (open squares). Quality factors derived from the Bloch-Redfield approach (see Sec. 13.4.2) are displayed as filled squares. The solid line denotes the quality factor derived from the NIBA approximation of Eq. (13.36).

Eq. (13.36) is known to describe the dynamics of the single spin-boson model in the famous Non-Interacting Blip Approximation (NIBA) [62, 141]. It can readily be solved by Laplace transformation. We refer to Refs. [62] and [108] for details.

In Fig. 13.13, we present a comparison of the quality factor of the oscillations Ω/γ for the single and two-spin boson systems as computed by TD-NRG and Bloch-Redfield. It is obtained by fitting the numerical results to the function $\langle\sigma^z_{1,2}(t)\rangle = e^{-\gamma t}\cos(\Omega t)$. In the ohmic case, we also include the prediction from the NIBA, which agrees with the TD-NRG results of the single spin-boson model (cf. Sec. 12.4.1). In general, we observe that the quality factor is smaller for the two-spin system. The Bloch-Redfield approach yields accurate results only in the ohmic case for small α. It fails completely in the subohmic case due to the increased spectral weight of slow oscillator modes, even for weak dissipation.

If we increase the dissipation strength further to values $\alpha > 1/2$, we observe an important difference between the single and the two-spin boson model. The two-spin boson model does not enter a localized phase for increasing values of α along the line $K_r = 0$.

For an ohmic bath, spin transitions occur even for a dissipation constant as large as $\alpha \geq 1.5$. This is in stark contrast to the single ohmic spin-boson model, which displays a localization phase transition at a critical dissipation strength of $\alpha_c = 1 + \mathcal{O}(\frac{\Delta}{\omega_c})$. This explicitly shows the breakdown of the approximations that lead to Eq. (13.36) for stronger coupling α.

In the subohmic case, the NIBA cannot be justified and erroneously yields localization for all $\alpha > 0$ [62], while TD-NRG results for the single spin-boson model [160] show that the system remains delocalized up to a finite critical value of α. Again, we find in Fig. 13.12 that unlike the single spin-boson system, the two-spin boson model always remains delocalized for $K_r = 0$.

We finally want to emphasize that the NIBA in the single spin-boson model breaks down

Δ/ω_c	a_i	$\sigma(a_i)$	b_i	$\sigma(b_i)$
0.002	1.03	0.03	2.54	0.26
0.004	0.93	0.02	1.81	0.10
0.006	0.84	0.02	1.64	0.06
0.01	0.76	0.01	1.56	0.04
0.02	0.71	0.01	1.45	0.04
0.04	0.66	0.01	1.20	0.04
0.06	0.64	0.01	0.94	0.04
0.1	0.61	0.01	0.72	0.01

Table 13.2: Fit parameters for single spin-boson model a_i and two-spin boson model b_i with standard error $\sigma(a_i)$ and $\sigma(b_i)$, for different values of Δ/ω_c, or $\gamma = \pi\Delta^2/2\omega_c$. We fit the TD-NRG results to an exponential decay function, which reads $f_i(t) = \exp[-a_i\gamma t]$ for the single spin-boson model. In the two spin-case we use the same function with a_i replaced by b_i.

for finite bias ε [108]. Thus, it cannot be applied to the two-spin problem away from the line $K_r = 0$, since the Ising interaction acts as a mutual bias between the spins. One common approach is to account for the interblip correlations up to first order in the spin-bath coupling α [108, 154]. This procedure is equivalent to the perturbative Redfield approach that we have discussed in Sec. 13.4.2.

Toulouse Point: Relation to the Single Spin Case

In this Section, we investigate the dynamics of the ohmic two-spin boson model at the special parameter point $K_r = 0$ and $\alpha = 1/2$.

It is well-known that one can map the ohmic single spin-boson Hamiltonian in the scaling limit $\Delta/\omega_c \ll 1$ onto a fermionic resonant level model using bosonization and refermionization techniques (see Sec. 12.4.2 or Ref. [62], for example). The fermionic model describes a localized level (dot) that is coupled via tunneling to a lead of free spinless fermions. In general the resulting model contains a Coulomb interaction term between the fermions on the dot and the ones in the lead. At the special (Toulouse) point of $\alpha = 1/2$, however, this interaction vanishes, and the fermionic model can be solved exactly, also in nonequilibrium situations [135, 173, 174].

For a spin that is initially polarized along the z-direction, one finds purely exponential relaxation for $t > 0$ (and $\varepsilon = 0$)

$$\langle\sigma^z(t)\rangle = \exp[-\gamma t] \tag{13.37}$$

with decay rate $\gamma = \pi\Delta^2/2\omega_c$. It is worth noting that the NIBA predicts the same behavior, since it becomes exact at the Toulouse point of the single spin-boson model [62].

To once more prove the validity of the TD-NRG method in this strong coupling regime, we compare in Fig. 13.14 our numerical results for a single spin-boson model with the exact solution of Eq. (13.37). We observe that the decay is indeed purely exponential, and the decay rate is given by $\gamma = \frac{\pi\Delta^2}{2\omega_c}$ in the scaling limit $\Delta/\omega_c \to 0$ (see Table 13.2).

From Eq. (13.36), we expect a similar behavior for the two-spin boson model at the (generalized) Toulouse point $K_r = 0$ and $\alpha = 1/2$. Indeed, as shown in Fig. 13.15, we observe

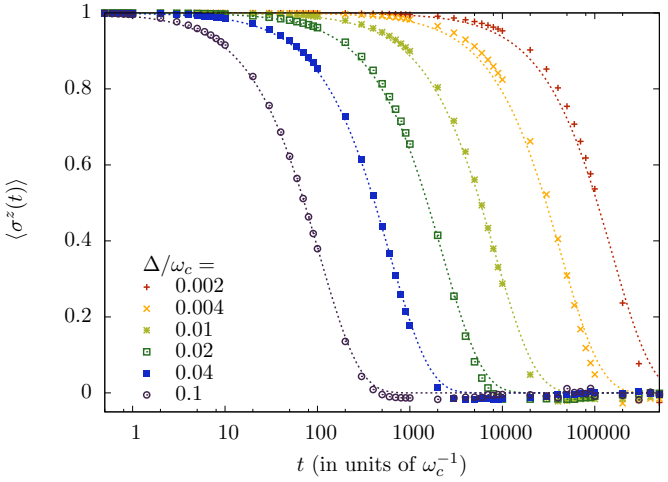

Figure 13.14: Exponential decay of $\langle\sigma^z(t)\rangle$ at the Toulouse point $\alpha = 1/2$ in the single spin-boson model. Symbols are TD-NRG results for different tunneling amplitudes Δ/ω_c which result in different decay rates $\gamma = \frac{\pi\Delta^2}{2\omega_c}$. Solid lines are fit with $f_i(t) = \exp[-a_i\gamma t]$ using fit parameters a_i given in Table 13.2.

that $\langle\sigma^z_{1,2}(t)\rangle$ decay purely exponentially in the two spin case as well. The decay rates of single and two spin models, however, are slightly different. We find in Table 13.2 that the decay rate of the two-spin boson model is about twice as large as the decay rate for the single spin-boson system $b_i/a_i \approx 2$ for the same value of Δ/ω_c. The difference in the two decay rates is, again, due to the retarded part of the bath induced Ising interaction neglected in the derivation to Eq. (13.36). We will qualitatively explain the factor two difference below, using a mapping to a fermionic resonance level model.

One might ask whether the two-spin boson model can also be solved exactly via the bosonization mapping to a fermionic resonant level model. For two spins, however, it turns out that the fermionic model remains interacting at the Toulouse point, and thus cannot be solved exactly. As we show in detail in Appendix E, the (additional) interaction term is proportional to the tunneling elements $\Delta_{1,2}$, which describe tunneling between dot and lead in the fermionic model. Since we are interested in a solution that is non-perturbative in $\Delta_{1,2}$ we cannot treat this additional term as a weak perturbation. In the fermionic language, however, we can qualitatively understand the factor two difference in the decay rates of the single and two-spin boson models (see Table 13.2).

Specifically, the ohmic two-spin boson Hamiltonian of Eq. (13.1) can be mapped to a resonant level model with two energy levels on the dot. As we derive in Appendix E, the mapping becomes exact in the scaling limit $\Delta_{1,2}/\omega_c \to 0$ [62]. The resulting fermionic model

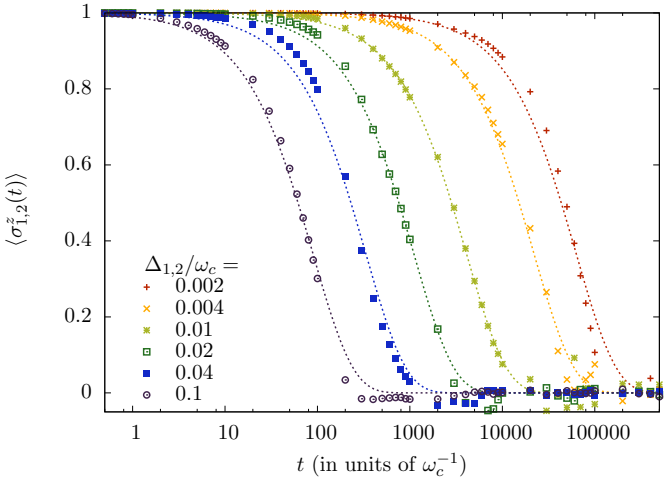

Figure 13.15: Exponential decay of $\langle\sigma^z_{1,2}(t)\rangle$ at the generalized Toulouse point $K = 2\omega_c$, $\alpha = 1/2$ in the two-spin boson model. Symbols are TD-NRG results for different tunneling amplitudes $\Delta_{1,2}/\omega_c$, which result in different decay rates $\gamma_{1,2} = \pi\Delta^2_{1,2}/(2\omega_c)$. Since $\Delta_1 = \Delta_2$, we observe $\gamma_1 = \gamma_2$. Solid lines are fit of $f_i(t) = \exp[-b_i\gamma t]$ with fit parameters b_i given in Table 13.2.

is described by the Hamiltonian

$$\begin{aligned}\hat{\mathcal{H}}_{\rm RL} =& v_F \sum_{k>0} k\hat{c}^\dagger_k\hat{c}_k + V\sum_{j=1}^{2}[\hat{d}^\dagger_j\psi(0) + \text{h.c.}] - V\left[(1-i)\hat{n}_1\hat{d}^\dagger_2\psi(0) + (1+i)\hat{n}_2\hat{d}^\dagger_1\psi(0) + \text{h.c.}\right] \\ &+ \sum_{j=1}^{2}\varepsilon_j\hat{d}^\dagger_j\hat{d}_j + 2U\sum_{j=1}^{2}\left(\hat{d}^\dagger_j\hat{d}_j - \frac{1}{2}\right) : \psi^\dagger(0)\psi(0) : + K_{\rm RL}\left(\hat{d}^\dagger_1\hat{d}_1 - \frac{1}{2}\right)\left(\hat{d}^\dagger_2\hat{d}_2 - \frac{1}{2}\right).\end{aligned} \tag{13.38}$$

Here, $\hat{c}_k$ annihilates a spinless fermion of momentum k and energy $\omega_k = v_F k$ in the lead (v_F is the Fermi velocity), and one defines $\psi(0) = L^{-1/2}\sum_k \hat{c}_k$, where L is the length of the lead. The colons denote normal ordering $:\psi^\dagger(0)\psi(0): = \psi^\dagger(0)\psi(0) - \langle\psi^\dagger(0)\psi(0)\rangle$. The spin operators have been expressed in terms of fermionic operators on the dot using the renowned Jordan-Wigner transformation in a symmetric form [175, 176]

$$\hat{\sigma}^-_1 = [1 - (1-i)\hat{n}_2]\hat{d}_1 \tag{13.39}$$

$$\hat{\sigma}^-_2 = [1 - (1+i)\hat{n}_1]\hat{d}_2 \tag{13.40}$$

$$\hat{\sigma}^z_j = 2\hat{n}_j - 1\,, \text{for } j = 1, 2\,, \tag{13.41}$$

where $\hat{n}_j = \hat{d}^\dagger_j\hat{d}_j$ are the dot occupation number operators. The parameters in $\hat{\mathcal{H}}_{RL}$ can be expressed in terms of the spin-boson parameters as

$$2\pi\rho V^2 \equiv \Gamma = \frac{\pi\Delta^2}{2\omega_c}, \quad \rho U = \frac{1-\sqrt{2\alpha}}{2}, \quad K_{RL} = K + 2\omega_c(1 - 2\sqrt{2\alpha})\,, \tag{13.42}$$

where the fermionic density of states is defined as $\rho = 1/(2\pi v_F)$. The bias field ε_j of the spin-boson model corresponds to the energy of the dot level j with respect to the Fermi energy of the lead.

The last two interaction terms vanish at the Toulouse point: $U = K_{\mathrm{RL}} = 0$ for $\alpha = 1/2$ and $K = 2\omega_c$. The term, $V\big[(1-i)\hat{n}_1\hat{d}_2^\dagger\psi(0) + (1+i)\hat{n}_2\hat{d}_1^\dagger\psi(0) + \mathrm{h.c.}\big]$, however, is proportional to the dot-lead tunneling and thus remains. It arises due to the Jordan-Wigner string that accounts for the distinct commutation rules of fermions and spins at different sites.

The dynamics of Eq. (13.38) cannot be solved exactly. Nevertheless, we can use the fermionic description to qualitatively understand that the decay rate of the two-spin boson model is about twice as large as in the single spin case: $b_i/a_i \approx 2$. To this end, we introduce the symmetric and antisymmetric combination of dot operators $\hat{D}_s = [\hat{d}_1 + \hat{d}_2]/\sqrt{2}$ and $\hat{D}_a = [\hat{d}_1 - \hat{d}_2]/\sqrt{2}$. The occupation numbers can then be expressed as $\hat{n}_{1,2} = \frac{1}{2}[\hat{D}_s^\dagger\hat{D}_s + \hat{D}_a^\dagger\hat{D}_a \pm \hat{D}_s^\dagger\hat{D}_s \pm \hat{D}_a^\dagger\hat{D}_s]$, where the upper sign refers to $\hat{n}_1$. At the Toulouse point, the Hamiltonian then takes the form

$$\hat{\mathcal{H}}_{\mathrm{RL}} = \hat{\mathcal{H}}_0 + E[\hat{n}_s + \hat{n}_a] + \Delta E[\hat{D}_s^\dagger\hat{D}_a + \mathrm{h.c.}] + \sqrt{2}V\big\{\big[\hat{D}_s^\dagger - \hat{D}_s^\dagger\hat{n}_a - i\hat{D}_a^\dagger\hat{n}_s\big]\psi(0) + \mathrm{h.c.}\big\}\,, \tag{13.43}$$

which contains the energy sum $E = (\varepsilon_1 + \varepsilon_2)/2$ and difference $\Delta E = (\varepsilon_1 - \varepsilon_2)/2$. We write $\hat{n}_s = \hat{D}_s^\dagger\hat{D}_s$, $\hat{n}_a = \hat{D}_a^\dagger\hat{D}_a$ and denote the free part of the lead electrons as $\hat{\mathcal{H}}_0 = v_F\sum_{k>0} k\hat{c}_k^\dagger\hat{c}_k$. Both, the symmetric and the antisymmetric state, have the same energy E, and the original energy level difference translates into an effective tunneling coupling between them.

For $\Delta E = 0$ and initially empty dots such that $\hat{n}_s = \hat{n}_a = 0$, the antisymmetric state decouples from the system completely. The tunneling coupling between the symmetric state $\hat{D}_s$ and the lead, however, is stronger than for each individual level $\hat{d}_{1,2}$. It is given by $\sqrt{2}V$ instead of V (see Eq. (13.38)), and the level will therefore fill twice as fast because $\Gamma \sim V^2$. As soon as $n_s > 0$, the antisymmetric state couples to the lead as well, and in equilibrium one finds that $\langle n_s\rangle = \langle n_a\rangle = 1/2$ for $E = 0$. For $\Delta E = 0$, symmetry requires that $\langle n_1\rangle = \langle n_2\rangle$ and the expectation values $\langle D_s^\dagger D_a\rangle$ and $\langle D_a^\dagger D_s\rangle$ are thus purely imaginary. It then follows that $\langle n_1\rangle = \langle n_2\rangle = 1/2$ and $\langle\sigma_1^z\rangle = \langle\sigma_2^z\rangle = 0$ in equilibrium. For $\Delta E \neq 0$ the level correlations acquire a finite real part which gives rise to a difference in the level occupations $\langle n_{1,2}\rangle$ in equilibrium.

13.4.5 Strong Spin Bath Coupling

In this section, we calculate using TD-NRG the spin dynamics for strong spin-bath coupling, where perturbative approaches are not applicable. We focus on the differences between the ohmic and subohmic case. We find that, qualitatively, the behavior in the two-spin boson system resembles the one known from the single spin-boson model. For an ohmic bath, we observe in the upper part of Fig. 13.16 that the coherence of oscillations is lost above a certain bath coupling strength, roughly given by $\alpha_c/2$, where $\alpha_c(K, \Delta_{1,2})$ denotes the critical value above which spin transitions are completely suppressed (localized regime).

The situation is completely different for a subohmic bath as shown in the lower part of Fig. 13.16. Here, oscillations persist even deep into the localized region. This phenomenon was only recently discovered in the single spin-boson model [160] and we confirm that it also holds in the two spin case.

This qualitative difference between the ohmic and subohmic models at which point the coherence of the spin oscillations is lost (as a function of α and K), is also reflected in the behavior of the static entanglement entropy (see Sec. 13.3.1).

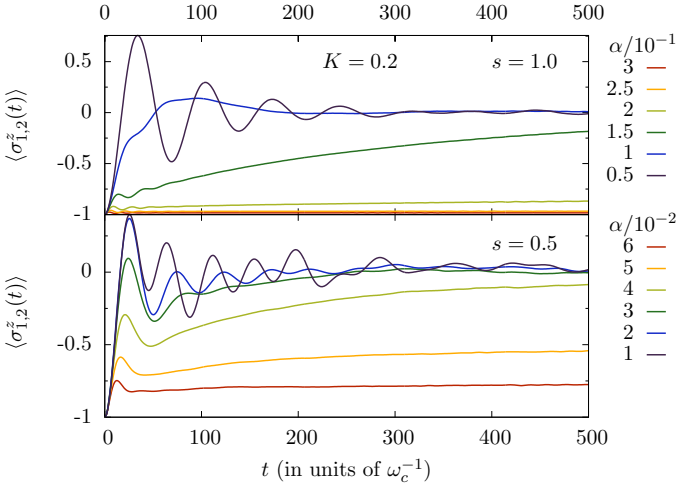

Figure 13.16: Spin dynamics $\langle\sigma^z_{1,2}(t)\rangle$ for different values of α in the regime of strong spin-bath coupling for ohmic (upper part) and subohmic bath with $s = 1/2$ (lower part). Other parameters read $\Delta = 0.1\omega_c$, $K = 0.2\,\omega_c$, $\varepsilon_{1,2} = 0$. For this choice of K the localization phase transition occurs at $\alpha_c \approx 0.25(0.043)$ in the ohmic (subohmic) system.

13.4.6 Generation of Highly Entangled Steady States

In this Section, we show that the two-spin boson model displays interesting nonequilibrium steady states for certain initial preparations. In this state, the spins are entangled with the bath while maintaining coherence between different spin configurations.

Let us ask the question what happens if we polarize the spins initially in an antiferromagnetic configuration such as $|\uparrow\downarrow\rangle$ in a region of the phase diagram where the ground state phase is localized. At $t = 0$, we then turn off the external bias fields completely, and follow the evolution of the spin reduced density matrix ρ_S over time. Note that the system can only localize in one of the ferromagnetic spin states $\{|\uparrow\uparrow\rangle, |\downarrow\downarrow\rangle\}$ as discussed in Sec. 13.2.2. We calculate $\rho_S(t)$ using TD-NRG and observe that after a time of the order $1/\gamma = 2\omega_c/(\pi\Delta^2)$ the system reaches a steady-state, where the spin reduced density matrix takes the form

$$\rho_{S,st} = \frac{1}{4}\begin{pmatrix} 1 & 0 & 0 & 0 \\ 0 & 1 & -1 & 0 \\ 0 & -1 & 1 & 0 \\ 0 & 0 & 0 & 1 \end{pmatrix} . \tag{13.44}$$

Here we use the standard basis $\{|\uparrow\uparrow\rangle, |\uparrow\downarrow\rangle, |\downarrow\uparrow\rangle, |\downarrow\downarrow\rangle\}$. With a probability of $\frac{1}{4}$, the spins are thus localized in one of the ferromagnetic spin states $\{|\uparrow\uparrow\rangle, |\downarrow\downarrow\rangle\}$, and with a probability of $\frac{1}{2}$ the spins are in the spin singlet state. The entanglement entropy $\mathcal{E}$, which is a measure of the entanglement between the two-spin subsystem and the bath, is nonzero in this state. Specifically, $\mathcal{E}(\rho_{S,ss}) = \frac{3}{2}$ from Eq. (13.44).

We can easily understand this form of the steady state by writing the initial state in terms of the singlet state $|m=0\rangle = [|\uparrow\downarrow\rangle - |\downarrow\uparrow\rangle]/\sqrt{2}$ and the triplet state $|m=0\rangle = [|\uparrow\downarrow\rangle + |\downarrow\uparrow\rangle]/\sqrt{2}$ as

$$|\uparrow\downarrow\rangle = \frac{1}{\sqrt{2}}\big(|m=0\rangle + |m=0\rangle\big)\,. \tag{13.45}$$

Whereas the singlet state does not couple to the bath at all, the triplet state localizes in one of the two ferromagnetic configurations. In this steady state, the spins are highly entangled with the bath modes, while developing and maintaining coherence between the two antiferromagnetic spin configurations.

13.5 Summary

We have presented an extensive study of a system of two Ising-coupled quantum spins in contact with a common bosonic bath. We have investigated several distinct equilibrium and nonequilibrium situation, both for the case of an ohmic as well as a subohmic bath.

First, we have elucidated the ground state phase diagram for an ohmic and a subohmic bath using a combination of bosonic numerical renormalization group (NRG), analytical techniques and intuitive arguments. Second, employing the time-dependent NRG we have investigated the system's rich dynamical behavior arising from the complex interplay between spin-spin and spin-bath interactions. Interestingly, spin oscillations can synchronize due to the proximity of the common non-Markovian bath and the system displays highly entangled steady states for certain nonequilibrium initial preparations. We have compared our non-perturbative numerical results to exact analytical solutions when available and provide quantitative limits on the applicability of the perturbative Bloch-Redfield approach at weak coupling.

Chapter 14

Decoherence in an Aharanov-Bohm Interferometer

We investigate an Aharonov-Bohm interferometer consisting of two quantum dots coupled in parallel to two lead electrodes and to a common Einstein phonon mode (see Fig. 14.1). Without coupling to phonons transport of noninteracting electrons is fully coherent and the interferometer can be tuned to complete destructive interference even for finite applied bias. If phonons couple differently to the electrons on the two dots, which-path information is transferred to the phononic bath and the electronic coherence is diminished. It is only this dephasing due to phonons which enables transport, making the device ideal for studying decoherence phenomenae. The focus of this chapter will be on NRG calculations for the conductance through the destructive interferometer in the strong coupling regime applying an AC bias. For details on the DC conductance and the accompanying analytic nonequilibrium Green's function method we refer to Ref. [177].

14.1 Aharanov-Bohm Interferometer

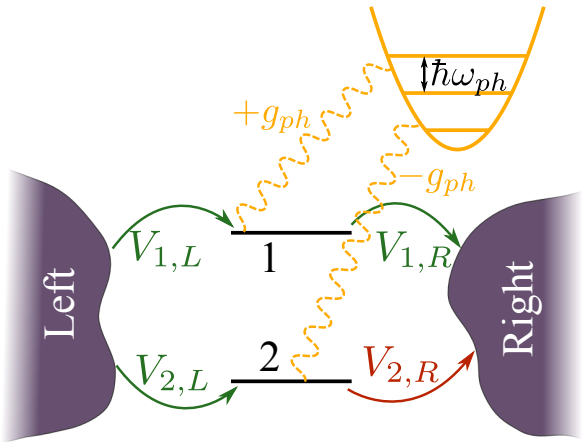

Figure 14.1: Sketch of the interferometer.

There are two qualitatively different processes altering the electronic transport through a system, if we allow a finite coupling to an environment: True decoherence has to be distinguished from a mere renormalization of the system's parameter due to the finite coupling to the environment. In case of an electronic system coupling to a heat bath via an electron-phonon coupling, incoherent processes are characterized by the absorption or emission of phonons, which may increase or decrease the electronic transport through a single site [178]. At the same time, the electron-phonon coupling will also alter the way coherent processes, where no phonons are emitted or absorbed, influence the electronic transport.

In an interferometer setup with perfectly symmetric arms, which is tuned to destructive interference, it can be shown that any finite current through the system is a true sign of decoherence [179, 180], since any renormalization processes due not lift the destructive interference and thus cancel, if we apply a finite bias.

In the setup we study, the two paths of the interferometer are realized by tunneling transport through two quantum dots placed between two electron reservoirs (see Fig. 14.1). Destructive interference is found, if the two paths enclose an Aharonov-Bohm flux of half a flux quantum. To achieve perfect destructive interference for the coherent transport contributions, the system parameters are tuned to have equal level energies on both dots ($\varepsilon = \varepsilon_1 = \varepsilon_2$) and equal tunneling matrix elements connecting dots and leads ($V_{1L} = V_{1R} = V_{2L} = -V_{2R}$). We will consider a single phononic mode ($\omega_{\rm ph}$) coupling to the electron charge on both quantum dots with a strength described by $g_{\rm ph}$.

The Hamilton operator for the full system consists of five independent parts

$$\hat{\mathcal{H}} = \hat{\mathcal{H}}_{imp} + \hat{\mathcal{H}}_{tun} + \hat{\mathcal{H}}_{lead} + \hat{\mathcal{H}}_{bath} + \hat{\mathcal{H}}_{coupl} \tag{14.1}$$

describing the isolated impurity ($\hat{\mathcal{H}}_{imp}$), the tunneling between the impurity and the impurity and the leads ($\hat{\mathcal{H}}_{tun}$), the fermionic leads ($\hat{\mathcal{H}}_{lead}$), the bosonic Einstein phonon mode ($\hat{\mathcal{H}}_{bath}$), and the coupling between the impurity "dots" and the phonon mode ($\hat{\mathcal{H}}_{coupl}$). In detail, each term reads

$$\hat{\mathcal{H}}_{imp} = \sum_{\nu} \varepsilon_\nu \hat{d}_\nu^\dagger \hat{d}_\nu + U \hat{n}_1 \hat{n}_2 - \frac{h_z}{2}(\hat{n}_1 - \hat{n}_2), \tag{14.2}$$

$$\hat{\mathcal{H}}_{tun} = \sum_{k,\nu,\sigma} V_{\nu\sigma} \left(\hat{d}_\nu^\dagger \hat{c}_{k\sigma} + \hat{c}_{k\sigma}^\dagger \hat{d}_\nu \right), \tag{14.3}$$

$$\hat{\mathcal{H}}_{lead} = \sum_{k,\sigma} \varepsilon_k \hat{c}_{k\sigma}^\dagger \hat{c}_{k\sigma}, \tag{14.4}$$

$$\hat{\mathcal{H}}_{bath} = \omega_{\rm ph} \hat{a}^\dagger \hat{a}, \tag{14.5}$$

$$\hat{\mathcal{H}}_{coupl} = g_{\rm ph} \left(\hat{a} + \hat{a}^\dagger \right) (\hat{n}_1 - \hat{n}_2), \tag{14.6}$$

where $\nu = \{1, 2\}$ labels the impurity "dot" and $\sigma = \{L, R\}$ denotes the left and right lead respectively. Please note that for simplicity we only consider *spinless* electrons in each electronic band. For the tunneling matrix elements we employ the standard rescaling $\Gamma_{\nu,\sigma} = V_{\nu,\sigma}^2 \frac{\pi}{2W}$, where W is introduced as a cut-off for the electron energy in the leads $-W < \varepsilon_k < W$.

This scenario can be experimentally realized in tunneling transport through two quantum dots placed between two electron reservoirs [181, 182]. On the one hand, one can then consider specifically engineered phononic environments, for instance, for quantum dots defined within free standing nanobeams [183], or a quantum dot coupling to a cantilever [184]; on

the other hand, the scenario can easily be generalized to model multiple phonon modes in standard heterostructures or molecular electronics [185, 186]. We will focus on the linear AC conductance, which is of great current interest in general [187, 188].

14.1.1 Mapping to Symmetric/Antisymmetric Dot Level

Some insight into the transport properties of the interferometer can be gained by rewriting the Hamiltonian in a new basis of symmetric $\hat{d}_\mathrm{s} = (\hat{d}_1 - \hat{d}_2)/\sqrt{2}$ and antisymmetric $\hat{d}_\mathrm{a} = (\hat{d}_1 + \hat{d}_2)/\sqrt{2}$ combination of the original dot levels. The symmetric (antisymmetric) level then couples to left (right) lead only with tunneling matrix elements $V_{sL} = V_{aR} = \sqrt{2}V_{1\sigma}$ and $V_{sR} = V_{aR} = 0$. The part of the Hamiltonian describing the central region (i.e. impurity and coupling to the phonon mode) in this new basis thus reads

$$\tilde{\mathcal{H}}_{central} = \tilde{\mathcal{H}}_{imp} + \tilde{\mathcal{H}}_{coupl} = \varepsilon(\hat{d}_\mathrm{s}^\dagger \hat{d}_\mathrm{s} + \hat{d}_\mathrm{a}^\dagger \hat{d}_\mathrm{a}) + g_\mathrm{ph}(\hat{a} + \hat{a}^\dagger)(\hat{d}_\mathrm{s}^\dagger \hat{d}_\mathrm{a} + \hat{d}_\mathrm{a}^\dagger \hat{d}_\mathrm{s}). \tag{14.7}$$

In this new basis it is obvious that without coupling to the phonons, the system decouples completely in left and right part and transport through the system is impossible. Transport is enabled by a term describing tunneling between the two new dot levels, which is proportional to the electron-phonon coupling g_ph and the phonon coordinate, $\hat{a} + \hat{a}^\dagger$. Fig. 14.2 illustrates the mapping of the system Hamiltonian to the new basis

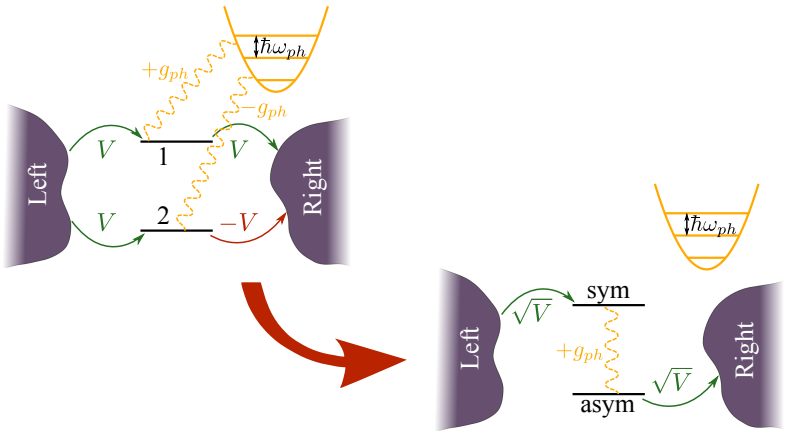

Figure 14.2: For $V_{1L} = V_{2L} = V_{1R} = -V_{2R}$ it is instructive to study the *symmetric* and *antisymmetric* combination of the impurity level, which only couple to the left or the right lead. The phonon mode couples the symmetric and antisymmetric level combination and facilitates transport through the interferometer.

14.2 Kubo Formalism

The finite frequency current I_σ flowing from lead σ to the impurity is to a good approximation given by the linear AC conductance

$$I_\sigma(\omega_\mathrm{ac}) = \mathcal{G}_{\sigma\sigma'}(\omega_\mathrm{ac})\, V_{\sigma'}(\omega_\mathrm{ac}). \tag{14.8}$$

In linear response with respect to the AC excitation, we can use Kubo formalism [189] to calculate the conductance (see e. g. Ref. [190] for an implementation of the Kubo formalism within the NRG approach). The standard Kubo approach directly yields the linear conductance $\mathcal{G}_{\sigma\sigma'}(\omega_{\rm ac})$ in terms of a (retarded) current-current correlator

$$\mathcal{G}_{\sigma\sigma'}(\omega_{\rm ac}) = \frac{1}{i\omega_{\rm ac}}(K_{\sigma\sigma'}(\omega_{\rm ac}) - K_{\sigma\sigma'}(0)), \tag{14.9}$$

where the correlator is given by

$$K_{\sigma\sigma'}(\omega_{\rm ac}) = -\frac{i}{\hbar}\int_0^\infty dt \quad e^{i\omega_{\rm ac}t}\langle\left[\hat{I}_\sigma(t), \hat{I}_{\sigma'}(0)\right]\rangle. \tag{14.10}$$

The current operator is defined via

$$\hat{I}_\sigma(t) = e\dot{\hat{N}}_\sigma, \tag{14.11}$$

where the time derivative of the electron number operator in lead σ can be calculated using the Heisenberg equation

$$\dot{\hat{N}}_\sigma = \frac{i}{\hbar}\left[\hat{\mathcal{H}}, \hat{N}_\sigma\right] = \frac{i}{\hbar}\left[\hat{\mathcal{H}}_{tun}, \sum_k \hat{c}^\dagger_{k\sigma}\hat{c}_{k\sigma}\right] \tag{14.12}$$

$$= \frac{i}{\hbar}\sum_k \left\{V_{1\sigma}\left(\hat{d}^\dagger_1\hat{c}_{k\sigma} - \hat{c}^\dagger_{k\sigma}\hat{d}_1\right) + V_{2\sigma}\left(\hat{d}^\dagger_2\hat{c}_{k\sigma} - \hat{c}^\dagger_{k\sigma}\hat{d}_2\right)\right\}. \tag{14.13}$$

The correlator $K_{\sigma\sigma'}(t,t') = K_{\sigma\sigma'}(t-t',0)$ has the same structure as a retarded Green's function, but with a pair of creation and destruction operators for each of the current operators at the two time variables.

14.2.1 Implementing the Kubo Formalism

The system belongs to the class of impurity models for which the bosonic degrees of freedom can be treated completely within the first iteration step of the NRG algorithm. Additionally to the eigenstates of the two quantum dots and the eigenstates describing the maximally localized conduction band degree of freedom, it is straightforward to add the Einstein phonon mode in the first step of the iterative diagonalization procedure. The Hilbert space described in the first NRG iteration is enlarged, since each of the $2^4 = 16$ electronic eigenstates, accounting for the presence or absence of an electron in the right (left) lead and on the first (second) quantum dot, is split up into N_b different eigenstates describing different occupations of the bosonic mode. In principle the single Einstein phonon mode can be occupied with an infinite number of bosons $N_b = \infty$. In practice one has to introduce a cut-off for the maximal number of bosons occupying the mode. Choosing $N_b \approx 10$ turns out to be sufficient, since the eigenstates with larger bosonic occupation can be neglected due to their large eigenenergies.

Inserting Eq. (14.11) into Eq. (14.10), the expression for the correlator K in the Kubo

formalism reads

$$\frac{i\hbar}{e^2}K_{\sigma\sigma'}(\omega_{\rm ac}) = \int_0^\infty dt \quad e^{i\omega_{\rm ac}t}\langle\left[\dot{\hat{N}}_\sigma(t),\dot{\hat{N}}_{\sigma'}(0)\right]\rangle \tag{14.14}$$

$$= \lim_{\delta\to 0^+}\int_0^\infty dt \quad e^{it\omega_{\rm ac}-\delta t}\langle\left[\dot{\hat{N}}_\sigma(t),\dot{\hat{N}}_{\sigma'}(0)\right]\rangle \tag{14.15}$$

$$= \lim_{\delta\to 0^+}\int_0^\infty dt \quad e^{it\omega_{\rm ac}-\delta t}{\rm Tr}\left\{\hat{\rho}\left[\dot{\hat{N}}_\sigma(t),\dot{\hat{N}}_{\sigma'}(0)\right]\right\} \tag{14.16}$$

$$= \lim_{\delta\to 0^+}\int_0^\infty dt \sum_{l,l',k}\left(e^{it(\omega_{\rm ac}+E_{l,l'})-\delta t}\langle l|\dot{\hat{N}}_\sigma|l'\rangle\langle l'|\dot{\hat{N}}_{\sigma'}|k\rangle\langle k|\hat{\rho}|l\rangle + \dots\right), \tag{14.17}$$

where we evaluate the expectation value by tracing over the system's density matrix $\hat{\rho}$. In the last line of Eq. (14.17), we only write down the first summand of the commutator explicitly.

The matrix elements of the reduced density matrix and of the time derivative of the electron number in the leads do not explicitly depend on the time variable t we integrate over. The integration over t thus can be evaluated as follows

$$\lim_{\delta\to 0^+}\int_0^\infty dt e^{it(\omega_{\rm ac}+E_{l,l'})-\delta t} = \lim_{\delta\to 0^+}\frac{e^{it(\omega_{\rm ac}+E_{l,l'})-\delta t}}{i(\omega_{\rm ac}+E_{l,l'})-\delta}\Big|_0^\infty \tag{14.18}$$

$$= \lim_{\delta\to 0^+}\left(0-\frac{1}{i(\omega_{\rm ac}+E_{l,l'})-\delta}\right) = -\lim_{\delta\to 0^+}\frac{1}{i(\omega_{\rm ac}+E_{l,l'})-\delta} \tag{14.19}$$

$$= \lim_{\delta\to 0^+}\left(\frac{i(\omega_{\rm ac}+E_{l,l'})}{(\omega_{\rm ac}+E_{l,l'})^2}+\frac{\delta}{(\omega_{\rm ac}+E_{l,l'})^2+\delta^2}\right) \tag{14.20}$$

$$= \left(\frac{i}{\omega_{\rm ac}+E_{l,l'}}+\pi\delta(\omega_{\rm ac}+E_{l,l'})\right). \tag{14.21}$$

Let us focus on the part containing the δ-distribution (which collecting all prefactors makes up the real part of the conductance). Since within the NRG algorithm only a finite set of eigenstates can be taken into account, the resulting conductance will only consist of a finite set of δ-peaks. To obtain a smooth curve describing for the conductance we utilize a log-Gaussian broadening, which is equivalent to replacing

$$\delta(\omega_{\rm ac}-\omega_n) = \frac{1}{|\omega_n|}\delta(\ln\omega_{\rm ac}-\ln\omega_n) \tag{14.22}$$

$$= \frac{1}{|\omega_n|}\lim_{b_{\rm d}\to 0^+}\frac{1}{\sqrt{\pi}b_{\rm d}}e^{-\frac{(\ln\omega_{\rm ac}-\ln\omega_n)^2}{b_{\rm d}^2}}. \tag{14.23}$$

In Sec. 10.3, more details of the criteria for choosing the right damping kernel are given.

A straightforward calculation of the imaginary part of the conductance, which consists of contributions given by the first term in Eq. (14.21), is difficult within the numerical renormalization group approach, since the denominator "ruins" the separation of energy scales crucial for any NRG calculation. The standard way to obtain the imaginary part is to first calculate the real part of the expression and then apply the Kramers-Kronig transformation

$${\rm Re}(K_{\sigma\sigma'}(\omega_{\rm ac})) = \frac{1}{\pi}\mathcal{P}\int_{-\infty}^\infty\frac{{\rm Im}(K_{\sigma\sigma'}(\omega'_{\rm ac}))}{\omega'_{\rm ac}-\omega_{\rm ac}}d\omega'_{\rm ac} \tag{14.24}$$

to obtain data for the imaginary part (here $\mathcal{P}$ denotes the Cauchy principal value).

To obtain more precise results for the high frequency part of the conductance, we employ the NRG algorithm using the complete basis already introduced in Chap. 7 and average over $N_z = 32$ different NRG calculations using slightly different discretizations of the conduction band (see Sec. 10.2 for more details on the so called z-trick). In all of our calculations of this chapter, we utilize a discretization parameter of $\Lambda = 1.8$ and consider a maximum of $N_b = 10$ different phonon modes on the impurity site.

14.3 DC Conductance

As a first step and a check of our implementation of the conductances, we qualitatively verify the shift in the DC conductance for a situation where one level is attached to left and right lead and an single phonon mode is coupled to the single level. The DC conductance is calculated as the low-frequency limit of the AC conductance $\lim_{\omega_{\rm ac}\to 0}\mathcal{G}_{\sigma\sigma'}(\omega_{\rm ac})$ within all of our NRG calculations. The dependence of the DC conductance on the level's position ε_1 should (in the linear response regime to zeroth-order) be given by a Breit-Wigner curve as derived for example in Ref. [191]

$$\mathcal{G}_{LL}^{BW}(\varepsilon_1) = \frac{e^2}{2\pi}\frac{\Gamma^2}{\Gamma^2+\varepsilon_1^2}. \tag{14.25}$$

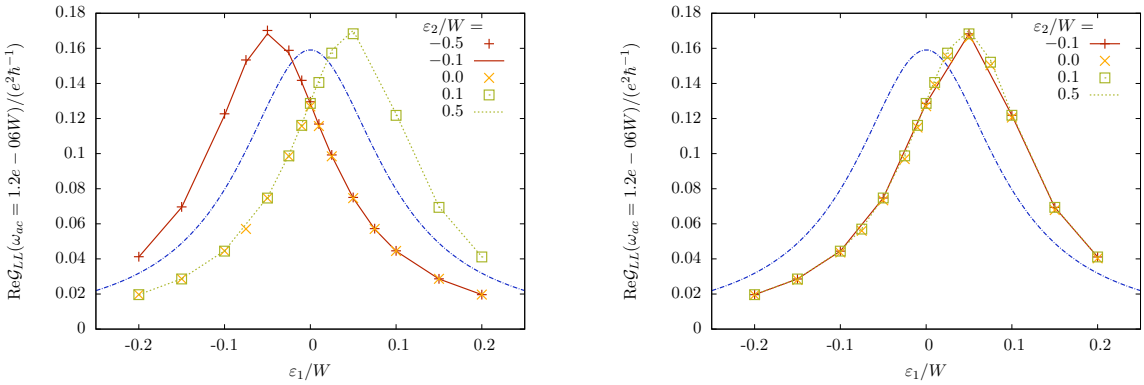

Figure 14.3: DC conductance $\mathcal{G}_{LL}(\omega_{\rm ac}\to 0)$ for the Aharanov-Bohm interferometer with $\Gamma_{2,\sigma} = 0$. Left panel: $\hat{\mathcal{H}}_{coupl} = g_{\rm ph}(\hat{a}+\hat{a}^\dagger)(\hat{n}_1-\hat{n}_2)$. Right panel: $\hat{\mathcal{H}}^{spec}_{coupl} = g_{\rm ph}(\hat{a}+\hat{a}^\dagger)\hat{n}_1$. $(\Gamma_{1,\sigma} = 0.1W, g_{\rm ph} = 0.075W, \omega_{\rm ph} = 0.1W)$

The expected shift to positive values of ε_1 for both, positive and negative values of ε_2 is only observed replacing the coupling term in the Hamiltonian (see Eq. (14.6)) by

$$\hat{\mathcal{H}}^{spec}_{coupl} = g_{\rm ph}\left(\hat{a}+\hat{a}^\dagger\right)(\hat{n}_1)\,. \tag{14.26}$$

We intensively checked, that the limit $\lim_{\omega_{\rm ac}}\to 0$ is taken carefully, considering only cases, where the conductance does not change over a range of at least two decades of $\omega_{\rm ac}$. For details on the DC conductance of the full interferometer with $\Gamma_{2,\sigma}\neq 0$ and an explanation of the analytic nonequilibrium Green's function method used to derive the results presented there, we refer to Ref. [177].

14.4 “Diagonal” AC Conductance $\mathcal{G}_{LL}(\omega_{\rm ac})$

For the remainder of this chapter, we concentrate on the linear AC conductance calculated via the numerical renormalization group (NRG) method. First, we investigate the “diagonal” AC conductance $\mathcal{G}_{LL}(\omega_{\rm ac})$ (or equivalently $\mathcal{G}_{RR}(\omega_{\rm ac})$).

14.4.1 Quantum RC Circuit

Our starting point is the relatively simple case of a single level attached to only one lead without the additional influence of the phonons. Albeit its simple nature, the model describes an experimentally relevant situation, namely the charge relaxation resistance of a mesoscopic capacitor. In Fig. 14.4, we sketch the experimental setup used in Ref. [187], where a cavity or quantum dot coupled via a quantum point contact to an electronic reservoir is studied. The capacitor can be viewed as a mesoscopic analogue to a classical RC circuit, where the “plate” of the classical capacitor is replaced by the cavity and the resistance by the quantum point contact connecting the cavity and the electronic reservoir.

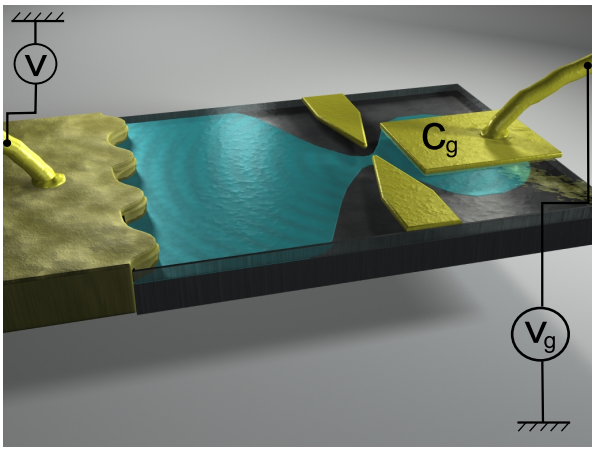

Figure 14.4: Sketch of the quantum RC circuit realized coupling a cavity or quantum dot via a quantum point contact to an electronic reservoir. Illustration taken from Ref. [192].

The low frequency response of the mesoscopic capacitor is given by the conductance $\mathcal{G}_{LL}(\omega_{\rm ac})$ attaching only the left lead to one of the two levels in our original interferometer setup. The frequency dependence of the response can be expressed as

$$\mathcal{G}_{LL}(\omega_{\rm ac}) = i\omega_{\rm ac}C_\mu + \omega_{\rm ac}^2 C_\mu^2 R_q + \mathcal{O}(\omega_{\rm ac}^3), \tag{14.27}$$

where C_μ is an electrochemical capacitance and R_q is the charge relaxation resistance [188]. Knowing the frequency-dependence of the real and imaginary part of the conductance $\mathcal{G}_{LL}(\omega_{\rm ac})$, we can thus determine the charge relaxation resistance

$$\lim_{\omega_{\rm ac}\to 0} \frac{{\rm Re}\mathcal{G}_{LL}(\omega_{\rm ac})}{({\rm Im}\mathcal{G}_{LL}(\omega_{\rm ac}))^2} = R_q, \tag{14.28}$$

which is predicted to be quantized [188, 135].

Without any influence of the phonons, i.e. choosing $N_b = 0$ and $g_{\rm ph} = 0$, the quantization of the charge relaxation resistance is reproduced by our numerical renormalization group method calculations: In Figs. 14.5 we plot the real and imaginary part of the conductance on a double-logarithmic scale, as well as the ratio $\frac{{\rm Re}\mathcal{G}_{LL}(\omega_{\rm ac})}{({\rm Im}\mathcal{G}_{LL}(\omega_{\rm ac}))^2}$, which is equivalent to the charge relaxation resistance for small frequencies $\omega_{\rm ac}$. For different values of $\Gamma_{1,L}$, and ε_1 we observe a ratio close to $R_q = \pi$.

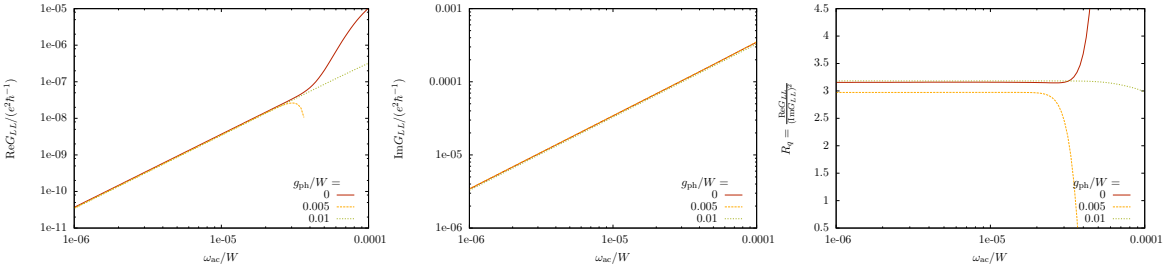

Figure 14.5: We study the interferometer model, where only one of the quantum dot levels is attached to the left lead to investigate the quantization of the charge relaxation resistance in the quantum RC circuit. The conductance $\mathcal{G}_{LL}(\omega_{\rm ac})$ should be given by Eq. (14.27). Left panels show ${\rm Re}\mathcal{G}_{LL}(\omega_{\rm ac})$ and ${\rm Im}\mathcal{G}_{LL}(\omega_{\rm ac})$, while the right panel shows the ratio $\frac{{\rm Re}\mathcal{G}_{LL}(\omega_{\rm ac})}{({\rm Im}\mathcal{G}_{LL}(\omega_{\rm ac}))^2}$. For very small frequencies $\omega_{\rm ac}$ this ratio yields the charge relaxation resistance, which should be given by $R_q = \pi$ [188, 135] ($\Gamma_{1,L} = 0.05W, \Gamma_{\nu,\sigma} = 0.0W, \omega_{\rm ph} = 10g, \varepsilon_1 = 0.05W, \varepsilon_2 = 0.5W$).

Considering the influence of the phonon mode on the mesoscopic conductor (i.e. allowing for small $g_{\rm ph} \neq 0$ in a coupling term, which is given by Eq. (14.26)), we still observe a quantization of the charge relaxation. For even larger electron-phonon coupling strengths $g_{\rm ph} > 0.01W$ though, the result is less definite and the values extracted for the charge relaxation resistance depend on all system parameters.

14.4.2 Renormalization of $\mathcal{G}_{LL}(\omega_{\rm ac})$

As we will investigate in more detail in Sec. 14.5, the the transconductance $\mathcal{G}_{LR}(\omega_{\rm ac})$ measuring the conductance across the interferometer, will vanish for an Aharanov-Bohm interferometer, where the two paths enclose half a flux quantum (i.e. $\Gamma_{1,\sigma} = \Gamma_{2,L} = -\Gamma_{2,R}$) and the level energies on both dots are equal ($\varepsilon_1 = \varepsilon_2$).

There are, however, diagrammatic contributions for the "diagonal" conductances $\mathcal{G}_{LL/RR}(\omega_{\rm ac})$, describing electrons tunneling back and forth between the (anti)symmetric level and the (left) right lead, as the chemical potential of the lead is varied with frequency $\omega_{\rm ac}$.

In Figs. 14.6, we present a direct comparison of our numerical renormalization group method results for $\mathcal{G}_{LL}(\omega_{\rm ac})$ to results from the analytic nonequilibrium Green's function method for small electron-phonon coupling (for details on the analytic perturbative method, see Ref. [177] and references therein). For a quantitative comparison of our NRG results to the analytic results, the NRG parameters have to be tuned such that features at relatively large frequencies $\omega_{\rm ac} = \mathcal{O}(0.1W)$ can be extracted with high accuracy. It is thus necessary to carefully choose the strength of the logarithmic Gaussian damping employed matching the sufficiently large number of different discretizations of the conduction band averaged over.

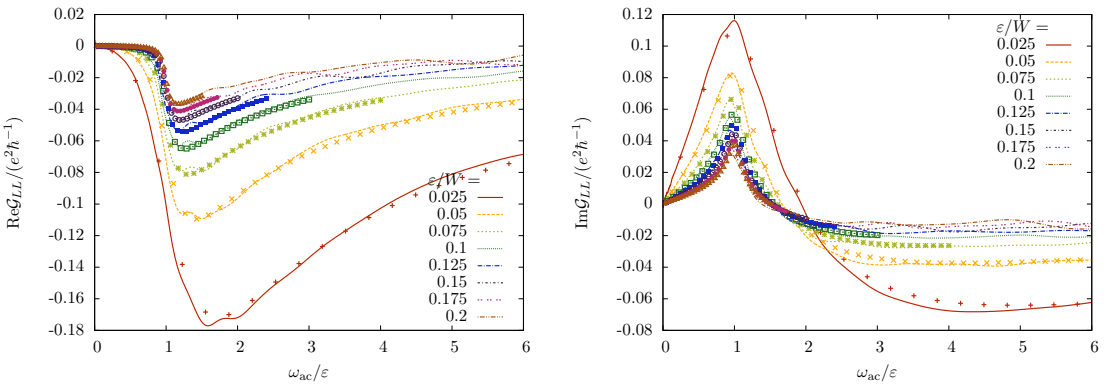

Figure 14.6: Real (left) and imaginary part (right) of the conductance $\mathcal{G}_{LL}(\omega_{\mathrm{ac}})$. Points represent the analytic results obtained by a nonequilibrium Green's function method, lines the numerical renormalization group method results. The AC frequency ω_{ac} has been scaled according to the eigenenergies of the eigenenergy on the dot $\varepsilon = \varepsilon_1 = \varepsilon_2$ ($\Gamma_{\nu,\sigma} = \pm 0.01W, \omega_{\mathrm{ph}} = 0.1W, g_{\mathrm{ph}} = 0.01W$).

For our calculations averaging over $N_z = 32$ slightly different discretizations and choosing a damping $b_{\mathrm{d}} = 0.1$ turns out to be a good choice (see Sec. 10.3 for details on the damping).

Observe in Figs. 14.6 that the incline of the real part as well as the peak in the imaginary part of the "diagonal" conductance $\mathcal{G}_{LL}(\omega_{\mathrm{ac}})$ is found for $\omega_{\mathrm{ac}} = \varepsilon$, while its absolute strength decreases with increasing eigenenergies of the levels on the quantum dot ε. Notice that even for relatively large eigenenergies of the quantum levels (e.g. $\varepsilon = 0.15W$) the shape of the conductances predicted by the analytic method is reproduced to very good accuracy by our results from the numerical renormalization group method.

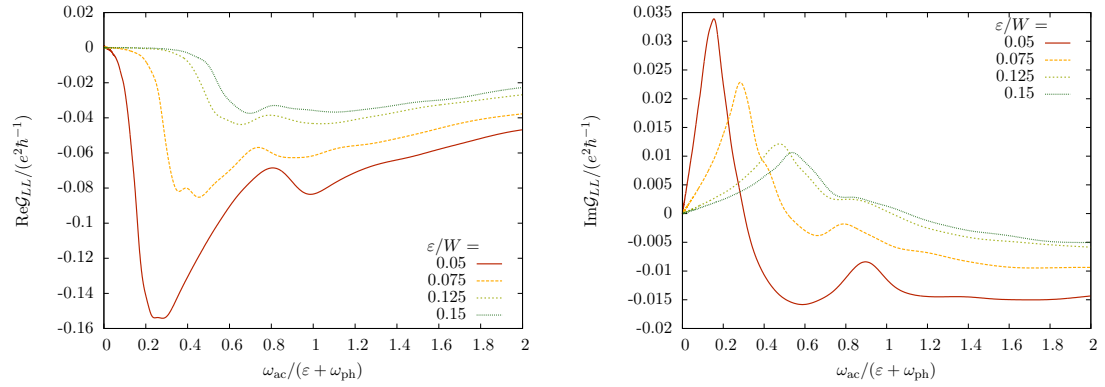

Figure 14.7: Investigating the real (left) and imaginary part (right) of the "diagonal" conductance $\mathcal{G}_{LL}(\omega_{\mathrm{ac}})$ carefully, we can observe an indication of the small correction in the numerical renormalization group method results at $\omega_{\mathrm{ac}} = \omega_{\mathrm{ph}} + \varepsilon$ ($\Gamma_{\nu,\sigma} = \pm 0.01W, \omega_{\mathrm{ph}} = 0.05W, g_{\mathrm{ph}} = 0.05W$).

The second-order contribution to $\mathcal{G}_{LL}(\omega_{\mathrm{ac}})$ constitutes a small correction to the nonin-

teracting result, which yields additional features at $\omega_{\rm ac} = \varepsilon + \omega_{\rm ph}$. This small correction is difficult to observe in our numerical results, see Figs. 14.7.

14.5 Purely Decoherent Transport $\mathcal{G}_{LR}(\omega_{\rm ac})$

In order to single out the effect of decoherent processes, we investigate the transconductance $\mathcal{G}_{LR}(\omega_{\rm ac})$ of the destructive Aharanov-Bohm interferometer, where $\Gamma = \Gamma_{1,\sigma} = \Gamma_{2,L} = -\Gamma_{2,R}$ and the energies of the level dots are equal $\varepsilon = \varepsilon_1 = \varepsilon_2$ in the following section.

Using a diagrammatic approach and exploiting the mapping to the symmetric and antisymmetric dot levels, it is straightforward to show that for the symmetric interferometer studied here the coherent contribution to zeroth order in the electron-phonon coupling $g_{\rm ph}$ vanishes. As we have demonstrated in Ref. [193], only a single second-order diagram can be constructed in this mapped basis. Thus contributions "merely renormalizing" the transconductance $\mathcal{G}_{LR}(\omega_{\rm ac})$ interfere destructively and vanish for an interferometer, where the two paths enclose half a flux quantum.

Applying Keldysh diagrammatic rules to this second-order diagram the corresponding integral expression can be evaluated. These analytic results for the transconductance $\mathcal{G}_{LR}(\omega_{\rm ac})$ are compared to our NRG results.

14.5.1 Sub-Threshold Transconductance

Evaluating the integral expression derived from the perturbative nonequilibrium Green's function (NEGF) calculation, we find contributions from the δ-peak at the phonon energy $\omega_{\rm ph}$ as well as from the principal value part of the integral. The latter yields a resonant peak at $\omega_{\rm ac} = \varepsilon$ in the real part of the transconductance ${\rm Re}\mathcal{G}_{LR}(\omega_{\rm ac})$ [193]. The δ-peaks on the other hand contribute a smaller negative peak at $\omega_{\rm ac} = \varepsilon + \omega_{\rm ph}$, where the excitation energy is in resonance with the dot level position after the excitation of a phonon.

In Figs. 14.8, we compare our NRG results for different level energies on the quantum dots ε to the results predicted by perturbative NEGF calculations. We find good qualitative and (depending on the values of the tunneling matrix elements Γ) even reasonable quantitative agreement between the results of the two methods for small electron-phonon coupling $g_{\rm ph}$. As intuitively expected, the maximal value of the transconductance decreases with increasing quantum dot level eigenenergy ε and scales with the electron-phonon coupling strength as $g_{\rm ph}^2$. This partially explains large influence of numerical inaccuracies leading to quantitative deviations of the NRG results for $\mathcal{G}_{LR}(\omega_{\rm ac})$ from the expected NEGF curve in case of small $g_{\rm ph}$ and large ε.

In the following, we want to highlight a particularly remarkable feature of our results at low frequency: AC transport is already possible for excitation frequencies smaller than the phonon energy $\omega_{\rm ac} < \omega_{\rm ph}$. Let us first emphasize, that this is in striking contrast to the case of finite-bias DC transport, where in the weak coupling limit there is a sharp threshold for incoherent transport processes becoming possible only for $eV_{\rm dc} \geq \omega_{\rm ph}$. Using the mapping to (anti)symmetric dot states the DC current through a destructive interferometer can be shown to contain only incoherent contributions. These contributions are characterized by explicit appearance of self-energies, $\Sigma^{\gtrless,\,\rm ph}$, due to emission or absorption of phonons (cf. for example, Eq. 66 in Ref. [194]). To lowest order in the electron-phonon coupling (and for zero temperature) transport takes place through two transport channels at $\omega = \varepsilon$ and $\varepsilon + \omega_{\rm ph}$ within a transport window, $\mu_L > \omega > \mu_R + \omega_{\rm ph}$. In particular, the resulting I-V curve

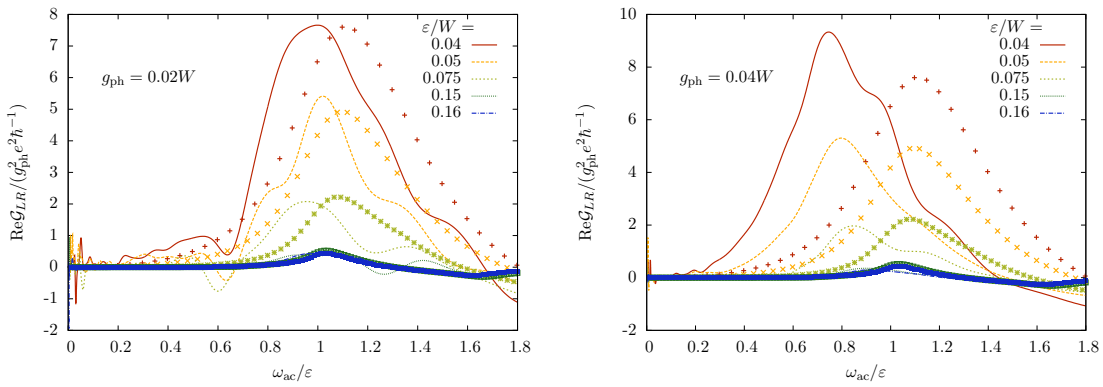

Figure 14.8: Comparing our NRG results for the real part of the transconductance $\mathcal{G}_{LR}(\omega_{\rm ac})$ (lines) to perturbative analytic results (points). The resonant peak at $\omega_{\rm ac} = \varepsilon$ is clearly visible in all of our NRG results, even for relatively large level energy $\varepsilon = 0.16W$, where the absolute value of the transconductance is small. Note that for small electron-phonon coupling $g_{\rm ph} = 0.02W$ (left panel) and large ε the NRG results become “wiggly”. For larger $g_{\rm ph} = 0.04W$ (right) the NRG results for $\mathcal{G}_{LR}(\omega_{\rm ac})$ are less sensitive to numerical errors, but a shift of the resonant peak to smaller AC frequencies $\omega_{\rm ac} < \varepsilon$ can be observed. ($\Gamma_{\nu,\sigma} = \pm 0.01W, \omega_{\rm ph} = 0.1W$).

has a sharp gap at low bias, $eV_{\rm dc} < \omega_{\rm ph}$, as any incoherent transport process necessarily involves the emission of a phonon, whose energy has to be provided by the applied bias. The naive expectation, that in AC transport the frequency of the infinitesimal AC excitation voltage providing energy for emission of phonons acts in a similar manner does not hold. In fact, sub-threshold AC transport apparently is possible without the real emission of phonons. Considering the Hamiltonian of the destructive Aharanov-Bohm interferometer in the mapped base, we observe that virtual tunneling back and forth processes between symmetric and antisymmetric levels with emission and absorption of phonons will yield an effective charge-charge interaction between the two sites. Such interaction then leads to finite AC conductance, but vanishing DC conductance, just like the electrostatic interaction in a plate capacitance.

14.5.2 “Polaron Shift” of Peak in Transconductance

Comparing the two panels in Fig. 14.8, we already observed a shift of the resonant peak located at $\omega_{\rm ac} = \varepsilon$ for small electron-phonon coupling $g_{\rm ph}$ to smaller AC frequencies $\omega_{\rm ac} < \varepsilon$ for larger values of $g_{\rm ph}$. To investigate the shift's functional dependence we evaluated the peak position for our calculations using different values of $g_{\rm ph}$ and ε, see Fig. 14.9.

We have evaluated the position of the resonant peak in the real part and plotted it against the electron-phonon strengths $g_{\rm ph}$ for different values of ε, see Fig. 14.10. The functional dependence of the shift observed is reminiscent of a polaron shift

$$\tilde{\varepsilon} = \varepsilon + \frac{g_{\rm ph}^2}{\omega_{\rm ph}}(2f(\varepsilon) - 1) \tag{14.29}$$

where $f(\varepsilon)$ can be replaced by the occupation of the quantum dot levels forming the interfer-

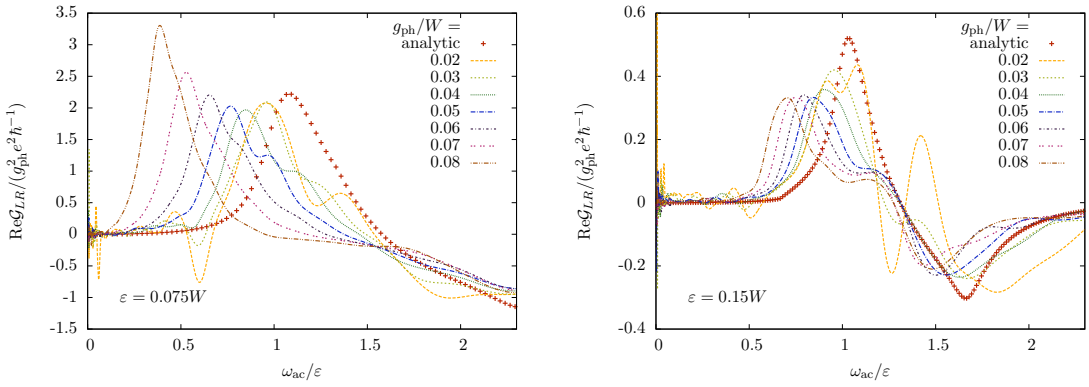

Figure 14.9: Real part of the transconductance $\mathcal{G}_{LR}(\omega_{\rm ac})$. The analytic results (points) for small electron-phonon coupling are compared to results from our numerical renormalization group method calculations for larger coupling strengths $g_{\rm ph}$. Notice the shift in the peak of $\mathcal{G}_{LR}$ to smaller values of $\omega_{\rm ac}$ increasing $g_{\rm ph}$, which can be observed for both, relatively small ($\varepsilon = 0.075W < \omega_{\rm ph}$ [left panel]) and relatively large ($\varepsilon = 0.15W > \omega_{\rm ph}$ [right panel]) eigenenergy of the quantum dot levels ($\Gamma_{\nu,\sigma} = \pm 0.01W, \omega_{\rm ph} = 0.1W$).

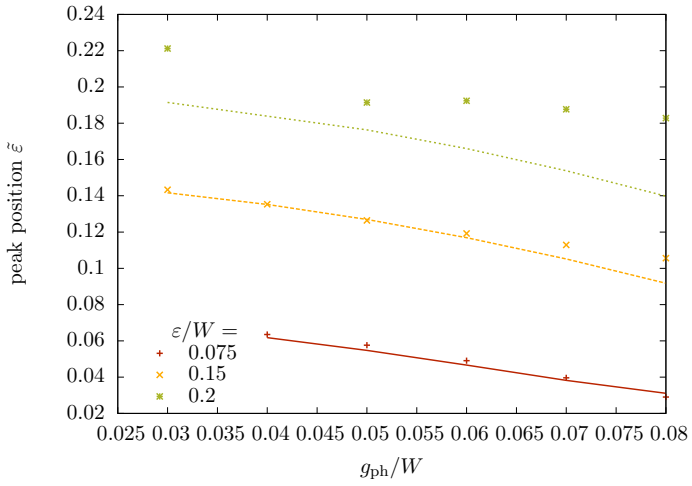

Figure 14.10: Evaluating the position of the resonant peak in the real part of the transconductance $\mathcal{G}_{LR}(\omega_{\rm ac})$ increasing the electron-phonon coupling $g_{\rm ph}$ and comparing against the analytical expression for the polaron shift (cf. Eq. (14.29)).

ometer

$$f(\varepsilon) \approx n(\varepsilon) = n_\uparrow + n_\downarrow. \tag{14.30}$$

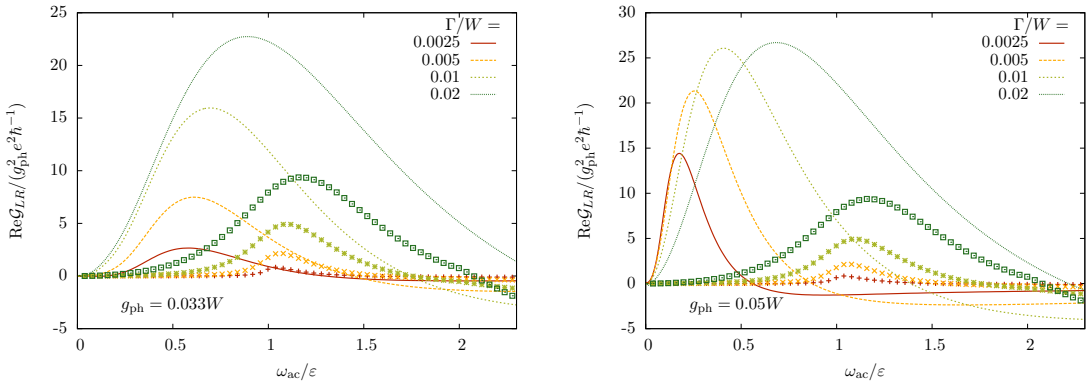

Figure 14.11: Choosing different values for the tunneling matrix elements $\Gamma_{\nu,\sigma}$ yields the expected reduction of the real part of the transconductance $\mathcal{G}_{LR}(\omega_{\mathrm{ac}})$ for small values of g_{ph} (left panel) for both the analytic (points) and NRG results (lines). For large g_{ph} an additional shift of the resonant peak of the transconductance to smaller values of ω_{ac} is observed as well ($\Gamma_{\nu,\sigma} = \pm 0.01W, \omega_{\mathrm{ph}} = 0.1W$).

Let us briefly comment on the Γ-dependence of transconductance: Choosing different values for the tunneling matrix elements $\Gamma_{\nu,\sigma}$, we observe in Fig. 14.11 how the real part of $\mathcal{G}_{LR}(\omega_{\mathrm{ac}})$ is altered. For small electron phonon coupling g_{ph} the maximal value of $\mathrm{Re}\mathcal{G}_{LR}$ decreases choosing smaller values for $\Gamma_{\nu,\sigma}$. As one might naively expect, the peak height scales to a good approximation linear with $\Gamma_{\nu,\sigma}$. For larger electron-phonon coupling, though, the effect is twofold: The height of the peak is reduced, while at the same time, the peak shifts to smaller AC frequencies choosing smaller tunneling matrix elements $\Gamma_{\nu,\sigma}$ (cf. right panel of Fig. 14.11).

14.5.3 Multiple Phonon Excitations

As we have mentioned in Sec. 14.5.1, there are two contributions evaluating the integral expression corresponding to the single second order diagram we constructed in the perturbative diagrammatic approach in Ref. [193]. While we have extensively discussed the peak in the real part of $\mathcal{G}_{LR}(\omega_{\mathrm{ac}})$ stemming from the principal part of the integral expression in the preceding section, we now want to focus on the contributions, which are connected to excitations of phonons.

For small electron-phonon coupling g_{ph}, the δ-peaks in the integral expression contribute a smaller negative peak at $\omega_{\mathrm{ac}} = \varepsilon + \omega_{\mathrm{ph}}$ to the real part of the transconductance $\mathcal{G}_{LR}(\omega_{\mathrm{ac}})$, where the excitation energy is in resonance with the dot level position after the excitation of a phonon. This is clearly visible in the left panel of Fig. 14.12, where we plot the results of the analytic NEGF calculations as well as our NRG results for different values of g_{ph}.

For larger values of electron-phonon coupling g_{ph}, additional "features" become evident in the numerical renormalization group results at high AC frequencies ω_{ac} in the transconductance $G_{LR}(\omega_{\mathrm{ac}})$. Carefully observing the left panel of Fig. 14.12 one finds additional

resonances at sidebands of the level energy $\omega_{\rm ac} = \varepsilon + n\omega_{\rm ph}$, where $n = 1, 2, \ldots$. We have verified that these additional features are not caused by band edge effects, scaling all parameters $(\Gamma_{\nu,\sigma}, \omega_{\rm ph}, g_{\rm ph}, \varepsilon)$ by a factor 2 (cf. Fig. 14.12). The additional features can be observed independent of the relative size of the electronic conduction band W, which is a strong indication that they are connected to processes involving several phonons.

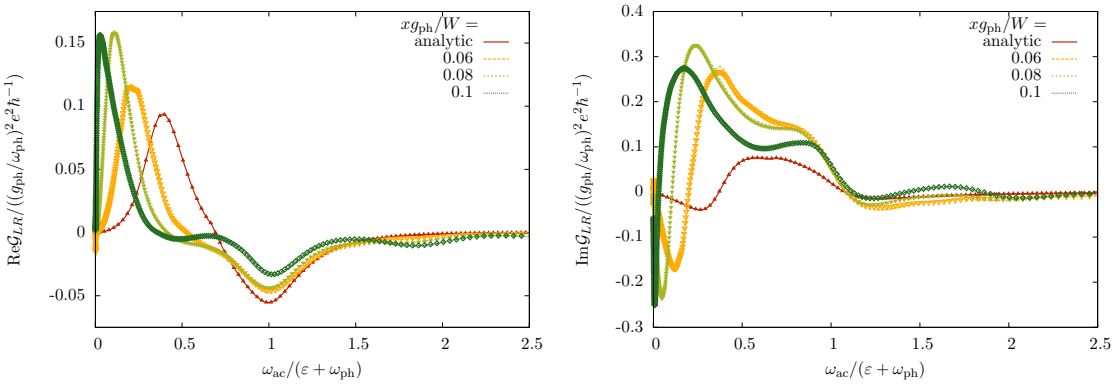

Figure 14.12: In the real part of the transconductance $\mathcal{G}_{LR}(\omega_{\rm ac})$ (left panel) the small negative peak at $\omega_{\rm ac} = \varepsilon + \omega_{\rm ph}$ is clearly visible. System parameters are chosen $x\Gamma_{\nu,\sigma} = \pm 0.02W, x\omega_{\rm ph} = 0.1W, x\varepsilon = 0.05W$, where $x = 1$ (lines) and $x = 2$ (points). Note that the described features do not change scaling the system parameters. For large $xg_{\rm ph} = 0.1W$ we find an additional sideband at $\omega_{\rm ac} = \varepsilon + 2\omega_{\rm ph}$ in the NRG results for the real part of $\mathcal{G}_{LR}(\omega_{\rm ac})$. The corresponding features can be extracted from the imaginary part of $\mathcal{G}_{LR}(\omega_{\rm ac})$ as well, though they are not as clearly distinguishable as in the real part (cf. left panel).

14.5.4 Vanishing Transconductance for $\omega_{\rm ac} \to 0$.

We have discussed the appearance of sub-threshold transconductance, i.e. a finite conductance for $\omega_{\rm ac} < \omega_{\rm ph}$ in the AC case, in Sec. 14.5.1. While the arguments given there explain the vanishing of conductance in the DC limit in lowest order in the electron-phonon coupling $g_{\rm ph}$, it is not obvious that higher-order processes do not change this picture.

One may naturally ask about the effects of the broadening of the phonon propagator due to coupling to the electrons. Some (though not all) higher-order effects can thus be captured by calculating the electronic self-energies with a phonon propagator dressed with electronic polarization bubbles. In the DC case, one finds that electrons can indeed absorb an energy up to eV from the phononic bath broadened by coupling to the electrons, instead of needing to emit $\omega_{\rm ph}$ as in lowest order. Nonetheless, the weight of such contributions is small leading to a current dependence $I \propto (eV)^3$ for small bias voltage for the considered higher-order contributions in the electron-phonon coupling and consequently a vanishing linear conductance at zero frequency. This agrees with the DC limit of our NRG results for the AC conductance presented in Fig. 14.13, which indicates as discussed that all higher-order contributions to the linear zero-temperature conductance vanish. We thus confirm the naive perturbative argument, that there are no incoherent transport processes at vanishing frequency, temperature and transport voltage.

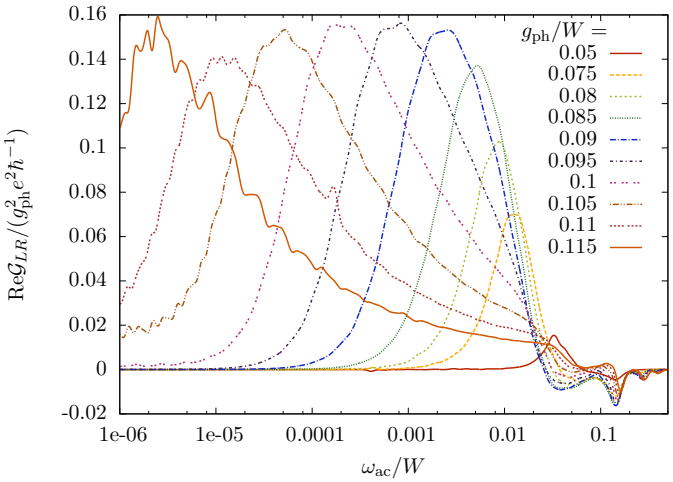

Figure 14.13: Real part of the transconductance $\mathcal{G}_{LR}(\omega_{\mathrm{ac}})$ on a logarithmic scale. Notice that even though for $g_{\mathrm{ph}} > \omega_{\mathrm{ph}}$ the peak in the transconductance shifts to smaller AC frequencies ω_{ac}, in the limit of very small frequencies we always obtain $\lim_{\omega_{\mathrm{ac}}\to 0} \mathcal{G}_{LR}(\omega_{\mathrm{ac}}) = 0$. ($\Gamma_{\nu,\sigma} = \pm 0.01, \varepsilon_\nu = 0.05, \omega_{ph} = 0.1$)

14.6 Summary

In this last chapter of this thesis, we have investigated the influence of an Einstein phonon mode on the transport through an Aharonov-Bohm interferometer consisting of two quantum dots coupled in parallel to two lead electrodes. We applied the numerical renormalization group to calculate the conductance through the interferometer applying an AC bias to the lead electrodes.

The main numeric results of our investigation confirm and back up the findings of a perturbative nonequilibrium Green's function method (see Ref. [193]). In contrast to the case of DC conductance, we find transport below the threshold $\omega_{\mathrm{ac}} < \omega_{\mathrm{ph}}$, i.e. transport through the interferometer without real emission of phonons is possible (analogous to the case of a plate capacitance, where the electrostatic interaction leads to a finite AC conductance, but a vanishing DC conductance). We confirm the naive perturbative argument, that there are no incoherent transport processes at vanishing frequency, temperature and transport voltage. Thus $\lim_{\omega_{\mathrm{ac}}\to 0} \mathcal{G}_{LR}(\omega_{\mathrm{ac}}) = 0$, which is equivalent to stating that all higher-order contributions to the linear zero-temperature conductance vanish. The peak in the real part of transconductance was investigated in some detail. We found that the height scales like $\left(\frac{g_{\mathrm{ph}}}{\omega_{\mathrm{ph}}}\right)^2$ and is shifted to smaller AC frequencies $\omega_{\mathrm{ac}} < \varepsilon$ at larger electron-phonon coupling reminiscent of polaron shift. Additional resonances at sidebands of the level energy $\varepsilon = \varepsilon + n\omega_{\mathrm{ph}}$, where $n = 1, 2, \ldots$, stem from processes involving multiple phonons and could be verified using our numerical renormalization group method calculations.

Conclusions

A short summary of the main results of our research projects is presented at the end of each chapter of part III of this thesis. We will thus not sum up our investigations in the conclusions again, but instead refer to the corresponding chapters, if there is a particular interest in the answer to one of the questions raised in the introduction. Instead, let us take the opportunity to make a few general statements on the method and mention interesting topics for future research.

The method mainly used to obtain the results presented in this thesis is the numerical renormalization group method. Albeit being developed quite some time ago, it continues to be state-of-the-art for good reasons. As we have hopefully convinced you reading the preceding chapters, applying it to different scenarios allows to answer some interesting questions concerning the physics of strongly correlated matter.

We have extensively used recent enhancements of the method for our investigations, such as its ability to calculate the time-dependency of local observables as a reaction to a sudden change of parameters, or to account for finite-temperatures, or to reproduce correct results for different sum rules using the concept of a reduced density matrix. These enhancements, together with its very efficient way of dealing with quantum impurity systems choosing an especially tailored eigenbasis as a starting point, still constitute a unique selling point of the numerical renormalization group method.

Therefore one interesting topic of future research is the further enhancement of the method. As we have mentioned in the introduction, the reaction of local observables in quantum impurity systems to a sudden change of system parameters is only a starting point of the investigation of nonequilibrium phenomena. Experimentally it is more feasible to probe the reaction of the system to a periodic perturbation, such as laser light shone on a quantum dot, for example. One small step towards this enhancement could be to calculate time-dependent impurity observables by "switching" the system's parameters twice.

Another interesting area of research is the application of the numerical renormalization group method to different quantum impurity models. There are still numerous interesting models describing relevant experimental situations, for which additional insight in the physics can be won applying the method and its recent enhancements. One example is the resonant level model resulting from the bosonization-mapping of the two-spin boson model presented in Appendix E.

Last but certainly not least, let us take the opportunity to mention the various applications of the numerical renormalization group method within dynamical mean-field theory (DMFT). As we have pointed out in Chap. 7, the requirement of being a "fast" enough impurity solver to be of practical use within DMFT calculations could be met employing the improved version of the numerical renormalization group method taking advantage of the complete basis first introduced by Anders and Schiller. Here, only a relatively small number of eigenstates has

to be kept in each NRG-iteration to generate high-quality results for single-particle spectral functions of interest.

Bibliography

[1] D. Loss and D. P. DiVincenzo: "Quantum computation with quantum dots". Phys. Rev. A, **57** (1), 120 (1998).
http://dx.doi.org/10.1103/PhysRevA.57.120

[2] W. de Haas, J. de Boer, and G. van den Berg: "The electrical resistance of gold, copper and lead at low temperatures". Physica, **1** (7-12), 1115 (1934).
http://dx.doi.org/10.1016/S0031-8914(34)80310-2

[3] J. Kondo: "Resistance Minimum in Dilute Magnetic Alloys". Progress of Theoretical Physics, **32** (1), 37 (1964).
http://dx.doi.org/10.1143/PTP.32.37

[4] J. R. Schrieffer and P. A. Wolff: "Relation between the Anderson and Kondo Hamiltonians". Phys. Rev., **149** (2), 491 (1966).
http://dx.doi.org/10.1103/PhysRev.149.491

[5] P. W. Anderson: "Localized Magnetic States in Metals". Phys. Rev., **124** (1), 41 (1961).
http://dx.doi.org/10.1103/PhysRev.124.41

[6] A. A. Abrikosov: Physics, **2** (5) (1965).

[7] F. D. M. Haldane: "Scaling Theory of the Asymmetric Anderson Model". Phys. Rev. Lett., **40** (6), 416 (1978).
http://dx.doi.org/10.1103/PhysRevLett.40.416

[8] A. C. Hewson and J. Kondo: "Kondo Effect". Scholarpedia, **4** (3), 7529 (2009).
http://www.scholarpedia.org/article/Kondo_effect

[9] P. W. Anderson: "A poor man's derivation of scaling laws for the Kondo problem". Journal of Physics C: Solid State Physics, **3** (12), 2436 (1970).
http://dx.doi.org/10.1088/0022-3719/3/12/008

[10] K. G. Wilson: "The renormalization group: Critical phenomena and the Kondo problem". Rev. Mod. Phys., **47** (4), 773 (1975).
http://dx.doi.org/10.1103/RevModPhys.47.773

[11] P. Nozières: "A fermi-liquid description of the Kondo problem at low temperatures". Journal of Low Temperature Physics, **17** (1), 31 (1974).
http://dx.doi.org/10.1007/BF00654541

[12] P. Nozières and A. Blandin: "Kondo effect in real metals". Journal de Physique, **41** (3), 193 (1980).
http://dx.doi.org/10.1051/jphys:01980004103019300

[13] N. Andrei: "Diagonalization of the Kondo Hamiltonian". Phys. Rev. Lett., **45** (5), 379 (1980).
http://dx.doi.org/10.1103/PhysRevLett.45.379

[14] N. Andrei, K. Furuya, and J. H. Lowenstein: "Solution of the Kondo problem". Rev. Mod. Phys., **55** (2), 331 (1983).
http://dx.doi.org/10.1103/RevModPhys.55.331

[15] P. Wiegmann: "Exact solution of s-d exchange model at T = 0". JETP Letters, **31** (7), 364 (1980).
http://www.jetpletters.ac.ru/ps/1353/article_20434.shtml

[16] A. Tsvelick and P. Wiegmann: "Exact results in the theory of magnetic alloys". Advances in Physics, **32** (4), 453 (1983).
http://dx.doi.org/10.1080/00018738300101581

[17] Z. Fisk, H. R. Ott, T. M. Rice, and J. L. Smith: "Heavy-electron metals". Nature, **320** (6058), 124 (1986).
http://dx.doi.org/10.1038/320124a0

[18] L. Kouwenhoven and L. Glazman: "Revival of the Kondo effect". Physics World, **14** (1), 33 (2001).
http://arxiv.org/abs/cond-mat/0104100

[19] T. K. Ng and P. A. Lee: "On-Site Coulomb Repulsion and Resonant Tunneling". Phys. Rev. Lett., **61** (15), 1768 (1988).
http://dx.doi.org/10.1103/PhysRevLett.61.1768

[20] L. I. Glazman and M. É. Raĭkh: "Resonant Kondo transparency of a barrier with quasilocal impurity states". JETP Letters, **47**, 452 (1988).
http://www.jetpletters.ac.ru/ps/1095/article_16538.shtml

[21] D. Goldhaber-Gordon, H. Shtrikman, D. Mahalu, D. Abusch-Magder, U. Meirav, and M. A. Kastner: "Kondo effect in a single-electron transistor". Nature, **391**, 156 (1998).
http://dx.doi.org/10.1038/34373

[22] W. G. van der Wiel, S. D. Franceschi, T. Fujisawa, J. M. Elzerman, S. Tarucha, and L. P. Kouwenhoven: "The Kondo Effect in the Unitary Limit". Science, **289** (5487), 2105 (2000).
http://dx.doi.org/10.1126/science.289.5487.2105

[23] R. Hanson and D. D. Awschalom: "Coherent manipulation of single spins in semiconductors". Nature, **453** (7198), 1043 (2008).
http://dx.doi.org/10.1038/nature07129

[24] T. Fujisawa, D. G. Austing, Y. Tokura, Y. Hirayama, and S. Tarucha: "Allowed and forbidden transitions in artificial hydrogen and helium atoms". Nature, **419**, 278 (2002).
http://dx.doi.org/10.1038/nature00976

[25] R. Hanson: "Single-shot readout of electron spin states in a quantum dot using spin-dependent tunnel rates". Phys. Rev. Lett., **94**, 196802 (2005).
http://dx.doi.org/10.1103/PhysRevLett.94.196802

[26] S. Amasha: "Electrical control of spin relaxation in a quantum dot". Phys. Rev. Lett., **100**, 046803 (2008).
http://dx.doi.org/10.1103/PhysRevLett.100.046803

[27] J. Levy: "Universal quantum computation with spin-1/2 pairs and Heisenberg exchange". Phys. Rev. Lett., **89**, 147902 (2002).
http://dx.doi.org/10.1103/PhysRevLett.89.147902

[28] J. R. Petta: "Coherent manipulation of coupled electron spins in semiconductor quantum dots". Science, **309**, 2180 (2005).
http://dx.doi.org/10.1126/science.1116955

[29] F. H. L. Koppens: "Driven coherent oscillations of a single electron spin in a quantum dot". Nature, **442**, 766 (2006).
http://dx.doi.org/10.1038/nature05065

[30] K. C. Nowack, F. H. L. Koppens, Y. V. Nazarov, and L. M. K. Vandersypen: "Coherent control of a single electron spin with electric fields". Science, **318**, 1430 (2007).
http://dx.doi.org/10.1126/science.1148092

[31] M. H. Mikkelsen, J. Berezovsky, N. G. Stoltz, L. A. Coldren, and D. D. Awschalom: "Optically detected coherent spin dynamics of a single electron in a quantum dot". Nature Phys., **3**, 770 (2007).
http://dx.doi.org/10.1038/nphys736

[32] C. Cohen-Tannoudji and J. Dupont-Roc: "Experimental study of Zeeman light shifts in weak magnetic fields". Phys. Rev. A, **5**, 968 (1972).
http://dx.doi.org/10.1103/PhysRevA.5.968

[33] J. Berezovsky, M. H. Mikkelsen, N. G. Stoltz, L. A. Coldren, and D. D. Awschalom: "Picosecond coherent optical manipulation of a single electron spin in a quantum dot". Science, **320**, 349 (2008).
http://dx.doi.org/10.1126/science.1154798

[34] F. Jelezko, I. Popa, A. Gruber, and J. Wrachtrup: "Single spin states in a defect center resolved by optical spectroscopy". Appl. Phys. Lett., **81**, 2160 (2002).
http://dx.doi.org/10.1063/1.1507838

[35] F. Jelezko, T. Gaebel, I. Popa, A. Gruber, and J. Wrachtrup: "Observation of coherent oscillations in a single electron spin". Phys. Rev. Lett., **92**, 76401 (2004).
http://dx.doi.org/10.1103/PhysRevLett.92.076401

[36] D. D. Awschalom, R. Epstein, and R. Hanson: "The Diamond Age Diamond Age of Spintronics". Scientific American, **297**, 84 (2007).
http://dx.doi.org/10.1038/scientificamerican1007-84

[37] L. Bogani and W. Wernsdorfer: "Molecular spintronics using single-molecule magnets". Nat Mater, **7** (3), 179 (2008).
http://dx.doi.org/10.1038/nmat2133

[38] H. B. Heersche, Z. de Groot, J. A. Folk, H. S. J. van der Zant, C. Romeike, M. R. Wegewijs, L. Zobbi, D. Barreca, E. Tondello, and A. Cornia: "Electron Transport through Single Mn[sub 12] Molecular Magnets". Phys. Rev. Lett., **96** (20), 206801 (2006).
http://dx.doi.org/10.1103/PhysRevLett.96.206801

[39] N. Roch, S. Florens, V. Bouchiat, W. Wernsdorfer, and F. Balestro: "Quantum phas transition in a single-molecul quantum dot". Nature, **453**, 633 (2008).
http://dx.doi.org/10.1038/nature06930

[40] S. Sasaki, S. De Franceschi, J. M. Elzerman, W. G. van der Wiel, M. Eto, S. Tarucha, and L. P. Kouwenhoven: "Kondo effect in an integer-spin quantum dot". Nature, **405** (6788), 764 (2000).
http://dx.doi.org/10.1038/35015509

[41] W. Hofstetter and H. Schoeller: "Quantum Phase Transition in a Multilevel Dot". Phys. Rev. Lett., **88** (1), 016803 (2001).
http://dx.doi.org/10.1103/PhysRevLett.88.016803

[42] M. Vojta, R. Bulla, and W. Hofstetter: "Quantum phase transitions in models of coupled magnetic impurities". Phys. Rev. B, **65** (14), 140405 (2002).
http://dx.doi.org/10.1103/PhysRevB.65.140405

[43] D. Gatteschi and R. Sessoli: "Quantum Tunneling of Magnetization and Related Phenomena in Molecular Materials". Angewandte Chemie International Edition, **42** (3), 268 (2003).
http://dx.doi.org/10.1002/anie.200390099

[44] G. Christou, D. Gatteschi, D. N. Hendrickson, and R. Sessoli: "Single-Molecule Magnets". Mater. Res. Soc. Bull., **25**, 66 (2000).
http://www.mrs.org/s_mrs/sec_subscribe.asp?CID=2940&DID=173220&action=detail

[45] L. Thomas, F. Lionti, R. Ballou, D. Gatteschi, R. Sessoli, and B. Barbara: "Macroscopic quantum tunnelling of magnetization in a single crystal of nanomagnets". Nature, **383** (6596), 145 (1996).
http://dx.doi.org/10.1038/383145a0

[46] J. R. Friedman, M. P. Sarachik, J. Tejada, and R. Ziolo: "Macroscopic Measurement of Resonant Magnetization Tunneling in High-Spin Molecules". Phys. Rev. Lett., **76** (20), 3830 (1996).
http://dx.doi.org/10.1103/PhysRevLett.76.3830

[47] W. Wernsdorfer and R. Sessoli: "Quantum Phase Interference and Parity Effects in Magnetic Molecular Clusters". Science, **284** (5411), 133 (1999).
http://dx.doi.org/10.1126/science.284.5411.133

[48] A. Ardavan, O. Rival, J. J. L. Morton, S. J. Blundell, A. M. Tyryshkin, G. A. Timco, and R. E. P. Winpenny: "Will Spin-Relaxation Times in Molecular Magnets Permit Quantum Information Processing?" Phys. Rev. Lett., **98** (5), 057201 (2007).
http://dx.doi.org/10.1103/PhysRevLett.98.057201

[49] F. Elste and C. Timm: "Transport through anisotropic magnetic molecules with partially ferromagnetic leads: Spin-charge conversion and negative differential conductance". Phys. Rev. B, **73** (23), 235305 (2006).
http://dx.doi.org/10.1103/PhysRevB.73.235305

[50] M. N. Leuenberger and D. Loss: "Quantum computing in molecular magnets". Nature, **410** (6830), 789 (2001).
http://dx.doi.org/10.1038/35071024

[51] M.-H. Jo, J. Grose, K. Baheti, M. Deshmukh, J. Sokol, E. Rumberger, D. Hendrickson, J. Long, H. Park, and D. Ralph: "Signatures of Molecular Magnetism in Single-Molecule Transport Spectroscopy". Nano Letters, **6** (9), 2014 (2006).
http://dx.doi.org/10.1021/nl061212i

[52] M. R. Pederson, N. Bernstein, and J. Kortus: "Fourth-Order Magnetic Anisotropy and Tunnel Splittings in $Mn12$ from Spin-Orbit-Vibron Interactions". Phys. Rev. Lett., **89** (9), 097202 (2002).
http://dx.doi.org/10.1103/PhysRevLett.89.097202

[53] R. Bulla, T. A. Costi, and T. Pruschke: "Numerical renormalization group method for quantum impurity systems". Reviews of Modern Physics, **80** (2), 395 (2008).
http://dx.doi.org/10.1103/RevModPhys.80.395

[54] H. R. Krishna-murthy, J. W. Wilkins, and K. G. Wilson: "Renormalization-group approach to the Anderson model of dilute magnetic alloys. I. Static properties for the symmetric case". Phys. Rev. B, **21** (3), 1003 (1980).
http://dx.doi.org/10.1103/PhysRevB.21.1003

[55] R. Bulla, T. Pruschke, and A. Hewson: "Anderson impurity in pseudo-gap Fermi systems". Journal of Physics: Condensed Matter, **9** (47), 10463 (1997).
http://dx.doi.org/10.1088/0953-8984/9/47/014

[56] S. R. White: "Density matrix formulation for quantum renormalization groups". Phys. Rev. Lett., **69** (19), 2863 (1992).
http://dx.doi.org/10.1103/PhysRevLett.69.2863

[57] U. Schollwöck: "The density-matrix renormalization group". Rev. Mod. Phys., **77** (1), 259 (2005).
http://dx.doi.org/10.1103/RevModPhys.77.259

[58] A. Hewson: The Kondo Problem to Heavy Fermions, volume 2 of *Cambridge Studies in Magnetism*. Cambridge University Press (1997).

[59] J. von Delft and H. Schoeller: "Bosonization for beginners - refermionization for experts". Annalen der Physik, **7** (4), 225 (1998).
http://dx.doi.org/10.1002/(SICI)1521-3889(199811)7:4<225::AID-ANDP225>3.0.CO;2-L

[60] R. Bulla, N.-H. Tong, and M. Vojta: "Numerical Renormalization Group for Bosonic Systems and Application to the Sub-Ohmic Spin-Boson Model". Phys. Rev. Lett., **91** (17), 170601 (2003).
http://dx.doi.org/10.1103/PhysRevLett.91.170601

[61] R. Bulla, H.-J. Lee, N.-H. Tong, and M. Vojta: "Numerical renormalization group for quantum impurities in a bosonic bath". Phys. Rev. B, **71** (4), 045122 (2005).
http://dx.doi.org/10.1103/PhysRevB.71.045122

[62] A. J. Leggett, S. Chakravarty, A. T. Dorsey, M. P. A. Fisher, A. Garg, and W. Zwerger: "Dynamics of the dissipative two-state system". Rev. Mod. Phys., **59** (1), 1 (1987).
http://dx.doi.org/10.1103/RevModPhys.59.1

[63] W. Hofstetter: "Generalized Numerical Renormalization Group for Dynamical Quantities". Phys. Rev. Lett., **85** (7), 1508 (2000).
http://dx.doi.org/10.1103/PhysRevLett.85.1508

[64] R. Bulla, T. A. Costi, and D. Vollhardt: "Finite-temperature numerical renormalization group study of the Mott transition". Phys. Rev. B, **64** (4), 045103 (2001).
http://dx.doi.org/10.1103/PhysRevB.64.045103

[65] A. Weichselbaum, F. Verstraete, U. Schollwöck, J. I. Cirac, and J. von Delft: "Variational matrix-product-state approach to quantum impurity models". Phys. Rev. B, **80** (16), 165117 (2009).
http://dx.doi.org/10.1103/PhysRevB.80.165117

[66] F. B. Anders and A. Schiller: "Real-Time Dynamics in Quantum-Impurity Systems: A Time-Dependent Numerical Renormalization-Group Approach". Phys. Rev. Lett., **95** (19), 196801 (2005).
http://dx.doi.org/10.1103/PhysRevLett.95.196801

[67] F. B. Anders and A. Schiller: "Spin precession and real-time dynamics in the Kondo model: Time-dependent numerical renormalization-group study". Phys. Rev. B, **74** (24), 245113 (2006).
http://dx.doi.org/10.1103/PhysRevB.74.245113

[68] R. Peters, T. Pruschke, and F. B. Anders: "Numerical renormalization group approach to Green's functions for quantum impurity models". Phys. Rev. B, **74** (24), 245114 (2006).
http://dx.doi.org/10.1103/PhysRevB.74.245114

[69] W. Metzner and D. Vollhardt: "Correlated Lattice Fermions in $d = \infty$ Dimensions". Phys. Rev. Lett., **62** (3), 324 (1989).
http://dx.doi.org/10.1103/PhysRevLett.62.324

[70] A. Georges and G. Kotliar: "Hubbard model in infinite dimensions". Phys. Rev. B, **45** (12), 6479 (1992).
http://dx.doi.org/10.1103/PhysRevB.45.6479

[71] A. Georges, G. Kotliar, W. Krauth, and M. J. Rozenberg: "Dynamical mean-field theory of strongly correlated fermion systems and the limit of infinite dimensions". Rev. Mod. Phys., **68** (1), 13 (1996).
http://dx.doi.org/10.1103/RevModPhys.68.13

[72] D. Semmler: "Where NRG as an impurity solver for the dynamical mean-field theory could be useful" (2010). Private communication with.

[73] A. Hackl and S. Kehrein: "Real time evolution in quantum many-body systems with unitary perturbation theory". Phys. Rev. B, **78** (9), 092303 (2008).
http://dx.doi.org/10.1103/PhysRevB.78.092303

[74] T. A. Costi and C. Kieffer: "Equilibrium Dynamics of the Dissipative Two-State System". Phys. Rev. Lett., **76** (10), 1683 (1996).
http://dx.doi.org/10.1103/PhysRevLett.76.1683

[75] A. Weichselbaum and J. von Delft: "Sum-Rule Conserving Spectral Functions from the Numerical Renormalization Group". Phys. Rev. Lett., **99** (7), 076402 (2007).
http://dx.doi.org/10.1103/PhysRevLett.99.076402

[76] T. Barthel, U. Schollwöck, and S. R. White: "Spectral functions in one-dimensional quantum systems at finite temperature using the density matrix renormalization group". Phys. Rev. B, **79** (24), 245101 (2009).
http://dx.doi.org/10.1103/PhysRevB.79.245101

[77] E. Noether: "Invariante Variationsprobleme". Nachrichten von der Gesellschaft der Wissenschaften zu Göttingen, Mathematisch-Physikalische Klasse, pages 235–257 (1918).
http://resolver.sub.uni-goettingen.de/purl?GDZPPN00250510X

[78] M. Yoshida, M. A. Whitaker, and L. N. Oliveira: "Renormalization-group calculation of excitation properties for impurity models". Phys. Rev. B, **41** (13), 9403 (1990).
http://dx.doi.org/10.1103/PhysRevB.41.9403

[79] R. Zitko and T. Pruschke: "Energy resolution and discretization artifacts in the numerical renormalization group". Phys. Rev. B, **79** (8), 085106 (2009).
http://dx.doi.org/10.1103/PhysRevB.79.085106

[80] R. Bulla, A. C. Hewson, and T. Pruschke: "Numerical renormalization group calculations for the self-energy of the impurity Anderson model". Journal of Physics: Condensed Matter, **10** (37), 8365 (1998).
http://dx.doi.org/10.1088/0953-8984/10/37/021

[81] A. Isidori, D. Roosen, L. Bartosch, W. Hofstetter, and P. Kopietz: "Spectral function of the Anderson impurity model at finite temperatures". Phys. Rev. B, **81** (23), 235120 (2010).
http://dx.doi.org/10.1103/PhysRevB.81.235120

[82] P. Kopietz, L. Bartosch, and F. Schütz: Introduction to the Functional Renormalization Group. Springer Heidelberg (2010).
http://www.springer.com/physics/book/978-3-642-05093-0

[83] L. Borda, M. Garst, and J. Kroha: "Kondo cloud and spin-spin correlations around a partially screened magnetic impurity". Phys. Rev. B, **79** (10), 100408 (2009).
http://dx.doi.org/10.1103/PhysRevB.79.100408

[84] S. Kehrein: The Flow Equation Approach to Many-Particle Systems, volume 217 of *Springer Tracts in Modern Physics*. Springer (2006).
http://www.springer.com/materials/book/978-3-540-34067-6

[85] W. Koller, A. C. Hewson, and D. Meyer: "Singular dynamics of underscreened magnetic impurity models". Physical Review B (Condensed Matter and Materials Physics), **72** (4), 045117 (2005).
http://dx.doi.org/10.1103/PhysRevB.72.045117

[86] D. Roosen, M. R. Wegewijs, and W. Hofstetter: "Nonequilibrium Dynamics of Anisotropic Large Spins in the Kondo Regime: Time-Dependent Numerical Renormalization Group Analysis". Phys. Rev. Lett., **100** (8), 087201 (2008).
http://dx.doi.org/10.1103/PhysRevLett.100.087201

[87] D. M. Cragg and P. Lloyd: "Universality and the renormalisability of rotationally invariant Kondo Hamiltonians". Journal of Physics C: Solid State Physics, **12** (16), 3301 (1979).
http://dx.doi.org/10.1088/0022-3719/12/16/018

[88] P. Coleman and C. Pépin: "Singular Fermi liquid behavior in the underscreened Kondo model". Phys. Rev. B, **68** (22), 220405 (2003).
http://dx.doi.org/10.1103/PhysRevB.68.220405

[89] G. González, M. N. Leuenberger, and E. R. Mucciolo: "Kondo effect in single-molecule magnet transistors". Phys. Rev. B, **78** (5), 054445 (2008).
http://dx.doi.org/10.1103/PhysRevB.78.054445

[90] P.-F. Braun, X. Marie, L. Lombez, B. Urbaszek, T. Amand, P. Renucci, V. K. Kalevich, K. V. Kavokin, O. Krebs, P. Voisin, and Y. Masumoto: "Direct Observation of the Electron Spin Relaxation Induced by Nuclei in Quantum Dots". Phys. Rev. Lett., **94** (11), 116601 (2005).
http://dx.doi.org/10.1103/PhysRevLett.94.116601

[91] M. Atature, J. Dreiser, A. Badolato, and A. Imamoglu: "Observation of Faraday rotation from a single confined spin". Nat Phys, **3** (2), 101 (2007).
http://dx.doi.org/10.1038/nphys521

[92] A. J. Daley, C. Kollath, U. Schollwöck, and G. Vidal: "Time-dependent density-matrix renormalization-group using adaptive effective Hilbert spaces". Journal of Statistical Mechanics: Theory and Experiment, **2004** (04), P04005 (2004). http://dx.doi.org/10.1088/1742-5468/2004/04/P04005

[93] S. R. White and A. E. Feiguin: "Real-Time Evolution Using the Density Matrix Renormalization Group". Phys. Rev. Lett., **93** (7), 076401 (2004). http://dx.doi.org/10.1103/PhysRevLett.93.076401

[94] U. Schollwöck and S. R. White: "Methods for Time Dependence in DMRG". In G. G. Batrouni and D. Poilblanc, editors, "EFFECTIVE MODELS FOR LOW-DIMENSIONAL STRONGLY CORRELATED SYSTEMS", volume 816 (1), pages 155–185. AIP (2006). http://dx.doi.org/10.1063/1.2178041

[95] H. Schoeller: An Introduction to Real-Time Renormalization Group, volume 544 of *Lecture Notes in Physics*, pages 137–166. Springer Berlin / Heidelberg (2000). http://dx.doi.org/10.1007/3-540-46438-7_7

[96] L. Mühlbacher and E. Rabani: "Real-Time Path Integral Approach to Nonequilibrium Many-Body Quantum Systems". Phys. Rev. Lett., **100** (17), 176403 (2008). http://dx.doi.org/10.1103/PhysRevLett.100.176403

[97] S. Weiss, J. Eckel, M. Thorwart, and R. Egger: "Iterative real-time path integral approach to nonequilibrium quantum transport". Phys. Rev. B, **77** (19), 195316 (2008). http://dx.doi.org/10.1103/PhysRevB.77.195316

[98] F. Wegner: "Flow-equations for Hamiltonians". Annalen der Physik, **506** (2), 77 (1994). http://dx.doi.org/10.1002/andp.19945060203

[99] S. D. Głazek and K. G. Wilson: "Renormalization of Hamiltonians". Phys. Rev. D, **48** (12), 5863 (1993). http://dx.doi.org/10.1103/PhysRevD.48.5863

[100] S. D. Glazek and K. G. Wilson: "Perturbative renormalization group for Hamiltonians". Phys. Rev. D, **49** (8), 4214 (1994). http://dx.doi.org/10.1103/PhysRevD.49.4214

[101] A. Hackl and S. Kehrein: "A unitary perturbation theory approach to real-time evolution problems". Journal of Physics: Condensed Matter, **21** (1), 015601 (2009). http://dx.doi.org/10.1088/0953-8984/21/1/015601

[102] A. Hackl, M. Vojta, and S. Kehrein: "Nonequilibrium magnetization dynamics of ferromagnetically coupled Kondo spins". Phys. Rev. B, **80** (19), 195117 (2009). http://dx.doi.org/10.1103/PhysRevB.80.195117

[103] M. Moeckel and S. Kehrein: "Interaction Quench in the Hubbard Model". Phys. Rev. Lett., **100** (17), 175702 (2008). http://dx.doi.org/10.1103/PhysRevLett.100.175702

[104] M. Heyl and S. Kehrein: "Interaction quench dynamics in the Kondo model in the presence of a local magnetic field". Journal of Physics: Condensed Matter, **22** (34), 345604 (2010).
http://dx.doi.org/10.1088/0953-8984/22/34/345604

[105] M. Pletyukhov, D. Schuricht, and H. Schoeller: "Relaxation versus Decoherence: Spin and Current Dynamics in the Anisotropic Kondo Model at Finite Bias and Magnetic Field". Phys. Rev. Lett., **104** (10), 106801 (2010).
http://dx.doi.org/10.1103/PhysRevLett.104.106801

[106] M. Moeckel and S. Kehrein: "Real-time evolution for weak interaction quenches in quantum systems". Annals of Physics, **324** (10), 2146 (2009).
http://dx.doi.org/10.1016/j.aop.2009.03.009

[107] F. Guinea, V. Hakim, and A. Muramatsu: "Bosonization of a two-level system with dissipation". Phys. Rev. B, **32** (7), 4410 (1985).
http://dx.doi.org/10.1103/PhysRevB.32.4410

[108] U. Weiss: Quantum Dissipative Systems; 3rd ed. Series in Modern Condensed Matter Physics. World Scientific, Singapore (2008).

[109] K. Le Hur: "Quantum Phase Transitions in Spin-Boson Systems: Dissipation and Light Phenomena". arXiv:0909.4822v1 (2009).
http://arxiv.org/abs/0909.4822

[110] R. A. Marcus: "On the Theory of Oxidation-Reduction Reactions Involving Electron Transfer. I". J. Chem. Phys., **24** (5), 966 (1956).
http://dx.doi.org/10.1063/1.1742723

[111] R. A. Marcus and N. Sutin: "Electron transfers in chemistry and biology". Biochim. Biophys. Acta, **811** (3), 265 (1985).
http://dx.doi.org/10.1016/0304-4173(85)90014-X

[112] Y. Makhlin, G. Schön, and A. Shnirman: "Quantum-state engineering with Josephson-junction devices". Rev. Mod. Phys., **73** (2), 357 (2001).
http://dx.doi.org/10.1103/RevModPhys.73.357

[113] J. E. Mooij, T. P. Orlando, L. Levitov, L. Tian, C. H. van der Wal, and S. Lloyd: "Josephson Persistent-Current Qubit". Science, **285** (5430), 1036 (1999).
http://dx.doi.org/10.1126/science.285.5430.1036

[114] V. E. Manucharyan, J. Koch, M. Brink, L. I. Glazman, and M. H. Devoret: "Coherent oscillations between classically separable quantum states of a superconducting loop". arXiv:0910.3039v1 (2009).
http://arxiv.org/abs/0910.3039

[115] D. Porras, F. Marquardt, J. von Delft, and J. I. Cirac: "Mesoscopic spin-boson models of trapped ions". Phys. Rev. A, **78** (1), 010101 (2008).
http://dx.doi.org/10.1103/PhysRevA.78.010101

[116] J. Kästel, M. Fleischhauer, S. F. Yelin, and R. L. Walsworth: "Tunable Negative Refraction without Absorption via Electromagnetically Induced Chirality". Phys. Rev. Lett., **99** (7), 073602 (2007).
http://dx.doi.org/10.1103/PhysRevLett.99.073602

[117] A. Recati, P. O. Fedichev, W. Zwerger, J. von Delft, and P. Zoller: "Atomic Quantum Dots Coupled to a Reservoir of a Superfluid Bose-Einstein Condensate". Phys. Rev. Lett., **94** (4), 040404 (2005).
http://dx.doi.org/10.1103/PhysRevLett.94.040404

[118] P. P. Orth, I. Stanic, and K. Le Hur: "Dissipative quantum Ising model in a cold-atom spin-boson mixture". Phys. Rev. A, **77** (5), 051601 (2008).
http://dx.doi.org/10.1103/PhysRevA.77.051601

[119] D. Pertot, B. Gadway, and D. Schneble: "Collinear Four-Wave Mixing of Two-Component Matter Waves". Phys. Rev. Lett., **104** (20), 200402 (2010).
http://dx.doi.org/10.1103/PhysRevLett.104.200402

[120] B. Gadway, D. Pertot, R. Reimann, and D. Schneble: "Superfluidity of Interacting Bosonic Mixtures in Optical Lattices". Phys. Rev. Lett., **105** (4), 045303 (2010).
http://dx.doi.org/10.1103/PhysRevLett.105.045303

[121] J. M. Raimond, M. Brune, and S. Haroche: "Manipulating quantum entanglement with atoms and photons in a cavity". Rev. Mod. Phys., **73** (3), 565 (2001).
http://dx.doi.org/10.1103/RevModPhys.73.565

[122] R. J. Schoelkopf and S. M. Girvin: "Wiring up quantum systems". Nature, **451** (7179), 664 (2008).
http://dx.doi.org/10.1038/451664a

[123] J. Koch and K. Le Hur: "Superfluid–Mott-insulator transition of light in the Jaynes-Cummings lattice". Phys. Rev. A, **80** (2), 023811 (2009).
http://dx.doi.org/10.1103/PhysRevA.80.023811

[124] M. Hartmann, F. Brando, and M. Plenio: "Quantum many-body phenomena in coupled cavity arrays". Laser & Photon. Rev., **2** (6), 527 (2008).
http://dx.doi.org/10.1002/lpor.200810046

[125] S. Chakravarty: "Quantum Fluctuations in the Tunneling between Superconductors". Phys. Rev. Lett., **49** (9), 681 (1982).
http://dx.doi.org/10.1103/PhysRevLett.49.681

[126] A. J. Bray and M. A. Moore: "Influence of Dissipation on Quantum Coherence". Phys. Rev. Lett., **49** (21), 1545 (1982).
http://dx.doi.org/10.1103/PhysRevLett.49.1545

[127] F. D. M. Haldane: "Luttinger liquid theory' of one-dimensional quantum fluids. I. Properties of the Luttinger model and their extension to the general 1D interacting spinless Fermi gas". Journal of Physics C: Solid State Physics, **14** (19), 2585 (1981).
http://dx.doi.org/10.1088/0022-3719/14/19/010

[128] M. Garst, S. Kehrein, T. Pruschke, A. Rosch, and M. Vojta: "Quantum phase transition of Ising-coupled Kondo impurities". Phys. Rev. B, **69** (21), 214413 (2004). http://dx.doi.org/10.1103/PhysRevB.69.214413

[129] K. Le Hur: "Entanglement entropy, decoherence, and quantum phase transitions of a dissipative two-level system". Annals of Physics, **323** (9), 2208 (2008). http://dx.doi.org/10.1016/j.aop.2007.12.003

[130] A. Kopp and K. Le Hur: "Universal and measurable entanglement entropy in the spin-boson model". Phys. Rev. Lett., **98** (22), 220401 (2007). http://dx.doi.org/10.1103/PhysRevLett.98.220401

[131] A. Kopp, X. Jia, and S. Chakravarty: "Replacing energy by von Neumann entropy in quantum phase transitions". Annals of Physics, **322** (6), 1466 (2007). http://dx.doi.org/10.1016/j.aop.2006.08.002

[132] J. von Neumann: "Thermodynamik quantenmechanischer Gesamtheiten". Nachrichten von der Gesellschaft der Wissenschaften zu Göttingen, Mathematisch-Physikalische Klasse, pages 273–291 (1927). http://resolver.sub.uni-goettingen.de/purl?GDZPPN002507285

[133] L. Amico, R. Fazio, A. Osterloh, and V. Vedral: "Entanglement in many-body systems". Rev. Mod. Phys., **80** (2), 517 (2008). http://dx.doi.org/10.1103/RevModPhys.80.517

[134] A. Wehrl: "General properties of entropy". Rev. Mod. Phys., **50** (2), 221 (1978). http://dx.doi.org/10.1103/RevModPhys.50.221

[135] A.-P. Jauho, N. S. Wingreen, and Y. Meir: "Time-dependent transport in interacting and noninteracting resonant-tunneling systems". Phys. Rev. B, **50** (8), 5528 (1994). http://dx.doi.org/10.1103/PhysRevB.50.5528

[136] L. Hartmann, I. Goychuk, M. Grifoni, and P. Hänggi: "Driven tunneling dynamics: Bloch-Redfield theory versus path-integral approach". Phys. Rev. E, **61** (5), R4687 (2000). http://dx.doi.org/10.1103/PhysRevE.61.R4687

[137] M.-L. Zhang, S. Zhang, and E. Pollak: "Low temperature extension of the generalized Zusman phase space equations for electron transfer". J. Chem. Phys., **120** (20), 9630 (2004). http://dx.doi.org/10.1063/1.1701837

[138] E. Martin-Fierro and E. Pollak: "Semiclassical initial value series solution of the spin boson problem". J. Chem. Phys., **126** (16), 164108 (2007). http://dx.doi.org/10.1063/1.2714520

[139] L. Mühlbacher and R. Egger: "Crossover from nonadiabatic to adiabatic electron transfer reactions: Multilevel blocking Monte Carlo simulations". J. Chem. Phys., **118** (1), 179 (2003). http://link.aip.org/link/?JCP/118/179/1

[140] A. J. Leggett, S. Chakravarty, A. T. Dorsey, M. P. A. Fisher, A. Garg, and W. Zwerger: "Erratum: Dynamics of the dissipative two-state system". Rev. Mod. Phys., **67** (3), 725 (1995).
http://dx.doi.org/10.1103/RevModPhys.67.725

[141] H. Dekker: "Noninteracting-blip approximation for a two-level system coupled to a heat bath". Phys. Rev. A, **35** (3), 1436 (1987).
http://dx.doi.org/10.1103/PhysRevA.35.1436

[142] F. Lesage and H. Saleur: "Boundary Interaction Changing Operators and Dynamical Correlations in Quantum Impurity Problems". Phys. Rev. Lett., **80** (20), 4370 (1998).
http://dx.doi.org/10.1103/PhysRevLett.80.4370

[143] R. Egger, H. Grabert, and U. Weiss: "Crossover from coherent to incoherent dynamics in damped quantum systems". Phys. Rev. E, **55** (4), R3809 (1997).
http://dx.doi.org/10.1103/PhysRevE.55.R3809

[144] H. Wang and M. Thoss: "From coherent motion to localization: dynamics of the spin-boson model at zero temperature". New Journal of Physics, **10** (11), 115005 (2008).
http://dx.doi.org/10.1088/1367-2630/10/11/115005

[145] T. Zell, F. Queisser, and R. Klesse: "Distance Dependence of Entanglement Generation via a Bosonic Heat Bath". Phys. Rev. Lett., **102** (16), 160501 (2009).
http://dx.doi.org/10.1103/PhysRevLett.102.160501

[146] F. R. Waugh, M. J. Berry, D. J. Mar, R. M. Westervelt, K. L. Campman, and A. C. Gossard: "Single-Electron Charging in Double and Triple Quantum Dots with Tunable Coupling". Phys. Rev. Lett., **75** (4), 705 (1995).
http://dx.doi.org/10.1103/PhysRevLett.75.705

[147] K. A. Matveev, L. I. Glazman, and H. U. Baranger: "Tunneling spectroscopy of quantum charge fluctuations in the Coulomb blockade". Phys. Rev. B, **53** (3), 1034 (1996).
http://dx.doi.org/10.1103/PhysRevB.53.1034

[148] J. M. Golden and B. I. Halperin: "Relation between barrier conductance and Coulomb blockade peak splitting for tunnel-coupled quantum dots". Phys. Rev. B, **53** (7), 3893 (1996).
http://dx.doi.org/10.1103/PhysRevB.53.3893

[149] L. D. Contreras-Pulido and R. Aguado: "Entanglement between charge qubits induced by a common dissipative environment". Phys. Rev. B, **77** (15), 155420 (2008).
http://dx.doi.org/10.1103/PhysRevB.77.155420

[150] G. Campagnano, A. Hamma, and U. Weiss: "Entanglement dynamics of coupled qubits and a semi-decoherence free subspace". Physics Letters A, **374** (3), 416 (2010).
http://dx.doi.org/10.1016/j.physleta.2009.10.081

[151] D. Solenov, D. Tolkunov, and V. Privman: "Exchange interaction, entanglement, and quantum noise due to a thermal bosonic field". Phys. Rev. B, **75** (3), 035134 (2007).
http://dx.doi.org/10.1103/PhysRevB.75.035134

[152] D. Braun: "Creation of Entanglement by Interaction with a Common Heat Bath". Phys. Rev. Lett., **89** (27), 277901 (2002).
http://dx.doi.org/10.1103/PhysRevLett.89.277901

[153] F. Benatti, R. Floreanini, and M. Piani: "Environment Induced Entanglement in Markovian Dissipative Dynamics". Phys. Rev. Lett., **91** (7), 070402 (2003).
http://dx.doi.org/10.1103/PhysRevLett.91.070402

[154] P. Nägele and U. Weiss: "Dynamics of coupled spins in the white- and quantum-noise regime". Physica E: Low-dimensional Systems and Nanostructures, **42** (3), 622 (2010). Proceedings of the international conference Frontiers of Quantum and Mesoscopic Thermodynamics FQMT '08.
http://dx.doi.org/10.1016/j.physe.2009.06.060

[155] P. Nägele, G. Campagnano, and U. Weiss: "Dynamics of dissipative coupled spins: decoherence, relaxation and effects of a spin-boson bath". New Journal of Physics, **10** (11), 115010 (2008).
http://dx.doi.org/10.1088/1367-2630/10/11/115010

[156] N.-H. Tong and M. Vojta: "Signatures of a Noise-Induced Quantum Phase Transition in a Mesoscopic Metal Ring". Phys. Rev. Lett., **97** (1), 016802 (2006).
http://dx.doi.org/10.1103/PhysRevLett.97.016802

[157] S. Kirchner and Q. Si: "Quantum Criticality Out of Equilibrium: Steady State in a Magnetic Single-Electron Transistor". Phys. Rev. Lett., **103** (20), 206401 (2009).
http://dx.doi.org/10.1103/PhysRevLett.103.206401

[158] S. Tornow, R. Bulla, F. B. Anders, and A. Nitzan: "Dissipative two-electron transfer: A numerical renormalization group study". Physical Review B (Condensed Matter and Materials Physics), **78** (3), 035434 (2008).
http://dx.doi.org/10.1103/PhysRevB.78.035434

[159] D. P. S. McCutcheon, A. Nazir, S. Bose, and A. J. Fisher: "Separation-dependent localization in a two-impurity spin-boson model". Phys. Rev. B, **81** (23), 235321 (2010).
http://dx.doi.org/10.1103/PhysRevB.81.235321

[160] F. B. Anders, R. Bulla, and M. Vojta: "Equilibrium and Nonequilibrium Dynamics of the Sub-Ohmic Spin-Boson Model". Phys. Rev. Lett., **98** (21), 210402 (2007).
http://dx.doi.org/10.1103/PhysRevLett.98.210402

[161] M. Vojta: "Impurity quantum phase transitions". Philosophical Magazine, **86** (13), 1807 (2006).
http://dx.doi.org/10.1080/14786430500070396

[162] A. Winter, H. Rieger, M. Vojta, and R. Bulla: "Quantum Phase Transition in the Sub-Ohmic Spin-Boson Model: Quantum Monte Carlo Study with a Continuous Imaginary Time Cluster Algorithm". Phys. Rev. Lett., **102** (3), 030601 (2009).
http://dx.doi.org/10.1103/PhysRevLett.102.030601

[163] M. Vojta, R. Bulla, F. Güttge, and F. Anders: "Mass-flow error in the numerical renormalization-group method and the critical behavior of the sub-Ohmic spin-boson model". Phys. Rev. B, **81** (7), 075122 (2010).
http://dx.doi.org/10.1103/PhysRevB.81.075122

[164] T. A. Costi and R. H. McKenzie: "Entanglement between a qubit and the environment in the spin-boson model". Phys. Rev. A, **68** (3), 034301 (2003).
http://dx.doi.org/10.1103/PhysRevA.68.034301

[165] M. Vojta, N.-H. Tong, and R. Bulla: "Erratum: Quantum Phase Transitions in the Sub-Ohmic Spin-Boson Model: Failure of the Quantum-Classical Mapping [Phys. Rev. Lett. 94, 070604 (2005)]". Phys. Rev. Lett., **102** (24), 249904 (2009).
http://dx.doi.org/10.1103/PhysRevLett.102.249904

[166] K. Le Hur, P. Doucet-Beaupré, and W. Hofstetter: "Entanglement and Criticality in Quantum Impurity Systems". Phys. Rev. Lett., **99** (12), 126801 (2007).
http://dx.doi.org/10.1103/PhysRevLett.99.126801

[167] M.-R. Li, K. Le Hur, and W. Hofstetter: "Hidden Caldeira-Leggett Dissipation in a Bose-Fermi Kondo Model". Phys. Rev. Lett., **95** (8), 086406 (2005).
http://dx.doi.org/10.1103/PhysRevLett.95.086406

[168] M. Dube and P. Stamp: "Dynamics of a Pair of Interacting Spins Coupled to an Environmental Sea". International Journal of Modern Physics B (IJMPB), **12** (11), 1191 (1998).
http://dx.doi.org/10.1142/S0217979298000661

[169] L.-M. Duan and G.-C. Guo: "Reducing decoherence in quantum-computer memory with all quantum bits coupling to the same environment". Phys. Rev. A, **57** (2), 737 (1998).
http://dx.doi.org/10.1103/PhysRevA.57.737

[170] M. J. Storcz and F. K. Wilhelm: "Decoherence and gate performance of coupled solid-state qubits". Phys. Rev. A, **67** (4), 042319 (2003).
http://dx.doi.org/10.1103/PhysRevA.67.042319

[171] C. Cohen-Tannoudji, J. Dupont-Roc, and G. Grynberg: Atom-Photon Interactions. Wiley Inter Science (2004).
http://dx.doi.org/10.1002/9783527617197

[172] F. K. Wilhelm, S. Kleff, and J. von Delft: "The spin-boson model with a structured environment: a comparison of approaches". Chemical Physics, **296** (2-3), 345 (2004). The Spin-Boson Problem: From Electron Transfer to Quantum Computing ... to the 60th Birthday of Professor Ulrich Weiss.
http://dx.doi.org/10.1016/j.chemphys.2003.10.010

[173] C. Guo, A. Weichselbaum, S. Kehrein, T. Xiang, and J. von Delft: "Density matrix renormalization group study of a quantum impurity model with Landau-Zener time-dependent Hamiltonian". Phys. Rev. B, **79** (11), 115137 (2009).
http://dx.doi.org/10.1103/PhysRevB.79.115137

[174] T. L. Schmidt, P. Werner, L. Mühlbacher, and A. Komnik: "Transient dynamics of the Anderson impurity model out of equilibrium". Phys. Rev. B, **78** (23), 235110 (2008).
http://dx.doi.org/10.1103/PhysRevB.78.235110

[175] S. Sachdev: Quantum Phase Transitions. Cambridge University Press, Cambridge, U.K. (1999).

[176] T. Giamarchi: Quantum Physics in One Dimension. International Series of Monographs on Physics. Oxford University Press, USA (2004).

[177] B. Kubala and F. Marquardt: "ac conductance through an interacting quantum dot". Phys. Rev. B, **81** (11), 115319 (2010).
http://dx.doi.org/10.1103/PhysRevB.81.115319

[178] O. Tal, M. Krieger, B. Leerink, and J. M. van Ruitenbeek: "Electron-Vibration Interaction in Single-Molecule Junctions: From Contact to Tunneling Regimes". Phys. Rev. Lett., **100** (19), 196804 (2008).
http://dx.doi.org/10.1103/PhysRevLett.100.196804

[179] F. Marquardt and C. Bruder: "Dephasing in sequential tunneling through a double-dot interferometer". Phys. Rev. B, **68** (19), 195305 (2003).
http://dx.doi.org/10.1103/PhysRevB.68.195305

[180] J. König and Y. Gefen: "Coherence and Partial Coherence in Interacting Electron Systems". Phys. Rev. Lett., **86** (17), 3855 (2001).
http://dx.doi.org/10.1103/PhysRevLett.86.3855

[181] A. W. Holleitner, C. R. Decker, H. Qin, K. Eberl, and R. H. Blick: "Coherent Coupling of Two Quantum Dots Embedded in an Aharonov-Bohm Interferometer". Phys. Rev. Lett., **87** (25), 256802 (2001).
http://dx.doi.org/10.1103/PhysRevLett.87.256802

[182] M. Sigrist, T. Ihn, K. Ensslin, D. Loss, M. Reinwald, and W. Wegscheider: "Phase Coherence in the Inelastic Cotunneling Regime". Phys. Rev. Lett., **96** (3), 036804 (2006).
http://dx.doi.org/10.1103/PhysRevLett.96.036804

[183] E. M. Weig, R. H. Blick, T. Brandes, J. Kirschbaum, W. Wegscheider, M. Bichler, and J. P. Kotthaus: "Single-Electron-Phonon Interaction in a Suspended Quantum Dot Phonon Cavity". Phys. Rev. Lett., **92** (4), 046804 (2004).
http://dx.doi.org/10.1103/PhysRevLett.92.046804

[184] S. D. Bennett, L. Cockins, Y. Miyahara, P. Grütter, and A. A. Clerk: "Strong Electromechanical Coupling of an Atomic Force Microscope Cantilever to a Quantum Dot". Phys. Rev. Lett., **104** (1), 017203 (2010).
http://dx.doi.org/10.1103/PhysRevLett.104.017203

[185] M. Galperin, M. A. Ratner, and A. Nitzan: "Molecular transport junctions: vibrational effects". Journal of Physics: Condensed Matter, **19** (10), 103201 (2007).
http://dx.doi.org/10.1088/0953-8984/19/10/103201

[186] R. Härtle, C. Benesch, and M. Thoss: "Multimode vibrational effects in single-molecule conductance: A nonequilibrium Green's function approach". Phys. Rev. B, **77** (20), 205314 (2008).
http://dx.doi.org/10.1103/PhysRevB.77.205314

[187] J. Gabelli, G. Feve, J.-M. Berroir, B. Placais, A. Cavanna, B. Etienne, Y. Jin, and D. C. Glattli: "Violation of Kirchhoff's Laws for a Coherent RC Circuit". Science, **313** (5786), 499 (2006).
http://dx.doi.org/10.1126/science.1126940

[188] M. Büttiker, H. Thomas, and A. Prêtre: "Mesoscopic capacitors". Physics Letters A, **180** (4-5), 364 (1993).
http://dx.doi.org/10.1016/0375-9601(93)91193-9

[189] R. Kubo: "Statistical-Mechanical Theory of Irreversible Processes. I. General Theory and Simple Applications to Magnetic and Conduction Problems". J. Phys. Soc. Jpn., **12** (6), 570 (1957).
http://dx.doi.org/10.1143/JPSJ.12.570

[190] W. Izumida, O. Sakai, and Y. Shimizu: "Many Body Effects on Electron Tunneling through Quantum Dots in an Aharonov-Bohm Circuit". J. Phys. Soc. Jpn., **66**, 717 (1997).
http://dx.doi.org/10.1143/JPSJ.66.717

[191] O. Entin-Wohlman, Y. Imry, and A. Aharony: "Voltage-induced singularities in transport through molecular junctions". Phys. Rev. B, **80** (3), 035417 (2009).
http://dx.doi.org/10.1103/PhysRevB.80.035417

[192] C. Mora and K. Le Hur: "Universal resistances of the quantum resistance-capacitance circuit". Nat Phys, **6** (9), 697 (2010).
http://dx.doi.org/10.1038/nphys1690

[193] B. Kubala, D. Roosen, M. Sindel, W. Hofstetter, and F. Marquardt: "Decoherence in a Double-Dot Aharonov-Bohm Interferometer" (2010).

[194] P. Hyldgaard, S. Hershfield, J. H. Davies, and J. W. Wilkins: "Resonant Tunneling with an Electron-Phonon Interaction". Annals of Physics, **236** (1), 1 (1994).
http://dx.doi.org/10.1006/aphy.1994.1106

[195] J. W. Negele and H. Orland: Quantum Many-Particle Systems. Westview Press, Boulder, CO, USA (1998).

[196] V. J. Emery and A. Luther: "Low- temperature properties of the Kondo Hamiltonian". Phys. Rev. B, **9** (1), 215 (1974).
http://dx.doi.org/10.1103/PhysRevB.9.215

[197] M. Vojta, N.-H. Tong, and R. Bulla: "Quantum Phase Transitions in the Sub-Ohmic Spin-Boson Model: Failure of the Quantum-Classical Mapping". Phys. Rev. Lett., **94** (7), 070604 (2005).
http://dx.doi.org/10.1103/PhysRevLett.94.070604

[198] M. E. Fisher, S.-k. Ma, and B. G. Nickel: "Critical Exponents for Long-Range Interactions". Phys. Rev. Lett., **29** (14), 917 (1972).
http://dx.doi.org/10.1103/PhysRevLett.29.917

[199] E. Luijten and H. W. J. Blöte: "Classical critical behavior of spin models with long-range interactions". Phys. Rev. B, **56** (14), 8945 (1997).
http://dx.doi.org/10.1103/PhysRevB.56.8945

[200] K. Ingersent and Q. Si: "Critical Local-Moment Fluctuations, Anomalous Exponents, and ω/T Scaling in the Kondo Problem with a Pseudogap". Phys. Rev. Lett., **89** (7), 076403 (2002).
http://dx.doi.org/10.1103/PhysRevLett.89.076403

[201] J. M. Kosterlitz: "Phase Transitions in Long-Range Ferromagnetic Chains". Phys. Rev. Lett., **37** (23), 1577 (1976).
http://dx.doi.org/10.1103/PhysRevLett.37.1577

Appendices

Appendix A

Details of the Mapping to the Wilson Chain

In this Appendix, we comment on the details of mapping a Hamiltonian of the general form

$$\hat{\mathcal{H}}_s = \hat{\mathcal{H}}_{\rm imp} + \sum_{n=0}^{\infty} \left(\xi_n^+ \hat{a}_{n\mu}^\dagger \hat{a}_{n\mu} + \xi_n^- \hat{b}_{n\mu}^\dagger \hat{b}_{n\mu} \right) + \sqrt{\frac{1}{\pi}} \sum_n \left(\gamma_n^+ \hat{a}_{n\mu}^\dagger + \gamma_n^- \hat{b}_{n\mu}^\dagger \right) \hat{d}_\mu + \sqrt{\frac{1}{\pi}} \hat{d}_\mu^\dagger \sum_n \left(\gamma_n^+ \hat{a}_{n\mu} + \gamma_n^- \hat{b}_{n\mu} \right) \quad \text{(A.1)}$$

to a semi-infinite chain form, the Wilson chain

$$\hat{\mathcal{H}}_c = \hat{\mathcal{H}}_{\rm imp} + \sum_{n=0}^{\infty} \left[\epsilon_{n,\mu} \hat{f}_{n,\mu}^\dagger \hat{f}_{n,\mu} + t_{n,\mu} \left(\hat{f}_{n,\mu}^\dagger \hat{f}_{n+1,\mu} + \hat{f}_{n+1,\mu}^\dagger \hat{f}_{n,\mu} \right) \right] + \sqrt{\frac{\xi_0}{\pi}} \left(\hat{f}_{0\mu}^\dagger \hat{d}_\mu + \hat{d}_\mu^\dagger \hat{f}_{0\mu} \right). \quad \text{(A.2)}$$

Please notice that both, the single impurity Anderson model (SIAM) (cf. Eq. (4.9)) as well as the spin-boson model (cf. Eq. (5.8)) can be brought in such a general form presented in Eq. (A.1). In case of the SIAM with a constant hybridization function $\Delta(\varepsilon) = \Delta(-\varepsilon) = \Gamma$, we find $\xi_n^+ = \xi_n^- = \frac{1+\Lambda^{-1}}{2}\sqrt{\pi}\Lambda^{-n}$ and $\gamma_n^+ = \gamma_n^- = \left[\frac{1-\Lambda^{-1}}{2}\frac{2\Gamma}{W}\Lambda^{-n}\right]^{1/2}$, while in case of the spin-boson model with its highly asymmetric spectral function $J(\omega) = 2\pi\alpha\omega_c^{1-s}\Theta(\omega)\Theta(\omega_c - \omega)$, the coefficients read $\xi_n^- = \gamma_n^- = 0$, and the coefficients $\xi_n^+ = \xi_n$, $\gamma_n^+ = \gamma_n$ have already been defined in Eq. (5.10).

Since in the semi-infinite chain form the impurity — represented by the operator $\hat{d}_\mu^{(\dagger)}$ in Eq. (A.2) — only couples to a single bath degree of freedom, the so called "maximally localized" bath eigenstate $\hat{f}_0$, it is obvious looking at Eq. (A.1) how to construct the operator for this state

$$\hat{f}_0 = \frac{1}{\sqrt{\xi_0}} \sum_n \left(\gamma_n^+ \hat{a}_n + \gamma_n^- \hat{b}_n \right), \quad \text{(A.3)}$$

where

$$\xi_0 = \sum_n \left[(\gamma_n^+)^2 + (\gamma_n^-)^2 \right]$$

ensures its normalization (the prefactor ξ_0 can be derived using the commutation relation $\left[\hat{f}_0, \hat{f}_0^\dagger\right]_\pm = 1$). For a simpler notation we have omitted the spin index μ in Eq. (A.3) and will do so in the remainder of this Appendix.

Of course the bath operators $\hat{a}, \hat{b}$ are in general not orthogonal to $\hat{f}_0$ anymore. Comparing the bath terms of the two expressions for $\hat{\mathcal{H}}_s$ in Eq. (A.1) and $\hat{\mathcal{H}}_c$ in Eq. (A.2) against each other

$$\sum_{n=0}^{\infty} \left(\xi_n^+ \hat{a}_n^\dagger \hat{a}_n + \xi_n^- \hat{b}_n^\dagger \hat{b}_n \right) = \sum_{n=0}^{\infty} \left[\epsilon_{n,} \hat{f}_n^\dagger \hat{f}_n + t_n \left(\hat{f}_{n,}^\dagger \hat{f}_{n+1} + \hat{f}_{n+1}^\dagger \hat{f}_n \right) \right] \tag{A.4}$$

we define a orthogonal transformation between the operators

$$\hat{f}_n = \sum_m^{\infty} (U_{nm} \hat{a}_m + V_{nm} \hat{b}_m) \tag{A.5}$$

such that

$$\hat{a}_n = \sum_{m=0}^{\infty} U_{mn} \hat{f}_m, \quad \text{and} \quad \hat{b}_n = \sum_{m=0}^{\infty} V_{mn} \hat{f}_m. \tag{A.6}$$

A comparison of Eqs. (A.3),(A.5) and (A.6) yields the "start term" for the matrices U, V

$$U_{0m} = \frac{\gamma_m^+}{\sqrt{\xi_0}}, \quad V_{0m} = \frac{\gamma_m^-}{\sqrt{\xi_0}}. \tag{A.7}$$

Plugging Eq. (A.6) in the right hand side of Eq. (A.4)

$$\sum_n \xi_n^+ \hat{a}_n^\dagger U_{mn} \hat{f}_m + \xi_n^- \hat{b}_n^\dagger V_{mn} \hat{f}_m = \epsilon_{n,} \hat{f}_n^\dagger \hat{f}_n + t_n \left(\hat{f}_n^\dagger \hat{f}_{n+1} + \hat{f}_{n+1}^\dagger \hat{f}_n \right) \tag{A.8}$$

and comparing the prefactors of $\hat{f}_m$ we obtain the following relation

$$\sum_n \xi_n^+ \hat{a}_n^\dagger U_{mn} + \xi_n^- \hat{b}_n^\dagger V_{mn} = \epsilon_m \hat{f}_m^\dagger + t_{m-1} f_{m-1}^\dagger + t_m f_{m+1}^\dagger, \tag{A.9}$$

which is our starting point for the next few steps in the derivation.

Taking the commutator with the operator $\hat{f}_m = \sum_{m'} U_{mm'} \hat{a}_{m'}^\dagger + V_{mm'} \hat{b}_{m'}^\dagger$ on both sides of Eq. (A.9) yields

$$\epsilon_m = \sum_n (\xi_n^+ U_{mn}^2 + \xi_n^- V_{mn}^2) \tag{A.10}$$

On the other hand, resorting Eq. (A.9) we obtain

$$t_m \hat{f}_{m+1}^\dagger = \sum_n \left(\xi_n^+ \hat{a}_n^\dagger U_{mn} + \xi_n^- \hat{b}_n^\dagger V_{mn} \right) - \epsilon_m \hat{f}_m^\dagger - t_{m-1} \hat{f}_{m-1}^\dagger \tag{A.11}$$

$$= \sum_n \left[\left(\xi_n^+ U_{mn} - \epsilon_m U_{mn} - t_{m-1} U_{m-1,n} \right) \hat{a}_n^\dagger + \left(\xi_n^- V_{mn} - \epsilon_m V_{mn} - t_{m-1} V_{m-1,n} \right) \hat{b}_n^\dagger \right]. \tag{A.12}$$

Using the definition of $\hat{f}^\dagger_{m+1}$ from Eq. (A.5) in Eq. (A.12), we find the following recursion relation for the orthogonal matrices U, V

$$U_{n+1,m} = \frac{1}{t_n}\left[(\xi^+_m - \epsilon_n)U_{nm} - t_{n-1}U_{n-1,m}\right] \text{ and} \tag{A.13}$$

$$V_{n+1,m} = \frac{1}{t_n}\left[(\xi^-_m - \epsilon_n)V_{nm} - t_{n-1}V_{n-1,m}\right], \tag{A.14}$$

while taking the commutator with the corresponding adjoint operator $\hat{f}_{m+1} = \sum_n^\infty (U_{m+1,n}\hat{a}_n + V_{m+1,n}\hat{b}_n)$ on both sides of Eq. (A.12) finally yields the last missing recursion relation for t_m:

$$t^2_m = \sum_n \left[\left(\xi^+_n\right)^2 U^2_{mn} + \left(\xi^-_n\right)^2 V^2_{mn}\right] - t^2_{m-1} - \epsilon^2_m. \tag{A.15}$$

To define a starting point of the recursion relations, we have to repeat the steps described in detail above for the case $m = 0$. This results in

$$\epsilon_0 = (\frac{1}{\xi_0}\int_{-1}^{1} d\varepsilon\varepsilon\Delta(\varepsilon)), \tag{A.16}$$

$$t^2_0 = \frac{1}{\xi_0}\sum_{m=0}^{\infty}\left[\left(\xi^+_m - \varepsilon_0\right)^2\left(\gamma^+_n\right)^2 + \left(\xi^-_m - \varepsilon_0\right)^2\left(\gamma^-_n\right)^2\right], \tag{A.17}$$

$$U_{1m} = \frac{1}{t_0}(\xi^+_m - \epsilon_0)U_{0m}, \tag{A.18}$$

$$V_{1m} = \frac{1}{t_0}(\xi^-_m - \epsilon_0)V_{0m}. \tag{A.19}$$

$$\tag{A.20}$$

Summing up, we have found the following recursion relations for the "hopping" and "on-site energy" parameters on the Wilson chain.

$$\epsilon_n = \sum_m (\xi^+_m U^2_{nm} + \xi^-_m V^2_{nm}), \tag{A.21}$$

$$t^2_n = \sum_m \left[\left(\xi^+_m\right)^2 U^2_{nm} + \left(\xi^-_m\right)^2 V^2_{nm}\right] - t^2_{n-1} - \epsilon^2_n, \tag{A.22}$$

$$U_{n+1,m} = \frac{1}{t_n}\left[(\xi^+_m - \epsilon_n)U_{nm} - t_{n-1}U_{n-1,m}\right], \tag{A.23}$$

$$V_{n+1,m} = \frac{1}{t_n}\left[(\xi^-_m - \epsilon_n)V_{nm} - t_{n-1}V_{n-1,m}\right]. \tag{A.24}$$

Since many different energy scales have to be taken into account, one usually has to implement these simple relations using arbitrary precision arithmetics (for example the mpfr library for C).

For the special case of a particle-hole symmetric hybridization function for fermionic baths $\Delta(\varepsilon) = \Delta(-\varepsilon)$, the on-site energies disappear $\epsilon_m = 0$, while for a bosonic spectral function, which is restricted to positive frequencies $J(\omega) \propto \Theta(\omega)$, $\xi^-_m = \gamma^-_m = 0$.

This derivation holds as well for a "shifted" discretization frequently used, if we apply Oliveira's z-trick averaging [78] described in Sec. 10.2. In this case, we carefully calculate the

coefficients $\xi_n^{\pm} = \frac{\int_{x_{n+1}}^{x_n} d\varepsilon \Delta(\varepsilon)\varepsilon}{\left(\gamma_n^{\pm}\right)^2}$ and $\left(\gamma_n^{\pm}\right)^2 = \int_{x_{n+1}}^{x_n} d\varepsilon \Delta(\varepsilon)$ using the respective intervals, which are then defined by $x_n = \Lambda^{-n+z}$ for $n \geq 1$ and $x_0 = 1$.

Appendix B

Detailed Derivation of Spectral Functions at Finite Temperatures

B.1 Full Density Matrix

The details of the derivation of how to calculate correlation functions at finite temperature within the numerical renormalization group method are presented in this Appendix. We elaborate on the work first presented in Refs. [75, 68] and make heavy use of the color coding, labeling discarded and kept states in each NRG iteration red and blue respectively.

We start from a general expression for the Green's function of a quantum impurity system at finite temperatures

$$\begin{aligned} G(\omega) &= -i \int_0^\infty dt\, e^{i\omega t} \langle \left[\hat{A}(t), \hat{B}(0) \right]_\pm \rangle_T = \langle \left[\hat{A}(t), \hat{B}(0) \right]_\pm \rangle_T \\ &= \mathrm{Tr} \left\{ \hat{\rho}_T \left[\hat{A}(t), \hat{B} \right]_\pm \right\} = \mathrm{Tr} \left\{ \hat{\rho}_T \left(\hat{A}(t) \hat{B} \pm \dots \right) \right\}, \end{aligned} \tag{B.1}$$

where $\hat{A}$ and $\hat{B}$ are "local" operators only acting on the degrees of freedom on the first few sites on the Wilson chain. Since the derivation is identical for both summands in the (anti-) commutator, we will only give a reasoning for the first term. Using that the trace of a product of two square matrices is independent of the order of the multiplication and inserting a unity operator we get

$$\begin{aligned} \mathrm{Tr} \left\{ \hat{\rho}_T \hat{A}(t) \hat{B} \right\} &= \mathrm{Tr} \left\{ \hat{A}(t) \hat{B} \hat{\rho}_T \right\} = \mathrm{Tr} \left\{ \hat{A}(t) \cdot \hat{\mathbb{1}} \cdot \hat{B} \hat{\rho}_T \right\} \\ &= \sum_{l,e;m} \sum_{l',e';m'} \langle l, e; m | \hat{A}(t) | l', e'; m' \rangle \langle l', e'; m' | \hat{B} \hat{\rho}_T | l, e; m \rangle. \end{aligned} \tag{B.2}$$

The expression in Eq. (B.2) includes a summation over matrix elements $\langle l, e; m | \hat{O} | l', e'; m' \rangle$ between states of different NRG iterations $m' \neq m$. Calculating these matrix elements is in general not feasible. Thus we have to simplify the expression further. Plugging the expression for the "full" finite temperature density matrix

$$\hat{\rho}_T = \sum_{\tilde{m}} \sum_{\tilde{l},\tilde{e}} |\tilde{l}, \tilde{e}; \tilde{m}\rangle \frac{\exp\left(-\beta E_{\tilde{l},\tilde{m}}\right)}{Z} \langle \tilde{l}, \tilde{e}; \tilde{m}| \tag{B.3}$$

(cf. Sec. 9.2) in Eq. (B.2) we obtain

$$\begin{aligned}\mathrm{Tr}\left\{\hat{\rho}_T\hat{A}(t)\hat{B}\right\} &= \sum_{l,e;m}\sum_{l',e';m'}\langle l,e;m|\hat{A}(t)|l',e';m'\rangle\langle l',e';m'|\hat{B}\sum_{\tilde{m}}\sum_{\tilde{l},\tilde{e}}|\tilde{l},\tilde{e};\tilde{m}\rangle\frac{e^{-\beta E_{\tilde{l},\tilde{m}}}}{Z}\langle\tilde{l},\tilde{e};\tilde{m}|l,e;m\rangle \\ &= \sum_{l,e;m}\sum_{l',e';m'}\langle l,e;m|\hat{A}(t)|l',e';m'\rangle\langle l',e';m'|\hat{B}|l,e;m\rangle\frac{e^{-\beta E_{l,m}}}{Z}, \qquad \text{(B.4)}\end{aligned}$$

where we used that $\langle\tilde{l},\tilde{e};\tilde{m}|l,e;m\rangle = \delta_{l,\tilde{l}}\,\delta_{e,\tilde{e}}\,\delta_{m,\tilde{m}}$ in the last step.

Dividing the summations over m and m' into three parts to differentiate the cases $m' = m$, $m' > m$, and $m' < m$ we obtain

$$\begin{aligned}\mathrm{Tr}\Big\{\hat{\rho}_T\hat{A}(t)\hat{B}\Big\} &= \sum_{l,e;m}\sum_{l',e';m'}\langle l,e;m|\hat{A}(t)|l',e';m'\rangle\langle l',e';m'|\hat{B}|l,e;m\rangle\frac{e^{-\beta E_{l,m}}}{Z} \\ &= \sum_{m}\sum_{l,e}\langle l,e;m|\hat{A}(t)\Big(\sum_{l',e'}|l',e';m\rangle\langle l',e';m|\Big)\hat{B}|l,e;m\rangle\frac{e^{-\beta E_{l,m}}}{Z} \qquad (m'=m) \\ &\qquad \text{(B.5)} \\ &+ \sum_{m}\sum_{l,e}\langle l,e;m|\hat{A}(t)\Big(\sum_{m'>m}\sum_{l',e'}|l',e';m'\rangle\langle l',e';m'|\Big)\hat{B}|l,e;m\rangle\frac{e^{-\beta E_{l,m}}}{Z} \qquad (m'>m) \\ &\qquad \text{(B.6)} \\ &+ \sum_{m}\sum_{m'<m}\sum_{l,e,l',e'}\langle l',e';m'|\hat{B}|l,e;m\rangle\frac{e^{-\beta E_{l,m}}}{Z}\langle l,e;m|\hat{A}(t)|l',e';m'\rangle \qquad (m'<m) \\ &\qquad \text{(B.7)}\end{aligned}$$

The $(m' = m)$-term in Eq. (B.5) can be calculated in a straightforward manner. For the remaining two terms in the summation we have to be more careful. The case $(m' > m)$ in Eq. (B.6) reminds us of the resummation trick we discussed in Sec. 7.3. Introducing their idea for the complete basis, Anders and Schiller [66] came up with the identity for the projectors

$$\hat{\mathbb{1}}^{+}_{m} = \sum_{k,e}|k,e;m\rangle\,\langle k,e;m| = \sum_{m'>m}\sum_{r',e'}|r',e';m'\rangle\,\langle r',e';m'|$$

(cf. Eq. (7.4)). With this identity the $(m' > m)$ part of the summation simplifies to

$$\begin{aligned}\text{(B.6)} &= \sum_{m}\sum_{l,e}\langle l,e;m|\hat{A}(t)\Big(\sum_{m'>m}\sum_{l',e'}|l',e';m'\rangle\langle l',e';m'|\Big)\hat{B}|l,e;m\rangle\frac{e^{-\beta E_{l,m}}}{Z} \\ &= \sum_{m}\sum_{l,e}\langle l,e;m|\hat{A}(t)\Big(\sum_{k,e'}|k,e';m\rangle\langle k,e';m|\Big)\hat{B}|l,e;m\rangle\frac{e^{-\beta E_{l,m}}}{Z}. \qquad \text{(B.8)}\end{aligned}$$

Notice that Eq. (B.8) only includes matrix elements of eigenstates calculated in the same step of the iterative diagonalization procedure $m' = m$.

The remaining third part of the sum where $m' < m$ is the most difficult one to calculate. Let us reorganize Eq. (B.7) using the relation $\sum_{m'<m}\sum_{m} = \sum_{m>m'}\sum_{m'}$ (for a sketch see

Fig. B.1)

$$(\text{B.7}) = \sum_{m} \sum_{m'<m} \sum_{l,e,l',e'} \langle l', e'; m'|\hat{B}|l, e; m\rangle \frac{e^{-\beta E_{l,m}}}{Z} \langle l, e; m|\hat{A}(t)|l', e'; m'\rangle$$

$$= \sum_{m'} \sum_{l,e,l',e'} \langle l', e'; m'|\hat{B} \left(\sum_{m>m'} |l, e; m\rangle \frac{e^{-\beta E_{l,m}}}{Z} \langle l, e; m| \right) \hat{A}(t)|l', e'; m'\rangle \tag{B.9}$$

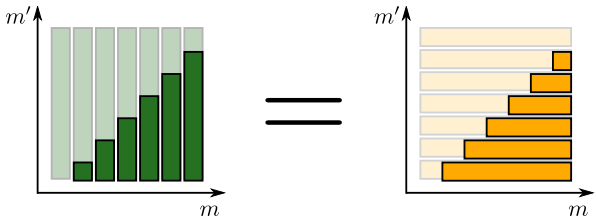

Figure B.1: Illustrating the identity $\sum_{m'<m} \sum_{m} = \sum_{m>m'} \sum_{m'}$.

How can we evaluate Eq. (B.9)? Let us again split up the summation over $m > m'$ and examine each term $\check{m} > m'$ on its own. The expression in the parentheses of Eq. (B.9) can be identified with the contribution of iteration $\check{m}$ to the "full" finite temperature density matrix of the Fock space

$$\frac{1}{Z}\hat{\check{\rho}}_T(\check{m}) = \sum_{\check{l},\check{e}} |\check{l}, \check{e}; \check{m}\rangle \frac{e^{-\beta E_{\check{l},\check{m}}}}{Z} \langle \check{l}, \check{e}; \check{m}|. \tag{B.10}$$

Transforming $\hat{\check{\rho}}_T(\check{m})$ to the eigenstates available in iteration m' using the transformation matrices between the different iteration steps

$$\frac{1}{Z}[\check{\rho}_T^{red}(m', \check{m})]_{j',k'} = \frac{1}{Z} \sum_{\{\alpha_i\}} U_{s,j'}^{\alpha_{m'+1}\dagger} \dots U_{\check{l},r}^{\alpha_{\check{m}}\dagger} [\check{\rho}_T(\check{m})]_{\check{l},\check{l}} U_{\check{l},r'}^{\alpha_{\check{m}}} \dots U_{s',k'}^{\alpha_{m'+1}} \tag{B.11}$$

$$= \sum_{\check{l},e',\check{e}} \langle j', e'; m'|\check{l}, \check{e}; \check{m}\rangle \frac{e^{-\beta E_{\check{l},\check{m}}}}{Z} \langle \check{l}, \check{e}; \check{m}|k', e'; m'\rangle. \tag{B.12}$$

The logic connecting Eq. (B.11) with Eq. (B.12) is the same as the one applied "reducing" the ground state density matrix in the "common" DM-NRG approach [63]. As Weichselbaum and coworkers pointed out in Refs. [75, 65], a common notation in terms of matrix product states can be employed highlight the connection. Using the (relatively) short notation of Eq. (B.12) we rewrite

$$(\text{B.9}) = \sum_{m'} \sum_{l,l',e,e'} \sum_{m>m'} \langle l', e'; m'|\hat{B}|l, e; m\rangle \frac{e^{-\beta E_{l,m}}}{Z} \langle l, e; m|\hat{A}(t)|l', e'; m'\rangle$$

$$= \sum_{\substack{m' \\ m>m'}} \sum_{\substack{j',k',l,l' \\ e,e'}} \langle l', e'; m'|\hat{B}|j', e'; m'\rangle\langle j', e'; m'|l, e; m\rangle \frac{e^{-\beta E_{l,m}}}{Z} \langle l, e; m|k', e'; m'\rangle\langle k', e'; m'|\hat{A}(t)|l', e'; m'\rangle. \tag{B.13}$$

We now collect the three terms of the sum and notice that for all "local" operators $\hat{O} = \{\hat{A}, \hat{B}\}$, which only act on the degrees of freedom of the first sites of the Wilson chain, the matrix elements $\langle r, e; m|\hat{O}|l, e'; m\rangle$ are independent of the environment configuration $\langle r, e; m|\hat{O}|l, e'; m\rangle = \delta_{ee'}\langle r, e; m|\hat{O}|l, e'; m\rangle$. This leads to

$$\mathrm{Tr}\left\{\hat{\rho}_T\hat{A}(t)\hat{B}\right\} = \sum_{l,e;m}\sum_{l',e';m'}\langle l, e; m|\hat{A}(t)|l', e'; m'\rangle\langle l', e'; m'|\hat{B}|l, e; m\rangle\frac{e^{-\beta E_{l,m}}}{Z}$$

$$= \sum_{m}\sum_{l,l'.e}\langle l, e; m|\hat{A}(t)|l', e; m\rangle\langle l', e; m|\hat{B}|l, e; m\rangle\frac{e^{-\beta E_{l,m}}}{Z} \tag{B.14}$$

$$+ \sum_{m}\sum_{l,k,e}\langle l, e; m|\hat{A}(t)|k, e; m\rangle\langle k, e; m|\hat{B}|l, e; m\rangle\frac{e^{-\beta E_{l,m}}}{Z} \tag{B.15}$$

$$+ \sum_{\substack{m'\\ m>m'}}\sum_{\substack{j',k',l,l'\\ e,e'}}\langle l', e'; m'|\hat{B}|j', e'; m'\rangle\langle j', e'; m'|l, e; m\rangle\frac{e^{-\beta E_{l,m}}}{Z}\langle l, e; m|k', e'; m'\rangle\langle k', e'; m'|\hat{A}(t)|l', e'; m'\rangle \tag{B.16}$$

Using $\hat{A}(t) = e^{it\hat{\mathcal{H}}}\hat{A}e^{-it\hat{\mathcal{H}}}$ as well as "the" NRG approximation

$$\hat{\mathcal{H}}|r, e; m\rangle \approx \hat{\mathcal{H}}_m|r, e; m\rangle = E_{r,m}|r, e; m\rangle$$

and relabeling in last term exchanging primed against non-primed our expression reads

$$\mathrm{Tr}\left\{\hat{\rho}_T\hat{A}(t)\hat{B}\right\} = \sum_{m}\sum_{l,l'.e}e^{it(E_{l,m}-E_{l',m})}\langle l, e; m|\hat{A}|l', e; m\rangle\langle l', e; m|\hat{B}|l, e; m\rangle\frac{e^{-\beta E_{l,m}}}{Z}$$

$$+ \sum_{m}\sum_{l,k,e}e^{it(E_{l,m}-E_{k,m})}\langle l, e; m|\hat{A}|k, e; m\rangle\langle k, e; m|\hat{B}|l, e; m\rangle\frac{e^{-\beta E_{l,m}}}{Z} \tag{B.17}$$

$$+ \sum_{\substack{m\\ m'>m}}\sum_{\substack{j,k,l,l'\\ e,e'}}e^{it(E_{k,m}-E_{l,m})}\langle l, e; m|\hat{B}|j, e; m\rangle\langle j, e; m|l', e'; m'\rangle\frac{e^{-\beta E_{l',m'}}}{Z}\langle l', e'; m'|k, e; m\rangle\langle k, e; m|\hat{A}|l, e; m\rangle \tag{B.18}$$

Since last equation still is hardly readable, we introduce an abbreviation for the part of the full finite temperature density matrix added in iterations $m' > m$

$$[\tilde{\rho}_T^{red}(m)]_{j,k} = \sum_{l',e',e;m'>m}\langle j, e; m|l', e'; m'\rangle\frac{e^{-\beta E_{l',m'}}}{Z}\langle l', e'; m'|k, e; m\rangle \tag{B.19}$$

and use the notation $O_{k,l}(m) = \langle k, e; m|\hat{O}|l, e; m\rangle$ for matrix elements of operators in iteration

m frequently used throughout this thesis. We thus end up with the following equation

$$\mathrm{Tr}\left\{\hat{\rho}_T \hat{A}(t)\hat{B}\right\} = \sum_m \sum_{l,l'.e} e^{it(E_{l,m}-E_{l',m})} A_{l,l'}(m) B_{l',l}(m) \frac{e^{-\beta E_{l,m}}}{Z} \tag{B.20}$$

$$+ \sum_m \sum_{l,k,e} e^{it(E_{l,m}-E_{k,m})} A_{l,k}(m) B_{k,l}(m) \frac{e^{-\beta E_{l,m}}}{Z} \tag{B.21}$$

$$+ \sum_{\substack{l,k,\check{k} \\ m}} e^{it(E_{k,m}-E_{l,m})} B_{l,j}(m) [\tilde{\rho}_T^{red}(m)]_{j,k} A_{k,l}(m), \tag{B.22}$$

which, of course, is only one out of two terms of the (anti-)commutator we want to evaluate for our finite temperature Green's function. Collecting both contributions

$$\langle\left[\hat{A}(t), \hat{B}(0)\right]_{\pm}\rangle_T = \mathrm{Tr}\left\{\hat{\rho}_T \left(\hat{A}(t)\hat{B} \pm \hat{B}\hat{A}(t)\right)\right\} \tag{B.23}$$

$$= \sum_m \sum_{l,l'.e} e^{it(E_{l,m}-E_{l',m})} A_{l,l'}(m) B_{l',l}(m) \frac{e^{-\beta E_{l,m}} \pm e^{-\beta E_{l',m}}}{Z} \tag{B.24}$$

$$+ \sum_m \sum_{l,k,e} e^{it(E_{l,m}-E_{k,m})} A_{l,k}(m) B_{k,l}(m) \frac{e^{-\beta E_{l,m}}}{Z} \tag{B.25}$$

$$+ \sum_{\substack{l,k,\check{k} \\ m}} e^{it(E_{k,m}-E_{l,m})} B_{l,j}(m) [\tilde{\rho}_T^{red}(m)]_{j,k} A_{k,l}(m) \tag{B.26}$$

$$\pm \sum_m \sum_{l,k,e} e^{it(E_{k,m}-E_{l,m})} A_{k,l}(m) B_{l,k}(m) \frac{e^{-\beta E_{l,m}}}{Z} \tag{B.27}$$

$$\pm \sum_{\substack{l,k,\check{k} \\ m}} e^{it(E_{l,m}-E_{k,m})} A_{l,j}(m) [\tilde{\rho}_T^{red}(m)]_{j,k} B_{k,l}(m). \tag{B.28}$$

A last Fourier transform leads to the final result for the improved calculation of the finite temperature Green's function $G(\omega) = -i \int_0^\infty dt\, e^{i\omega t} \langle\left[\hat{A}(t), \hat{B}(0)\right]_{\pm}\rangle_T$ within the NRG formalism

$$G(\omega) = \frac{1}{Z} \sum_m \sum_{l,l'.e} A_{l,l'}(m) B_{l',l}(m) \frac{e^{-\beta E_{l,m}} \pm e^{-\beta E_{l',m}}}{\omega + (E_{l,m} - E_{l',m})}$$

$$+ \frac{1}{Z} \sum_m \sum_{l,k,e} A_{l,k}(m) B_{k,l}(m) \frac{e^{-\beta E_{l,m}}}{\omega + (E_{l,m} - E_{k,m})}$$

$$+ \sum_{\substack{l,j,k \\ m}} B_{l,j}(m) [\tilde{\rho}_T^{red}(m)]_{j,k} A_{k,l}(m) \frac{1}{\omega + (E_{k,m} - E_{l,m})}$$

$$\pm \frac{1}{Z} \sum_m \sum_{l,k,e} A_{k,l}(m) B_{l,k}(m) \frac{e^{-\beta E_{l,m}}}{\omega + (E_{k,m} - E_{l,m})}$$

$$\pm \sum_{\substack{l,j,k \\ m}} A_{l,j}(m) [\tilde{\rho}_T^{red}(m)]_{j,k} B_{k,l}(m) \frac{1}{\omega + (E_{l,m} - E_{j,m})}.$$

B.2 Single Shell Approximation

Approximating the finite temperature density matrix given by Eq. (B.3) using only the eigenstates of a single NRG iteration, the derivation simplifies considerably. Without loss of generality we may consider the single iteration in which we set up the reduced density matrix to be the last iteration of our iterative diagonalization procedure. The "single shell" density matrix then reads

$$\hat{\rho}_N = \sum_{\tilde{l},\tilde{e}} |\tilde{l},\tilde{e};N\rangle \frac{\exp\left(-\beta E_{\tilde{l},N}\right)}{Z} \langle \tilde{l},\tilde{e};N|. \tag{B.29}$$

The general expression for the Green's function evaluated using the "single shell" density matrix $\hat{\rho}_N$ is given by

$$G(\omega) = -i\int_0^\infty dt\; e^{i\omega t}\langle\left[\hat{A}(t),\hat{B}(0)\right]_\pm\rangle = -i\int_0^\infty dt\; e^{i\omega t}\mathrm{Tr}\left\{\hat{\rho}_N\left(e^{it\hat{\mathcal{H}}}\hat{A}e^{-it\hat{\mathcal{H}}}\hat{B}\pm\ldots\right)\right\}, \tag{B.30}$$

where as before we focus on the first term in the (anti-)commutator and split up the double summation over m and m'

$$\begin{aligned}
\mathrm{Tr}\left\{\hat{\rho}_N\hat{A}(t)\hat{B}\right\} &= \sum_{l,e;m}\sum_{l',e',m'}\langle l,e;m|\hat{A}e^{-it\hat{\mathcal{H}}}|l',e';m'\rangle\langle l',e';m'|\hat{B}\hat{\rho}_N e^{it\hat{\mathcal{H}}}|l,e;m\rangle \\
&= \sum_{l,e;m}\langle l,e;m|\hat{A}e^{-it\hat{\mathcal{H}}}\Big(\sum_{l',e'}|l',e';m\rangle\langle l',e';m|\Big)\hat{B}\hat{\rho}_N e^{it\hat{\mathcal{H}}}|l,e;m\rangle \qquad (m'=m) \qquad \text{(B.31)} \\
&+ \sum_{l,e;m}\langle l,e;m|\hat{A}e^{-it\hat{\mathcal{H}}}\Big(\sum_{l',e';m'>m}|l',e';m'\rangle\langle l',e';m'|\Big)\hat{B}\hat{\rho}_N e^{it\hat{\mathcal{H}}}|l,e;m\rangle \qquad (m'>m) \qquad \text{(B.32)} \\
&+ \sum_{l,e;m}\sum_{l',e';m'<m}\langle l,e;m|\hat{A}e^{-it\hat{\mathcal{H}}}|l',e';m'\rangle\langle l',e';m'|\hat{B}\hat{\rho}_N e^{it\hat{\mathcal{H}}}|l,e;m\rangle \qquad (m'<m). \qquad \text{(B.33)}
\end{aligned}$$

Using the resummation identity of Eq. (7.4) on the two last summands and exploiting that the observables are "local" we obtain

$$\begin{aligned}
\mathrm{Tr}\left\{\hat{\rho}_N\hat{A}(t)\hat{B}\right\} &= \sum_{l,l',e;m} e^{-it(E_{l,m}-E_{l',m})}\langle l,e;m|\hat{A}|l',e;m\rangle\langle l',e;m|\hat{B}\hat{\rho}_N|l,e;m\rangle \qquad (m'=m) \qquad \text{(B.34)} \\
&+ \sum_{l,k,e;m} e^{-it(E_{l,m}-E_{k,m})}\langle l,e;m|\hat{A}|k,e;m\rangle\langle k,e;m|\hat{B}\hat{\rho}_N|l,e;m\rangle \qquad (m'>m) \qquad \text{(B.35)} \\
&+ \sum_{l,k,e;m} e^{it(E_{k,m}-E_{l,m})}\langle l,e;m|\hat{B}\hat{\rho}_N|k,e;m\rangle\langle k,e;m|\hat{A}|l,e;m\rangle \qquad (m'<m). \qquad \text{(B.36)}
\end{aligned}$$

Plugging in the expression of Eq. (B.29) for the density matrix we evaluate the three terms in the summation separately. For $m = m'$ the expression simplifies as follows

$$\text{Eq. (B.34)} = \sum_{l,l',e;m} e^{it(E_{l,m}-E_{l',m})}\langle l,e;m|\hat{A}|l',e;m\rangle\langle l',e;m|\hat{B}\sum_r |r;N\rangle\frac{e^{-\beta E_{r,N}}}{Z_N}\langle r;N|l,e;m\rangle \tag{B.37}$$

$$= \sum_{l,l'} e^{it(E_{l,N}-E_{l',N})}\langle l;N|\hat{A}|l';N\rangle\langle l';N|\hat{B}|l;N\rangle\frac{e^{-\beta E_{l,N}}}{Z_N}, \tag{B.38}$$

since $\langle r;N|l,e;m\rangle = \delta_{r,l}\delta_{m,N}$. The $(m' > m)$-term in the summation vanishes

$$\text{Eq. (B.35)} = \sum_{l,k,e;m} e^{it(E_{l,m}-E_{k,m})}\langle l,e;m|\hat{A}|k,e;m\rangle\langle k,e;m|\hat{B}\sum_r |r;N\rangle\frac{e^{-\beta E_{r,N}}}{Z_N}\langle r;N|l,e;m\rangle \tag{B.39}$$

$$= 0, \tag{B.40}$$

since $\langle k,e;m|\hat{B}|r;N\rangle = 0$ for $m = N$ and $\langle r;N|l,e;m\rangle = 0$ for $m < N$.

The last term in the summation requires a little bit more attention. For $m' < m$ the expression reads

$$\begin{aligned}\text{Eq. (B.36)} &= \sum_{l,k,e;m} e^{it(E_{k,m}-E_{l,m})}\langle l,e;m|\hat{B}\hat{\rho}_N|k,e;m\rangle\langle k,e;m|\hat{A}|l,e;m\rangle \\ &= \sum_{l,k,e;m} e^{it(E_{k,m}-E_{l,m})}\langle l,e;m|\hat{B}\sum_r |r;N\rangle\frac{e^{-\beta E_{r,N}}}{Z_N}\langle r;N|k,e;m\rangle\langle k,e;m|\hat{A}|l,e;m\rangle\end{aligned} \tag{B.41}$$

Here the term $\langle l,e;m|\hat{B}|r;N\rangle$ can be rewritten

$$\begin{aligned}\langle l,e;m|\hat{B}|r;N\rangle &= \langle l,e;m|\hat{B}\cdot\hat{\mathbb{1}}|r;N\rangle \\ &= \langle l,e;m|\hat{B}\sum_{s,e',m'\le m}|s,e';m'\rangle\langle s,e';m'|r;N\rangle + \langle l,e;m|\hat{B}\sum_{s,e',m'>m}|s,e';m'\rangle\langle s,e';m'|r;N\rangle \\ &= \langle l,e;m|\hat{B}\sum_{s,e',m'>m}|s,e';m'\rangle\langle s,e';m'|r;N\rangle = \langle l,e;m|\hat{B}\sum_{k',e'}|k',e';m\rangle\langle k',e';m|r;N\rangle\end{aligned}$$

which leads to

$$\begin{aligned}\text{Eq. (B.36)} &= \sum_{l,k,k';m} e^{it(E_{k,m}-E_{l,m})}\langle l,e;m|\hat{B}|k',e;m\rangle\langle k',e;m|r;N\rangle\frac{e^{-\beta E_{r,N}}}{Z_N}\langle r;N|k,e;m\rangle\langle k,e;m|\hat{A}|l,e;m\rangle \\ &= \sum_{l,k,k';m} e^{it(E_{k,m}-E_{l,m})}B_{l,k'}(m)\rho^{red}_{k',k}(m)A_{k,l}(m).\end{aligned} \tag{B.42}$$

Combining the three summands of Eqs. (B.40), (B.41) and (B.42) (and the corresponding ones for the other summand in the (anti-)commutator) and Fourier transforming the result,

the final expression for the "single shell" approximation to the finite temperature spectral function reads

$$\begin{aligned} G(\omega) =& \frac{1}{Z_N} \sum_{l,l'} A_{l,l'}(N) B_{l',l}(N) \frac{e^{-\beta E_{lN}} \pm e^{-\beta E_{l'N}}}{\omega + (E_{l,N} - E_{l',N})} \\ &+ \sum_{l,k,k';m} B_{l,k'}(m) \rho^{red}_{k',k}(m) A_{k,l}(m) \frac{1}{\omega + (E_{k,m} - E_{l,m})} \\ &\pm \sum_{l,k,k';m} A_{l,k}(m) \rho^{red}_{k,k'}(m) B_{k',l}(m) \frac{1}{\omega + (E_{l,m} - E_{k,m})}, \end{aligned} \tag{B.43}$$

which coincides with the result given in Eq. (7.8) in Sec. 7.4.

Comparing this result to Hofstetter's DM-NRG approach leading to Eq. (6.15) in Sec. 6.2, the only difference consists that not using the complete basis for the Fock space, we sum over all possible states in each iteration and do not exclude terms where both states l and l' are kept.

Appendix C

Details of Bosonization

1-D abelian bosonization is a technique where one-dimensional fermionic fields ψ_η are represented as bosonic fields ϕ_η. The bosonization formula

$$\psi_\eta \sim F_\eta \exp^{i\phi_\eta}, \tag{C.1}$$

where η labels the spin or species, is a crucial ingredient demonstrating the equivalence of the anisotropic Kondo model and the single spin-boson model using the bosonization method (see Sec. 12.2).

While the standard reference on constructive bosonization is Haldane's paper from 1981 [127], we summarize the derivation of the bosonization formula presented by von Delft and Schoeller in Ref. [59] in this Appendix.

C.1 Prerequisites

There are two prerequisites which have to be fulfilled in order to be able to apply bosonization to a theory:

1. The theory can be formulated using a set of fermionic creation and annihilation operators which obey the commutation relations.

$$\left\{c_{k\eta}, c^\dagger_{k\eta}\right\} = \delta_{\eta\eta'}, \qquad k \in [-\infty, \infty], \qquad \eta = 1, 2, \cdots, M\,, \tag{C.2}$$

   where η labels the species.

2. The momentum index k is *unbounded* and *discrete* and has the form

$$k = \frac{2\pi}{L}\left(n_k - \frac{1}{2}\delta_b\right), \qquad n_k \in \mathbb{Z} \qquad \text{and} \qquad \delta_b \in [0, 2)\,. \tag{C.3}$$

   n_k are integers, L is associated to the system size, δ_b will determine the boundary conditions of fermionic fields to be defined.

The discreteness of k allows for book-keeping, the unboundedness is essential to properly define a bosonic field. Discreteness is achieved by finite system size and definite boundary conditions, or taking the continuum limit $L \to \infty$ after the bosonization rules have been established. If k is not unbounded, add (unphysical) negative-energy "positron" states.

C.2 Fermionic Fields

One can define fermionic fields using the already introduced operators

$$\psi_\eta(x) = \sqrt{\frac{2\pi}{L}} \sum_{k=\infty}^{\infty} \exp^{-ikx} c_{k\eta} \tag{C.4}$$

and its inverse

$$c_{k\eta} = (2\pi L)^{-1/2} \int_{-L/2}^{L/2} \mathrm{d}x \exp^{ikx} \psi_\eta(x). \tag{C.5}$$

The fermionic field obeys period "boundary conditions" $\psi_\eta(x + L/2) = \exp^{i\pi\delta_b} \psi_\eta(x - L/2)$.

Using the identity $\sum_{n\in\mathbb{Z}} \exp^{iny} = 2\pi \sum_{\bar{n}\in\mathbb{Z}} \delta(y - 2\pi\bar{n})$, Eq. (C.1) and Eq. (C.4) it is easy to derive the anti-commutation relations

$$\left\{\psi_\eta(x), \psi^\dagger_{\eta'}(x')\right\} = \delta_{\eta\eta'} \frac{2\pi}{L} \sum_{n\in\mathbb{Z}} \exp^{-i(x-x')(n-\delta_b/2)2\pi/L} \tag{C.6}$$

$$= \delta_{\eta\eta'} 2\pi \sum_{\bar{n}\in\mathbb{Z}} \delta(x - x' - \bar{n}L) \exp^{i\pi\bar{n}\delta_b} \tag{C.7}$$

$$\left\{\psi_\eta(x), \psi_{\eta'}(x')\right\} = 0, \tag{C.8}$$

which are standard anti-commutation relations for fermionic fields if $x, x' \in [-L/2, L/2]$ and generalized ones for the unrestricted case.

C.3 Bosonic Reorganization of Fock Space

The "deep reason" why the bosonization theory works goes as follows: The Fock space $\mathcal{F}$ can be rewritten in a sum over Hilbert spaces with fixed particle number: $\mathcal{F} = \sum_{\bigoplus \vec{N}} \mathcal{H}_{\vec{N}}$. All excitations within this Fock space are particle-hole like, which means that they obey bosonic commutation relations. Let us put together the ingredients we need for the bosonic reorganization of a fermionic theory:

The vacuum state $|\vec{0}\rangle_0$ which obeys

$$c_{k\eta}|\vec{0}\rangle_0 \equiv 0 \qquad \text{for } k > 0 \qquad (n_k > 0) \tag{C.9}$$

$$c^\dagger_{k\eta}|\vec{0}\rangle_0 \equiv 0 \qquad \text{for } k \leq 0 \qquad (n_k \leq 0). \tag{C.10}$$

Relative to this vacuum state (or Fermi sea $n_k = 0$) the occupation numbers are defined.

A fermionic-normal-ordering $\overset{*}{*}\ \overset{*}{*}$, by which all operators $c_{k\eta}$ with $k > 0$ and $c^\dagger_{k\eta}$ with $k \leq 0$ are moved right of all other operators ($c_{k\eta}$ with $k \leq 0$ and $c^\dagger_{k\eta}$ with $k > 0$).

The $\vec{N}$-particle ground state $|\vec{N}\rangle_0$. The set of states with identical $\hat{N}_\eta$-eigenvalues $\vec{N} = (N_1, \cdots, N_M) \in \mathbb{Z}^M$, where the bosonic number operator is defined by

$$\hat{N}_\eta \equiv \sum_{k=-\infty}^{\infty} \overset{*}{*} c^\dagger_{k\eta} c_{k\eta} \overset{*}{*} = \sum_{k=-\infty}^{\infty} \left[c^\dagger_{k\eta} c_{k\eta} - {}_0\,\langle\vec{0}|c^\dagger_{k\eta} c_{k\eta}|\vec{0}\rangle_0\right] \tag{C.11}$$

is called the $\vec{N}$-particle Hilbert space. All states will be denoted by $|\vec{N}\rangle$. The ground state for this Hilbert space is constructed according to the following ordering of operators:

$$|\vec{N}_\eta\rangle_0 \equiv (C_1)^{N_1}(C_2)^{N_2}\dots(C_M)^{N_M}|\vec{0}\rangle_0\ , \tag{C.12}$$

$$(C_\eta)^{N_\eta} \equiv \begin{cases} c^\dagger_{N_\eta\,\eta}c^\dagger_{(N_\eta-1)\,\eta}\cdots c^\dagger_{1\,\eta} & \text{for} \quad N_\eta > 0\ , \\ 1 & \text{for} \quad N_\eta = 0\ , \\ c_{(N_\eta+1)\,\eta}c_{(N_\eta+2)\,\eta}\cdots c_{0\,\eta} & \text{for} \quad N_\eta < 0\ . \end{cases} \tag{C.13}$$

Bosonic particle-hole operators $b^\dagger_{q\eta}b_{q,\eta}$ are defined to construct the $\vec{N}$-particle Hilbert space upon the ground state $|\vec{N}\rangle_0$:

$$b^\dagger_{q\eta} \equiv \frac{i}{\sqrt{n_q}}\sum_{k=-\infty}^{+\infty} c^\dagger_{k+q\eta}c_{k\eta}, \qquad b_{q\eta} \equiv \frac{-i}{\sqrt{n_q}}\sum_{k=-\infty}^{+\infty} c^\dagger_{k-q\eta}c_{k\eta}. \tag{C.14}$$

Here $q \equiv \frac{2\pi}{L}n_q > 0$ and $n_q \in \mathbb{Z}^+$ is a positive integer. For any $|\vec{N}\rangle$, the state $b^\dagger_{q\eta}|\vec{N}\rangle$ (or $b_{q\eta}|\vec{N}\rangle$) consists of a linear combination of particle-hole excitations relative to $|\vec{N}\rangle$.
The normalization of the bosonic operators is chosen such that the standard commutation relations for bosonic operators are fulfilled.

The bosonic ground states $|\vec{N}\rangle_0$ for each Hilbert space $H_{\vec{N}}$ is, as intuitively clear, given by the $\vec{N}$-particle ground state $|\vec{N}\rangle_0$ which is defined by

$$b_{q\eta}|\vec{N}\rangle_0 = 0, \tag{C.15}$$

for all q, η.

A bosonic normal ordering with respect to this ground state

$$^*_*ABC\dots^*_* = ABC\dots\ -\ {}_0\langle\vec{N}|ABC\dots|\vec{N}\rangle_0\ ;, \qquad \text{for} \quad A, B, C, \dots \in \{b_{q\eta}; b^\dagger_{q\eta}\}\ . \tag{C.16}$$

can be defined as well. Since we may take $\vec{N} = \vec{0}$ in Eq. (C.16), boson normal ordered are automatically fermion normal ordered.

The completeness of states in bosonic representation can be reformulated in the following statement:

For every $|\vec{N}\rangle$, there exists a function $f(b^\dagger)$ of $b^\dagger$s such that $|\vec{N}\rangle = f(b^\dagger)|\vec{N}\rangle_0$, (C.17)

which is equivalent to saying that the $b^\dagger$'s, acting on $|\vec{N}\rangle_0$, span the complete $\vec{N}$-particle Hilbert space $H_{\vec{N}}$.
To make plausible the validity of assertion (Eq. (C.17)), we offer a (logically non-rigorous) "circular argument": By Eq. (C.5), we have

$$c^\dagger_{k\eta}c_{k'\eta} = \frac{1}{2\pi L}\int_{-L/2}^{L/2}dx\int_{-L/2}^{L/2}dx'\, e^{i(k'x'-kx)}\,\psi^\dagger_\eta(x)\psi_\eta(x')\ . \tag{C.18}$$

Assuming that assertion Eq. (C.17) holds, we can deduce that $\psi^\dagger_\eta(x)\psi_\eta(x')$ can be expressed purely in terms of the $b^\dagger_{q\eta}$ and $b_{q\eta}$s. Therefore $\overline{f}(c^\dagger_{k\eta}c_{k'\eta})|\vec{N}\rangle_0$ has the form Eq. (C.17) [using Eq. (C.18), rearranging its right-hand-side into boson-normal-ordered form and exploiting Eq. (C.15)], so that we have "proven" our starting assumption. A rigorous proof of assertion Eq. (C.17) is given in the appendix of Ref. [59].

The Klein factors $F^\dagger_\eta$ and F_η raise or lower the total fermion number by one and thus connect the various $\vec{N}$-particle Hilbert spaces. They are defined by their commutation relations

$$[b_{q\eta}, F^\dagger_{\eta'}] = [b^\dagger_{q\eta}, F^\dagger_{\eta'}] = [b_{q\eta}, F_{\eta'}] = [b^\dagger_{q\eta}, F_{\eta'}] = 0 \tag{C.19}$$

for all q, η, η' and their action on a state $|\vec{N}\rangle = f(b^\dagger)|\vec{N}\rangle_0$ is given by

$$F^\dagger_\eta|\vec{N}\rangle \equiv f(b^\dagger)c^\dagger_{N_\eta+1}|N_1,\ldots,N_\eta,\ldots N_M\rangle_0 \equiv f(b^\dagger)\widehat{T}_\eta|N_1,\ldots,N_\eta+1,\ldots N_M\rangle_0 \ , \tag{C.20}$$

$$F_\eta|\vec{N}\rangle \equiv f(b^\dagger)c_{N_\eta}|N_1,\ldots,N_\eta,\ldots N_M\rangle_0 \equiv f(b^\dagger)\widehat{T}_\eta|N_1,\ldots,N_\eta-1,\ldots N_M\rangle_0 \ . \tag{C.21}$$

Putting this action in words, $F^\dagger_\eta$ (or F_η) commutes past $f(b^\dagger)$ and then adds (or removes) an η-electron to the lowest empty (from the highest occupied) η-level of $|\vec{N}\rangle_0$ resulting in a new ground state $c^\dagger_{N_\eta+1}|\vec{N}\rangle_0$ (or $c_{N_\eta}|\vec{N}\rangle_0$), on which the set of particle-hole excitations $f(b^\dagger)$ is then recreated.
The phase-counting operator

$$\widehat{T}_\eta \equiv (-)^{\sum_{\bar{\eta}=1}^{\eta-1}\widehat{N}_{\bar{\eta}}} \ . \tag{C.22}$$

keeps track of the number of signs picked up when acting with a fermion operator $c_{k\eta}$ on $|\vec{N}\rangle_0$ to obtain a different $|\vec{N}'\rangle_0$:

$$c_{k\eta}(C_1)^{N_1}\ldots(C_\eta)^{N_\eta}\ldots(C_M)^{N_M}|\vec{0}\rangle_0 = \widehat{T}_\eta(C_1)^{N_1}\ldots(C_{\eta-1})^{N_{\eta-1}}c_{k\eta}(C_\eta)^{N_\eta}\ldots(C_M)^{N_M}|\vec{0}\rangle_0 \ . \tag{C.23}$$

As a consequence of Eqs. (C.19) and (C.21) the spectrum of $\widehat{N}_\eta$ is unbounded from above or below (F_η is unitary: $F^{-1}_\eta = F^\dagger_\eta$) and the Klein factors obey the following commutation relations:

$$\left\{F^\dagger_\eta, F_{\eta'}\right\} = 2\delta_{\eta\eta'} \text{for all } \eta,\eta' \text{ (with } F_\eta F^\dagger_\eta = F^\dagger_\eta F_\eta = 1) \tag{C.24}$$

$$\left\{F^\dagger_\eta, F^\dagger_{\eta'}\right\} = \left\{F_\eta, F_{\eta'}\right\} = 0, \text{ for } \eta \neq \eta'; \tag{C.25}$$

$$\left[\widehat{N}_\eta, F^\dagger_{\eta'}\right] = \delta_{\eta\eta'}F^\dagger_\eta \ , \text{ and } \left[\widehat{N}_\eta, F_{\eta'}\right] = -\delta_{\eta\eta'}F_\eta \ . \tag{C.26}$$

C.4 Boson Fields – Definition and Properties

The boson fields $\phi_\eta(x)$ are defined as Fourier sums over the $b_{q\eta}$ and $b^\dagger_{q\eta}$ operators

$$\varphi_\eta(x) \equiv -\sum_{q>0}\frac{1}{\sqrt{n_q}}e^{-iqx}b_{q\eta}e^{-aq/2} \ , \tag{C.27}$$

$$\varphi^\dagger_\eta(x) \equiv -\sum_{q>0}\frac{1}{\sqrt{n_q}}e^{iqx}b^\dagger_{q\eta}e^{-aq/2}. \tag{C.28}$$

Their Hermitian combination thus reads

$$\phi_\eta(x) \equiv \varphi_\eta(x) + \varphi_\eta^\dagger(x) \;= -\sum_{q>0} \frac{1}{\sqrt{n_q}} \left(e^{-iqx} b_{q\eta} + e^{iqx} b_{q\eta}^\dagger \right) e^{-aq/2} \; . \tag{C.29}$$

Here $a > 0$ is an infinitesimal parameter needed to regularize ultraviolet ($q \to \infty$) divergent momentum sums that arise in certain non-normal-ordered expressions and commutators. Although a is often taken to be on the order of a lattice spacing, i.e. $a \simeq 1/k_F$, it was emphasized by Haldane [127] that it "in no way plays the role of a 'cut-off' length". Nevertheless, $1/a$ can be interpreted as a kind of "effective band-width" in the sense that it represents the "maximum momentum difference" for the $c_{k\pm q}^\dagger c_k$-combinations occuring in ϕ. By construction, $\varphi_\eta(x)$ and $\phi_\eta(x)$ are periodic in x with period L. All properties of these fields follow directly from those of the $b_{q\eta}$, $b_{q\eta}^\dagger$ operators.

C.5 Derivation of the Bosonization Identity

Since it is an eigenstate of $b_{q\eta}$, $\psi_\eta|\vec{N}\rangle_0$ is a boson coherent state. A short proof of this statement goes as follows.

By definition (see Eqs. (C.4) and (C.14)) $\psi_\eta(x)$ and $b_{q\eta}$ obey

$$[b_{q\eta'}, \psi_\eta(x)] = \delta_{\eta\eta'} \alpha_q(x) \psi_\eta(x) \; , \tag{C.30}$$

$$[b_{q\eta'}^\dagger, \psi_\eta(x)] = \delta_{\eta\eta'} \alpha_q^*(x) \psi_\eta(x) \; , \tag{C.31}$$

where $\alpha_q(x) = \frac{i}{\sqrt{n_q}} e^{iqx}$. Since $b_{q\eta}|\vec{N}\rangle_0 = 0$ [see Eq. (C.15)], Eq. (C.30) shows that $\psi_\eta(x)|\vec{N}\rangle_0$ is an eigenstate of the boson annihilation operator $b_{q\eta}$, with eigenvalue $\alpha_q(x)$:

$$b_{q\eta'} \psi_\eta(x)|\vec{N}\rangle_0 = \delta_{\eta\eta'} \alpha_q(x) \psi_\eta(x)|\vec{N}\rangle_0 \tag{C.32}$$

Hence this state must have a coherent-state representation of the form (see e.g. Ref. [195])

$$\psi_\eta(x)|\vec{N}\rangle_0 \;=\; \exp\left[\sum_{q>0} \alpha_q(x) b_{q\eta}^\dagger \right] F_\eta \hat{\lambda}_\eta(x)|\vec{N}\rangle_0 \;=\; e^{-i\varphi_\eta^\dagger(x)} F_\eta \hat{\lambda}_\eta(x)|\vec{N}\rangle_0 \; , \tag{C.33}$$

where Eq. (C.28) was used for the second equality. Since ψ_η removes exactly one η-particle, the Klein factor F_η is needed.

The operator $\hat{\lambda}_\eta(x)$ is given by

$$\hat{\lambda}_\eta(x) = \left(\frac{2\pi}{L} \right)^{1/2} e^{-i\frac{2\pi}{L}(\widehat{N}_\eta - \frac{1}{2}\delta_b)x}, \tag{C.34}$$

which can be seen evaluating the expectation value ${}_0\langle\vec{N}|F_\eta^\dagger \psi_\eta(x)|\vec{N}\rangle_0$ in two different ways

$${}_0\langle\vec{N}|F_\eta^\dagger \psi_\eta(x)|\vec{N}\rangle_0 = \lambda_\eta(x) \tag{C.35}$$

$$= \left(\frac{2\pi}{L} \right)^{1/2} e^{-i\frac{2\pi}{L}(N_\eta - \frac{1}{2}\delta_b)x} \; . \tag{C.36}$$

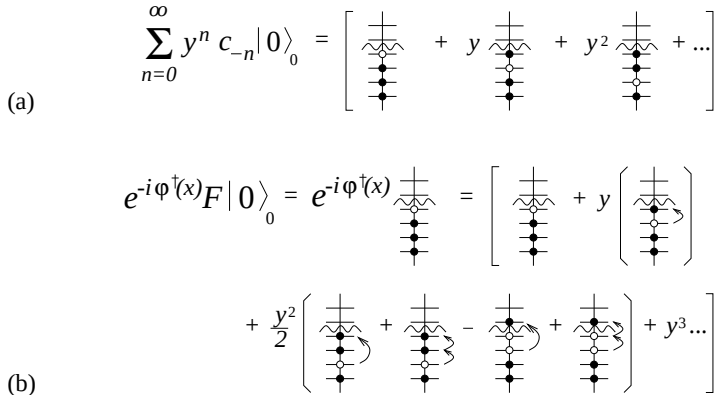

Figure C.1: The action of $\psi(x)$ on $|0\rangle_0$ is depicted in two different ways, using either (a) the Fourier expansion of Eq. (C.4), $\psi(x)|0\rangle_0 \sim \sum_{n=0}^{\infty} y^n c_{-n}|0\rangle_0$, where $y = e^{i2\pi x/L}$; or (b) the coherent state representation of Eq. (C.33), $\psi_\eta(x)|0\rangle_0 \sim e^{-i\varphi^\dagger(x)}F|0\rangle_0$. As discussed in detail in Ref. [59] the cancellations of prefactors guarantees that they are identical. Illustration taken from Ref. [59].

To obtain Eq. (C.35) we inserted Eq. (C.33) for $\psi_\eta(x)$, commuted $e^{-i\varphi^\dagger_\eta(x)}$ to the left past $F^\dagger_\eta$ [using Eq. (C.19)], and used ${}_0\langle\vec{N}|e^{-i\varphi^\dagger_\eta(x)} = {}_0\langle\vec{N}|$ [by Eq. (C.15)]. Eq. (C.36) can be derived replacing $\psi_\eta(x)$ by the Fourier series of Eq. (C.4) and observing that only the term with $n_k = N_\eta$ [i.e. $k = \frac{2\pi}{L}(N_\eta - \frac{1}{2}\delta_b)$] contributes.

As illustrated in Fig. C.1, Eq. (C.33) states that we can obtain two equivalent representations for the state $\psi(x)|0\rangle_0$ by either Fourier-expanding ψ using Eq. (C.4), or bosonizing it using Eq. (C.40). For a more elaborate discussion of the remarkable properties of Eq. (C.33) we refer to Ref. [59].

Now we want to focus on the action of $\psi_\eta(x)$ on an arbitrary state $|\vec{N}\rangle$. First, let us introduce two useful identities:

$$\psi_\eta(x) f(\{b^\dagger_{q\eta'}\}) = f(\{b^\dagger_{q\eta'} - \delta_{\eta\eta'}\alpha^*_q(x)\})\,\psi_\eta(x)\,, \tag{C.37}$$

$$f(\{b^\dagger_{q\eta'} - \delta_{\eta\eta'}\alpha^*_q(x)\}) = e^{-i\varphi_\eta(x)}\, f(\{b^\dagger_{q\eta'}\})\, e^{i\varphi_\eta(x)}. \tag{C.38}$$

The first follows from Eqs. (C.4) and the operator identity: "if $[A,B] = DB$ and $[A,D] = [B,D] = 0$, then $f(A)B = Bf(A+D)$", with $A = b^\dagger_{q\eta'} - \delta_{\eta\eta'}\alpha^*_q(x)$, $B = \psi_\eta(x)$ and $D = \delta_{\eta\eta'}\alpha^*_q(x)$. The second from Eq. (C.27) and the operator identity: "if $C \equiv [A,B]$ satisfies $[A,C] = [B,C] = 0$, then $e^{-B}f(A)e^B = f(A+C)$", with $A = b^\dagger_{q\eta'}$, $B = i\varphi_\eta(x)$ and $C = -\delta_{\eta\eta'}\alpha^*_q(x)$.

Now we may evaluate $\psi_\eta|\vec{N}\rangle$ by commuting ψ_η past $f(\{b^\dagger_{q\eta'}\})$, then inserting Eq. (C.33)

for $\psi_\eta|\vec{N}\rangle_0$, and finally rearranging

$$\begin{aligned}
\psi_\eta(x)|\vec{N}\rangle &= \psi_\eta(x)\, f(\{b^\dagger_{q\eta'}\})|\vec{N}\rangle_0 \\
&= f(\{b^\dagger_{q\eta'} - \delta_{\eta\eta'}\alpha^*_q(x)\})\, \psi_\eta(x)|\vec{N}\rangle_0 && \text{[by Eq. (C.37)]} \\
&= f(\{b^\dagger_{q\eta'} - \delta_{\eta\eta'}\alpha^*_q(x)\})\, e^{-i\varphi^\dagger_\eta(x)}\, F_\eta\hat{\lambda}_\eta(x)|\vec{N}\rangle_0 && \text{[by Eq. (C.33)]} \\
&= F_\eta\hat{\lambda}_\eta(x)\, e^{-i\varphi^\dagger_\eta(x)}\, f(\{b^\dagger_{q\eta'} - \delta_{\eta\eta'}\alpha^*_q(x)\})|\vec{N}\rangle_0 && \text{[by Eq. (C.19)]} \\
&= F_\eta\hat{\lambda}_\eta(x)\, e^{-i\varphi^\dagger_\eta(x)} \left[e^{-i\varphi_\eta(x)} f(\{b^\dagger_{q\eta'}\}) e^{i\varphi_\eta(x)}\right]|\vec{N}\rangle_0 && [byEq.\ (C.38)] \\
&= F_\eta\hat{\lambda}_\eta(x) e^{-i\varphi^\dagger_\eta(x)}\, e^{-i\varphi_\eta(x)}\, f(\{b^\dagger_{q\eta'}\})|\vec{N}\rangle_0 && [byEq.\ (C.15)] \\
&= F_\eta\hat{\lambda}_\eta(x)\, e^{-i\varphi^\dagger_\eta(x)} e^{-i\varphi_\eta(x)}|\vec{N}\rangle\ . && [byEq.\ (C.17)]
\end{aligned}$$

Since $|\vec{N}\rangle$ is an arbitrary state in the Fock space $\mathcal{F}$, (and *all* states in $\mathcal{F}$ have the form Eq. (C.17)), we conclude that the following so-called *bosonization formulas* for $\psi_\eta(x)$ hold as *operator identities* in Fock space, valid for all L (i.e. all orders in an $1/L$ expansion)

$$\psi_\eta(x) = F_\eta\hat{\lambda}_\eta(x) e^{-i\varphi^\dagger_\eta(x)} e^{-i\varphi_\eta(x)} \tag{C.39}$$

$$= F_\eta \left(\frac{2\pi}{L}\right)^{1/2} e^{-i\frac{2\pi}{L}(\widehat{N}_\eta - \frac{1}{2}\delta_b)x} e^{-i\varphi^\dagger_\eta(x)} e^{-i\varphi_\eta(x)} \tag{C.40}$$

$$= F_\eta\, a^{-1/2} e^{-i\frac{2\pi}{L}(\widehat{N}_\eta - \frac{1}{2}\delta_b)x} e^{-i\phi_\eta(x)} \tag{C.41}$$

$$= F_\eta\, a^{-1/2}\, e^{-i\Phi_\eta(x)} \qquad \text{with} \qquad \Phi_\eta(x) \equiv \phi_\eta(x) + \frac{2\pi}{L}(\widehat{N}_\eta - \frac{1}{2}\delta_b)x\ , \tag{C.42}$$

which is the central bosonization formula used throughout Sec. 12.2 (cf. Eq. (12.5)).

The different expressions for the bosonization formula presented above are all equivalent. Eq. (C.40) is the "most rigorous", since it is normal ordered and hence valid even for $a = 0$. Eq. (C.41) is the un-normal-ordered version of Eq. (C.40), obtained using

$$e^{i\varphi^\dagger_\eta(x)} e^{i\varphi_\eta(x)} = e^{i(\varphi^\dagger_\eta + \varphi_\eta)(x)} e^{[i\varphi^\dagger_\eta(x), i\varphi_\eta(x)]/2} = \left(\frac{L}{2\pi a}\right)^{1/2} e^{i\phi_\eta(x)}\ , \tag{C.43}$$

$$e^{-i\varphi_\eta(x)} e^{-i\varphi^\dagger_\eta(x)} = e^{-i(\varphi_\eta + \varphi^\dagger_\eta)(x)} e^{[-i\varphi_\eta(x), -i\varphi^\dagger_\eta(x)]/2} = \left(\frac{2\pi a}{L}\right)^{1/2} e^{-i\phi_\eta(x)} \tag{C.44}$$

and evidently requires $a \neq 0$ [which is needed when unnormalordering to evaluate $[\varphi, \varphi^\dagger]$ in Eq. (C.44)]. The most common form is Eq. (C.42), which absorbs the factor $e^{-i\frac{2\pi}{L}(\widehat{N}_\eta - \frac{1}{2}\delta_b)x}$ into the definition of a new Boson field $\Phi_\eta(x)$, following Haldane [127].

This completes the short overview over the step by step derivation of the bosonization formulas from first principles given in Ref. [59]. "Checks" for the validity of the bosonization formulas by using them to calculate, for example, the anti-commutator $\{\psi_\eta, \psi^\dagger_{\eta'}\}$ or the correlator $\langle\psi_\eta\psi^\dagger_{\eta'}\rangle$, are performed in Ref. [59].

Appendix D

Derivation of Scaling Laws for the Subohmic Two-Spin Boson Model

In this chapter, we derive scaling relations for the magnetization of the two-spin boson model for subohmic bath dispersion $s = \frac{1}{2}$. We proceed in the following manner. First, in Sec. D.1, we derive an effective spin action functional by integrating over the bosonic degrees of freedom. From this action we determine the scaling dimension of the spin operators in a mean-field approximation from which follow scaling laws in Sec. D.2.

D.1 Effective Spin Action Functional

An effective action functional $S_{\rm eff}$ for the spins can be obtained by integrating over the bosonic degrees of freedom using a functional integral description [195]. This can be done exactly, because the Hamiltonian of Eq. (13.1) is quadratic in bosonic operators.

We start with the action of the full system $S = S_S + S_B + S_{SB}$, where

$$S_S = \int_0^\beta d\tau \sum_{j=1}^{2} [\frac{\Delta_j}{2}\sigma_j^x(\tau) + \frac{\epsilon_j}{2}\sigma_j^z(\tau)] + \frac{K}{4}\sigma_1^z(\tau)\sigma_2^z(\tau) \tag{D.1}$$

depends on spin variables only, and

$$S_B = \int_0^\beta d\tau \sum_n a_n^*(\tau)[\frac{\partial}{\partial\tau} + \omega_n]a_n(\tau) \tag{D.2}$$

denotes the action of the free bath. The spin-bath interaction is described by

$$S_{SB} = \frac{1}{2}\int_0^\beta d\tau \sum_k \sum_{j=1}^{2} \lambda_n \sigma_j^z(\tau)[a_n^*(\tau) + a_n(\tau)]. \tag{D.3}$$

Here, $\beta = 1/T$ ($k_B = 1$) is an inverse temperature, τ is an imaginary time variable and $a(\tau)$ are the usual complex boson coherent state variables. Note that in the end we will take the zero temperature limit which is well-defined in this formalism [195].

Integrating over the (complex) bosonic variables [118] $\int \mathcal{D}[a_n^*(\tau), a_n(\tau)] \exp[-S_B - S_{SB}] = \exp[-S']$, leads to an effective spin action $S_{\rm eff} = S_S + S'$. In the zero temperature limit, it

takes the form

$$S_{\text{eff}} = \int_0^\infty d\tau \Big\{ \sum_{j=1}^{2} \Big[\frac{\Delta}{2} \sigma_j^x(\tau) + \frac{\epsilon_j}{2} \sigma_j^z(\tau) \Big] + \frac{K_r}{4} \sigma_1^z(\tau)\sigma_2^z(\tau) \Big\} \\ + \int_0^\infty \frac{d\tau d\tau'}{16\pi} \int d\omega J(\omega) e^{-\omega|\tau-\tau'|} \Big\{ \sum_{j=1}^{2} \Big[\sigma_j^z(\tau) - \sigma_j^z(\tau') \Big] \Big\}^2 . \tag{D.4}$$

The effect of the bosons on the spins is twofold: First, the Ising interaction constant gets renormalized to $K_r = K - 4\alpha\omega_c/s$ by the term that is local in imaginary time. Second, the bath introduces dissipation as described by the last term of Eq. (D.4), which is purely non-local in imaginary time. Integrating over frequency ω, we observe that this last term describes a *long-range interaction* in imaginary time

$$\int_0^\infty d\omega J(\omega) e^{-\omega|\tau-\tau|} = \frac{2\pi\alpha\omega_c^2 \Gamma(1+s)}{(1+\omega_c|\tau-\tau'|)^{1+s}} , \tag{D.5}$$

where $\Gamma(x)$ is the Gamma function and we have used an exponential cutoff for the spectral density $J(\omega) = 2\pi\alpha\omega_c^{1-s}\omega^s \exp[-\omega/\omega_c]$ for convenience.

Note that although the dissipative part still contains a term that couples the two different spins (at different times), this corresponds to a retarded Ising interaction and can thus be neglected compared to the equal-time contribution, if one is interested in ground-state properties. More specifically, the retarded term is of the form $\int d\tau d\tau' \frac{\sigma_1^z(\tau)\sigma_2^z(\tau')}{|\tau-\tau'|^{1+s}}$, which under a Fourier transformation becomes $\sum_{\omega_n} |\omega_n|^s \sigma_1^z(\omega_n)\sigma_2^z(-\omega_n)$. Thus, if we pass to real frequencies $\omega_n \to \omega + i\delta$ and take the low-frequency limit $\omega \to 0$ these terms can be neglected compared to the static Ising interaction part $\frac{K_r}{4}\sigma_1^z(\tau)\sigma_2^z(\tau)$. This reasoning can also be justified by noting that one arrives at the same formula for the renormalized Ising constant by applying the polaron unitary transformation to the Hamiltonian of Eq. (13.1) as we have presented in Sec. 13.2.2 (see Eq. (13.4)).

D.2 Scaling Analysis: Deriving Mean-Field Exponents

Below, we derive mean-field critical exponents from the effective spin action of Eq. (D.4), which we compare with exponents that we have extracted from our NRG calculations in Sec. 13.3.2.

To proceed, we resort to a mean-field-like decoupling of the Ising term $\frac{K_r}{4}\sigma_1^z(\tau)\sigma_2^z(\tau) \approx \frac{K_r}{4}[\sigma_1^z\langle\sigma_2^z\rangle + \langle\sigma_1^z\rangle\sigma_2^z]$. This term then acts as a single-spin detuning, depending on the expectation value of the other spin magnetization.

Scaling of both spins will thus be identical and we can follow the analysis for the single spin-boson model [162, 161, 129], and employ the quantum-to-classical mapping [196, 62, 175] of the spin-boson model to the one-dimensional classical Ising model

$$\hat{\mathcal{H}}_{\text{classical}} = -\sum_{i,j} J_{ij} \hat{S}_i^z \hat{S}_j^z + \hat{\mathcal{H}}_{\text{short-range}} \tag{D.6}$$

with long-range interaction $J_{ij} = J/|i-j|^{1+s}$. Here, $\hat{S}_i^z = \pm 1$ are classical Ising spins. There is an additional generic short-range interaction $\hat{\mathcal{H}}_{\text{short-range}}$ arising from the transverse field, but

it is believed to be irrelevant for the critical behavior [197, 198, 199]. The scaling dimensions of $\sigma^z_{1,2}$ are thus solely determined by the dissipative term, and we find from the condition that the total action is dimensionless $[S] = 1$ that

$$[\sigma^z_{1,2}] = T^{\frac{1-s}{2}} \tag{D.7}$$

Here, we have used units of energy (or temperature): $[\tau] = T^{-1}$. From this follows the scaling dimension of the detuning and Ising constants as

$$[\epsilon] = T^{\frac{1+s}{2}}, \qquad [K] = T^s\,. \tag{D.8}$$

In order to derive scaling relations, we need to make an ansatz for the impurity part of the free energy. Since the fixed point is "interacting" for $s > 1/2$, [161, 200] we use

$$F_{\text{imp}} = T f(|\Delta - \Delta_c| T^{-1/\nu}, \epsilon T^{-b}, |K - K_c| T^{-\kappa})\,. \tag{D.9}$$

This ansatz can be applied for $s < 1$ since the transition is continuous. Further, for a Gaussian fixed point, which occurs at $s < 1/2$, the reduced free energy would also depend on dangerously irrelevant variables.

In this ansatz we have used that in a quantum phase transition, which occurs at $T = 0$, the distance to criticality is measured by the parameter deviation from the critical value of the most relevant perturbation, in this case $|\Delta - \Delta_c|$. Analogous to a classical system, where the correlation length diverges as a function of this distance, here the correlation length in imaginary time obeys $\xi \sim |\Delta - \Delta_c|^{-\nu}$ with the correlation length exponent ν. The dynamic critical exponent is formally set equal to $z = 1$ in this $0+1$-dimensional system. This defines a characteristic energy scale

$$T^* \equiv \xi^{-1} \sim |\Delta - \Delta_c|^{\nu} \tag{D.10}$$

above which critical behavior is observed [175].

Using the ansatz for the free energy given in Eq. (D.9), we can immediately infer from $[\epsilon T^{-}b] = [|K - K_c| T^{-\kappa}] = 1$ that $b = \frac{1+s}{2}$ and $\kappa = s$. If we define the critical exponents describing the scaling of the magnetization as

$$\langle \sigma^z_{1,2} \rangle \sim |\Delta - \Delta_c|^{\beta} \tag{D.11}$$

$$\langle \sigma^z_{1,2} \rangle \sim |\epsilon_{1,2}|^{1/\delta} \tag{D.12}$$

$$\langle \sigma^z_{1,2} \rangle \sim |K - K_c|^{\zeta}\,, \tag{D.13}$$

we can derive scaling relations. For instance from Eqs. (D.8), (D.8) it immediately follows that

$$\delta_{MF} = \frac{1+s}{1-s}, \qquad \zeta_{MF} = \frac{1-s}{2s}\,. \tag{D.14}$$

We have to invoke Eq. (D.10) to arrive at

$$\beta_{MF} = \nu\Big(\frac{1-s}{2}\Big)\,. \tag{D.15}$$

If we use the result that $\nu = 1/s$ for small s, derived in Ref. [197], we find that $\zeta_{MF} = \beta_{MF}$. Close to $s = 1$ it is more appropriate to use $1/\nu = \sqrt{2(1-s)}$ as obtained in Ref. [201]. The resulting values for the critical exponents are shown in Table 13.1.

Appendix E

Mapping the Two-Spin Boson Model to the Fermionic Resonant Level Model

In this Appendix we provide details of the mapping of the two-spin boson model to the fermionic resonant level model. Due to the Jordan-Wigner string, the corresponding fermionic model remains interacting at the Toulouse point in the case of two spins.

Using bosonization techniques (see App. C), one can map the two-spin boson Hamiltonian in Eq. (13.1) with an ohmic spectral density $J(\omega) = 2\pi\alpha\omega \exp[-\omega/\omega_c]$ onto a fermionic resonant level model, which describes a central region (dot) coupled via tunneling to free spinless electrons in the lead. The number of spins in the spin-boson model is equal to the number of levels on the dot, and the number of bosonic baths is equal to the number of leads.

Our starting point is the two-spin boson Hamiltonian in Eq. (13.1)

$$\hat{\mathcal{H}}_{2SB} = \sum_n \omega_n \left(\hat{a}_n^\dagger \hat{a}_n + \frac{1}{2} \right) + + \sum_{\alpha=1}^{2} \left\{ \frac{\hat{\sigma}_\alpha^z}{2} \sum_n \lambda_{\alpha,n} \left(\hat{a}_n + \hat{a}_n^\dagger \right) + \Delta_\alpha \frac{\hat{\sigma}_\alpha^x}{2} + \varepsilon_\alpha \frac{\hat{\sigma}_\alpha^z}{2} \right\} + \frac{K}{4} \hat{\sigma}_1^z \hat{\sigma}_2^z . \tag{E.1}$$

To obtain the mapping to the resonant level model (and similarly to the Kondo model), where the bath consists of free fermions, we choose the oscillator dispersion to be linear $\omega_k = v_F k$, with Fermi velocity v_F, and the coupling constants

$$\lambda_k = -\sqrt{\alpha} 2 v_F \Big[\frac{\pi k}{L} \Big]^{1/2} e^{-\omega_k/2\omega_c} . \tag{E.2}$$

The bath spectral density $J(\omega) = \pi \sum_{k>0} \lambda_k^2 \delta(\omega - \omega_k)$ is then of ohmic form $J(\omega) = 2\pi\alpha\omega \exp(-\omega/\omega_c)$ up to an exponential cutoff at ω_c. If we insert this into Eq. (E.1), the spin-bath coupling term becomes

$$\sum_{j=1}^{2} \pi \hat{\sigma}_j^z \sum_{k>0} \Big[-\sqrt{2\alpha} v_F \Big] \Big[\frac{k}{2\pi L} \Big]^{1/2} e^{-ak/2} (\hat{a}_k^\dagger + \hat{a}_k) , \tag{E.3}$$

where we have defined the small distance cutoff $a = k_c^{-1} = v_F/\omega_c$.

We now apply a unitary (Luther-Emery) transformation to the Hamiltonian: $\hat{\tilde{\mathcal{H}}}_{\rm 2SB} = U_\gamma \hat{\mathcal{H}}_{\rm 2SB} U_\gamma^{-1}$ where $U_\gamma = \exp\Big[\frac{\gamma}{2}\sum_{j=1}^{2}\hat{\sigma}_j^z \xi\Big]$ with

$$\xi = \sum_{k>0} e^{-ak/2}\Big[\frac{4\pi}{kL}\Big]^{1/2}(\hat{a}_k - \hat{a}_k^\dagger)\,. \tag{E.4}$$

Evaluating this transformation term by term, and performing the sum over wavevectors $\frac{\pi v_F}{L}\sum_{k>0} e^{-ak} = \frac{v_F}{2a} = \frac{\omega_c}{2}$, one finally obtains the Hamiltonian

$$\begin{aligned}\hat{\tilde{\mathcal{H}}}_{\rm 2SB} = \sum_{j=1}^{2}\Big\{\frac{\Delta_j}{2}\big(\hat{\sigma}_j^+ e^{\gamma\xi} + \text{h.c.}\big) + \frac{\varepsilon_j}{2}\hat{\sigma}_j^z + \pi v_F(\sqrt{2}\gamma - \sqrt{2\alpha})\hat{\sigma}_j^z \sum_{k>0} e^{-ak/2}\Big[\frac{k}{2\pi L}\Big]^{1/2}(\hat{a}_k + \hat{a}_k^\dagger)\Big\} \\ + v_F\sum_{k>0} k\left(\hat{a}_k^\dagger\hat{a}_k + \frac{1}{2}\right) + \big(K + 4\omega_c\gamma^2 - 8\omega_c\sqrt{\alpha}\gamma\big)\frac{\hat{\sigma}_1^z\hat{\sigma}_2^z}{4}\,.\end{aligned} \tag{E.5}$$

One can show that a particular combination of the Bose operators $\hat{a}_k, \hat{a}_k^\dagger$ can be made into an anticommuting Fermi field $\psi(x) = \frac{1}{\sqrt{2\pi a}}\exp j(x)$ with [62]

$$j(x) = \sum_{k>0} e^{-ak/2}\Big[\frac{2\pi}{kL}\Big]^{1/2}(b_k e^{ikx} - b_k^\dagger e^{-ikx})\,. \tag{E.6}$$

The coefficients have been chosen such that $[j(x), j(y)] = -i\pi\,\text{sign}(x-y)$ for $a \to 0$ and thus $\{\exp \pm j(x), \exp \pm j(y)\} = 0$, for $x \neq y$. Choosing $\gamma = 1/\sqrt{2}$, one can thus identify the exponential $\exp[\xi/\sqrt{2}]$ which multiplies $\hat{\sigma}_{1,2}^+$ in Eq. (E.5) as a localized spinless fermionic field $\psi(0) = (2\pi a)^{-1/2}\exp\xi/\sqrt{2}$. The bosonic oscillator degrees of freedom are then interpreted as the density excitations $\hat{\rho}(k) = \sum_p \hat{c}_{p+k}^\dagger \hat{c}_p$, $\hat{\rho}(-k) = \hat{\rho}^\dagger(k)$ of the fermions $\psi(x) = L^{-1/2}\sum_{k>0}\hat{c}_k e^{ikx}$ via the bosonization identity $\hat{a}_k = \Big[\frac{2\pi}{kL}\Big]^{1/2}\hat{\rho}(-k)$ [62].

Using refermionization we can replace the free bosonic with a free fermionic Hamiltonian $v_F\sum_{k>0} k\hat{a}_k^\dagger\hat{a}_k \to v_F\sum_{k>0} k\hat{c}_k^\dagger\hat{c}_k$ and

$$\sum_{k>0} e^{-ak/2}\Big[\frac{k}{2\pi L}\Big]^{1/2}(\hat{a}_k + \hat{a}_k^\dagger) = \sum_{k>0}\frac{e^{-ak/2}}{L}[\hat{\rho}(-k) + \hat{\rho}(k)] = :\psi^\dagger(0)\psi(0):\,, \tag{E.7}$$

where $:\psi^\dagger(0)\psi(0):= \psi^\dagger(0)\psi(0) - \langle\psi^\dagger(0)\psi(0)\rangle$ denotes normal ordering. Finally, we write the spin operators in terms of fermionic dot operators using the Jordan-Wigner transformation (in symmetric form)

$$\hat{\sigma}_1^- = [1 - (1-i)\hat{n}_2]\hat{d}_1 \tag{E.8}$$

$$\hat{\sigma}_2^- = [1 - (1+i)\hat{n}_1]\hat{d}_2 \tag{E.9}$$

$$\hat{\sigma}_j^z = 2\hat{n}_j - 1\,,\text{for } j = 1, 2\,. \tag{E.10}$$

We note that a less symmetric form of the transformation is equivalent. The Hamilto-

nian (E.1) thus reads in terms of fermionic fields as

$$\hat{\mathcal{H}}_{\mathrm{RL}} = v_F \sum_{k>0} k \hat{c}_k^\dagger \hat{c}_k + \sum_{j=1}^{2} V_j \left[\hat{d}_j^\dagger \psi(0) + \mathrm{h.c.}\right] - \left[V_2(1-i) n_1 \hat{d}_2^\dagger \psi(0) + V_1(1+i)\hat{n}_2 \hat{d}_1^\dagger \psi(0) + \mathrm{h.c.}\right] + \sum_{j=1}^{2} \varepsilon_j \hat{d}_j^\dagger \hat{d}_j + 2U \sum_{j=1}^{2} \left(\hat{d}_j^\dagger \hat{d}_j - \frac{1}{2}\right) : \psi^\dagger(0)\psi(0) : + K_{\mathrm{RL}} \left(\hat{d}_1^\dagger \hat{d}_1 - \frac{1}{2}\right)\left(\hat{d}_2^\dagger \hat{d}_2 - \frac{1}{2}\right), \tag{E.11}$$

with tunneling coupling constant $V_j = \frac{\Delta_j}{2}\left(\frac{1}{\rho\omega_c}\right)^{1/2}$, dot-lead interaction $U = (1-\sqrt{2\alpha})/2\rho$ and onsite coupling $K_{\mathrm{RL}} = K + 2\omega_c(1-2\sqrt{2\alpha})$. The interaction parameters U and K_{RL} vanish at the Toulouse point $\alpha = 1/2$ and $K = 2\omega_c$. The additional interaction term $\left[V_2(1-i) n_1 \hat{d}_2^\dagger \psi(0) + V_1(1+i)\hat{n}_2 \hat{d}_1^\dagger \psi(0) + \mathrm{h.c.}\right]$, however, is proportional to the tunneling couplings V_j and remains present at the Toulouse point. As a result, the fermionic model cannot be solved exactly.

Miscellaneous

Publications

Part of the results presented in this thesis was already published in the following articles:

Björn Kubala, David Roosen, Michael Sindel, Walter Hofstetter, and Florian Marquardt,
Decoherence in a Double-Dot Aharonov-Bohm Interferometer,
preprint. [arXiv:1011.3518]

Peter P. Orth, David Roosen, Walter Hofstetter, and Karyn Le Hur,
Dynamics, Synchronization and Quantum Phase Transitions of Two Dissipative Spins,
Physical Review B **82**, 144423 (2010). [arXiv:1007.2857]

Aldo Isidori, David Roosen, Lorenz Bartosch, Walter Hofstetter, and Peter Kopietz,
Spectral function of the Anderson impurity model at finite temperatures,
Physical Review B **81**, 23512 (2010). [arXiv:1003.3188]

Andreas Hackl, David Roosen, Stefan Kehrein, and Walter Hofstetter,
Nonequilibrium Spin Dynamics in the Ferromagnetic Kondo Model,
Physical Review Letters **102**, 196601 (2009). [arXiv:0903.1079]

David Roosen, Maarten R. Wegewijs, and Walter Hofstetter,
Nonequilibrium Dynamics of Anisotropic Large Spins in the Kondo Regime: Time-Dependent Numerical Renormalization Group Analysis,
Physical Review Letters **100**, 087201 (2008). [arXiv:0705.3654]

Curriculum Vitae

Name	David Roosen
Date of birth	06 May 1980
Place of birth	Mönchengladbach
Nationality	German

Education

Sept. 1986 - June 1990	Kath. Will Sommer Grundschule in Mönchengladbach
Aug. 1990 - June 1999	Gymnasium Rheindahlen in Mönchengladbach
Sept. 1996 - Feb. 1997	Visiting student at the St. Francis High School in Traverse City, Michigan, USA
June 1999	Abitur
Oct. 1999 - May 2000	Civil services

Studies

Oct. 2000 - Sept. 2006	Study of physics at the RWTH Aachen
Oct. 2003 - June 2004	Visiting student at the Universidad Autónoma de Madrid in Madrid, Spain
Dec. 2005 - Sept. 2006	Diploma thesis supervised by Prof. W. Hofstetter *Time-dependent numerical renormalization group for quantum impurity models*
Sept. 2006	Diploma in physics
since Sept. 2006	PhD studies in the group of Prof. W. Hofstetter at the J. W. Goethe-Universität Frankfurt am Main

Acknowledgments

I would like to take this opportunity to thank persons.

First of all I would like to thank Prof. Walter Hofstetter for giving me the opportunity to work on my thesis in his group. Without his support and guidance throughout the last years this work would not have been possible.

Furthermore I would like to express my gratitude to all the people I collaborated with. I would like to mention Karyn Le Hur, who guided me through the maze of the physics of the spin-boson model, as well Peter P. Orth for keeping the good spirit in our collaboration. I also want to mention Andreas Hackl and Stefan Kehrein for a very productive collaboration on the ferromagnetic Kondo model, as well as Björn Kubala and Florian Marquardt for taking the time to explain their ideas and motivations. Thank you Aldo Isidori, Lorenz Bartosch and Peter Kopietz for a very efficient way of collaborating, and Maarten M. Wegewijs for sharing his knowledge about single molecular magnets with me.

To Irakli Titvinidze, who I shared a room with for the last years. Thank you for all of the discussions, your suggestions and the time you took to help. Thanks also to the other members of our group for making the institute a place I enjoyed working at, especially Daniela Wirth-Pagano for her organizing skills, but equally important Denis Semmler, Ulf Bissbort, Julia Wernsdorfer, Reza Bakthiari, Antonio Privitera, Michiel Snoek, Csaba Toke, Yongqiang Li, Liang He, Falk May, Christoph Eichler, Andreas Hubener, the IT-crowd: Andreas Kreisel, Thomas Weber, Alexander Achenbach, Andrea Salguero and everyone I forgot to mention.

Of course, I would also like to thank my family for their encouragement and support. Last but not least, I would like to express my deepest gratitude to Isabella for her love, patience and support.

Deutsche Zusammenfassung

Die fortschreitende Miniaturisierung elektronischer Bauteile stößt an ihre Grenzen. Die einzelnen Strukturen, welche für die Herstellung integrierter Schaltungen in verschiedenen Halbleitern benötigt werden, schrumpfen immer mehr und könnten in den nächsten Jahren die Größenordnung einzelner Atomen erreichen. Spätestens dann wird die Physik der Nanostrukturen auch im Alltag durch neuartige Technologie an Bedeutung gewinnen.

Die vorliegende Doktorarbeit beschäftigt sich mit der Physik von Quantenstörstellenmodellen. Diese Art der Modelle verbindet ein identischer Aufbau: die Störstelle besteht aus einem relativ simplen Teilsystem aus nur wenigen Atomen (z.B. einem einzelnen Molekül), welches meist exakt beschrieben werden kann. Die Komplexität der Beschreibung entsteht erst aus der Anbindung dieser Störstelle an eine sehr große Anzahl quantenmechanischer Teilchen. Diese Teilchen können, im Fall einer Anbindung an elektronische Leiter, Elektronen sein. Genauso gut kann es sich aber auch um quantisierte Schwingungen (sogenannte Phononen) oder andere Teilchen, die einer bosonischen Statistik genügen, handeln. Diese große Anzahl wechselwirkender Teilchen macht eine exakte Lösung der Heisenberg-Gleichungen auch numerisch unmöglich. Ebenso ist es in vielen Fällen nicht möglich die auftretenden physikalischen Effekte, wie zum Beispiel den Kondo Effekt, bei dem eine große Anzahl von Elektronen aus dem fermionischen Bad eine "Wolke" bildet, welche das freie magnetische Moment der Störstelle abschirmt, störungstheoretisch zu beschreiben und zu erklären.

Die Arbeit ist wie folgt strukturiert: Im ersten Teil wird der dominante physikalische Effekt, der Kondo Effekt, eingeführt und verständlich gemacht. Des Weiteren werden in diesem Teil die experimentellen Fortschritte, die eine kohärente Kontrolle einzelner Spins ermöglichen, anhand einer Auswahl aktueller experimenteller Arbeiten erläutert. Zu guter letzt werden zwei weitere experimentelle Arbeiten vorgestellt, die einen kurzen Einblick in das spannende Gebiet der molekularen Elektronik bieten.

Der zweite Teil der Arbeit führt die Methode ein mithilfe derer ein Großteil der Ergebnisse erlangt wurden: die *numerische Renormierungsgruppe*. Die numerische Renormierungsgruppe ist eine Methode, die im Gegensatz zu vielen anderen Methoden der Renormierungsgruppe, frei von störungstheoretischer Behandlung aller Systemparameter ist. Sie hat sich deshalb, seit ihrer erstmaligen Anwendung in den 1970er Jahren, zu einem Standardwerkzeug der computergestützten Physik entwickelt. Mit ihrer Hilfe lassen sich Korrelationseffekte in Quantenstörstellenmodellen bei Temperaturen nahe des absoluten Nullpunktes sehr gut beschreiben. Nach einer allgemeinen Einführung in die Grundkonzepte sowohl für fermionische als auch für bosonische Bäder, werden relevante kürzlich eingeführte Erweiterungen der numerischen Renormierungsgruppe erläutert. Hierzu zählen die Dichte-Matrix Numerische Renormierungsgruppe, die geschickte Wahl einer vollständigen Eigenbasis des Fock-Raumes, die zeitabhängige Numerische Renormierungsgruppe, sowie die Berücksichtigung endlicher Temperaturen und einiger Tricks zur Verbesserung der Genauigkeit der berechneten Ergebnisse.

Der dritte Teil der Arbeit beinhaltet die Anwendung der numerischen Renormierungsgruppen-Methoden auf verschiedene Quantenstörstellenmodelle. Dies ist der Hauptteil und beleuchtet die wissenschaftliche Arbeit, welche während der vergangenen Jahre geleistet wurde. Die untersuchten Modelle werden jeweils erläutert und separat motiviert, bevor die Ergebnisse der eingehenden Analysen dargelegt werden.

Dieser Hauptteil lässt sich in folgende Kapitel, die einen Überblick über die untersuchten Themenbereiche erlauben, unterteilen:

- Ferromagnetisches Kondo Modell,
- Spin-Dynamik im anisotropen Kondo und Spin-Boson Modell,
- Zwei gekoppelte Spins in einem bosonischen Bad,
- Dekohärenz in einem Aharanov-Bohm Interferometer.

Eine kurze Erklärung der einzelnen Themenbereiche sowie eine Zusammenfassung der wichtigsten Ergebnisse der im Rahmen der vorliegenden Doktorarbeit durchgeführten Forschung wird in den folgenden Abschnitten gegeben.

Ferromagnetisches Kondo Modell

Am Anfang des Teils über die Anwendungen der numerischen Renormierungsgruppe steht die Untersuchung des ferromagnetischen Kondo Modells. Dieses Modell beschreibt einen einzelnen Spin, welcher ferromagnetisch an die Spins der Elektronen in den elektronischen Zuleitungen koppelt. Eine experimentelle Realisierung dieses Modells kann zum Beispiel durch die Anbindung eines molekularen Magneten an elektronische Leitungen geschehen. Wir analysieren die zeitliche Entwicklung des Spins, welcher sich zu Anfang (zum Zeitpunkt $t = 0$) in einem polarisierten Zustand befindet. Dazu verwenden wir die zeitabhängige numerische Renormierungsgruppe. Aufgrund der nur sehr geringen relativen Änderung der Spinausrichtung (und damit der Magnetisierung der Störstelle) ist eine Feinabstimmung der Parameter der Methode unabdingbar. Diese Abstimmung gelang und wir konnten unsere numerischen Ergebnisse mit den "exakten" analytischen Ergebnissen der erweiterten Flussgleichungs-Methode vergleichen. Beide Methoden weisen eine ausreichend hohe Genauigkeit auf und erlauben einen guten quantitativen Vergleich der Ergebnisse.

Im Fall des isotropen, ferromagnetischen Kondo Modells finden wir eine logarithmische Reduktion der Spin-Magnetisierung, wohingegen eine anisotrope, ferromagnetische Anbindung des Störstellen-Spins an das elektronische Bad zu einem algebraischen Abfall der Magnetisierung führt. Des Weiteren zeigen wir, dass die asymptotischen Werte der Spin-Magnetisierung, die durch die Entwicklung eines nicht-Gleichgewichtszustandes entstehen, von den erwarteten Gleichgewichts-Magnetisierungen abweichen. Mit Hilfe beider Methoden, der erweiterten Flussgleichungs-Methode und der zeitabhängigen numerischen Renormierungsgruppe, bestätigen wir, dass die Störstelle auch für asymptotisch lange Zeiten, ein "Gedächtnis" ihres Anfangszustandes beibehält. Dies führen wir auf eine Kombination der Präperation in einem nicht-Gleichgewichtszustand und der bereits im Gleichgewichts-System gebrochenen Ergodizität zurück.

Spin-Dynamik im anisotropen Kondo und Spin-Boson Modell

In diesem Teil der Arbeit vergleichen wir die statischen und zeitabängige Magnetisierung der Störstellen in zwei unterschiedlichen Quantenstörstellenmodellen: dem anisotropen Kondo und dem ohmschen Spin-Boson Modell. Das erste Modell beschreibt einen Spin-Freiheitsgrad, welcher anisotrop an ein Bad fermionischer Elektronen koppelt, das zweite Modell hingegen stellt ein Spin, welcher mit einem Bad bosonischer Teilchen wechselwirkt dar. Die statischen, longitudinalen Spin-Magnetisierungen der beiden Modelle können durch die Abbildung des fermionischen Modells auf das bosonische im Rahmen der Bosonisierung miteinander in Verbindung gebracht werden. Hier überprüfen wir nun, ob diese Äquivalenz auch auf die Magnetisierung der beiden Störstellen außerhalb des statischen Gleichgewichts angewandt werden kann. Als Ergebnis kann festgehalten werden, dass dies – zu Teilen auch quantitativ – der Fall ist. In allen untersuchten Bereichen der Wechselwirkungsstärken zwischen Störstelle und Bad finden wir eine identische funktionale Beschreibung der Zeitentwicklungen der longitudinalen Magnetisierungen, während unterschiedliche quantitative Werte für Oszillationsfrequenzen und Zeitskalen der Relaxation in allen Bereichen, die vom sogenannten Toulouse Punkt abweichen, gefunden werden. Diese Ergebnisse rechtfertigen die Anwendung der Bosonisierung zum Vergleich der longitudinalen Störstellen-Magnetisierung auch weit außerhalb des Gleichgewichts.

Darüber hinaus haben wir dargelegt, dass die Verschränkung des Störstellen-Spins mit dem jeweiligen Bad von der Art des Bades abhängt. Im Falle des anisotropen Kondo Modells lässt sich die Verschränkungs-Entropie vollständig durch Kenntnis der longitudinalen Magnetisierung berechnen. Die Verschränkung des Spins mit dem bosonischen Bad im Spin-Boson Modell hingegen ist ohne Kenntnis der vollen reduzierten Dichtematrix der Störstelle $\rho_A(t)$ nicht möglich. Wir zeigen, dass für kleine Kopplungen des zentralen Spins an das bosonische Bad α der Beitrag der transversalen Spin-Magnetisierung $\langle \sigma_x(t \to \infty) \rangle$ sogar die zeitabhängige Verschränkungsentropie bei großen Zeiten dominiert.

Zwei gekoppelte Spins in einem bosonischen Bad

Wir behandeln ein System aus zwei direkt gekoppelten Spins, welche mit einem einzelnen bosonischen Bad wechselwirken. Die direkte Kopplung der beiden Spins ist hierbei vom Ising-Typ, d.h. nur die beiden z-Komponenten des Spins koppeln aneinander. Ausführlich beleuchten wir sowohl die Gleichgewichts- als auch die nicht-Gleichgewichts-Situation für den Fall einer ohmschen und einer subohmschen Dispersion der bosonischen Anregungen.

Zuerst berechnen wir das Phasendiagramm des Systems im Grundzustand für ohmsches und subohmsches Bad. Hierbei benutzen wir eine Kombination verschiedener Methoden: die numerische Renormierungsgruppe für bosonische Bäder, verschiedene analytische Techniken und intuitive Argumenten. Im Anschluss daran benutzen wir die zeitabhängige numerische Renormierungsgruppe, um das reichhaltige dynamische Verhalten des Systems, welches aus dem komplexen Zusammenspiel der Spin-Spin und der Spin-Bad Wechselwirkung entsteht, genauer zu verstehen. Interessanterweise können voneinander unabhängige Oszillationen der beiden Spins durch die Kopplung an ein gemeinsames nicht-Markov'sches Bad synchronisieren. Ebenso kann das System auch in komplizierte, hochgradig verschränkte Zustände relaxieren, sofern man die Anfangszustände der beiden Spins und des Bades richtig präpariert. Unsere numerischen Ergebnisse für dieses Zwei-Spin-System haben wir, sofern sie vorhanden waren, mit exakten analytischen Rechnungen verglichen. Wir geben quantitative Werte für die Grenzen der Anwendbarkeit des störungstheoretischen Bloch-Redfield Ansatzes bei schwacher Kopplung an das bosonische Bad.

Dekohärenz in einem Aharanov-Bohm Interferometer

In dem zuletzt beschriebenen Projekt der Doktorarbeit untersuchen wir den Einfluß einer einzelnen Phonon-Mode auf die elektronische Leitfähigkeit in einem Aharanov-Bohm Interferometer. Das Interferometer besteht aus zwei Quantenpunkten, welche parallel zueinander an zwei verschiedenen Elektroden koppeln. Die beiden Quantenpunkte koppeln an eine gemeinsame Phonon-Mode. Unser Interesse bei dieser Untersuchung gilt dem Einfluß des Phonons auf die elektrische Leitfähigkeit, wenn wir eine Wechselspannung anlegen. Insbesondere fokussieren wir unsere Untersuchung auf den Fall eines symmetrischen, destruktiven Interferometers, für das der elektrische Transport durch das Interferometer ausschließlich aufgrund dekohärenter Prozesse zustande kommt. Dazu benutzen wir die numerische Renormierungsgruppe, um mit Hilfe des Kubo-Formalismus die lineare Leitfähigkeit zu berechnen.

Unsere numerischen Ergebnisse bestätigen zu großen Teilen, die ebenfalls durchgeführten analytischen Rechnungen, für die die eine nicht-Gleichgewichts-Erweiterung der Methode der Green'schen Funktionen (nonequilibrium Green's function method) heran gezogen wird. Im

Gegensatz zu dem Fall, bei dem eine Gleichspannung an dem Interferometer anliegt, finden wir im Falle einer anliegenden Wechselspannung eine endliche Leitfähigkeit, auch wenn die Frequenz der Wechselspannung unterhalb der Anregungsenergie des Phonons liegt. Das heißt, dass der Transport auch ohne direkte Anregung eines Phonons möglich ist (dies ist analog zum Fall eines Plattenkondensators, bei dem die elektrostatische Wechselwirkung ebenfalls zu einem endlichen Strom führt, wenn man eine Wechselspannung anlegt, welcher aber eine verschwindend geringe Leitfähigkeit bei anliegender Gleichspannung aufweist). Ebenso bestätigen wir durch unsere Rechnungen das störungstheoretische Argument, nach dem kein inkohärenter Transport bei sehr kleinen Wechselspannungsfrequenzen, Temperaturen und Spannungen möglich ist. Dies ist gleichbedeutend mit der Aussage, dass in einer störungstheoretischen Betrachtung alle Terme höherer Ordnung in der Wechselwirkung zwischen den Elektronen auf den Quantenpunkten und dem einzelnen Phonon verschwinden. Das Maximum des Realteils der Leitfähigkeit durch das Interferometer untersuchen wir sehr gründlich und finden, dass es mit dem Quadrat der Elektron-Phonon-Wechselwirkungsstärke skaliert und bei starker Wechselwirkung zu kleineren Wechselstromfrequenzen verschoben wird. Diese Verschiebung erinnert an eine Verschiebung aufgrund von Polaronen. Zu guter Letzt finden wir in unseren numerischen Rechnungen auch endliche Leitfähigkeiten bei hohen Frequenzen, die durch gleichzeitige Anregung mehrerer Phononen zustande kommt.

Erklärung

Hiermit erkläre ich, dass die vorliegende Arbeit von mir selbst angefertigt wurde, dass ich dies selbständig getan und dabei andere als die angegebenen Quellen nicht verwendet habe. Die den benutzten Werken wörtlich oder inhaltlich entnommenen Stellen sind als solche kenntlich gemacht.

Frankfurt, den 4. August 2011